Guidelines to Develop Efficient Photocatalysts for Water Splitting

Dissertation by

Angel Tonatiuh Garcia Esparza

In Partial Fulfillment of the Requirements

For the Degree of

Doctor of Philosophy

King Abdullah University of Science and Technology

Thuwal, Kingdom of Saudi Arabia

The dissertation of Angel Tonatiuh Garcia Esparza is approved by the examination committee.

Committee Chair	Prof. Kazuhiro Takanabe
Committee Member	Prof. Akihiko Kudo
Committee Member	Prof. Mohamed Eddaoudi
Committee Member	Prof. Osman M. Bakr

King Abdullah University of Science and Technology

2016

ABSTRACT

Guidelines to Develop Efficient Photocatalysts for Water Splitting

Angel Tonatiuh Garcia Esparza

Photocatalytic overall water splitting is the only viable solar-to-fuel conversion technology. The research discloses an investigation process wherein by dissecting the photocatalytic water splitting device, electrocatalysts, and semiconductor photocatalysts can be independently studied, developed and optimized. The assumption of perfect catalysts leads to the realization that semiconductors are the limiting factor in photocatalysis. This dissertation presents a guideline for efficient photocatalysis using semiconductor particles developed from idealized theoretical simulations. No perfect catalysts exist; then the discussion focus on the development of efficient non-noble metal electrocatalysts for hydrogen evolution from water reduction. Tungsten carbide (WC) is selective for the catalysis of hydrogen without the introduction of the reverse reaction of water formation, which is critical to achieving photocatalytic overall water splitting as demonstrated in this work. Finally, photoelectrochemistry is used to characterize thoroughly Cu-based *p*-type semiconductors with potential for large-scale manufacture. Artificial photosynthesis may be achieved by following the recommendations herein presented.

ACKNOWLEDGMENTS

“He who would learn to fly, one day must first learn to stand and walk and run and climb and dance; one cannot fly into flying”

—Friedrich Nietzsche

A transition from Mechatronics, to Environmental Science, to a Ph.D. in Chemical Science, does not occur without a struggle, and unquestionably not without support. First and foremost, I want to thank Professor Kazuhiro Takanabe. It has been an honor to be his first Ph.D. student. He took a genuine risk with me, and opened my eyes to science; I will always be grateful for that gift.

I would like to thank the support, criticism and motivation provided by Prof. Kazunari Domen, Prof. Jun Kubota, Prof. Akihiko Kudo, Prof. Mohamed Eddaoudi, Prof. Osman Bakr, Prof. Jean-Marie Basset, and Prof. Luigi Cavallo.

My sincere gratitute also goes to all the brilliant French scientists that educated me at some point of my graduate studies: Dr. Samy Ould-Chikh, Dr. Paco Laveille, Dr. Ugo Ravon, Dr. Gregory Biausque, and Dr. Eric Puzenat. I am gratefull with all the scientists from whom I learned something new: Dr. Anna Kachina, Dr. Dr. Guijun Ma, Dr. Dongkyu Cha, Dr. Xuyuan Peng, Dr. Dilshad Masih, Dr. Shahid Rasul, Dr. Abdesslem Jedidi, Dr. Ahmed Ziani, Dr. Natalia Morlanes, , Dr. Dalaver H. Anjum, Dr. Weili Yu, Dr. Manas, K. Bhunia, Dr. Tarek Kandiel, Dr. Somphonh Peter Phivilay, Dr. Jung-Hyun Park, Dr. Dimosthenis

Sokaras, Dr. Tsu-Chien Weng, Dr. Dennis Nordlund, and many others in KCC, IRCELYON, U. C. Berkeley and SSRL-SLAC.

There is an extensive list of friends and collaborators that were an essential part of my journey in the middle of the Saudi desert: Dr. Ela Nurlaela, Tatsuya Shinagawa, Dalal Noureldine, Saad Sarfraz, Dr. Kevin Limkrailassiri, Yiwei Ou, Frederic Leroy, Xiaohui Deng, Bedour Al-Sabban, Shuo Liu, Roseanne Warren, Anaam Al-ShaikhAli, Amal Baqais, Muhammad Qureshi, and all the people who made my days unique at KAUST.

In the journey of discovering our passion, a companion is vital to enduring the challenges ahead. All my scientific efforts will always be dedicated to my life partner Julieta Salazar. Without her, there are no dreams; curiosity is non-existent, and there would be no wonder.

Education is a perpetual state, not an ultimate end. My parents are wise professors, and they showed me that one never stops learning. My little sister will someday change the world, and I know I must make her proud because I am proud of her. Their support is the foundation of my scientific career.

To my family.

TABLE OF CONTENTS

LIST OF ABBREVIATIONS

AM 1.5G	air mass 1.5 global solar spectrum
AQE	apparent quantum efficiency
BET	Brunauer–Emmett–Teller theory
BJH	Barrett-Joyner-Halenda analysis
CA	chronoamperometry
CE	counter electrode
CIGS	copper indium gallium selenide solar cells
CO2RR	CO_2 reduction reaction
CP	chronopotentiometry
CV	cyclic voltammetry
DFT	density functional theory
DOE	Department of Energy
DSC	differential scanning calorimetry
EC	electrocatalyst
ECSA	electrochemically active surface area
EDX	energy-dispersive X-ray spectroscopy
EIS	electrochemical impedance spectroscopy
EPFL	Ecole Polytechnique Federale de Lausanne
FTIR	Fourier transform infrared spectroscopy
GC	gas chromatography
GM	General Motors
GCE	glassy carbon electrode
HER	hydrogen evolution reaction
HOR	hydrogen oxidation reaction

HPLC	high-performance liquid chromatography
HRTEM	high resolution transmission electron microscope
HZB	Helmholtz-Zentrum Berlin
IEA	International Energy Agency
IR	infrared radiation
JCAP	Joint Center for Artificial Photosynthesis
mpg	mesoporous graphitic
MW	molecular weight
MIT	Massachusetts Institute of Technology
MS	mass spectrometry
NREL	National Renewable Energy Laboratory
OER	oxygen evolution reaction
ORR	oxygen reduction reaction
PEC	photoelectrochemical cell
PEMFC	proton exchange membrane fuel cell
POWS	photocatalytic overall water splitting
PV	photovoltaic
QE	quantum efficiency
QY	quatum yield
RDE	rotating disk electrode
RRDE	rotating ring disk electrode
RDS	rate determining step
RE	reference electrode
RHE	reversible hydrogen electrode
SBH	Schottky barrier height
SC	semiconductor

SEM	scanning electron microscopy
SLJ	solid-liquid-junction
SRH	Schockley-Read-Hall mechanism
STEM	scanning transmission electron microscopy
STF	solar-to-fuel
STH	solar-to-hydrogen
STH	solar to hydrogen conversion efficiency
TGA	thermogravimetric analysis
TCD	thermal conductivity detector
TEM	transmission electron microscopy
TGA	thermogravimetric analysis
UV	ultraviolet light
VIS	visible light
WE	working electrode
XAS	X-ray absorption spectroscopy
XPS	X-ray photoelectron spectroscopy
XRD	X-ray diffraction
2J	dual junction
3J	triple junction

LIST OF SYMBOLS

Symbol	*Unit*	*Description*
α	m^{-1}	absorption coefficient
α_T		charge transfer coefficient
β	m	light penetration depth
e^-		electron
h^+		hole
ε_0	$F\ m^{-1}$	vacuum permittivity
ε_r		relative permittivity
q	C	elementary charge
k_B	$J\ K^{-1}$	Boltzmann constant
h	J s	Planck constant
c	$m\ s^{-1}$	speed of light
F	$C\ mol^{-1}$	Faraday constant
R	$J\ K^{-1}\ mol^{-1}$	gas constant
D	$m^2\ s^{-1}$	diffusivity
ν_k	$m^2\ s^{-1}$	kinematic viscocity
ω	$rad\ s^{-1}$	angular rotation rate
N_A	mol^{-1}	Avogadro constant
ν	s^{-1}	frequency
λ	m	wavelength
t	s	time
T	K	temperature
C_P	$mol\ m^{-3}$	concentration of particles
L	m	reactor height

ϕ	V	electrostatic potential
$\mathbf{E}$	V m^{-1}	electric field
$\mathbf{B}$	T	magnetic flux density
$\mathbf{H}$	A m^{-1}	magnetic field
$\mathbf{J}$	A m^{-2}	current density vector
$\mathbf{D}$	C m^{-2}	electric displacement field
V	V	applied potential
V_{OC}	V	open circuit potential
V_{bi}	V	built-in potential
j_{sc}	A m^{-2}	short circuit current density
R_{sh}	Ω m^{-2}	shunt resistance
C	F	capacitance
I	A	average net current
i	A	current
j	A m^{-2}	current density variable
j_0	A m^{-2}	exchange current density
j_L	A m^{-2}	Levich current density
η	V	overpotential
η_E		energy efficiency
η_F		Faradaic efficiency
η_{STH}		solar-to-hydrogen conversion efficiency
a		activity coefficient
z		number of transferred electrons
B_T	V dec^{-1}	Tafel slope
n, p	m^{-3}	electron and hole concentration
n_i	m^{-3}	intrinsic carrier concentration

n_0, p_0	m^{-3}	quasi-equilibrium carrier density
N_d, N_a	m^{-3}	donor and acceptor density
N_C, N_V	m^{-3}	effective density of states, conduction/valence band
$\mathbf{J}_n$, $\mathbf{J}_p$	A m^{-2}	electron and hole current density
U_n, U_p	m^{-3} s^{-1}	net electron and hole recombination rate
G_n, G_p	m^{-3} s^{-1}	electron and hole generation rate
R_n, R_p	m^{-3} s^{-1}	electron and hole recombination rate
D_n, D_p	m^2 s^{-1}	electron and hole diffusion constant
μ_n, μ_p	m^2 V^{-1} s^{-1}	electron and hole mobility
τ_n, τ_p	s	electron and hole lifetime
τ_c	s	collision time
σ	S m^{-1}	electrical conductivity
P_0	m^2 s^{-1}	photons absorbed from AM 1.5G
P_{total}	W m^{-2}	incident power density in AM 1.5G
x	m	depth into the bulk of a semiconductor
x_s	m	radious of the particle
ρ	m^{-3}	space charge density
r_0, r_s	m	catalyst and semiconductor particle size (diameter)
θ	rad	angle defining interparticle distance
W_D	m	depletion layer width
L_n, L_p	m	electron and hole diffusion length
L_D	m	Debye length
χ	eV	semiconductor electron affinity
Φ_B	eV	emission barrier height
Φ_M	eV	metal work function

E_g	eV	band gap
E_{redox}	eV	standard redox potential
E_f	eV	semiconductor Fermi level
E_{fm}	eV	metal Fermi level
E_{fn}, E_{fp}	eV	quasi-Fermi level of electrons and holes
E_C	eV	conduction band edge
E_V	eV	valence band edge
E_T	eV	thermal potential
E^0	V	standard electrode potential
E_c	V	cell potential
V_{fb}	V	flat-band potential
m_e	kg	electron mass
$m^*_{n,\,p}$		effective electron and hole mass
$A^*_{n,\,p}$	A m^{-2} K^{-2}	effective Richardson constant for electrons and holes
v_n, v_p	m s^{-1}	recombination velocity
A	m^2	effective area
P	J s^{-1}	power

LIST OF FIGURES

LIST OF TABLES

CHAPTER 1

1. Introduction

"Yes my friends, I believe that water will one day be employed as fuel, that hydrogen and oxygen which constitute it, used singly or together, will furnish an inexhaustible source of heat and light, of an intensity of which coal is not capable.... When the deposits of coal are exhausted we shall heat and warm ourselves with water. Water will be the coal of the future."

—Jules Verne, The Mysterious Island (1874)

1.1. Solar energy

Some of the biggest global challenges that humans have ever encountered are related to food, water, energy and the environment. Among these four major thrusts of scientific research, the notion of energy security supports the sustainable development and welfare of our society. Providing clean water and enough food to end famine in the world intrinsically requires a large amount of energy. In fact, energy insecurity creates significant political instability and threatens our global economic system. A major shift in the way we supply energy to our society is required due to the unstable and rising prices of conventional energy sources.[1] Hence, a sustainable supply of energy is one of the most critical challenges to target in this generation.

The use of fossil fuels catalyzed the exponential growth of our highly demanding society more than a century ago.[2] The industrial revolution not only accelerated the technological advancement of our species but also, the development of an exponentially growing scientific knowledge. Nevertheless, we are still burning carbon-based compounds despite the fact of the imminent climate change caused by anthropogenically generated global warming.[1–5] In simple words, the way we power our world threatens our species survival.

The global population grew at a rate of 1.2% per year between 2002 and 2012 with a rough estimation of more than 7 billion people. Along with this number, there was an approximate 3% annual increase in energy demand during the same period.[6] In 2012, the global energy consumption was 1.55×10^{3} TWh, equivalent to ca. 5.6×10^{20} J.[7] As mentioned earlier and observed in Figure 1.1, fossil fuels still represent the main source of energy for the world. Leaders and stakeholders from different countries aim to supply around 50% of the energy consumption in the world with renewable energy by 2050.[7] At the present stage, our society still relies on non-renewable sources, despite the fact that Earth absorbs 3.85×10^{24} J per year of solar energy,[8]. The amount of energy arriving at our planet in the form of light photons is four orders of magnitude larger than the world energy consumption. All of our energy needs may be satisfy by taking advantage of approximately 0.01% of the total solar energy irradiation.[7] Hence, the decarbonisation goals to eliminate our dependency on fossil fuels must focus on the development of innovative solar energy technology.

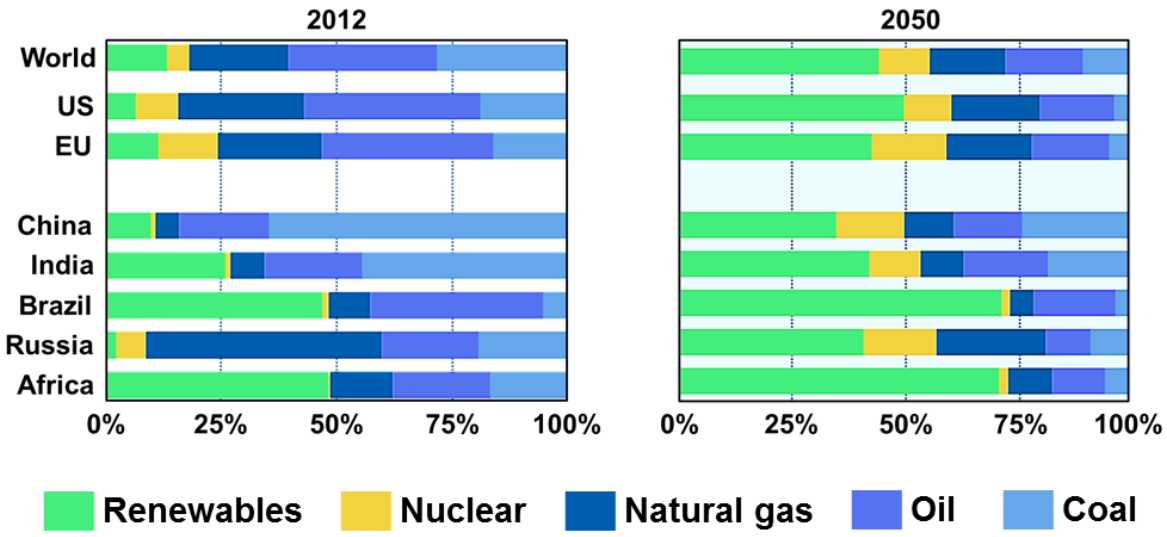

Figure 1.1 World primary energy demand by fuel (left) and expected decarbonisation towards the proposed climate change goals set at the UN Framework Convention on Climate Change (UNFCC) for year 2050 to achieve the 2°C scenario. The renewables include solar, wind, geothermal, tide, hydro, biofuels and waste. Adapted from the International Energy Agency.[6] Based on IEA data from Energy Technology Perspectives executive summary © OECD/IEA 2015, IEA Publishing; modified by A. T. Garcia-Esparza. Licence: http://www.iea.org/t&c/termsandconditions/

Harvesting solar energy represents the most viable renewable energy technology to alleviate our growing energy crisis. It is, however, important to understand the dimensions of the required solar collection area to achieve extensive conversion of the solar flux into usable energy. With a simple calculation using the standard Air Mass 1.5 Global (AM 1.5G) solar spectrum (ASTM G173-03),[9] it is possible to estimate the area needed to meet global energy demands. By assuming a 10% efficiency in a practical system, the approximate solar collection area adds up to 1.8×10^5 km^2 at current rates of energy consumption in the world.[8] Conceptually, this represents covering areas of approximately half the

size of Japan or little over half the size of Germany. It is then evident that large-scale application is essential for the deployment of solar energy worldwide irrespective of the technology used for collecting solar photons.

The implementation of photovoltaic (PV) solar cells has been gaining momentum, and this technology represents an immediate but partial answer for renewable energy supply.[6,10] The solar photovoltaic industry grew at an average annual rate of 46.6% since 1999; representing the largest growing rate of any renewable energy system (Figure 1.2).[10] PV solar cells directly transform photons into electrical currents that must be instantly consumed or stored. Nevertheless, energy storage in the form of electricity is a very expensive commodity.[1,11] Moreover, the required scalability to become a truly competitive and disruptive technology in the energy market involves an enormous capital cost.[9,11] Thus, we must envision simpler devices capable of harvesting the solar spectrum on a huge scale.

It is important to note that PV research is at maturity stage for commercial deployment and societies around the world are adopting the technology at a faster rate.[10] This trend exhibits an important point; leaders and stakeholders are reaching agreements on a much-needed paradigm shift. We must turn away from fossil fuels and provide energy to the world in a carbon-neutral and sustainable way by using solar energy.

At this point, we must learn from nature how to efficiently harvest energy from the sun. Photosynthesis, in its more basic definition, is the process of

transforming light into chemical energy. The complex self-organization of the biological system enables plants with the capability of storing photon energy in the form of chemical bonds.[12] Humans may not strive on the challenging task of mimicking a highly evolved machinery that nature created throughout the centuries. Humankind-time is relatively limited, and we must attempt to roughly recreate a process where we can use the inexhaustible energy of the sun, and catalyze a thermodynamically uphill reaction to gain energy in the form of fuels using photochemistry.[13]

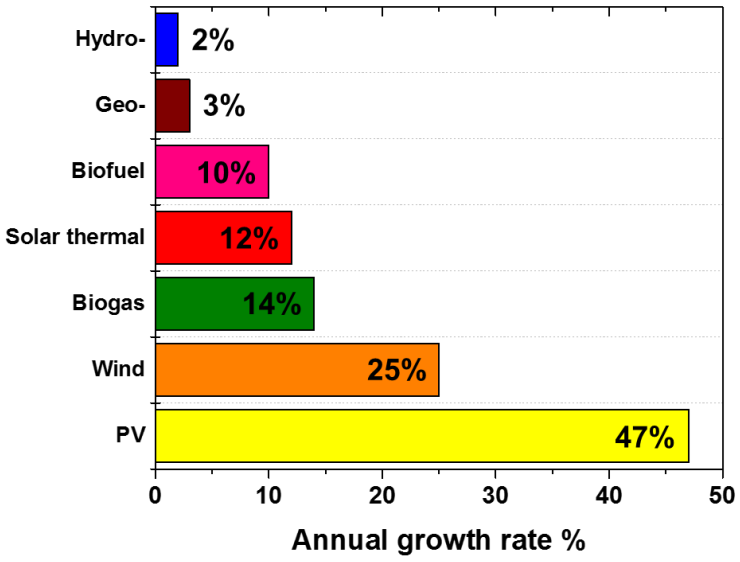

Figure 1.2 Average annual growth rates of world renewable supply from 1999 to 2013. Adapted from the International Energy Agency.[10] Based on IEA data from Key Renewable Trends in Renewables Information © OECD/IEA 2015, IEA Publishing; modified by A. T. Garcia-Esparza. Licence: http://www.iea.org/t&c/termsandconditions/

1.2. Water splitting

"On the arid lands there will spring up industrial colonies without smoke and without smokestacks; forests of glass tubes will extend over the plains and glass buildings will rise everywhere; inside of these will take place the photochemical processes that hitherto have been the guarded secret of the plants, but that will have been mastered by human industry which will know how to make them bear even more abundant fruit than nature, for nature is not in a hurry and mankind is. And if in a distant future the supply of coal becomes completely exhausted, civilization will not be checked by that, for life and civilization will continue as long as the sun shines!"

—Giacomo Luigi Ciamician, Science (1912)[14]

$$H_2O \xrightarrow{h\nu} H_2(g, 1\ atm) + \frac{1}{2}O_2(g, 1\ atm) \qquad (1.1)$$

Splitting water to gain gaseous hydrogen and oxygen has long been a dream reaction for many scientists for over a century.[15] H_2 is a promising and flexible energy sorce with applications in diverse energy sectors. It can be used directly as a fuel, or it can be directly transformed into higher value hydrocarbon molecules and liquid fuels for transportation using existingt infrastructure.[16] H_2 is one of the most suitable energy carrier candidates due to its large energy density. The water splitting reaction driven with nothing more than sunlight using a photoelectrochemical (PEC) cell or a photocatalyst does not have any carbon footprint.[17] Large amounts of energy can be stored for long time using this molecule. Storing solar energy in the form of transportable chemicals and fuels

using an abundant raw material as water is a highly desirable scientific and economic goal, sometimes termed as artificial photosynthesis.

The water splitting reaction is a two-electron reaction with a Gibbs free energy of 237 kJ mol^{-1}. The reaction represents 2.46 eV per water molecule with a two electron transfer for water splitting.[13] Thus, photon energy of at least 1.23 eV is required ($\lambda \cong 1000$ nm) to drive the reaction from a thermodynamic perspective. Such energy is contained in the solar spectrum. Similar to plants, we need to employ a light-absorber to translate radiant energy into charge carriers capable of driving redox reactions. A semiconductor material can be used for such purpose, just as is done in PV technology. The electronic configuration of the semiconductor crystal makes possible photon absorption and with this, the creation of photo-exited electron-hole pairs.[18] In PV solar cells, charges are used directly as electric energy. Here, we may use these excited carriers to participate in the water splitting reaction.[19,20]

Based on the thermodynamic criteria for water splitting, a semiconductor with a band gap greater than 1.23 eV is ideally required to provide the necessary electromotive force for the reaction (from absorption of suitable photon energy).[13] However, it is essential to consider the overpotential required to overcome the activation energy of the redox reactions and other unavoidable efficiency losses in the system.[7,8] Hence, a light absorber capable of visible light absorption (1.7 eV < λ < 2.7 eV) is required to achieve high efficiency, for solar energy conversion to chemical energy (as discussed in the following section and more in detail in Chapter 2).[7,8,21]

1.2.1. Efficiency

In general, the efficiency of any solar-energy conversion device (η_E) can be defined as the amount of power output generated from the power input.[22]

$$\eta_E = \frac{P_{f0} + P_{e0}}{P_{ei} + P_i} = \left\{ \frac{P_{f0} + P_{e0}}{P_{ei} + P_{total}} \right\}_{\text{AM 1.5G}} \tag{1.2}$$

Irrespective of the solar technology, the power out can be described in general as the summation of power energy contained in the form of a measurable electrical current (P_{e0}) and/or chemical fuel (P_{f0}). We may input power in the form of electrical power (P_{ei}); or preferentially, as a radiative source of photons such as the sun ($P_i = P_{total}$; when using the AM 1.5G standard).

For photocatalytic water splitting, we must discuss efficiency in terms of the ratio of the fuel-value of H_2 to the amount of incident solar energy. From Equation 1.2 a general solar-to-fuel (STF) term can be easily derived.[22]

$$\eta_{\text{STF}} = \left\{ \frac{P_{f0}}{P_{total}} \right\}_{\text{AM1.5 G}} \tag{1.3}$$

The fuel efficiency relation reduces to the solar-to-hydrogen (STH) efficiency, specifically used for a photocatalytic system producing stoichiometric amounts of H_2 and O_2 as the products of the water splitting reaction. This metric represents the benchmark parameter upon all solar-to-hydrogen conversion technologies must be compared.[23] It is important to emphasize that the STH efficiency is the most important parameter to evaluate the performance of any

photoelectrochemical and photocatalytic device generating hydrogen.[23,24] Experimentally, it is necessary to determine certain system parameters to compare fairly distinct solar-to-hydrogen technologies. In general STH can be defined in the following forms.

$$\eta_{\mathrm{STH}} = \left\{ \frac{(\text{mmol } H_2\ s^{-1}) \times (237\ \text{kJ mol}^{-1})}{P_{total}(\text{mW cm}^{-2}) \times \text{Area (cm}^2)} \right\}_{AM1.5\ G} \quad (1.4)$$

$$\eta_{\mathrm{STH}} = \left\{ \frac{\left| j_{sc}(\text{mA cm}^{-2}) \right| \times (1.23\ \text{V}) \times \eta_F}{P_{total}(\text{mW cm}^{-2})} \right\}_{AM1.5\ G} \quad (1.5)$$

Equation 1.5 indicates the power output in the form of the product of the available chemical potential of the reaction product ($\Delta G°$ = 237.2 KJ mol^{-1} = 1.23 eV), the short-circuit current density (j_{sc}) and the Faradaic efficiency (η_F) for hydrogen production.[23]

$$\eta_{\mathrm{STH}} = \left\{ \frac{2F(\text{C mol}^{-1}) \times (\text{mmol } H_2\ s^{-1}) \times \left(1.23\ \text{V} - V_{bias}\right)}{P_{total}(\text{mW cm}^{-2}) \times A_r\left(\text{cm}^2\right)} \right\}_{AM1.5\ G} \quad (1.6)$$

$$\eta_{\mathrm{STH}} = \left\{ \frac{N_A \times C_P(\text{mol cm}^{-3}) \times L_r(\text{cm}) \times I_P(\text{A}) \times QY \times \left(1.23\ \text{V} - V_{bias}\right)}{P_{total}(\text{mW cm}^{-2})} \right\}_{AM1.5\ G} \quad (1.7)$$

Equation 1.6 and 1.7 were recently described in the literature because the used parameters are relevant for particulate suspensions.[25] To derive the above equations, the solar reactor was assumed perpendicular to the illumination source

with an apparent geometric area A_r. N_a is Avogadro's constant, F is Faraday's constant, P_{total} is the incident solar irradiance (i.e. AM 1.5G), C_P is the concentration of particles in solution, L_r is the solar reactor height in the direction of light irradiation, I_P is the average net current and *QY* is the quantum yield of collected hydrogen. The system is only relevant and the equations only apply when the applied bias V_{bias} is smaller than the formal potential for H_2-evolution and O_2-evolution half-reactions (1.23 V). If the applied external bias is larger than the potential energy available from the product (i.e. H_2); then, no net solar energy would be stored in the form of chemical bonds. Ideally, we must strive for a bias-free photocatalytic technology.

1.2.2. Technology

Water splitting may be achieved using different photoelectrochemical (PEC) and photocatalytic configurations. A water splitting PEC system can achieve the goal of H_2 fuel production by various technological pathways; however, the large capital cost associated with a massive large-scale deployment impacts the commercial feasibility of the system. For example, it is possible to split water using current technologies: PV solar cells and electrolyzers, or using sunlight concentrators to drive thermally the reaction at 1500-2500 K.[13] Capital costs account to ≈ 80% of the final levelized cost of H_2; hence, scalability is an obstacle using such technologies. Hydrogen from water electrolyzers is expensive and keeping the price at a competitive level with fossil-fuel-derived H_2 may be challenging.[11,25,26]

The practical implementation of the photoelectrochemical technology can be analyzed in terms of dollars per kg of H_2 produced. A detailed techno-economic analysis of the production of hydrogen via PEC and photocatalysis has been done for the US Department of Energy in 2009.[26] Recently, the economic analysis and the technical feasibility of the assumptions used for the 2009 report was revisited by the Jaramillo group.[11] Water splitting systems designated as Type I, II, III and IV have been thoroughly analyzed for large-scale operation (Figure 1.3).

Type I and II are fairly similar, with the difference of using a solar concentrator to enhance irradiance intensity and consequently efficiency. Type II is the one of the most studied and typical PEC water splitting devices in the literature.[27] A planar device, similar to a PV cell, is immersed in the solution with integrated electrocatalysts or with a wired configuration composed of independent electrodes for water electrolysis (Type I and II).

Type III and IV reactors use particulate devices in the solution for solar absorption. The main difference is that Type IV photocatalyzes water splitting generating a stoichiometric mixture of H_2 and O_2 in the same space; whereas Type III consist of separated particles, each independently driving the water-splitting half-reactions in containers connected through an ionic bridge. A major difference of Type III is that it depends upon a redox shuttle that resembles the Z-scheme known in photosynthesis.

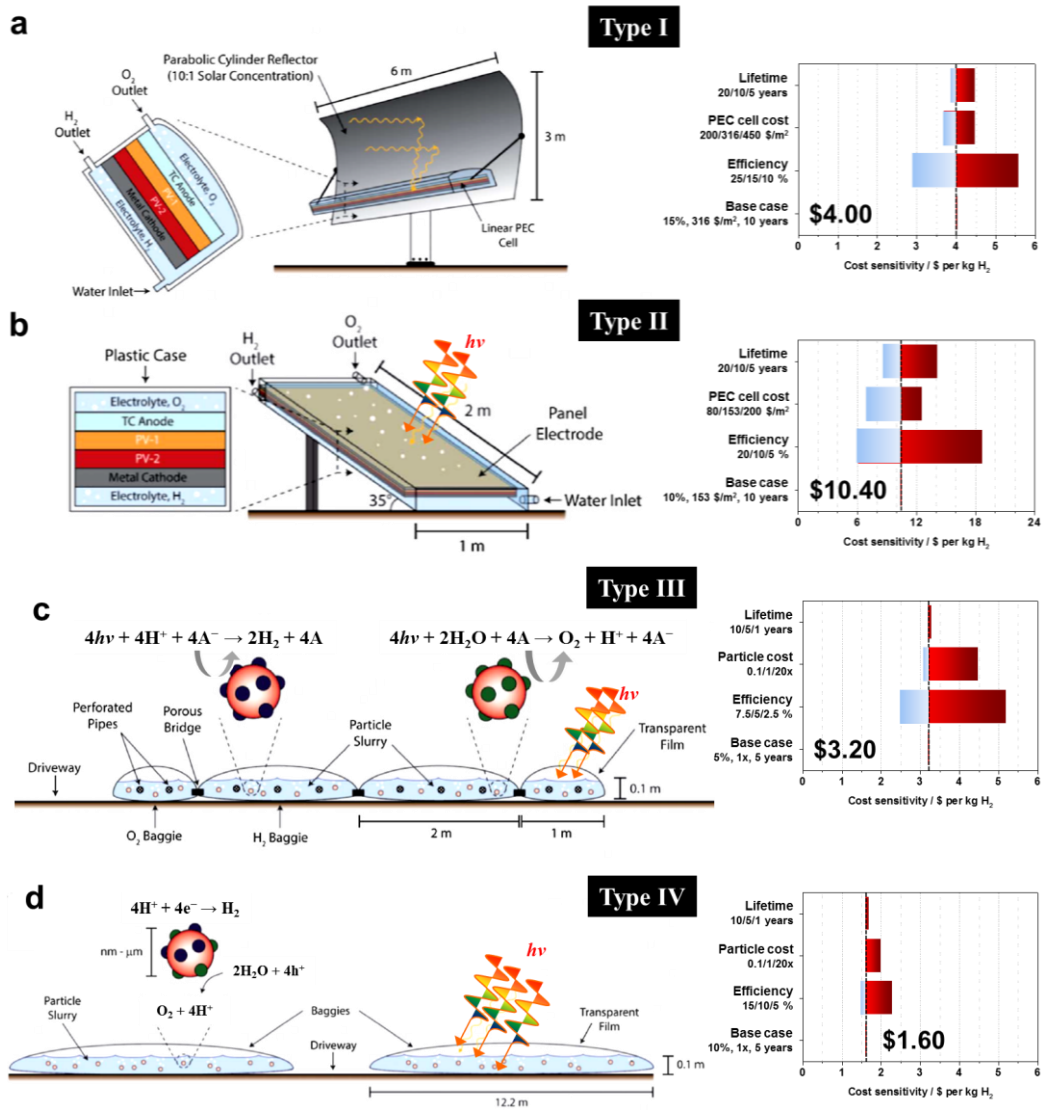

Figure 1.3 (a) Type I. Solar concentrator PEC water splitting reactor. (b) Type II. Monolithic PEC-panel based on multi-junction PV arrays. (c) Type III. Dual electrolyte reactor-beds with photocatalytic colloidal suspensions that are independently catalyzing half-reactions with a membrane for gas separation and ionic transfer (redox mediator required). (d) Type IV. Single electrolyte reactor-bed containing a photocatalytic slurry producing a mixture of H_2 and O_2 from overall water splitting. Sensitivity analysis of the H_2 cost (right). The variability of the calculations based on the effects of the systems efficiency, particles or PV panels costs, and systems lifetime for the different reactor types (I-IV). Schemes are not to scale and the diagrams were adapted from the © US DOE Contract No. GS-10F-009J. Adapted from B. A. Pinaud et al. with permission from © The Royal Society of Chemistry.[11,26]

The target cost of H_2 out of the pump must be similar to untaxed gasoline.[26] The DOE has an objective of $2.00 to $4.00 U.S. dollars per kg of H_2.[11] In the DOE report, all types of reactors resulted in competitive H_2 prices at the level or less than a gallon of gasoline in the United States of America.[25] Nevertheless, a 25% STH efficiency was predicted necessary for reactors Type I and II to produce competitive H_2 (Figure 1.3a-b). If a more conservative STH efficiency was considered (ca. 10%), the baseline levelized H_2 cost was $4.00 and $10.40 for Type I and II, respectively.

It is remarkable that the use of particle suspensions generates prices of $3.20 and $2.30 US dollars per kg of H_2 when assuming a conservative 5% STH efficiency for Type III and IV respectively. If a more ambitious goal of 10% STH is set as objective for particulate photocatalysis (Type III and IV), then we may expect to meet the DOE cost target for H_2 at a competitive price against gasoline (Type $III_{(7.5\%\ STH)}$ = $2.50 USD; Type $IV_{(10\%\ STH)}$ = $1.60 USD). That being said, it is important to note that many assumptions are made to produce such projected costs; nevertheless, three independent techno-economic analysis done in 1998, 2009 and 2013 have arrived to the conclusion that a particulate photocatalytic system is more viable than PEC panels (with and without concentrated sunlight) and commercial PV solar cells integrated to electrolyzers.[11,26,28] The projected low-cost of the powdered photocatalytic system clearly indicates the direction that research in water-splitting should follow.

1.2.3. History

"We suggest that water can be decomposed by visible light into oxygen and hydrogen, without the application of any external voltage, [...] if a p-type semiconductor is used instead of the platinum electrode, electrochemical photolysis of water may occur effectively."

—Akira Fujishima and Kenichi Honda, Nature (1972)[29]

The seminal work of Fujishima and Honda on the electrochemical photolysis of water without the use of an electrical bias initiated the rise of the artificial photosynthesis research field. The work was done using an *n*-type TiO_2 single-crystal wired to a Pt counter electrode. After the simple single liquid-junction device, many research efforts were dedicated to the development of an efficient PEC water splitting cell that uses visible light. Later, Nozik reproduced the work of Fujishima and established the required conditions for sustainable and spontaneous water splitting in detail.[30] The first demonstration of a tandem device consisting of a *p*-GaP (cathode) wired to an *n*-type TiO_2 (anode) was performed in Osaka in 1975 by Yoneyama et al. without the use of any external bias; producing H_2 and O_2 in the photocathode and photoanode compartments respectively upon irradiation.[31] Nozik proposed that the tandem dual-absorber architecture could potentially lead to higher efficiencies than a single absorber configuration.[32,33]

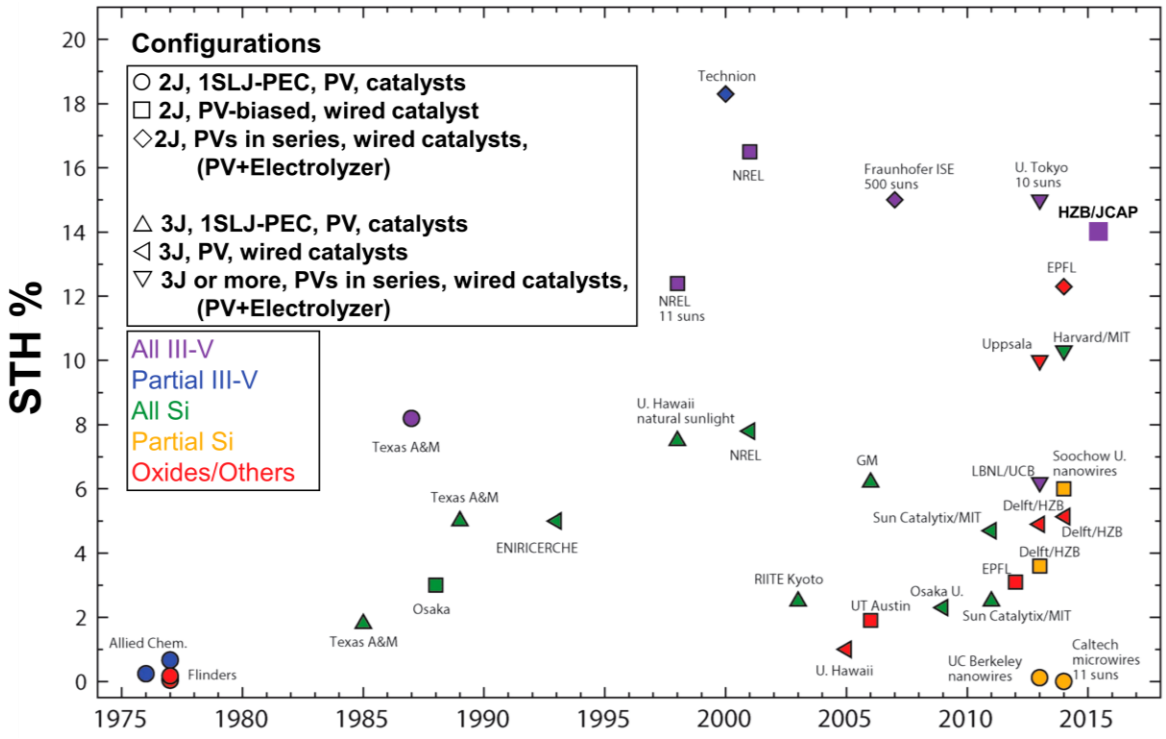

Figure 1.4 Solar-to-hydrogen conversion efficiencies for photoelectrochemical technologies with multiple tandem photovoltaic junctions. The degree of integration is categorized by the different symbols describing different systems such as: complete monolithic devices immersed in the liquid with coupled electrocatalysts and at least one solid-liquid-junction (SLJ), two-electrode system PEC cells with wired counter-electrocatalyst and multi-junction photovoltaics in series driving electrolysis reactions with wired electrocatalysts. The colors represent the types of semiconductor materials used in the water-splitting system. Adapted from J. W. Ager et al. with permission from © The Royal Society of Chemistry.[27]

Before the 1980s, the interest for the tandem configuration expanded with many examples in the literature for unbiased decomposition of water with STH efficiencies of less than 1% (PEC-cells with two wired photoelectrodes).[27] A promising point in history developed in 1987 from the Brockris group (circle, Texas A&M, Figure 1.4); they developed a theory based on solid-state and electrochemical properties to predict optimum efficiencies for tandem

photoelectrodes.[34,35] Interestingly, they discussed the effects of electrocatalysts to enhance the efficiency of the PEC cells and how to use thin electrocatalytic layers to protect the semiconductor material from corrosion. Using a *p*-InP photocathode covered with a Pt catalyst and wired to an *n*-GaAs photoanode protected with a thin anti-corrosion/electrocatalytic layer of MnO_x they achieved 8% STH efficiency with 10 h stability.[36]

In the last decade, there have been significant efforts to fully integrate the tandem photoabsorbers into a monolithic PEC device with multiple semiconductor junctions (Type II, Figure 1.3b). To this day, the most efficient demonstrations of water splitting have been done with PEC cells that are based on well-developed PV designs (Figure 1.4).[27] One of the most efficient PEC water-splitting cell was recently reported using a monolithic two-junction device made with III-V materials with 14% STH.[37] The absorber consist of a *n*-*p* GaInP top cell (E_g = 1.78 eV) and *n*-i-*p* GaInAs (E_g = 1.26 eV) bottom PV cell with an integrated Rh electrocatalyst and wired RuO_2 (HZB-JCAP, 2015 in Figure 1.4). This is similar to the 1998 Turner cell exhibiting a 12% STH using a semiconductor-liquid junction with GaAs.[38] The Turner group at NREL later improved the two-buried-junction GaAs/$GaInP_2$ PEC device with an integrated Pt anode and a wired Pt cathode exhibiting a 16% STH efficiency (square, NREL, Figure 1.4).

The highest point in Figure 1.4 represents a contribution from Licht et al. using a PV-inspired monolithic PEC-cell made using a two-junction *p*-*n* Si (E_g = 1.1 eV) with a *p*-*n* $Al_{0.15}Ga_{0.85}As$ (E_g = 1.6 eV) integrated device wired to RuO_2 and Pt electrocatalysts. Photo-electrolysis of water was achieved at a 18% STH

efficiency.[39] We must note that all these efforts required wired electrocatalysts, and suffer from a poor stability with operational lifetimes of less than 20 h.[27,37–40]

A fully integrated wireless device was developed by the Nocera group in 2011. The contribution not only demonstrated a fully coupled light absorber in contact with the electrocatalysts (without wires), it also displayed the use of only abundant elements with the objective to replace the noble metals used as catalysts for water-splitting.[41] The so-called artificial leaf consisted of a commercial triple-junction amorphous-Si solar cell (*a*-Si) decorated with NiMoZn ternary-alloy and a Co-based electrocatalysts for H_2 and O_2 evolution respectively. The monolithic device performed with a 2.5% STH efficiency. It was shown that when the device was wired as a PV+electrolyzer, the water-splitting system was capable of 4.7% STH efficiency and it was stable for one day (Sun Catalytix-MIT, Figure 1.4). Five year before the artificial leaf, Kelly and Gibson protected a triple-junction *n*-i-*p* *a*-Si solar cell using fluorinated tin oxide (SnO_2:F) as a transparent conducting layer. The back ohmic contact of the *a*-Si solar cell was wired to a Pt counter electrode driving H_2 production, whereas O_2 was evolved on the surface of the SnO_2:F. This device still holds the record for the maximum stability of any PEC water-splitting technology with a continuous performance with an average of 6% STH for more than 31 days (GM, 2006, Figure 1.4).[42] A similar strategy was recently reported to protect unstable photoanodes by using an amorphous TiO_2 layer that is capable of hole conduction for water oxidation.[43]

Researchers can avoid dealing with the stability issues of semiconductors in solutions by using PV solar cells wired to independently optimized

electrocatalysts. Recently, several reports demonstrated this PV+elecrolyzer approach using series-connected photovoltaics such as crystalline *poly*-Si solar cells, $CuIn_xGa_{1-x}Se_2$ (CIGS) solar cells, and $CH_3NH_3PbI_3$ perovskite solar cells capable of reaching 10-12% STH efficiencies (Harvard-MIT, Uppsala, and EPFL in Figure 1.4).[44–46]

At this point, it is interesting to note that the highest performing device in the form of a Type II reactor for PEC water splitting reached only 18% STH for less than 15 h.[39] As previously discussed, it is expected that STH efficiencies of 25% must be achieved with Type I and II reactors to ensure a competitive H_2 price (based on the DOE targets). Recent PV+electrolyzer demonstrations of around 10% STH fall short from the required efficiency to achieve an economically feasible large-scale deployment. Moreover, the required stability and longevity of Type I and II technologies has been calculated to be of 5 to 10 years to achieve a complete positive energy payback.[47] Once more, we must turn our attention to the Type IV solar reactor in Figure 1.3. Photocatalytic overall water splitting may offer the opportunity to supply H_2 at low competitive prices.[7,8,11,17,25–27,48] Research efforts must be directed into this field for the development of highly efficient and stable photocatalysts.

1.3. Photocatalysis

Photocatalytic water splitting represents one of the most appealing approaches due to its large scale potential application.[25] The technology is simple: a powdered material is suspended in water and directly produces H_2 and O_2 in a single reactor by sunlight irradiation (Type IV, Figure 1.3),[17] yet it represents a comprehensive scientific fundamental challenge. The typical photocatalytic particle is composed of two components: a semiconductor (i.e. photocatalyst) and electrocatalysts dispersed on the surface of the photocatalyst (Figure 1.5). The semiconductor is responsible for the light absorption, and the intrinsic properties of the material determine the charge carrier dynamics. Electrocatalysts are dispersed on the surface not only to catalyze redox reactions but also to enhance charge extraction by accommodating electrons or holes.

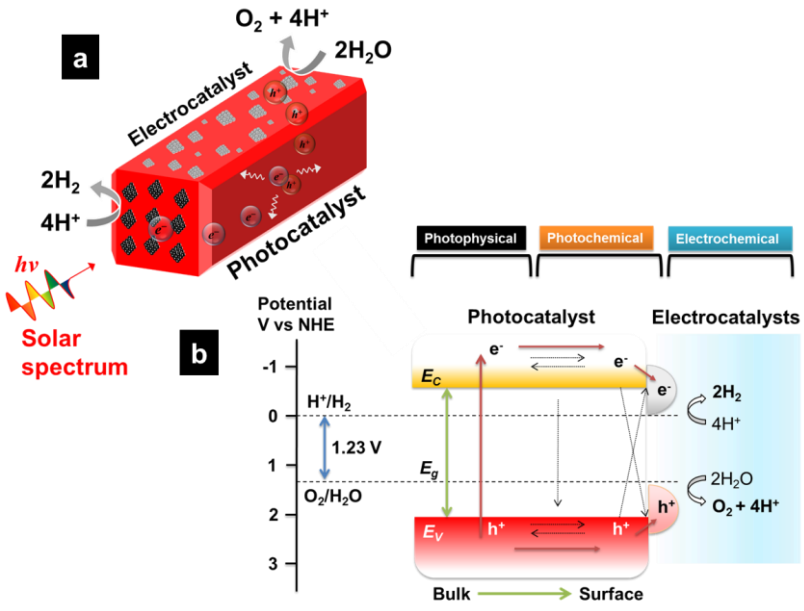

Figure 1.5 Scheme of a photocatalyst particle under a photo-induced reaction process and its idealized band diagram.

The heterogeneous photocatalysis phenomena can be idealized and schematically summarized as depicted in Figure 1.5b. A semiconductor with a band gap (E_g) larger than the thermodynamic potential for water splitting can, in principle, potentially absorb and use visible light photons to drive the reaction (>1.23 eV). The electronic configuration of the semiconductor crystal ultimately determines if the material is capable of providing the charge carriers with adequate potentials to split water. The ideal band diagram in Figure 1.5b indicates that the conduction band E_C and valence band E_V must straddle the formal potentials for the hydrogen evolution reaction (HER) and the oxygen evolution reaction (OER). In this diagram, E_C must be more negative than the standard potential for HER and E_V must be more positive than the standard potential for water oxidation. Upon light irradiation, excited electron-hole pairs are generated in the semiconductor photocatalyst by photon absorption. After a charge separation process, the carriers migrate to the surface to initiate electrochemical redox reactions or undergo recombination by relaxation into their respective bands (and other recombination mechanisms). In Figure 1.5b, metal nanoparticles are attracting photo-excited electrons from the semiconductor and were assumed to be the hydrogen evolution site. Metal oxide nanoparticles were considered the oxygen evolution site by accommodating holes.[49,50] In fact, the harmonious coordination of all the involved photophysical, photochemical and electrochemical phenomena is necessary and must be perfectly orchestrated to achieve successfull overall water splitting. A scheme with some of the most relevant parameters in photocatalysis is presented in Figure 1.6 along with their associated timescales.

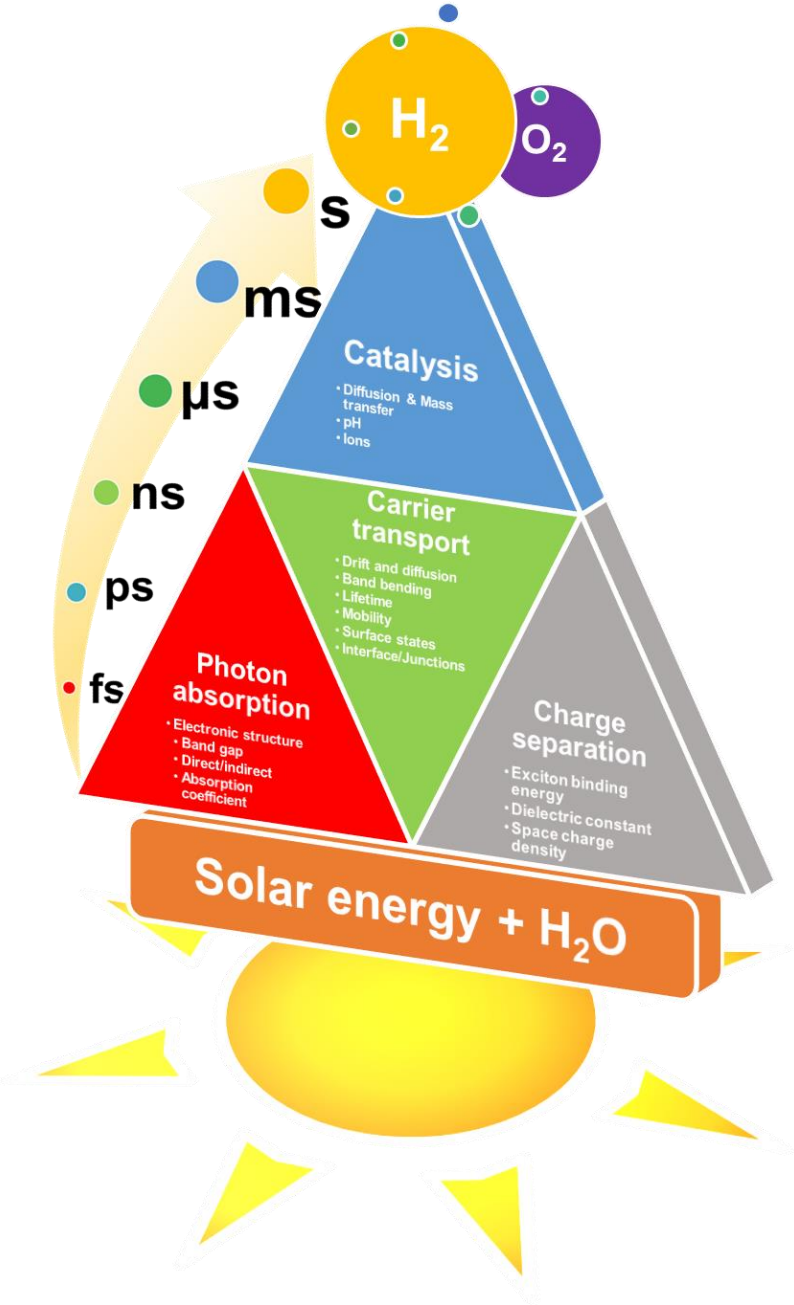

Figure 1.6 Photocatalytic overall water splitting parameters. The pyramidal scheme illustrates that a comprehensive understanding and efficient optimization of each constituent is necessary in order to gain energy from water and the sun in the form of hydrogen fuel. The involved timescales of the overall reaction are displayed for photophysical, photochemical, electrochemical and mass transport processes.

The pyramidal analogy states that is rigorously not possible to split water via photocatalysis without the systematic understanding and optimization of all the parameters involved in the different physicochemical processes. The four components of the pyramid are equally important and each block is composed of more detailed variables that must be thoroughly studied. Photocatalysis is a complex scientific problem that may only be confronted by dividing it into experimentally relevant constituents. As a starting point, the pyramid can be split into two sections: The base and the top of the pyramid. The development of the semiconductor material represents the base of the pyramid. And, the upper part of the pyramid represents the catalysis of water splitting.

Photocatalytic overall water splitting can further be divided into four study blocks. In fact, we can elaborate on this segmentation and mention that there are five working research blocks on the pyramid presented in Figure 1.6. We can start our research from sunlight absorption and charge generation (1). The photo-exited electron-hole pairs (excitons) must be separated before relaxation (2). Transportation of photo-exited charge carriers must occur efficiently to avoid any efficiency losses due to recombination events (3). Electrons and holes must be properly collected in their respective active sites for the efficient electrocatalysis of the water redox reactions (4). Finally, it is essential that all the *interfaces* are intimately coupled to inhibit charge recombination by creating essential electronic pathways for charge separation and transport (5). The later study block was represented as the white lines at the interface of the four photocatalysis constituents in the pyramid of Figure 1.6.

1.3.1. Visible-light absorption

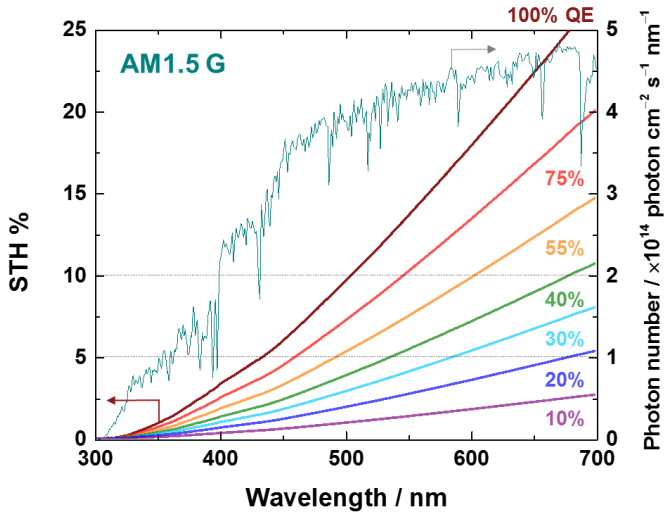

Figure 1.7 Theoretical integrated STH efficiency as a function of the wavelength of sunlight for a single semiconductor photo-absorber assuming different quantum efficiencies for H_2 production via water splitting. The photon numbers as a function of wavelength from simulated solar radiation using the AM 1.5G standard (photon energy $h\nu = hc\lambda^{-1}$). Broken lines mark the target efficiencies required for cost-effective large scale application.

Human eyes detect electromagnetic radiation with wavelengths in the range of approximately 400 to 700 nm. This visible energy range corresponds nearly to energies of 3.1 to 1.77 eV. Typically, the solar energy spectrum is defined to have a total energy of 1000 W m^{-2} accumulated to 4000 nm wavelengths. Figure 1.7 shows the solar spectrum and the expected STH efficiency that we could obtain if all photons contained in the visible range are used for water splitting. From the photon number distribution, the abundance of photons in the UV ($\lambda \leq 400$ nm) and visible (400 nm < $\lambda \leq 700$ nm) portions of the solar spectrum can be deduced. The

UV-region accounts for less than 9% of the total sunlight with an integrated irradiance of almost 90 W m^{-2}. Visible light constitutes more than 50% of the solar spectrum with an integrated irradiance of ca. 524 W m^{-2} ($\lambda \leq 700$ nm). By roughly estimating potential losses in photocatalysis (assume ≈ 0.5 V overpotential), the total usable solar irradiance for water splitting may be calculated up to wavelengths larger than 700 nm (> 1.7 eV). If we focus only on these usable photons, visible light represents around 83% of the usable energy to split water. From these basic numbers, even a common rule of thumb will indicate to focus on utilizing visible light energy to split water.

A general definition of quantum efficiency (QE) in heterogeneous photocatalysis can be defined as the ratio of the number of products (i.e. H_2) to the number of absorbed photons. It is convenient however to measure experimentally the incident photon number in the reactor; hence, researchers adopted the term of apparent quantum efficiency.[51,52] It is clear that the 5% STH target cannot be achieved if we use photons with energies larger than 3.0 eV (≤ 410 nm). Ideally, with a 100% QE it should be possible to reach 5% and 10% STH by absorbing photons with energies of 2.8 eV and 2.4 eV. A semiconductor capable of absorbing 600 nm photons may reach efficiencies close to the 18% STH level if perfect conditions are met. A more conservative and realistic 30% QE in photocatalysis indicates that a semiconductor with E_g = 2.1 eV may only achieve 5% STH without the consideration of any other source of efficiency losses. As a rule of thumb, we must strive to achieve QE larger than 50% with semiconductors capable of absorbing photons with wavelengths longer than 550 nm but shorter than 700 nm.

Typical semiconductor oxides (i.e. TiO_2 and ZnO) only absorb UV light photons, rendering the maximum attainable efficiency meaningless for practical large-scale applications. As shown in Figure 1.7, even when assuming a 100% quantum efficiency; the highest STH efficiency will remain < 2%. Photons with band-edge energy are less likely to be used for reaction, and there are always inevitable losses in the system. Hence, STH efficiencies < 1% can be calculated while assuming 100% QE for large band gap materials (e.g. TiO_2 E_g = 3.2 eV, ≈ 380-390 nm absorption band edge).

We must focus our attention on only materials capable of absorbing visible light because those photons are the most abundant in the solar spectrum, and this point cannot be overemphasized. Semiconductors with optical band gaps of 1.9 eV are capable of visible light absorption up to 650 nm. Using semiconductor materials with this or larger band gap energy represent the possibility to achieve values of ca. 6.7%, 12.3% and 16.7% STH when we assume 30%, 55% and 75% QE respectively. Nevertheless, all these simple calculations based only on the available energy do not take into account other variables that contribute to efficiency losses in the photocatalytic system.

A recent study by the Jaramillo group estimated that when using a single photo-absorber material, the optimal band gap to achieve the highest theoretical maximum efficiency would be 2.26 eV (11.2% STH). [25,53] Their study takes kinetic overpotentials and entropic losses into consideration for the calculations, and their results are presented in Figure 1.8.

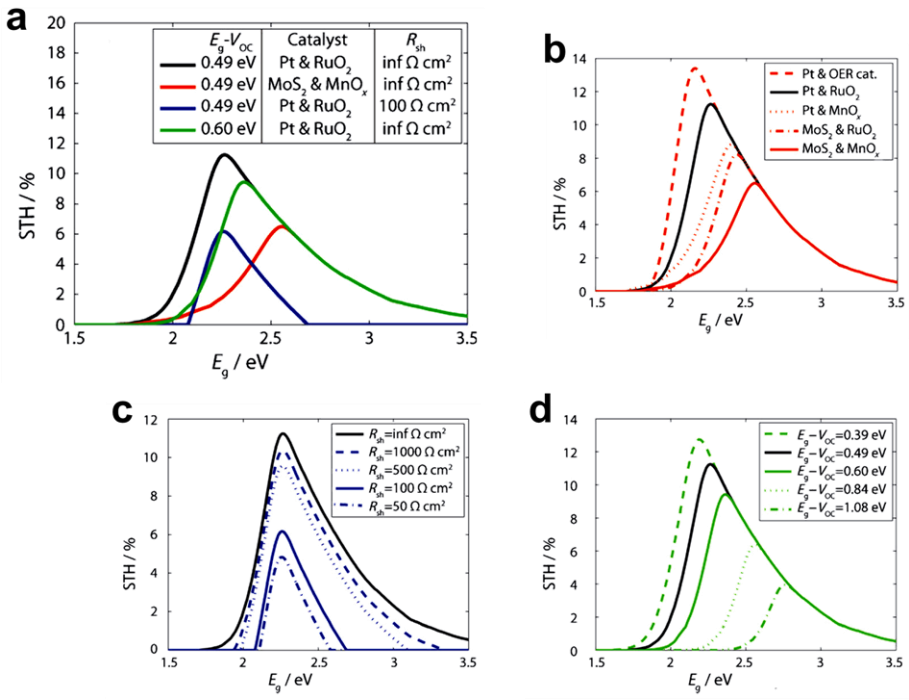

Figure 1.8 Maximum theoretical STH efficiency for a single absorber in a PEC cell or photocatalytic water splitting device (a-d). The calculations consider the semiconductor entropic losses and decreased photo-voltage (d), typical electrocatalysts with their respective kinetic losses (b) and shunt current losses (c). (a-d) The black signal is the baseline considering a high V_{OC} (free energy losses from E_g ≈ 0.49 eV), Pt and RuO_2 electrocatalysts (i.e. high activity) and negligible shunt losses (R_{sh} = inf$\Omega \times cm^{-2}$). (a) The plot indicates the effects of the studied parameters when the losses increase. (b-d) The sensitivity analysis for the calculations and effect of each type of loss on the STH efficiency. (b) Effect of different electrocatalysts combinations used for water splitting. (c) Effect of the magnitude of the shunt losses. (d) The effects of changes in free energy losses reflected as decreased available photo-voltage for water splitting. Figures adapted from L. C. Seitz et al. Copyright © 2013 WILEY-VCH Verlag GmbH & Co. KGaA.[53]

As we replace expensive and noble metals with more abundant elements, it was possible to observe a gradual increase in the overpotential energy for water-splitting along with decreasing efficiencies (Figure 1.8b). The required semiconductor band gap energy increases from 2.26 eV to around 2.6 eV just by

the kinetic overpotential to drive redox reactions, and the maximum theoretical STH decreases by more than half of the ideal scenario. One idealized system may consist of a Pt catalyst combined with an ideal highly active oxygen evolution catalyst (represented as OER cat. In Figure 1.8b). The impact of the development of highly active electrocatalyst results in a shift of the maximum STH to values greater than 13% using a semiconductor with a band gap of 2.15 eV.[53] These calculations clearly indicate the significant role of electrocatalysts in photocatalytic water splitting. Moreover, the kinetic considerations were performed under the assumption of extreme pH conditions (pH ≤ 1 or pH ≥ 13), to experimentally obtain the electrocatalysts parameters.[53] Clearly, there is the need to expand research efforts in the development of highly active electrocatalyst for HER and OER under varied pH conditions.[54] Typically in the literature, photocatalytic overall water splitting operates under neutral pH conditions.[17,25,55,56] Under such environment, kinetics are significantly different, and there are other limiting factors; such as, diffusion and mass transport, concentration overpotentials, kinetic overpotentials, higher resistance, etc.[57,58] In general, the discovery of new electrocatalysts that operate at 4 ≤ pH ≤ 10 is essential, as Pt alone is not the most active material for HER as it is generally perceived.[58,59]

There is a clear balance with an optimum point in the curves, the efficiency at the right side of the figures is limited by the absorption of photons (wide band gap materials) and the efficiency at the left side is limited by the generated photovoltage and kinetics (narrow band gap and catalyst activity). Better catalysts may compensate the lower photovoltage expected in narrower band gaps, but only

to a certain extent. The photovoltage effect can be observed in Figure 1.8d. Taking into consideration free energy losses results in the optimum STH value shifting towards larger band gap materials while decreasing the efficiency to almost one-third of the idealized value.[53] The shunt resistance factor exhibited in Figure 1.8c may be taken simply as an indication of the density of defects in the semiconductor. This type of loss may relate to the amount of *leaked* current. We can understand the effects considering that a decrease in the magnitude of the shunt resistance will increase the rate of charge recombination in the photocatalyst. Thus, the optimum band gap remains constant while the total STH efficiency decreases to almost half of the ideal value at infinite resistance (Figure 1.8c). The development of highly crystalline semiconductor photocatalysts is crucial to avoid this type of losses.[49,53,60] One of the main assumptions to extract all of the above ideal STH values is the proper band-alignment and position of the conduction and valence bands relative to the redox potentials for HER and OER. As mentioned earlier, the semiconductor must exhibit a conduction band position more negative than HER and a valence band more positive than OER for the successful unassisted splitting of water. Deviations and misalignments will only result in an increased potential for driving the reaction. Now, it starts to become clear why materials development in the photocatalysis field is very challenging. Up to this point, we can now reasonably recommend the use of semiconductors with 2.1 eV ≤ E_g < 2.7 eV. As observed in Figure 1.9, the conduction and valence bands must be properly align and the material must be chemicaly stable in the aqueous environment. These conditions represent challenging design constraints for photocatalysis research.

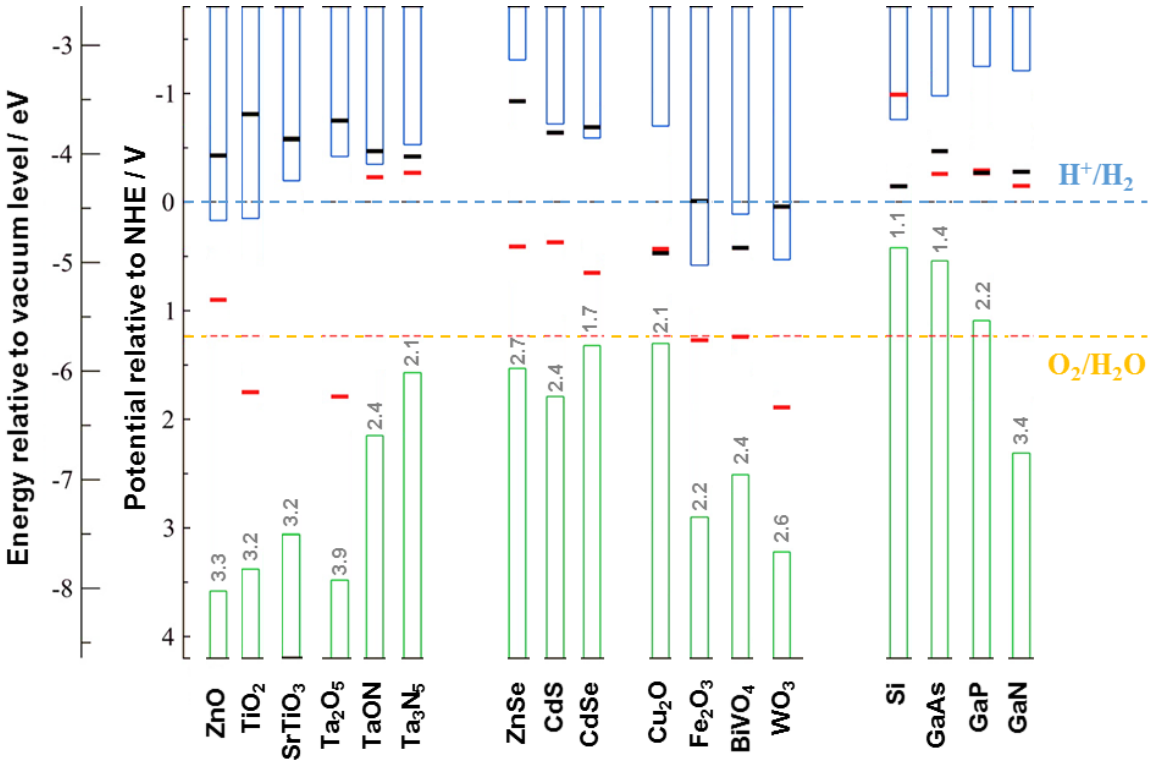

Figure 1.9 Calculated compilation of semiconductors conduction band (blue) and valence band (green) positions relative to the formal standard redox potentials for H_2 evolution and water oxidation at pH 0. Calculated thermodynamic oxidation (red bar) and reduction (black bar) potentials of the semiconductors in aqueous solutions indicate their stability against photo-corrosion. The band gap energy E_g (eV) is shown at the top of the valence band in the figure. Adapted with permission from S. Chen and L.-W. Wang, *Chem*. *Mater*., **2012**, 24, 3659–3666. Copyright © 2012 American Chemical Society.[61]

Oxide materials have been extensively studied in the literature since the pioneering work on TiO_2 by Honda and Fujishima.[62] Most of the metal oxides have excellent stability against corrosion under a broad range of pH. TiO_2 and Ta_2O_5 are two examples from Figure 1.9, the horizontal black and red bars are located outside of the H^+/H_2 and H_2O/O_2 redox potential window. Unfortunately, most of the oxides are not capable of visible light absorption because of the highly positive

valence bands mainly formed by O 2p orbital. TiO_2 was a critical material for the proof-of-concept back in the 1970s and 1980s; nowadays, the material is not appropriate for large-scale solar fuel generation.

A good example of band engineering for the synthesis of visible light absorbers is also presented in Figure 1.9. Moving from oxides to nitrides as in the case of Ta_2O_5 (E_g = 3.9) < TaON (E_g = 2.4) < Ta_3N_5 (E_g = 2.1); the band gap decreases due to the much more negative energy level of N 2p orbitals relative to the O 2p orbitals, hence making the top of the valence band more negative than the oxide.[55] Note that the conduction band of the materials remains mostly unchanged because it is predominantly composed of empty Ta orbitals. The material design strategy of TaON and Ta_3N_5 involves the nitridation of the oxide precursor under NH_3 atmosphere at high temperatures.[7] The valence band is drastically altered as the ammonolysis proceeds and the new electronic structure develops. A similar strategy with H_2S can be applied for the synthesis of oxysulfides such as $Sm_2Ti_2O_5S$, where S 3p orbitals contribute to the upper part of the valence band hybridizing with O 2p atomic orbitals to achieve the lowering of the band gap energy.[63]

Cu_2O exhibits an appropriate band gap for visible light absorption, nevertheless stability is an important issue (both redox bars in the middle of the band gap in Figure 1.9). Moreover, the valence band may be too close to the water oxidation potential making the semiconductor not capable of driving the reaction. WO_3, Fe_2O_3 and $BiVO_4$ also possess suitable band gaps for the absorption of visible light. However, their conduction bands are more positive than the formal

potential for HER; thus, the materials cannot split water. Sulfides and selenides are generally highly unstable to drive the redox reactions, as indicated by the potential redox bar located in the middle of their band gap. Nevertheless, CdS and CdSe appear to be potential candidates for overall water splitting if a protection strategy can be employed to inhibit the photo-corrosion of the semiconductors (see reference 42 and 43 for a protection strategy). As a reference, other typical semiconductors used in PV solar cells are shown in Figure 1.9. With the exception of GaN, III-V semiconductors like GaAs and GaP are not capable of water splitting due to their band positions and lack of stability. In Figure 1.9, only TiO_2,[64,65] $SrTiO_3$,[66] Ta_2O_5,[67] and GaN[56,68,69] are active photocatalysts for overall water splitting when selective electrocatalysts are dispersed on the surface of the semiconductors. Before discussing further particulate materials capable of splitting water into H_2 and O_2, we must first consider the mechanisms of charge separation and transport that make the uphill reaction feasible.

1.3.2. Band bending and charge separation

The concept of band bending is well known in semiconductor physics and is one of the central concepts in semiconductors photoelectrochemistry.[18–20] In the field of particulate photocatalysis, one of the most common structures is that of an *n*-type semiconductor particle decorated with metal nanoparticles on its surface immersed in an electrolyte. When a semiconductor particle is immersed in the solution, equilibration of the charges occurs at the interface leading to a so-called band bending phenomenon (under dark conditions, Figure 1.10a-d).

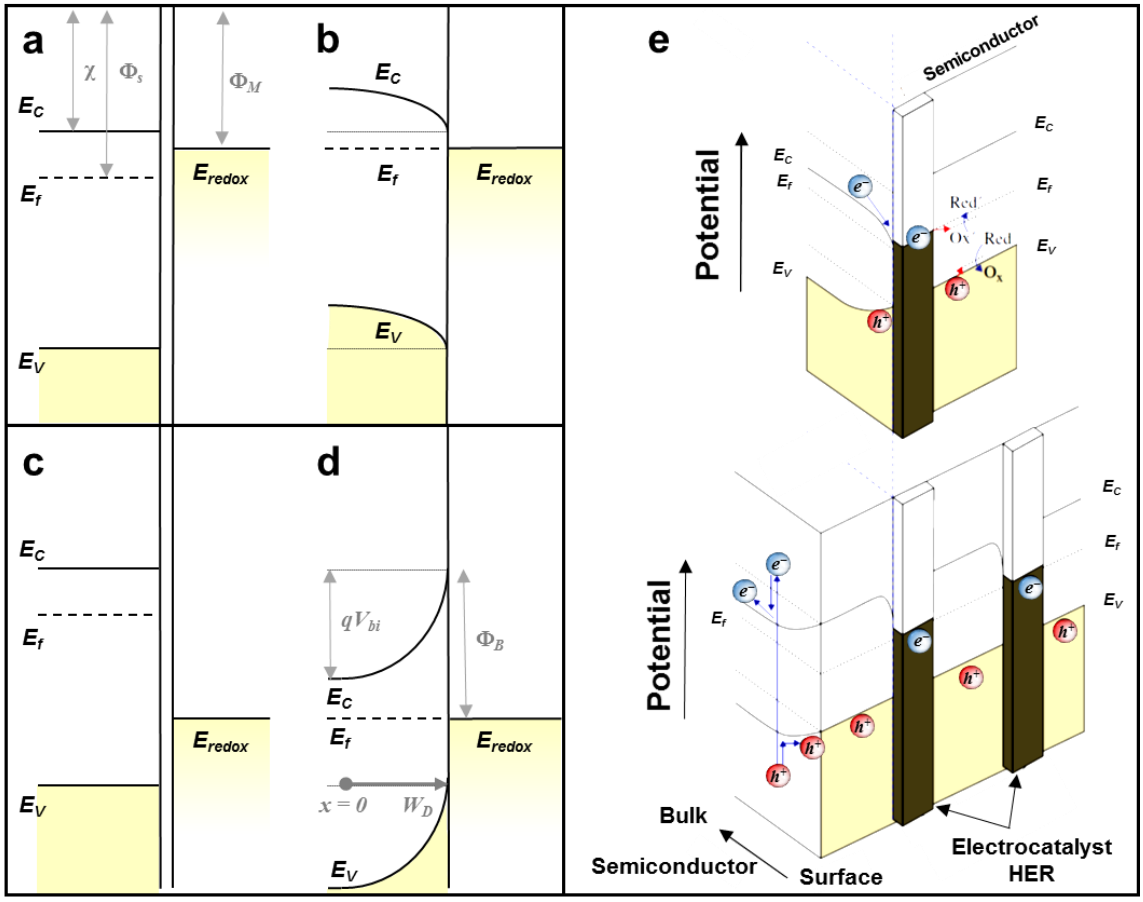

Figure 1.10 Energy band diagrams of an *n*-type semiconductor in contact with an electrolyte. Flat band conditions are represented before contact with the liquid junction (a, c). Charge equilibrium at the semiconductor-electrolyte interface in the dark exhibiting the band-bending phenomena (b, d). The band bending of an *n*-type semiconductor decorated with infinite metallic contacts periodically dispersed on its surface (e). The flow of the photo-excited charges can be observed where electrons reach the electrocatalyst junction (metal site in ohmic contact), whereas the holes are collected at the liquid-semiconductor junction (e). Adapted from K. Takanabe and K. Domen Copyright © 2015 WILEY-VCH.[7]

The behavior is fairly similar to that found for a Schottky junction, and the case of an *n*-type semiconductor is presented in Figure 1.10. The difference between the Fermi level potential of the semiconductor (E_f) and the redox potential of the electrolyte (E_{redox}) will determine the magnitude of the energy barrier (Φ_B)

and the size of the space charge layer formed at the interface (W_D). The diagrams represent accumulation and depletion conditions after charge distribution in the semiconductor-liquid interface at steady-state equilibrium as shown in Figure 1.10b and Figure 1.10d respectively. The schemes resemble ohmic and Schottky type of contacts similar to a metal-semiconductor junction.[18]

The band bending concept developed by Schottky and Mott describes the rectifying behavior measured at the metallic junction. To achieve equilibrium, free electrons transfer between the metal with work function Φ_M and the semiconductor Φ_s due to their energy differences. In the case of a semiconductor-liquid junction, we substitute the metal with a well-defined redox potential E_{redox} as exhibited in Figure 1.10c. When E_{redox} (or Φ_M) is higher (more positive) than that of the *n*-type semiconductors electron affinity χ. A depletion layer (i.e. space charge region, W_D) is formed due to the transfer of electrons from the semiconductor to the electrolyte solution (or to a metal in Figure 1.10c-d). A built-in electronic potential V_{bi} is generated and defined as the difference between Φ_M and χ. The energy barrier observed in Figure 1.10d at the junction is called Schottky barrier and can be described in function of E_{redox} or Φ_M depending on the analyzed junction (see Equation 2.16 in Chapter 2).

$$\Phi_B = \Phi_M - \chi \tag{1.8}$$

The preservation of the band edge position (i.e. pinning effect) generates the discussed band bending and it can be described by Poisson's equation with

the assumption of a one-dimensional infinite interface as the one observed in Figure 1.10a-d.

$$\frac{d^2\phi(x)}{dx^2} = -\frac{\rho}{\varepsilon_0\varepsilon_r} \quad 0 \le x \le W_D \tag{1.9}$$

Where W_D is the depletion layer thickness, ρ is the space charge density, ε_r and ε_0 are the relative dielectric constant of the semiconductor and the vacuum permittivity respectively.[70] Solving the equation for boundary conditions for an *n*-type semiconductor ($\rho = qN_d$; $0 \le x \le W_D$) where N_d is the majority carrier density and $\rho = 0$ beyond the depletion layer; the electric field $E(x)$ and the electric potential $V(x)$ within the space charge region can be obtained.

$$E(x) = \frac{qN_d}{\varepsilon_r\varepsilon_0}x \quad 0 \le x \le W_D \tag{1.10}$$

$$E_{\max} = \frac{qN_d}{\varepsilon_r\varepsilon_0}W_D \tag{1.11}$$

$$V(\mathrm{x}) = -\frac{qN_d}{2\varepsilon_r\varepsilon_0}x^2 \quad 0 \le x \le W_D \tag{1.12}$$

$$V_{bi} = -\frac{qN_d}{2\varepsilon_r\varepsilon_0}{W_D}^2 \tag{1.13}$$

$$W_D = \sqrt{\frac{2\varepsilon_0\varepsilon_r|V_{bi}|}{qN_d}} \tag{1.14}$$

From the above equations, it is possible to determine the depletion layer thickness W_D if the band-bending potential value at the surface is known (V_{bi}). Such built-in potential represents the amount of voltage drop across the semiconductor or the total change in the electric potential.[19] However it is necessary to note that this model only apply when the lateral width of the metal-semiconductor junction is higher than the order of the space charge region (~tenths of nm). Therefore, it is necessary to consider a *finite* interface approximation when studying nanoscale junctions (e.g. < 10 nm).[71] If the size of the semiconductor particle is in the order of the depletion layer, then the degree of band bending diminishes and does not penetrate into the bulk as shown in Figure 1.11.[17]

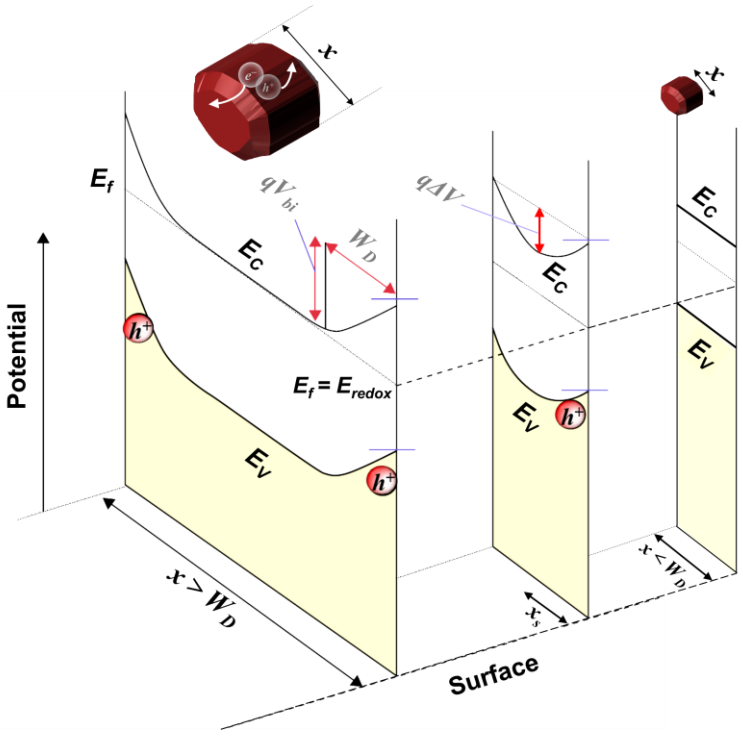

Figure 1.11 Influence of an *n*-type semiconductors particle-size on band bending. The depletion layer changes when the size of the photocatalyst is similar to the size of W_D. Adapted from K. Takanabe and K. Domen. Copyright © 2015 Wiley-VCH Verlag GmbH.[7]

In fact, it has been suggested that when the photocatalysts size is much smaller than the space charge region no such layer exist at this scale.[72] Actually, in semiconductor nanoparticles with an average carrier concentration >10^{17} cm^{-3} the space charge layer is not as effective; thus, making charge separation more challenging.[48] Under the condition ($x << W_D$, Figure 1.11) near-flat-band conditions are theoretically expected, and as a consequence, that charge carriers may reach the surface easily. At first sight, one expect an increase in the quantum efficiency; however, this may not be the case. In the absence of electric fields, electron and hole injection rates are mostly governed by interfacial transfer alone; increasing undesirable leakage currents which basically short-circuit the photocatalytic system stopping the water splitting reaction.[48] The non-existent mechanism for charge separation intrinsically increases the recombination of photoexcited electron-hole pairs.[7]

Semiconductor nanocrystals have an apparent essential advantage of a larger surface area; nevertheless, the surface is intrinsically defective. An abrupt termination of the lattice possess dangling bonds and possibly adsorbed potential-determining ions with pinned potential states. Such a defective region implies an increase in the site density responsible for charge recombination.[8] Finally, the size-confinement produces a volume fraction with a limited number of carriers. Hence, electron-hole pairs with a size smaller than the Bohr exciton radius results in an increase in the exciton binding energy decreasing the probability of charge separation.[48] When the radius of the nanoparticle is ($x_s < 3^{½} W_D$), a potential barrier height ΔV at the center of a spherical semiconductor particle may be estimated in

function of the Debye length L_D.[73] Based on the expected lower degree of band bending, the main mechanism for charge transport in semiconductor nanocrystals may be governed by diffusion only.[8]

$$\Delta V = \frac{1}{6}\left(\frac{x_s}{L_D}\right)^2 \qquad (1.15)$$

The formation of a Schottky barrier with a rectifying behavior at the electrolyte interface is very important for the systems efficiency.[74] Modification of the different *interfaces* in the system may create new electronic structures perturbing and possibly enhancing charge separation. Some of the typical interfaces found in photocatalysts are the semiconductor-liquid junction, semiconductor-semiconductor heterojunctions, semiconductor-metal contacts and even some semiconductor-insulator interfaces. According to the literature, the band bending phenomena generated at the interface is the driving force to separate charge carriers and generate current flow from the bulk to the surface.[49,70,75,76] For the purpose of efficient charge separation, it has also been implied that the formation of an ohmic contact at the metal-semiconductor interface is beneficial for electron collection in *n*-type semiconductors (see an ideal example in Figure 1.10e).[17,49,74,77] The interplay of these types of interfaces generate intricate potential profiles in the semiconductor. In a photocatalytic particulate system such effects are highly complex and may be even severely affected by other phenomena such as probable surface states due to the termination of the lattice periodicity,[78] externally induced field-effects[79] and adsorption-induced band bending on the semiconductor surface (i.e. potential determining ions).[48,80]

1.3.3. Drift and Diffusion

The understanding that we have about semiconductor photochemistry and semiconductor-liquid junctions was developed based on PEC cells using macroscopic semiconductors photo-electrodes.[77,81–83] In most cases, the knowledge developed from PEC-cells has been extrapolated to semiconductor particles. Basically, we may consider the photocatalysts particles as photoelectrodes under open-circuit conditions and the device operates bias-free. Although most of the same principles apply to the photocatalytic system, specific theories for semiconductor particles are limited in the literature.[71,73,74,77,84–86] We can reasonably theoretically simulate the expected experimental behaviour of a PEC water-splitting cell;[87–93] however simulations of particulate photocatalytic water-splitting devices are rare in the literature.[71,73,85,86,94]

The semiconductor device equations have been used extensively to simulate semiconductor devices in different forms.[18,95] The equations can be applied to the bulk domain of the semiconductor material, highly doped regions, dielectric sections and regions with doping transitions. The classic semiconductor equations can be derived from the Maxwell's equations developed in 1864. The equations were later reformulated in the following forms.[96]

$$\nabla \times \mathbf{E} = -\frac{\partial \mathbf{B}}{\partial t} \tag{1.16}$$

$$\nabla \cdot \mathbf{B} = 0 \tag{1.17}$$

$$\nabla \times \mathbf{H} = \mathbf{J} + \frac{\partial \mathbf{D}}{\partial t} \tag{1.18}$$

$$\nabla \cdot \mathbf{D} = \rho \tag{1.19}$$

E is the electric field, **B** is the magnetic flux density, **H** is the magnetic field, **J** represents the current density, **D** is the electrical displacement, and ρ is the charge density. Equation 1.16 represents the change in the magnetic field in time space and the generation of an electric field from the Faraday law of induction. The next expression implies that no magnetic sources exist. Equation 1.18 express the Ampere-Maxwell law where the effects of the changes in an electric field in time along with the electric current influence the generation of a magnetic field. The last of the four equations expresses Gauss law of electric charges.[96]

From the the relation of the charge distribution (Equation 1.19 in Maxwell's equations) we can derive the general expression of electrostatic potential (Poisson's Equation) by using the electric field with the permittivity parameter for materials in a stationary case ($\nabla \times \mathbf{E} = 0$) when the semiconductonr exhibits negligible anisotropy of the permittivity **ε**.[96]

$$\mathbf{D} = \varepsilon_0 \varepsilon_r \mathbf{E} \tag{1.19}$$

$$\mathbf{E} = -\nabla \phi \tag{1.20}$$

Using the above expressions and the electric displacement relation we can obtain the Poisson's equation.

$$\nabla \cdot (\nabla \phi) = -\frac{\rho}{\varepsilon_0 \varepsilon_r} \tag{1.21}$$

The one-dimensional version with strict boundary conditions has been already discussed as Equation 1.9 and the space the charge density ρ was expanded later on Chapter 2 as Equation 2.1.

The continuity equations are derived by using ∇ operator in Equation 1.18 and considering that the divergence of any vector field equals zero.[96]

$$\nabla \cdot \nabla \times \mathbf{H} = \nabla \cdot \mathbf{J} + \nabla \cdot \frac{\partial \mathbf{D}}{\partial t} = 0 \tag{1.22}$$

The current density is composed of hole and electron currents.

$$\mathbf{J} = \mathbf{J}_p + \mathbf{J}_n \tag{1.23}$$

From Equation 1.19, the definition of $\rho = q(p - n + N_d - N_a + \rho_p - \rho_n)$, and considering that impurities are time invariant, it is possible to define[96]

$$\nabla \cdot \mathbf{J}_n + \nabla \cdot \mathbf{J}_p + q(\frac{\partial p}{\partial t} - \frac{\partial n}{\partial t} + \frac{\partial N_d}{\partial t} - \frac{\partial N_a}{\partial t} + \frac{\partial \rho_p}{\partial t} - \frac{\partial \rho_n}{\partial t}) = 0 \tag{1.24}$$

$$\nabla \cdot \mathbf{J}_n - q\frac{\partial n}{\partial t} - q\frac{\partial \rho_n}{\partial t} = U_n \tag{1.25}$$

$$\nabla \cdot \mathbf{J}_p + q\frac{\partial p}{\partial t} + q\frac{\partial \rho_p}{\partial t} = -U_p \tag{1.26}$$

p and n represent the concentration of holes and electrons respectively. ρ_p and ρ_n symbolize additional concentrations due to trap holes and electrons, respectively. The $U_{p,n}$ term represent the net recombination rate as the summation of all generation and recombination events upon the absorption of light by the semiconductor material. Once charges are generated, the flow of current is governed by two phenomena. Drift of the carriers results as consequence of electric fields and diffusion due to differences in concentration gradients.

Using Ohm's law, the electric current component due to the electric field can be expressed in the following form by using the definition of conductivity as a function of the mobility; $\sigma_{p,n} = q(n, p)\mu_{p,n}$ for holes and electrons, respectively.

$$\mathbf{J}_n^{\mathbf{E}} = qn\mu_n\mathbf{E} \tag{1.27}$$

$$\mathbf{J}_p^{\mathbf{E}} = qp\mu_p\mathbf{E} \tag{1.28}$$

Where the superscript expresses that the current density is caused by drift of the carriers due to the influence of changing electric fields. Concentration gradients influence the random thermal motion of carriers into lower concentration regions.[96] The diffusion coefficient can be related, in thermal equilibrium for non-degenerate semiconductors, to the mobility of the carrier by using the Einstein relation $D = \mu k_B T q^{-1}$.

$$\mathbf{J}_n^{\nabla n} = qD_n\nabla n \tag{1.29}$$

$$\mathbf{J}_p^{\nabla p} = qD_p \nabla p \tag{1.30}$$

Using all the above-discussed definitions we can finally revisit the semiconductor device equations describing the transport of an homogeneous isotropic semiconductor with a Maxwellian distribution of carriers.

$$\mathbf{J}_n = q\left(\mu_n n\mathbf{E} + D_n \nabla n\right)$$

(1.31a)

$$\mathbf{J}_p = q\left(\mu_p p\mathbf{E} - D_p \nabla p\right) \tag{1.31b}$$

$$\nabla \cdot \mathbf{J}_n - q\frac{\partial n}{\partial t} = U_n \tag{1.32a}$$

$$\nabla \cdot \mathbf{J}_p + q\frac{\partial p}{\partial t} = -U_p \tag{1.32b}$$

When Equation 1.31 is inserted in Equation 1.32, we generate a system of two non-linear equations in two unknown results. With the appropriate boundary conditions and by solving Poisson's equation to describe the electrostatic potential, these equations satisfy the transport problem in semiconductors and a simulation may be performed.[97]

Electrons and holes are continuously being generated and recombined by different mechanisms ($U_{p,n}$) such as band-to-band generation/recombination, trap-assisted recombination and Auger recombinations. Energy and momentum must be conserved; hence generation of excitons is possible due to absorption of

radiative photons or non-radiative phonons. In a similar manner, direct recombination of conduction band electrons and valence band holes are possible in semiconductors. If direct band-to-band transitions are allowed by the electronic structure of the semiconductor, then band-to-band recombination is one of the main recombination mechanisms. In semiconductor photocatalysts with an indirect type of band gap, the minima of the conduction band do not align in momentum *k*-space with the maxima of the valence band. In that case, band-to-band recombination losses are negligible. Schockley-Read-Hall mechanisms (SRH),[98,99] also known as trap-assisted recombinations, become the primary efficiency loss mechanism dominated by the defect density in the material. If excess energy is available after relaxation, another carrier particle may receive the transferred kinetic energy. The later process is only relevant for high carrier concentrations in heavily degenerate semiconductors and is known as the Auger process.[100] The surface may act as a trapping region due to the high density of surface states. Moreover, the interface may enhance surface recombination rates and their effect should be considered when analyzing different contacts as semiconductor-metal junctions and semiconductor-insulator boundaries.

Charge carrier transport is primarily influenced by the mobility and lifetime of electrons and holes. Ionized impurities dominate the scattering time of the carriers in semiconductor photocatalysts, due to the high carrier concentrations generally measured for powders. Based on the collision time of charge carriers τ_c, hole and electron mobilities $\mu_{p,n}$ can be described using their respective effective masses as $\mu_{p,n} = q\tau_c(m^*_{p,n})^{-1}$. Electrons have higher mobilities than holes, as

observed in Figure 1.12 and deduced from the mobility as a function of their effective mass and collision lifetime. At a lower doping concentration, the mobility is unaffected because is mainly determined by phonon scattering.

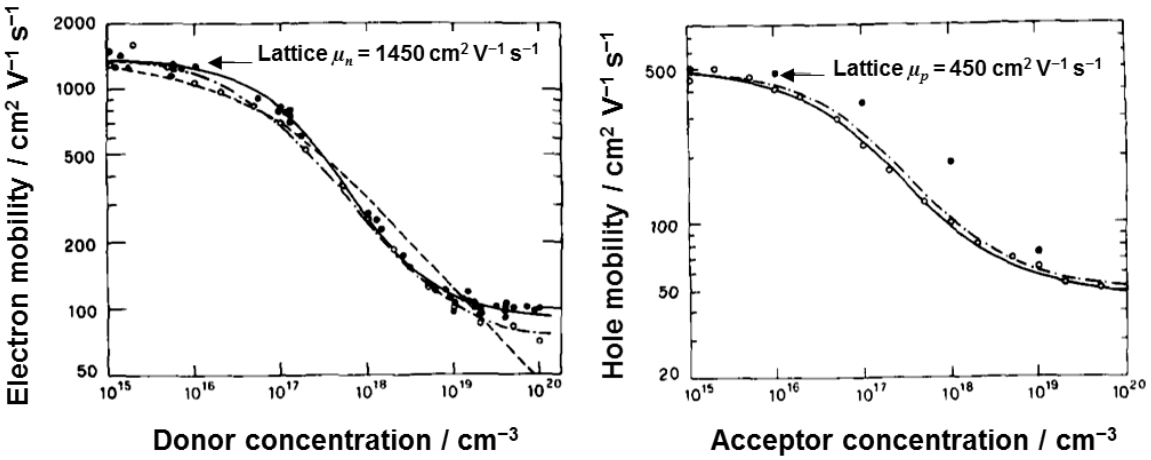

Figure 1.12 Electron and hole mobility in Si at 300 K as a function of impurity concentrations. Data points are experimentally obtained values and the lines represent best fits for different empirical models found in the literature. Adapted from C. Jacoboni et al. *Solid State Electron*., **1977**, 20, 77-89, with permission from © Elsevier.[101]

At high doping concentration, holes and electrons mobility decreases dominated by ionized impurity scattering. For *n*-type materials, the minority carrier is the hole, and for *p*-type materials electrons are the limiting carrier. Typically, the lifetime of the minority carrier is a critical benchmark to determine the performance of a semiconductor photocatalyst because it is contingent upon the recombination rate. The minority carrier lifetime can be defined as the average time before the photoexcited carrier recombines and the parameter can be experimentally determined. For quasi-steady-state and quasi-transient measurements, the effective lifetime may be described from experiments in the following form.[8]

$$\tau_{eff} = \frac{\Delta n(t)}{G(t) - \frac{d\Delta n(t)}{dt}} \tag{1.33}$$

The excess electron density $\Delta n \equiv n - n_0$ derives from the continuity equation 1.25. The equation is valid with the consideration of a uniform photogeneration rate $G(t)$ and assuming zero surface recombination. If the lifetime of the minority carrier at low doping levels is known ($\tau_{p,n}^0$), then we can describe the minority carrier lifetime in the SRH recombination form.[102]

$$\tau_{p,n} = \frac{\tau_{p,n}^0}{1 + \frac{\left(N_d + N_a\right)^{\gamma_{p,n}}}{N_{p,n}^0}} \tag{1.34}$$

$N_{p,n}^0$ and $\gamma_{p,n}$ are fitting parameters for holes and electrons respectively.[95] The minority carrier lifetime in heavily doped photocatalysts is typically a function of the carrier concentration, because it is directly related to the trapping rate of electrons or holes at the defect sites. The lifetime of Si as a function of carrier concentration is a well-known example in the literature, where the lifetime can be described by semi-empirical models as illustrated in Figure 1.13.

Once the lifetime is known, we can define the diffusion length as the average traveled distance of a minority carrier from the photo-generation point until recombination; which is a very important parameter for transport studies in semiconductors. In general, longer diffusion lengths and lifetimes are often associated with the least possible defects in semiconductors with high crystallinity.

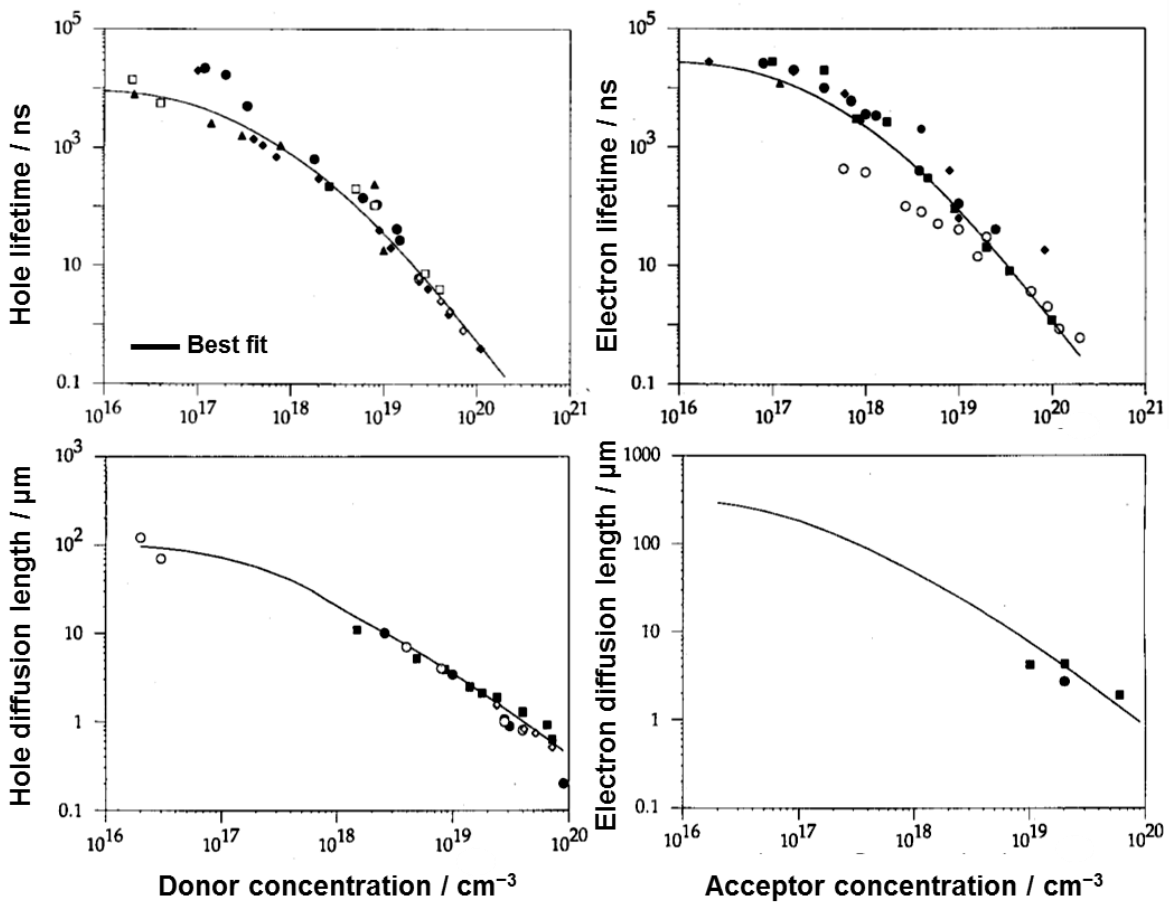

Figure 1.13 Lifetimes and diffusion lengths of the minority carriers for *n*-type (left) and *p*-type (right) Si. Symbols represent experimentally measured values and the curve illustrate the best empirical fit. Adapted from M. E. Law et al. © 1991 IEEE.[103]

$$L_{p,n} \equiv \sqrt{D_{p,n}\tau_{p,n}} \tag{1.35}$$

In photocatalysts used for water-splitting, the electric fields are seldom controlled nor designed; hence, diffusion may be the dominant transport mechanism.[8] The later argument implies that the mobility, lifetime and diffusion length of the charge carriers must be large to achieve high STH efficiencies. We

can reasonably propose that the intrinsic semiconductor electronic properties and the quality of the crystal may dominate successful overall water splitting. When high electric fields are present in the semiconductor, charge carriers may gain energies greater than their thermal energy decreasing the impurity scattering events (defect-assisted recombination).[97] Figure 1.14 illustrates a hypothetical spherical *n*-type semiconductor photocatalyst particle under ideal conditions for overall water splitting. The simulation was performed assuming a typical and relatively high donor concentration of 10^{18} cm^{-3}. The semiconductor has a proper band gap for visible light absorption, a relative dielectric constant of 17 and a relatively long effective lifetime of 4.5×10^{2} ps. The simulation was performed under illumination of AM 1.5G standard using the drift-diffusion expressions coupled with the Poisson's equation. The idealized scheme shows metal nanoparticles dispersed on the surface assumed as the hydrogen evolution site with an ohmic type of contact with the *n*-type semiconductor. The surface was assumed as a semiconductor-liquid junction with a well-defined redox potential for water oxidation (Figure 1.14). The arrows and cones indicate current flow for electrons and holes respectively. Briefly, electron transport can occur from the bulk to the metal site efficiently whereas holes transfer to the semiconductor's surface. Details of the simulation and the effect of the semiconductor parameters on quantum efficiency are discussed in detail in Chapter 2. Further research is required to control the distribution of the electric fields in the semiconductor crystal. Interface design may be essential to achieving high efficiency.

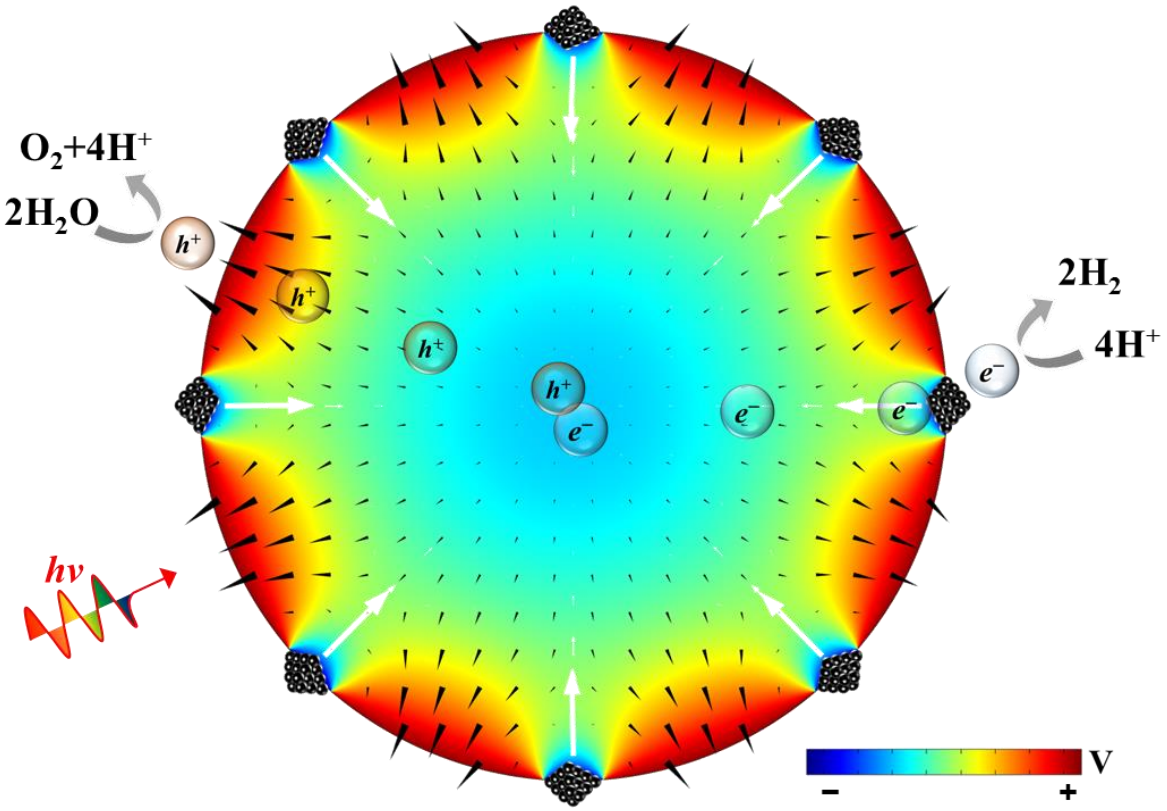

Figure 1.14 Representation of an *n*-type semiconductor particle under overall water splitting conditions using sunlight illumination. White arrows represent vectors for electron currents whereas black cones indicate drift and diffusion of holes. The surface is decorated with metallic particles assumed to be in ohmic contact with the semiconductor. The surface was assumed in contact with an electrolyte interface. The liquid junction was assumed as a Schottky contact under water splitting conditions. Numerical simulations were used to solve the classic semiconductor equations as described in Chapter 2. (r_0 = 8 nm, r_s = 100 nm, E_g = 2.1 eV, χ = 4.3 eV, N_d = 1×10^{18} m^{-2}, ε_r = 17, m^*_n = 1.9, m^*_h = 3.4, $\mu_{p,n}$ = 2 cm^2 V^{-1} s^{-1}, $\tau_{p,\,n}$ = 450 ps, P_0 = 7×10^{20} m^{-2} s^{-1}). Adapted with permission from A. T. Garcia-Esparza and K. Takanabe, *J. Mater. Chem. A.*, **2016**, 4, 2894-2908. © The Royal Society of Chemistry 2016.

1.3.4. Electrocatalysis of water

Aqueous electrochemistry is an essential and critical part of photocatalytic overall water splitting. In fact, without the use of proper and effective so-called cocatalysts, water splitting via photocatalysis is not possible.[66,104] Electrocatalysis of water involves the study of the hydrogen evolution reaction (HER),[105–111] the oxygen evolution reaction (OER),[108,110,112–126] oxygen reduction reaction (ORR)[113,127–140] and hydrogen oxidation reaction (HOR).[59,108,141–144] Typically, researchers focus on the development of efficient catalysts for HER,[145–147] and OER;[117,118,120,124,148–152] without the systematic analysis of the corresponding reverse reactions. Catalytic formation of water is one of the main limitations for the successful photocatalytic electrolysis of water.[104,153–157]

Electrocatalytic reactions are studied via voltammetry. The reaction rate is directly related to the current through the electrodes measured with changing potentials. Hence, all forward and backward reaction rates are potential dependent. The changing potential also affects the intermediate species (i.e. surface coverage). Typically, the empirical Tafel analysis can be employed since 1905 to study electrocatalytic reactions and their elementary steps.[158]

$$\eta = A_T + B_T \log\left(j\right) \tag{1.35}$$

In this form, we express the overpotential η as a function of the measured current density j. The overpotential is defined as the difference between the applied potential on the electrode and the formal standard redox potential of the

reaction to as $\eta = E - E_{eq}$. The Tafel equation indicates that a linear relation is expected, yet this may be only valid if the associated reverse reaction rate is negligible. The implication is that the Tafel analysis can only be valid if the overpotential is large, then a so-called Tafel region can be achieved in the experiment. Two important parameters can be extracted, A_T and B_T which can unveil the electrocatalytic reaction mechanisms. The Tafel slope is denoted as B_T and the exchange current density may be extracted from A_T as discussed below.

Ideally, for a simple one-electron, single-step electrochemical redox reaction we can describe the kinetics using an approximate form of the Butler-Volmer equation.[159]

$$j = j_0(e^{(-\alpha_T f \eta)} - e^{(1-\alpha_T) f \eta}) \qquad (1.36)$$

The constant f is defined as $f = FR^{-1}T^{-1}$, where F is the Faraday's constant, R is the universal gas constant and T is the absolution temperature. The transfer coefficient α_T is an indication of the symmetry of the energy barrier to activate the reaction. In general, the transfer coefficient takes values between 0.3 and 0.7 and in the literature is typically approximated to 0.5. The free energies of activation in a chemical system are in the order of a few electron volts, yet kinetics correspond to changes in activation energy of only 50-200 meV.[158] In most reaction systems, the potential region in which kinetics operate may be very narrow. This implies that as the rate constant (i.e. current) rises exponentially with potential, mass transfer may become rate-limiting close to the point where transfer kinetics can control the experiments. Nevertheless, we can consider a situation where only the forward

reaction of a single-electron transfer reaction operates. Using the Butler-Volmer relation we can theoretically derive an expression related to the Tafel behaviour.

$$\eta = \frac{RT}{\alpha_T F}\ln\left(j_0\right) - \frac{RT}{\alpha_T F}\ln\left(j\right) \tag{1.37}$$

Now we can relate A with the first term of Equation 1.37 containing the so-called exchange current density j_0. From experiments, a plot of η *vs.* $\log j$ can be use to extract a linear intercept with a value that can be converted to j_0. At equilibrium, forward and backward rates must be equal near the standard potential, hence current should be zero. Nevertheless, we can still analyze a balanced faradaic activity expressed in terms of an exchange current in the absence of overpotential. This parameter is proportional to the standard rate constant of the reaction k^0 in the kinetic equations, and it is used as a measure of catalytic performance.[158] The Tafel slope B_T can provide reaction mechanisms details if the elementary steps are described.

The hydrogen evolution reaction is one the most well-studied reactions in the literature. The reaction can be described depending on the pH of the electrolyte in the following two forms.

$$2\mathrm{H_3O^+} + 2e^- \leftrightarrow \mathrm{H_2} + 2\mathrm{H_2O} \tag{1.38}$$

$$2\mathrm{H_2O} + 2e^- \leftrightarrow \mathrm{H_2} + 2\mathrm{OH^-} \tag{1.39}$$

The standard potential for HER/HOR follows the well-known Nerst equation.

$$E_c = E^0 + \frac{RT}{zF}\ln\left(\frac{a^2_{H_3O^+}}{a_{H_2O}\,p_{H_2}}\right) \quad (1.40)$$

$$E_c = E^0 - 0.0591\times \mathrm{pH} - 0.0128\times \ln\left(p_{H_2}\right) \quad (1.41)$$

When the partial pressure of H_2 is large and the fugacity of the gas is assumed close to unity, a pH dependence is expected for HER/HOR expressed as $E_c = E^0 - 0.0591\times \mathrm{pH}$. For each pH step, we should expect ca. 59 mV potential shifts. The pH effects apply to all reactions where hydronium or hydroxide ions are involved.[54] From Equation 1.38, hydronium ion reduction proceeds following elementary steps defined as Volmer, Heyrovsky and Tafel steps.[106,160,161]

$$H_3O^+ + e^- + M \leftrightarrow M\text{-}H^* + H_2O \quad (1.42a)$$

$$M\text{-}H^* + H_3O^+ + e^- \leftrightarrow H_2 + H_2O + M \quad (1.42b)$$

$$2M\text{-}H^* \leftrightarrow H_2 + 2M \quad (1.42c)$$

and for water reduction, in a similar manner the following equations are named as Volmer, Heyrovsky and Tafel steps respectively.

$$H_2O + e^- + M \leftrightarrow M\text{-}H^* + OH^- \quad (1.43a)$$

$$M\text{-}H^* + H_2O + e^- \leftrightarrow H_2 + OH^- + M \quad (1.43b)$$

$$2M\text{-}H^* \leftrightarrow H_2 + 2M \quad (1.43c)$$

An empty site is designated using M, and H* indicates a chemically adsorbed hydrogen atom in the active site on the surface of the electrocatalyst. By using rigorous microkinetic analysis it is possible to study those elementary steps and derive theoretical descriptions by assuming different steps as rate-determining.

For hydronium ion reduction, if the Volmer, Heyrovsky or Tafel steps (Equation 1.42) are each considered as the rate-dermining step, it is possible to show that a relation for current-potential can be obtained.[159]

$$j = zFk_V^0 a_{\mathrm{H_3O^+}} e^{(-\alpha_V f \eta_V)} \tag{1.44a}$$

$$j = zF \frac{k_H^0 K_V^0 a_{\mathrm{H_3O^+}}^2}{K_V^0 a_{\mathrm{H_3O^+}} + a_{\mathrm{H_2O}} e^{(f\eta_V)}} e^{(-\alpha_H f \eta_H)} \tag{1.44b}$$

$$j = zFk_T^0 \left(\frac{K_V^0 a_{\mathrm{H_3O^+}}}{K_V^0 a_{\mathrm{H_3O^+}} + a_{\mathrm{H_2O}} e^{(f\eta_V)}} \right)^2 \tag{1.44c}$$

The subscripts indicate that the variable relates to each of the steps expanded in Equation 1.42 as V (Volmer), H (Heyrovsky) and T (Tafel). z represents the number of transferred electrons in the reaction, k^0 is the standard rate constant and K^0 defines the equilibrium ratio of the forward and backward reaction rate constant. Following the same procedure, one can derive similar expressions when water reduction takes place as described in Equation 1.43 for Volmer, Heyrovsky, and Tafel as limiting steps, respectively.

$$j = zFk_V^0 a_{H_2O} e^{(-\alpha_V f \eta_V)} \quad (1.45a)$$

$$j = zF \frac{k_H^0 K_V^0 a_{H_2O}^2}{K_V^0 a_{H_2O} + a_{OH^-} e^{(f\eta_V)}} e^{(-\alpha_H f \eta_H)} \quad (1.45b)$$

$$j = zFk_T^0 \left(\frac{K_V^0 a_{H_2O}}{K_V^0 a_{H_2O} + a_{OH^-} e^{(f\eta_V)}} \right)^2 \quad (1.45c)$$

The reverse reactions of Equation 1.42 and 1.43 describe the oxidation of hydrogen (HOR), either with water or in the presence of hydronium ions, and similar expressions may be derived using the microkinetic analysis. For a detailed description of this work, the reader is referred to the work of T. Shinawaga et al. (2015).[159]

The oxygen evolution reaction is a multi-step and multi-electron transfer process. The mechanism of water oxidation is complex and still under discussion.[112,113,118,120,121,125,162–167] However, it is possible to consider the following elementary steps with hydroxide ions in alkaline conditions assuming a single site mechanism.

$$M + OH^- \leftrightarrow MOH + e^- \quad (1.46)$$

$$MOH + OH^- \leftrightarrow MO + H_2O + e^- \quad (1.47)$$

$$MO + OH^- \leftrightarrow MOOH + e^- \quad (1.48)$$

$$MOOH + OH^- \leftrightarrow MOO^- + H_2O \quad (1.49)$$

$$MOO^{-} \leftrightarrow M + O_2 + e^{-} \quad (1.50)$$

The microkinetic analysis approach is a valuable tool to study the kinetics and mechanisms of electrocatalytic reactions. The derived current-potential relations can, in principle, theoretically describe the polarization curve expected if a specific rate-determining step dominates the reaction.[159] At first sight, it is possible to observe that the simple Butler-Volmer equation may fail to describe a potential dependent mechanism, especially for multiple electron-transfer steps, and if the reactants change in separate elementary steps. From Equations 1.44 and 1.45 it is possible to simulate the Tafel slopes even under changing surface coverage. Hence, a more detailed analysis can be performed to elucidate the probable reaction mechanisms in electrocatalytic reactions. HER/HOR are not simple reversible reactions as different limiting steps are involved. Thus, it can be misleading to model them using Butler-Volmer kinetics as the relation is only applicable under restricted assumptions.[158,159] In the other hand, Tafel is always applicable under the proper kinetic conditions.

During overall splitting of water, HER and OER should take place efficiently, which requires a catalyst that minimizes the activation energy.[81,168] It is well known that under acidic conditions noble metals are excellent HER electrocatalysts. However, there are a limited number of catalysts that are highly active for OER under such harsh conditions (IrO_x, RuO_x). Such catalysts possess appropriate bonding energy with the adsorbed intermediates, thus providing a low overpotential for the HER or OER.[169] Nevertheless, the development of alternative

non-noble metal catalysts is essential for a sustainable large-scale deployment of solar conversion technologies. Moreover, other pH conditions must be investigated for the development of photocatalytic devices.

As a starting point, benchmarks for heterogeneous electrocatalysts with application in solar-to-hydrogen generation were developed in the literature.[110,116] The electrocatalysts must operate at current densities in the order of 10 mA cm^{-2} to become commercially relevant. The benchmark parameter has been recently defined as the required overpotential to achieve 10 mA cm^{-2}. Typical electrocatalysts for HER and OER working under extreme conditions (pH ≤ 1 or pH ≥ 13) were compiled in Figure 1.15. The horizontal axis of Figure 1.15 represents the benchmark of pristine samples operating at the levels required for practical solar-fuel generation. The vertical axis indicates the performance of the same electrocatalysts after 2 h of continues electrolysis operation. The diagonal line in the figure represents an initial representation of the stability of the material. Extreme acidic and basic conditions are generally studied in the literature; yet, most photocatalysts exhibit larger stability under neutral conditions. Commercial electrocatalysts as Pt and NiMoM catalysts (M = Zn, Co, Fe) outperformed other samples for HER in both acid and alkaline environments. It can be also observed, that there are several HER electrocatalysts competing at the level of activity that noble-metals display. As mentioned before, the oxidation of water in acid is extremely challenging, and very few examples are known due to the stability problems of most materials.[121,166]

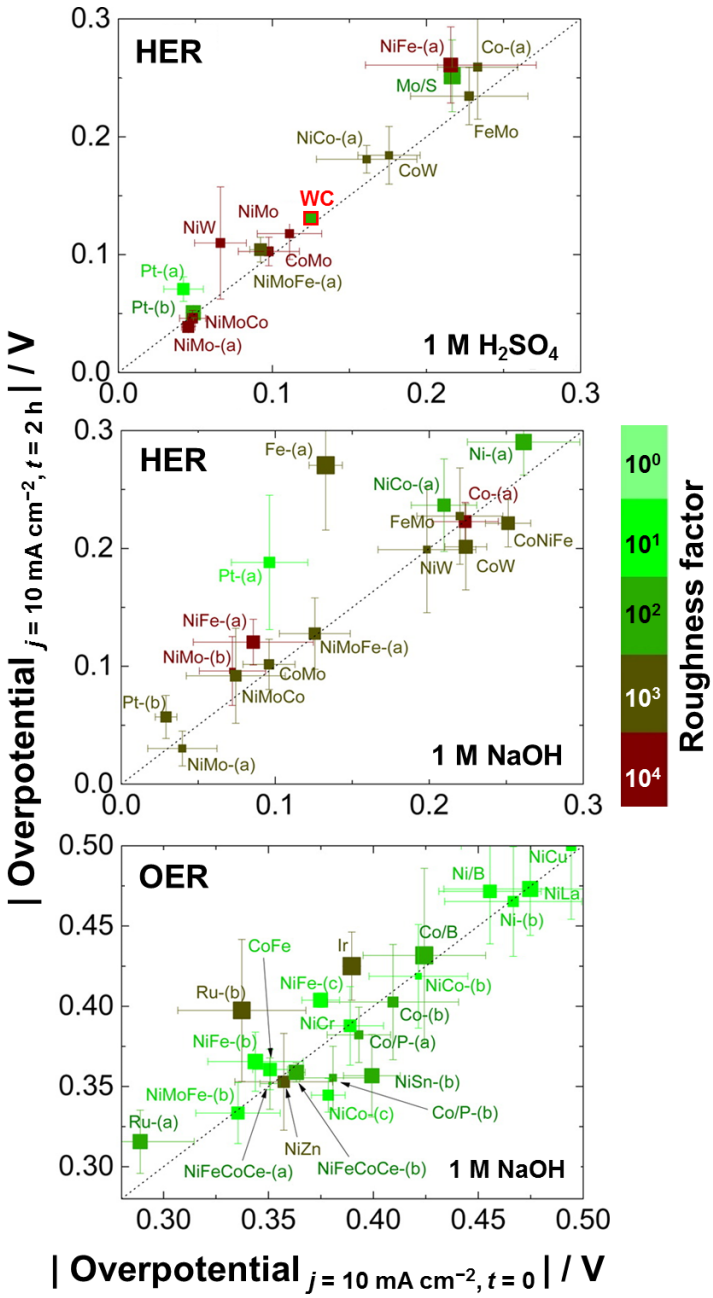

Figure 1.15 Electrocatalysts for HER and OER. The figure of merit used is the overpotential required to achieve 10 mA cm^{-2} (geometric area). The x-axis indicates the overpotential for a fresh sample and the y-axis indicates the change in overpotential after 2 h of electrolysis. The size of the symbol is inversely proportional to the experimentally calculated ECSA. Colors indicate the roughness factor with incremental steps of one order of magnitude. Adapted with permission from C. C. L. McCrory at al. *J. Am. Chem. Soc*., **2015**, 137, 4347–4357, Copyright © 2015 American Chemical Society.[110]

Based on the overpotential required to drive 10 mA per geometric areas, it is reasonable to suggest that development of OER catalysts is still needed. The OER overpotential losses may contribute significantly to the increase photovoltage required for water splitting as discussed based on Figure 1.8. It is possible to notice that bimetallic and multimetallic oxides are good electrocatalysts. The binding energy of the intermediates may be tuned by the introduction of foreign atoms. In the most simple way to look at the problem, we may understand that activity and selectivity can be modulated if the electrocatalysts are designed to interact too strongly or too weakly with the reaction intermediates. An optimum balance must be achieved for effective catalysis, as shown first by Trassati and later calculated by Nørskov (Figure 1.18b).[169–171]

Recently, the interest in developing alternative materials to Pt for HER have increased significantly.[111,172,173] A lot of progress has been made in the last 5 years as observed in Figure 1.16. Pt is one of the most active examples of hydrogen evolution, it generally exhibits (depending on the exposed facets) low Tafel slopes and it only requires < 25 mV to drive 10 mA per electrochemically active surface area (ECSA). Transition metal sulfides, phosphides and carbides have shown improved activities for HER. Carbide and nitride nanoparticles have been developed in our group for HER under acidic conditions.[174,175] WC nanoparticles exhibited remarkable stability and activity for HER/HOR with minimum overpotential requirements, as points marked WC indicate in Figure 1.15 and Figure 1.16.[176]

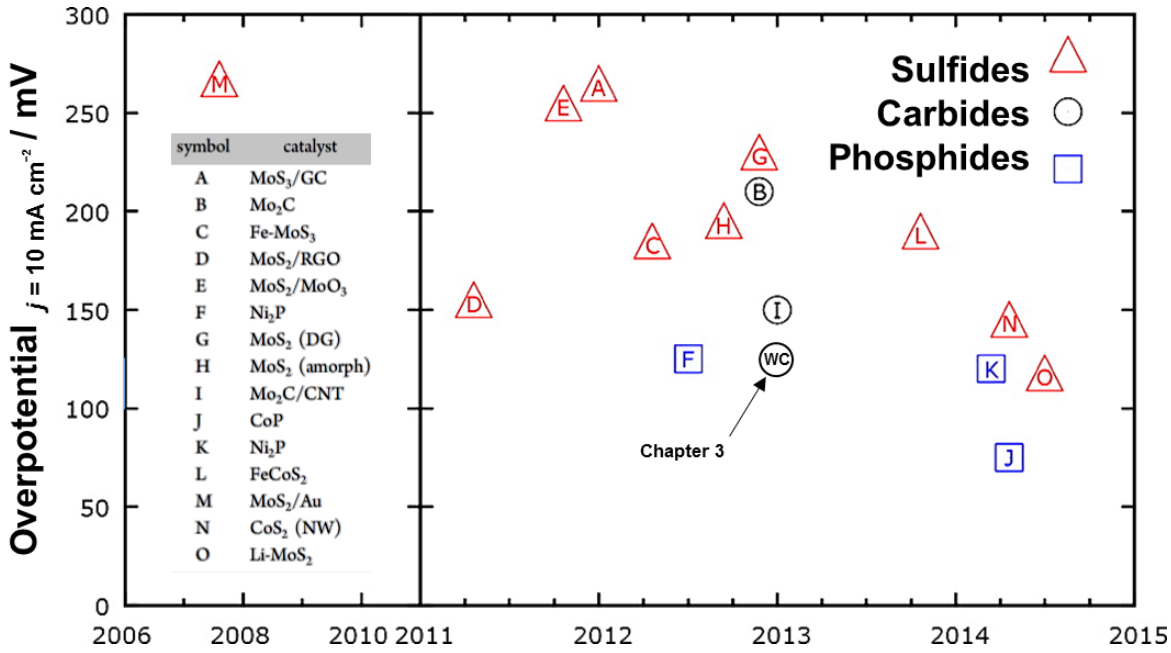

Figure 1.16 Operational benchmark for HER electrocatalysts indicating the overpotential required to achieve 10 mA cm^{-2} (geometric). State-of-the-art transition metal sulfides, carbides and phosphides electrocatalysts in acidic conditions. Pt requires a 25-50 mV overpotential to sustain similar current densities at such conditions. Adapted with permission from P. C. K. Vesborg, B. Seger, I. Chorkendorff, *J. Phys. Chem. Lett.,* **2015**, 6, 951–957, Copyright © 2015 American Chemical Society.[111]

At the time of the report, it was one of the most active non-noble metal electrocatalysts and still is one of the most active transition metal carbides reported in the literature (see details in Chapter 3).[172,177–185] Later developments in the field are reporting benchmark overpotential values of < 100 mV (10 mA cm^{-2} geometric) for Ni_2P and CoP nanoparticles.[147,186] The discussed advances in HER offer catalytic performances that compete against Pt-like activities.

It is interesting to notice that most of the described electrocatalytic studies are done at extreme pH conditions. A general agreement and understanding exist in the literature for HER and OER in acid and basic media; however, studies

dealing with neutral and near-neutral pH are still lacking. Even for one of the most developed catalysts, Pt exhibits significantly different kinetics under different pH conditions.[54,59] Figure 1.17a presents current-potential curves for water electrocatalysis by Pt under changing pH conditions. Figure 1.17b defines the onset potential for HER when the measured current density reaches −0.25 mA cm^{-2}.[58] Three well-defined regions can be observed in the figures. In Region I, the reaction proceeds as established in Equation 1.42 with hydronium ion reduction. As pH increases (Region II), a clear limiting current is observed in Figure 1.17a that can be assigned to mass transport limitation of hydronium ion reduction. As the activity of hydroxide ion increases, water reduction takes places with only thermodynamic limitations (Region III).[54] The regions can be analyzed based on the concentration of hydronium and hydroxide ions as Region I (pH ≤ 5), Region II (5 < pH ≤ 9) and Region III (pH > 10). First, for a highly active catalyst like Pt, the activity follows thermodynamic expectations with a 59.1 mV potential shifts per pH at values near zero volts vs. the reversible hydrogen electrode (Region I). Later, there is a pH-independent onset potential for the reaction, due to the kinetic limitations that are intrinsic to Pt (and Ni) in the neutral region. Finally, in alkaline conditions the onset potential follows again Nernstian expectations.

In neutral conditions, limiting diffusion currents due to mass transport of the reactants can be described using the Levich equation $j_L = 0.62zFD^{2/3}\nu_k^{-1/6}\omega^{1/2}\delta C$. The equation describes the current parameter under diffusion-control in a flat and geometrically well-defined electrode using controlled rotation conditions.[159] D is the diffusion coefficient, ν_k is the kinematic viscocity, z is the number of transferred

electrons, F is the Faraday constant, and δC is the reactant activity difference between the surface and the bulk of the electrolyte. At pH 4.6, is possible to calculate that the maximum attainable current due to mass-transport limitations is −0.25 mA cm^{-2} (Figure 1.17c).[58]

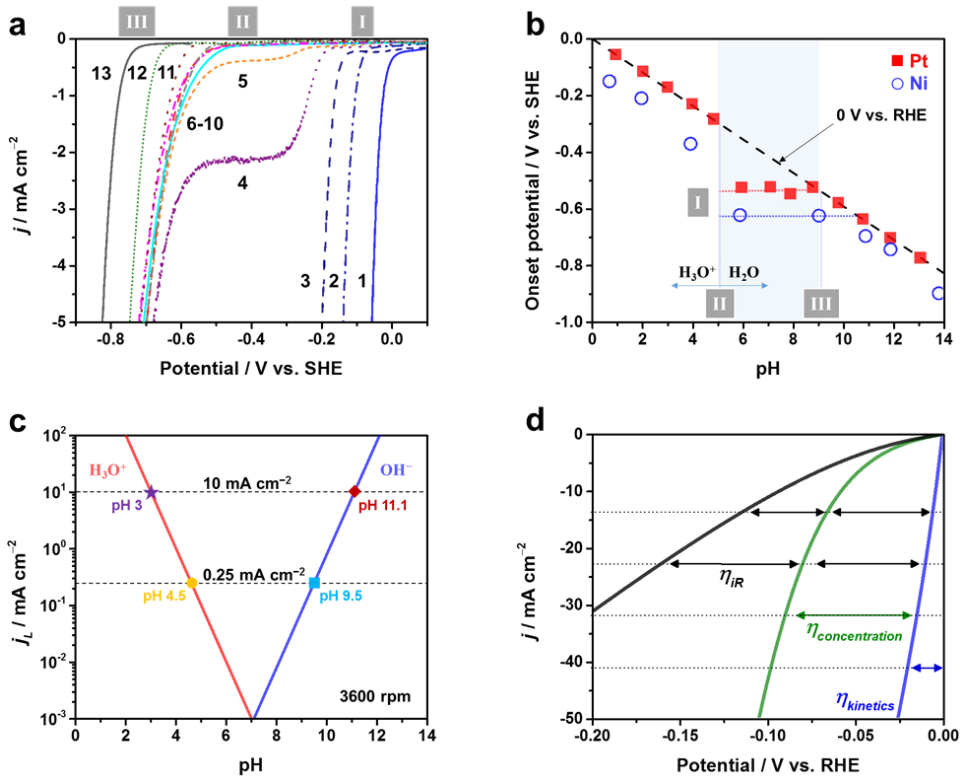

Figure 1.17 Hydrogen evolution half-reaction in neutral conditions without (a-c) and with buffers (d) in solution. (a) Cathodic polarization of a Pt rotating disk electrode under different unbuffered pH conditions. (b) Pt and Ni onset potentials defined to −0.25 mA cm^{-2} HER with changing unbuffered pH (0.5 M Na_2SO_4, 50 mV s^{-1}, 3600 rpm, Ar). Regions are marked in the figure for acid (I), neutral (II) and alkaline (III). (c) Limiting diffusion current density simulations using the Levich equation for H_3O^+ or OH^- as a function of unbuffered pH conditions. (d) Simulations of the HER polarization curves in a buffered electrolyte with and without the effect of the solution resistance and the concentration overpotential (1.0 M NaH_2PO_4). Adapted with permission from T. Shinagawa and K. Takanabe; Copyright © 2014 WILEY-VCH, Copyright © 2015 American Chemical Society, © The Owner Societies 2015.[54,57,58]

For photocatalytic water splitting systems, the repercussions of this calculation are significant. If one must strive to achieve a large STH efficiency, we must drive large electrolysis currents. If hydronium ions are involved in HER, a solution of pH 3 must be used to achieve the benchmark current densities. Electrolyte engineering can be use to circumvent this issue.[57] By using a buffer in the electrolyte, it is possible to shift the reactant involved in HER by keeping the local activity of hydronium ions at constant values near the active site when working in Region II (Figure 1.17d).[57]

To achieve overall water splitting, the surfaces of the catalysts should also be insensitive to the back-reaction of the produced H_2 and O_2 that produces H_2O, i.e., the oxygen reduction reaction (ORR). The hydrogen evolution catalysts must keep their activity intact in the presence of O_2 partial pressures.[187] Hence, the only successful cases reported for photocatalytic overall water splitting in a particulate type of system have used core-shell metal/metal oxide nanoparticles.[49] One of the few exceptions is the work on tungsten carbide presented herein in Chapter 3. WC nanoparticles catalyzed the hydrogen evolution reaction while being inactive for the back reaction of water formation, which will be discussed in detail in Chapter 3. In the literature, the Ni/NiO[188,189] core-shell structure and RuO_2[190] have been extensively utilized as successful cocatalysts for overall water splitting.

One of the successful methods to achieve overall water splitting is to coat metal particles with a Cr layer, thereby forming Cr/metal-core/shell particles on the semiconductor.[104] A study with a model electrode (i.e. Pt electrode with a Cr layer material) revealed that the Cr layer functions to selectively permeate proton and

hydrogen molecules but not oxygen molecules as illustrated in Figure 1.18a.[191] Apparently, the core-shell structure of the chromium-based layer protects the metallic nanoparticle surfaces to suppress the ORR (back-reaction) while maintaining HER (i.e., water reduction).[191] Once most metal particles were coated with a Cr layer, the overall water splitting activity correlated well with HER electrocatalysis when using *n*-type GaN:ZnO as the photocatalyst as observed in Figure 1.18b.[7,8,17,154] The classic volcano-plot indicates that there is an optimal value for HER in acidic media due to the optimize free energy of hydrogen adsorption on metals.[169–171]

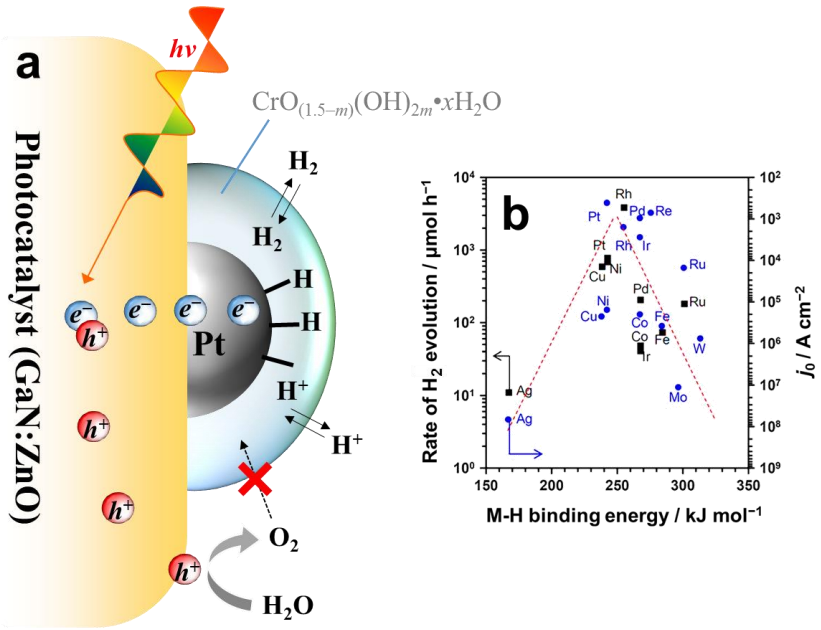

Figure 1.18 (a) Schematic diagram of Rh-core/Cr-shell structure on the surface of GaN:ZnO photocatalyst representing the probable function of the Cr shell based on electrochemical results. (b) Volcano relation exhibiting trends in exchange current density and photocatalytic rates of H_2 evolution as a function of M-H binding energy. Adapted with permission from M. Yoshida et al. *J. Phys. Chem. C*, **2009**, 113, 10151–10157, Copyright © 2009 American Chemical Society and S. Trasatti, *J. Electroanal. Chem.,* **1972**, 39, 163-184, Copyright © 1972 Elsevier.[7,8,154]

As discussed earlier, there are numerous factors to take into account to achieve a highly efficient photocatalytic device: the crystallinity of the semiconductor, electronic configuration and optoelectronic properties of the material, anisotropic effects, photocatalyst morphology, the optimization of the semiconductor-electrocatalyst/semiconductor-liquid junctions, spatial distribution of the electrocatalysts; and the electrolyte environment.[7,8,17,21,24,192] Nonetheless, the development of suitable and *selective* electrocatalysts for overall water splitting is still necessary. An important aspect often overlooked in the literature is the study and understanding of the fundamental electronic effects at the electrocatalyst-semiconductor interface. By varying the electrocatalyst size, morphology and spatial location it may be possible to significantly impact the development of efficient photocatalytic devices. The question is then, how to precisely measure the band-bending effect at the semiconductor surfaces?; moreover, how to extrapolate electrocatalytic rates for the redox reactions, and connect this knowledge with photocatalytic rates along with the overall efficiency of the system?

1.3.5. State of the art

In recent years, the number of scientific groups around the world focusing in the development of particulate photocatalytic technology has seen an exponential increase.[70] Research in the field of photocatalysis have focus in the development of visible-light absorbers,[17,193–195] surface modification with oxygen evolution catalysts[196–199] and hydrogen evolution active sites,[200–202] two-photon systems[203–205] and composite nanostructures for efficient charge transfer.[206–209]

Photocatalytic overall water splitting with semiconductor particles can be summarize briefly as follows.[25,210] The first definitive demonstrations of bias-free water-splitting with powdered semiconductors were done in the 80s via TiO_2[64,65] and $SrTiO_3$[66] with the splitting of water vapor. From the beginning, all the results indicated that suppressing the back reaction of water formation was crucial for success. Platinized TiO_2 cannot split water due to the fast kinetics of water formation, however when NaOH was coated on the surface, it was possible to observe the splitting of water into stoichiometric amounts of H_2 and O_2. A recent study showed that it is possible to selectively suppress water formation resulting from the oxidation of hydrogen using oxydized Pt clusters; it was demonstrated that photocatalytic water splitting occurs in PtO/TiO_2.[153]

$K_4Nb_6O_{17}$ was later found to be active for water-splitting when modified with Ni nanoparticles.[211–213] Since this discovery, different layered perovskites, niobates, and tantalates have been reported to be successful photocatalysts for overall water splitting.[214–219] Particularly, the Kudo group developed a La-doped $NaTaO_3$ photocatalyst with supported NiO electrocatalysts with one of the highest QE ever reported (56% AQE at 270 nm).[188,214] To this point, metal oxides with an empty d orbital configuration were found to be highly active for water splitting.[210] The Inoue group developed semiconductors with d^{10} configurations as a new group of photocatalysts (with RuO_2) for overall water splitting back in 2001.[220–225] Later in 2004 and 2005, it was found that d^{10}-semiconductors such as β-Ga_2O_3 and β-Ge_3N_4 loaded with NiO or RuO_2 respectively were able to split water.[226–229] Actually, this was the first demonstration of water splitting using a non-oxide

photocatalyst particle.[228] Nevertheless, the splitting of water was still being performed under UV-light (β-Ge_3N_4, E_g = 3.8 eV) with a 9% AQE at 300 nm. A recent review compiled particle suspensions performing photocatalytic overall water splitting using visible light and the data is summarized in Figure 1.19.

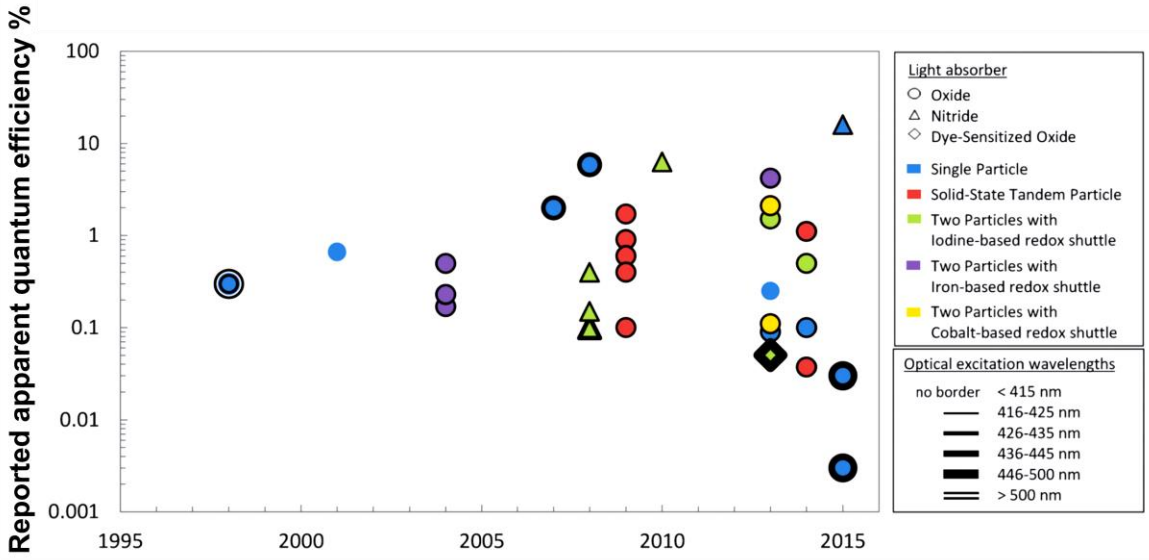

Figure 1.19 Experimental demonstrations of photocatalytic water splitting using different types of photocatalytic systems with their maximum reported AQE in logarithmic scale. The symbol indicates the type of material used as photoabsorber, the color of the data point presents the type of photocatalytic system (Type III or Type IV) and the border thickness of the symbols indicates the wavelengths used to generate photoexcited electron-hole pairs in the particles. Type IV reactor is represented in blue color by Single Particle photocatalysis. Adapted from D. M. Fabian et al. with permission from © The Royal Society of Chemistry 2015.[25]

The figure displays different types of photocatalytic systems in the form of Type III and IV reactors as discussed in Figure 1.3. The first point in the figure refers to Cu_2O photocatalyst (E_g = 2.1 eV). The work reported the evolution of stoichiometric amounts of H_2 and O_2 for >1900 h when irradiated with visible light

(≥ 450 nm) without the use of any electrocatalysts.[230] However, later reports indicated that H_2 was evolved when no O_2 was co-evolved and that the material was oxidized to CuO.[231] As previously discussed, Cu_2O is a highly unstable material as observed in Figure 1.9. Chalcogenides semiconductors (i.e. CdS or CdSe) also suffer from very poor stability, nevertheless recent anti-corrosion strategies may enable the use of unstable materials in aqueous environments for photocatalytic water splitting.[43] The challenge is to efficiently collect the charge carriers before self-photo-oxidation or photo-reduction can occur.[232]

A $NiO/In_{1-x}Ni_xTaO_4$ (x=0.1; Eg = 2.3 eV) photocatalyst was reported in 2001 to split-water under visible light (0.6% $AQE_{420-540nm}$).[233,234] Four years later, GaN:ZnO solution-solid coupled with RuO_2 was reported splitting water using wavelengths ≤ 460 nm with 0.14% $AQE_{300-480nm}$.[56] In 2006, the discovery of a highly selective electrocatalyst ($Rh_{2-y}Cr_yO_3$) enabled higher rates of water splitting using the same $(Ga_{1-x}Zn_x)(N_{1-x}O_x)$ solid-solution achieving a 2.5% $AQE_{420-440nm}$.[104] Interestingly, the photocatalytic reaction performed best at pH 4.5 H_2SO_4 solution.[235] By further optimizations, the Domen group was able to increase the efficiency to 5.9% $AQE_{420-440nm}$.[236] The photocatalyst exhibited a 3 months stability maintaining 50% of the original photocatalytic activity after 6 months of constant operation at a reduced AQE of 0.16%.[237]

Important milestones in photocatalysis were achieved. The development of a selective electrocatalyst for HER insensitive to the water formation reaction (reverse reaction of water splitting) was crucial for the breakthrough. The pH environment of the reaction was considered. The photocatalytic reaction was

performed at pH 3, 4.5 and 6.2 and the water splitting rate was highest in the order of 4.5 > 6.2 > 3.[235] The authors mentioned that at pH 6.2 there was an induction period of high activity, followed by decreasing water splitting rates. The later may be attributed to mass-trasport limited rates and to the kinetic limitations of the Rh metal at neutral conditions. At pH 3 the photocatalyst exhibited the lowest acitvity; three reasons may be discussed: the stability of the GaN:ZnO (1), the formation of a different interface at the outermost atomic layer of the photocatalyst similar to the Ta_3N_5 case (2, see reference for details on Ta_3N_5),[238] and the adsorption of potential determining ions changing the electronic structure-distribution in the semiconductor, ultimately affecting charge separation (3). The highest activity was observed at pH 4.5. Based on the consideration of hydronium ion diffusion, as previously discussed, there would be a limiting rate due to mass transport limitations and concentration overpotentials. Thus, the activity of the system may be improved by electrolyte engineering. Moreover, it exposes an important idea: Although it is in principle possible to optimize electrocatalysts at different pH conditions, the semiconductor predominantly determines the proper operation conditions for water splitting. Unless, one can develop a strategy to inhibit photocorrosion and; more importantly, to control the electronic effects originating from adsorb ions in the solution, and the intrinsic charge distribution ocurring at the semiconductor-liquid junction (depletion or accumulation layers).

Visible-light absorption was finally achieved in photocatalysis along stable photocatalytic generation of hydrogen fuel for relatvely long periods. In 2008, $(Zn_{1+x}Ge)(N_2O_x)$ was loaded with the Cr-Rh mixed oxide electrocatalyst and

generated H_2 and O_2 from water with a 2% $AQE_{420\text{-}440nm}$.[239,240] An interesting point in Figure 1.19 appears in 2013, a photocatalytic system working at λ = 600 nm.[25] Au nanorods were created in a porous insulating alumina template. The nanorods were coverd with TiO_2 and were decorated with Pt and Co-based electrocatalyts for HER and OER respectively. Photocatalysis was performed at pH 9.6 buffered electrolyte and the evolution of H_2 and O_2 was detected when the suspension was illuminated with AM 1.5G standard spectrum (3-suns). Gold surface plasmons were claimed as responsible for light absorption with a 0.25% AQE_{600nm} for more than 60 h of reaction.[241] The report is interesting because it demonstrates overall water splitting using surface plasmons and extraction of carriers from structures confined in an insulating material.

High-aspect ratio nano-structures (so-called nanotrees) were reported to split water using a buried junction of Si in tandem-configuration with TiO_2 nanowires. The Si side was covered with Pt and the TiO_2 surface was loaded with IrO_x electrocatalyst in 0.5 M H_2SO_4 solution.[25] The authors claimed a mimetic approach to photosynthesis with a reported 0.1% STH efficiency by illumination of simulated sunlight.[242] Recenlty, a report using Rh/Cr_2O_3 supported on *p*-GaN/*p*-$In_{0.2}Ga_{0.8}N$ wafer-level nanowire-array claimed a 12.3% $AQE_{400\text{-}475nm}$ and a 1.8% STH efficiency under concentrated AM 1.5G illumination (26 suns).[243] During this year (2015), a metal-free photocatalyst was reported in the form of carbon nitride-carbon nanodots composites (C_3N_4/Cdots).[244] In pure water with a 2-electron pahtway, the nanocomposite was evolving H_2 and O_2 with a 16% AQE_{420nm} and

4.4% AQE_{600nm}. It was possible to measure 2% STH efficiency with AM 1.5G illumination for 200 days.[244]

The Domen group have recently developed a strategy to enable oxynitride photocatalysts as efficient photocatalysts for overall water splitting.[245,246] The discovery consists of using an amorphous hydrous $TiO_{2-m}(OH)_{2m}$ to coat semiconductor materials such as $LaMg_xTa_{1-x}O_{1+3x}N_{2-3x}$ and $CaTaO_2N$. After this modification, the materials are loaded with $RhCrO_y$ mixed-oxide electrocatalysts and they are ready for the water-splitting reaction. Although the reported apparent quantum efficiencies remained low (< 0.1% at λ > 420 nm), the thin amorphous layer allows previously inactive materials to photocatalytically split water. The function of the layer was claimed to be as a protection layer to inhibit photo-corrosion of the oxy-nitride materials. Chapter 2 will illustrate that inhibiting the influence of the electrolyte in *n*-type semiconductors by the use of insulating interfaces may be beneficial to enhance the electron transfer rates to the active sites for hydrogen evolution.

As it was described above, most of the reported photocatalytic systems (Type IV reactors) are still far from from the benchmark target of 5-10% STH. The highest apparent quantum efficiency is ≈ 50% at 270 nm and the report was made more than a decade ago.[188] Nonetheless, this result is still promising because it indicates that efficient photocatalysis is feasible. One of the main challenges consist of using long-wavelength photons efficiently due to their larger penetration depths (see details in Chapter 2). C_3N_4/Cdots composites achieved 2% STH in pure water using visible light (16% AQE_{420nm}, 6.3% AQE_{580nm} and 4.4% AQE_{600nm}).

The result closely approaches the 5% STH target for a cost-effective large scale production of solar hydrogen. Water splitting can be achieved using metal-free, low-cost, abundant and environmentally benign materials.[244]

Despite the fact that the notion of photocatalysis has been known for more than four decades; fundamental understanding of the phenomena governing the efficiency of photocatalytic water splitting is still not well developed. Most of the fundamental physico-chemical mechanisms governing heterogeneous photocatalysis and their impact on the photocatalytic activity are yet to be elucidated.

1.4. Scope of the dissertation

Chapter 2 discusses the fundamental understanding of charge generation, separation and transport in photocatalytic particles. Theoretical simulations were performed to study the intrinsic efficiency limitations of powdered photocatalysts. The semiconductor device equations were numerically solved to study the effects of the semiconductor properties in the overall quantum efficiency of the photocatalytic system. By the use of rigid boundary conditions and assumptions, it was possible to calculate trends with the objective to understand why particulate photocatalysts generally exhibit low quantum efficiencies in the literature. The work presented in Chapter 2 has the objective to analyze an idealized scenario for water splitting. Before the study of a highly complex system; first, the ideal requirements for efficient photocatalysis are discussed.

Chapter 3 contributes to the development of a selective electrocatalyst for overall water splitting. Non-noble metal catalysts are essential for the sustainable development of solar fuels. The synthesis of tungsten carbide nanoparticles was developed by a systematic study of the synthesis conditions using a C_3N_4 reactive-template as the carbon source. Different carbide phases can be made by tuning the reaction conditions. The carbide nanoparticles were used in applications for HER/HOR and ORR. Different phases exhibited distinct catalytic properties. The selectivity of the carbide nanoparticles to HER in the presence of O_2 was investigated in detail. Then, WC nanoparticles were utilized as effective co-catalysts for photocatalytic overall water splitting.

Chapter 4 deals with attempts to develop methods for large-scale production of semiconductor materials. CuO_x is studied as an abundant visible-light absorbing *p*-type photocatalyst. Photoelectrodes are made by simple and reproducible methods with the potential for large-scale manufacture. The Cu-oxide-based semiconductor materials electrochemical and photoelectrochemical properties are thoroughly characterized. PEC current-potential curves were studied under illumination and dark conditions with possible applications for PEC water splitting. The copper-based materials were also used as electrocatalysts for the selective electrochemical reduction of CO_2 in aqueous carbonate electrolytes.

The dissertation proposes a simple guideline for efficient photocatalytic overall water splitting, which was developed from theoretical simulations of idealized photocatalytic particles (Chapter 2). A consistent and general methodology is implicitly presented for the development of selective catalysts via

electrochemical methods. The optimized electrocatalysts, for the fuel-producing reactions of interest (HER or CO2RR), may be later coupled with an independently optimized semiconductor. The coupled photocatalytic device can operate under systematically studied environments for the efficient conversion of solar energy to fuels (Chapter 3). A strategy for the large-scale manufacture of a highly active and abundant semiconductor material is discussed. Proper characterization methodologies are presented in a way that can be followed for any semiconductor materials. Particularly semiconductors with stability challenges. Additionally, the Cu-based materials are studied and presented as promising catalysts for the selective electroreduction of CO_2 by providing a systematic characterization of the electrocatalyst (Chapter 4).

1.5. REFERENCES

1 M. Z. Jacobson, *Energy Environ. Sci.*, **2009**, 2, 148.

2 M. Eby, K. Zickfeld, A. Montenegro, D. Archer, K. J. Meissner, A. J. Weaver, *J. Clim.*, **2009**, 22, 2501–2511.

3 M. R. Allen, D. J. Frame, C. Huntingford, C. D. Jones, J. A. Lowe, M. Meinshausen, N. Meinshausen, *Nature*, **2009**, 458, 1163–1166.

4 T. L. Frölicher, M. Winton and J. L. Sarmiento, *Nat. Clim. Chang.*, **2014**, 4, 40–44.

5 IEA data from World Energy Outlook Special Report: Energy and Climate Change, © *OECD/IEA 2015, IEA Publ.*, **2015**.

6 IEA data from Tracking Clean Energy Progress in Energy Technology Perspectives, © *OECD/IEA 2015, IEA Publ.*, **2015**.

7 K. Takanabe and K. Domen, in *Heterogeneous Catalysis at Nanoscale for Energy Applications*, eds. F. F. Tao, W. F. Schneider and P. V. Kamat, John Wiley & Sons, Inc, Hoboken, NJ, **2014**.

8 K. Takanabe, in *Topics in current chemistry*, Springer Berlin Heidelberg, **2015**, 371, 73–103.

9 Reference Solar Spectral Irradiance: Air Mass 1.5 Global (ASTM G173-03), National Renewable Energy Laboratory (NREL), Accessed on September 30th, **2015**. http://rredc.nrel.gov/solar/spectra/am1.5/

10 IEA data from Renewables Information: Key Renewable Trends, © *OECD/IEA 2015, IEA Publ.*, **2015**.

11 B. A. Pinaud, J. D. Benck, L. C. Seitz, A. J. Forman, Z. Chen, T. G. Deutsch, B. D. James, K. N. Baum, G. N. Baum, S. Ardo, H. Wang, E. Miller, T. F. Jaramillo, *Energy Environ. Sci.*, **2013**, 6, 1983–2002.

12 D. Gust and T. A. Moore, *Science*, **1989**, 244, 35–41.

13 A. J. Bard and M. A. Fox, *Acc. Chem. Res.*, **1995**, 28, 141–145.

14 G. Ciamician, *Science*, **1912**, 36, 385–94.

15 D. M. Schultz and T. P. Yoon, *Science*, **2014**, 343, 1239176.

16 IEA data from Technology Roadmap: Hydrogen and Fuel Cells, © *OECD/IEA 2015, IEA Publ.*, **2015**.

17 K. Takanabe and K. Domen, *Green*, **2011**, 1, 313–322.

18 S. M. M. Sze and K. K. Ng, *Physics of Semiconductor Devices*, John Wiley & Sons Inc., 3rd Edition, **2007**.

19 M. X. Tan, P. E. Laibinis, S. T. Nguyen, J. M. Kesselman, C. E. Stanton, N. S. Lewis, in *Progress in Inorganic Chemistry, Volume 41*, ed. K. D. Karlin, John Wiley & Sons, Inc., Hoboken, NJ, USA, **1994**, vol. 41, pp. 21–144.

20 W. Schmickler and E. Santos, in *Interfacial electrochemistry*, Springer Berlin Heidelberg, Berlin, Heidelberg, 2nd Editio., **2010**, vol. 131, pp. 117–131.

21 T. Hisatomi, K. Takanabe and K. Domen, *Catal. Letters*, **2014**, 145, 95–108.

22 R. H. Coridan, A. C. Nielander, S. A. Francis, M. T. McDowell, V. Dix, S. M. Chatman, N. S. Lewis, *Energy Environ. Sci.*, **2015**, 8, 2886–2901.

23 Z. Chen, H. N. Dinh and E. Miller, *Photoelectrochemical Water Splitting*, Springer New York, New York, NY, **2013**.

24 Z. Chen, T. F. Jaramillo, T. G. Deutsch, A. Kleiman-Shwarsctein, A. J. Forman, N. Gaillard, R. Garland, K. Takanabe, C. Heske, M. Sunkara, E. W. McFarland, K. Domen, E. L. Miller, J. A. Turner, H. N. Dinh, *J. Mater. Res.*, **2011**, 25, 3–16.

25 D. M. Fabian, S. Hu, N. Singh, F. A. Houle, T. Hisatomi, K. Domen, F. Osterloh, S. Ardo, *Energy Environ. Sci.*, **2015**, 8, 2825–2850.

26 B. D. James, G. N. Baum, J. Perez, K. N. Baum, *Technoeconomic Analysis of Photoelectrochemical (PEC) Hydrogen Production*, Directed Technologies Inc., (US DOE Contract no. GS-10F-009J), Arlington, VA, **2009**.

27 J. W. Ager III, M. Shaner, K. Walczak, I. D. Sharp, S. Ardo, *Energy Environ. Sci.*, **2015**, 8, 2811–2824.

28 D. L. Block, in *Proceedings of the 12th World Hydrogen Energy Conference*, Asociacion Argentina del Hidrogeno, Buenos Aires, Argentina, **1998**, pp. 185–194.

29 A. Fujishima and K. Honda, *Nature*, **1972**, 238, 37–38.

30 A. J. Nozik, *Nature*, **1975**, 257, 383–386.

31 H. Yoneyama, H. Sakamoto and H. Tamura, *Electrochim. Acta*, **1975**, 20, 341–345.

32 A. J. Nozik, *Appl. Phys. Lett.*, **1976**, 29, 150–153.

33 A. J. Nozik, *Appl. Phys. Lett.*, **1977**, 30, 567–569.

34 S. Khan, R. Kainthla and J. Bockris, *Int. J. Hydrogen Energy*, **1988**, 13, 225–230.

35 R. Kainthla, S. Khan and J. Bockris, *Int. J. Hydrogen Energy*, **1987**, 12, 381–392.

36 R. C. Kainthla, *J. Electrochem. Soc.*, **1987**, 134, 841–845.

37 M. M. May, H.-J. Lewerenz, D. Lackner, F. Dimroth, T. Hannappel, *Nat. Commun.*, **2015**, 6, 8286.

38 O. Khaselev and J. A. Turner, *Science*, **1998**, 280, 425–427.

39 S. Licht, B. Wang, S. Mukerji, T. Soga, M. Umeno, H. Tributsch, *J. Phys. Chem. B*, **2000**, 104, 8920–8924.

40 O. Khaselev, A. Bansal and J. A. Turner, *Int. J. Hydrogen Energy*, **2001**, 26, 127–132.

41 S. Y. Reece, J. A. Hamel, K. Sung, T. D. Jarvi, A. J. Esswein, J. J. H. Pijpers, D. G. Nocera, *Science*, **2011**, 334, 645–648.

42 N. Kelly and T. Gibson, *Int. J. Hydrogen Energy*, **2006**, 31, 1658–1673.

43 S. Hu, M. R. Shaner, J. A. Beardslee, M. Lichterman, B. S. Brunschwig, N. S. Lewis, *Science*, **2014**, 344, 1005–1009.

44 J. Luo, J.-H. Im, M. T. Mayer, M. Schreier, M. K. Nazeeruddin, N.-G. Park, S. D. Tilley, H. J. Fan, M. Grätzel, *Science*, **2014**, 345, 1593–1596.

45 T. J. Jacobsson, V. Fjällström, M. Sahlberg, M. Edoff, T. Edvinsson, *Energy Environ. Sci.*, **2013**, 6, 3676–3683.

46 C. R. Cox, J. Z. Lee, D. G. Nocera, T. Buonassisi, *Proc. Natl. Acad. Sci.*, **2014**, 111, 14057–14061.

47 P. Zhai, S. Haussener, J. Ager, R. Sathre, K. Walczak, J. Greenblatt, T. McKone, *Energy Environ. Sci.*, **2013**, 6, 2380.

48 F. E. Osterloh, in *Topics in current chemistry*, Springer Berlin Heidelberg, **2015**, 371, 105–142.

49 K. Takanabe and K. Domen, *ChemCatChem*, **2012**, 4, 1485–1497.

50 F. Dionigi, P. C. K. Vesborg, T. Pedersen, O. Hansen, S. Dahl, A. Xiong, K. Maeda, K. Domen, I. Chorkendorff, *J. Catal.*, **2012**, 292, 26–31.

51 I. E. Wachs, S. P. Phivilay, C. A. Roberts, *ACS Catal.,* **2013,** 3, 2606–2611.

52 N. Serpone and A. Salinaro, *Pure Appl. Chem.*, **1999**, 71, 303–320.

53 L. C. Seitz, Z. Chen, A. J. Forman, B. A. Pinaud, J. D. Benck, T. F. Jaramillo, *ChemSusChem*, **2014**, 7, 1372–1385.

54 T. Shinagawa, A. T. Garcia-Esparza and K. Takanabe, *ChemElectroChem*, **2014**, 1, 1497–1507.

55 R. Abe, *J. Photochem. Photobiol. C Photochem. Rev.*, **2010**, 11, 179–209.

56 K. Maeda, T. Takata, M. Hara, N. Saito, Y. Inoue, H. Kobayashi, K. Domen, *J. Am. Chem. Soc.*, **2005**, 127, 8286–8287.

57 T. Shinagawa and K. Takanabe, *J. Phys. Chem. C*, **2015**, 119, 20453-20458.

58 T. Shinagawa and K. Takanabe, *Phys. Chem. Chem. Phys.*, **2015**, 17, 15111–15114.

59 D. Strmcnik, M. Uchimura, C. Wang, R. Subbaraman, N. Danilovic, D. van der Vliet, A. P. Paulikas, V. R. Stamenkovic, N. M. Markovic, *Nat. Chem.*, **2013**, 5, 300–306.

60 T. Hisatomi, T. Minegishi and K. Domen, *Bull. Chem. Soc. Jpn.*, **2012**, 85, 647–655.

61 S. Chen and L.-W. Wang, *Chem. Mater.*, **2012**, 24, 3659–3666.

62 A. Kudo, *Pure Appl. Chem.*, **2007**, 79, 1917–1927.

63 K. Maeda and K. Domen, *J. Phys. Chem. C*, **2007**, 111, 7851–7861.

64 S. Sato and J. M. White, *Chem. Phys. Lett.*, **1980**, 72, 83–86.

65 T. Kawai and T. Sakata, *Chem. Phys. Lett.*, **1980**, 72, 87–89.

66 K. Domen, S. Naito, M. Soma, T. Onishi, K. Tamaru, *J. Chem. Soc. Chem. Commun.*, **1980**, 543–544.

67 Y. Takahara, J. N. Kondo, T. Takata, D. Lu, K. Domen, *Chem. Mater.*, **2001**, 13, 1194–1199.

68 N. Arai, N. Saito, H. Nishiyama, Y. Inoue, K. Domen, K. Sato, *Chem. Lett.*, **2006**, 35, 796–797.

69 D. Wang, A. Pierre, M. G. Kibria, K. Cui, X. Han, K. H. Bevan, H. Guo, S. Paradis, A.-R. Hakima, Z. Mi, *Nano Lett.*, **2011**, 11, 2353–2357.

70 Z. Zhang and J. T. Yates, *Chem. Rev.*, **2012**, 112, 5520–5551.

71 T. Ioannides and X. Verykios, *J. Catal.*, **1996**, 569, 560–569.

72 R. Memming, in *Topics in current chemistry*, ed. J. Mattay, Springer Berlin Heidelberg, Berlin, Heidelberg, **1994**, vol. 169.

73 W. J. Albery, *J. Electrochem. Soc.*, **1984**, 131, 315–325.

74 H. Gerischer, *J. Phys. Chem.*, **1984**, 88, 6096–6097.

75 A. Hagfeldt and M. Gratzel, *Chem. Rev.*, **1995**, 95, 49–68.

76 P. V Kamat, K. Tvrdy, D. R. Baker, J. G. Radich, *Chem. Rev.*, **2010**, 110, 6664–6688.

77 M. Schiavello, *Photoelectrochemistry, Photocatalysis and Photoreactors*, Springer Netherlands, Dordrecht, **1985**.

78 L. Brillson, *Surf. Sci.*, **1994**, 300, 909–927.

79 M. McEllistrem, G. Haase, D. Chen, R. Hamers, *Phys. Rev. Lett.*, **1993**, 70, 2471–2475.

80 Z. Zhang and J. T. Yates, *J. Phys. Chem. Lett.*, **2010**, 1, 2185–2188.

81 M. G. Walter, E. L. Warren, J. R. McKone, S. W. Boettcher, Q. Mi, E. Santori, N. S. Lewis, *Chem. Rev.*, **2010**, 110, 6446–6473.

82 H. Lewerenz and L. Peter, *Photoelectrochemical Water Splitting*, Royal Society of Chemistry, Cambridge, **2013**.

83 K. Rajeshwar, in *Encyclopedia of Electrochemistry*, ed. A. J. Bard, Wiley-VCH Verlag GmbH & Co. KGaA, Weinheim, Germany, **2007**.

84 Y. Nosaka, K. Norimatsu and H. Miyama, *Chem. Phys. Lett.*, **1984**, 106, 128–131.

85 J. S. Curran, J. Domenech, N. Jaffrezic-Renault, R. Philippe, *J. Phys. Chem.*, **1985**, 89, 957–963.

86 Y. Nosaka, Y. Ishizuka and H. Miyama, *Berichte der Bunsengesellschaft für physikalische Chemie*, **1986**, 90, 1199–1204.

87 P. Cendula, S. D. Tilley, S. Gimenez, J. Bisquert, M. Schmid, M. Grätzel, J. O. Schumacher, *J. Phys. Chem. C*, **2014**, 118, 29599–29607.

88 J. Bisquert, P. Cendula, L. Bertoluzzi, S. Gimenez, *J. Phys. Chem. Lett.*, **2014**, 5, 205–207.

89 F. Lin and S. W. Boettcher, *Nat. Mater.*, **2014**, 13, 81–86.

90 T. J. Mills, F. Lin and S. W. Boettcher, *Phys. Rev. Lett.*, **2014**, 112, 148304.

91 D. Bae, T. Pedersen, B. Seger, M. Malizia, A. Kuznetsov, O. Hansen, I. Chorkendorff, P. C. K. Vesborg, *Energy Environ. Sci.*, **2014**, 8, 650–660.

92 R. C. Rossi and N. S. Lewis, *J. Phys. Chem. B*, **2001**, 105, 12303–12318.

93 R. C. Rossi, M. X. Tan and N. S. Lewis, *Appl. Phys. Lett.*, **2000**, 77, 2698–2700.

94 A. T. Garcia-Esparza and K. Takanabe, *J. Mater. Chem. A*, **2015**, DOI: 10.1039/C5TA06983A.

95 S. Selberherr, *Analysis and Simulation of Semiconductor Devices*, Springer Vienna, Vienna, **1984**.

96 R. Entner, *Modeling and Simulation of Negative Bias Temperature Instability*, PhD Dissertation, Technischen Universitat Wien, **2007**.

97 M. Lundstrom, *Fundamentals of Carrier Transport*, Cambridge University Press, Cambridge, **2000**.

98 W. Shockley and W. Read, *Phys. Rev.*, **1952**, 87, 835–842.

99 R. Hall, *Phys. Rev.*, **1952**, 87, 387–387.

100 P. Auger, *C.R.A.S.*, **1923**, 177, 169–171.

101 C. Jacoboni, C. Canali, G. Ottaviani, A. Alberigi Quaranta, *Solid. State. Electron.*, **1977**, 20, 77–89.

102 J. M. Park, *Novel power devices for smart power applications*, PhD Disseration, Technischen Universität Wien, **2004**.

103 M. E. Law, E. Solley, M. Liang, D. E. Burk, *IEEE Electron Device Lett.*, **1991**, 12, 401–403.

104 K. Maeda, K. Teramura, D. Lu, T. Takata, N. Saito, Y. Inoue, K. Domen, *Nature*, **2006**, 440, 295.

105 S. Trasatti, *J. Electroanal. Chem. Interfacial Electrochem.*, **1972**, 39, 163–184.

106 B. E. Conway and L. Bai, *J. Electroanal. Chem. Interfacial Electrochem.*, **1986**, 198, 149–175.

107 J. Greeley, T. F. Jaramillo, J. Bonde, I. B. Chorkendorff, J. K. Nørskov, *Nat. Mater.*, **2006**, 5, 909–913.

108 R. Subbaraman, D. Tripkovic, K.-C. Chang, D. Strmcnik, A. P. Paulikas, P. Hirunsit, M. Chan, J. Greeley, V. Stamenkovic, N. M. Markovic, *Nat. Mater.*, **2012**, 11, 550–557.

109 Q. Lu, G. S. Hutchings, W. Yu, Y. Zhou, R. V. Forest, R. Tao, J. Rosen, B. T. Yonemoto, Z. Cao, H. Zheng, J. Q. Xiao, F. Jiao, J. G. Chen, *Nat. Commun.*, **2015**, 6, 6567.

110 C. C. L. McCrory, S. Jung, I. M. Ferrer, S. Chatman, J. C. Peters, T. F. Jaramillo, *J. Am. Chem. Soc.*, **2015**, 137, 4347–4357.

111 P. C. K. Vesborg, B. Seger and I. Chorkendorff, *J. Phys. Chem. Lett.*, **2015**, 6, 951–957.

112 J. O. Bockris, *J. Chem. Phys.*, **1956**, 24, 817.

113 A. J. Appleby, *J. Electroanal. Chem. Interfacial Electrochem.*, **1970**, 24, 97–117.

114 L. Trotochaud, J. K. Ranney, K. N. Williams, S. W. Boettcher, *J. Am. Chem. Soc.*, **2012**, 134, 17253–17261.

115 S. Cobo, J. Heidkamp, P.-A. Jacques, J. Fize, V. Fourmond, L. Guetaz, B. Jousselme, V. Ivanova, H. Dau, S. Palacin, M. Fontecave, V. Artero, *Nat. Mater.*, **2012**, 11, 802–807.

116 C. C. L. McCrory, S. Jung, J. C. Peters, T. F. Jaramillo, *J. Am. Chem. Soc.*, **2013**, 135, 16977–16987.

117 M. Gong, Y. Li, H. Wang, Y. Liang, J. Z. Wu, J. Zhou, J. Wang, T. Regier, F. Wei, H. Dai, *J. Am. Chem. Soc.*, **2013**, 135, 8452–8455.

118 A. Grimaud, K. J. May, C. E. Carlton, Y.-L. Lee, M. Risch, W. T. Hong, J. Zhou, Y. Shao-Horn, *Nat. Commun.*, **2013**, 4, 2439.

119 F. Song and X. Hu, *Nat. Commun.*, **2014**, 5, 4477.

120 E. A. Paoli, F. Masini, R. Frydendal, D. Deiana, C. Schlaup, M. Malizia, T. Hansen, S. Horch, I. Stephens, I. Chorkendorff, *Chem. Sci.*, **2015**, 6, 190–196.

121 S. H. Chang, N. Danilovic, K.-C. Chang, R. Subbaraman, A. P. Paulikas, D. D. Fong, M. J. Highland, P. M. Baldo, V. R. Stamenkovic, J. W. Freeland, J. A. Eastman, N. M. Markovic, *Nat. Commun.*, **2014**, 5, 4191.

122 W. Hong, M. Risch, K. A. Stoerzinger, A. J. L. Grimaud, J. Suntivich, Y. Shao-Horn, *Energy Environ. Sci.*, **2015**, 8, 1404–1427.

123 D. Friebel, M. W. Louie, M. Bajdich, K. E. Sanwald, Y. Cai, A. M. Wise, M.-J. Cheng, D. Sokaras, T.-C. Weng, R. Alonso-Mori, R. C. Davis, J. R. Bargar, J. K. Norskov, A. Nilsson, A. T. Bell, *J. Am. Chem. Soc.*, **2015**, 137, 1305–1313.

124 Y. Wu, M. Chen, Y. Han, H. Luo, X. Su, M.-T. Zhang, X. Lin, J. Sun, L. Wang, L. Deng, W. Zhang, R. Cao, *Angew. Chemie*, **2015**, 127, 4952–4957.

125 M. Risch, F. Ringleb, M. Kohlhoff, P. Bogdanoff, P. Chernev, I. Zaharieva, H. Dau, *Energy Environ. Sci.*, **2015**, 8, 661–674.

126 Y. Gorlin, C.-J. Chung, J. D. Benck, D. Nordlund, L. Seitz, T.-C. Weng, D. Sokaras, B. M. Clemens, T. F. Jaramillo, *J. Am. Chem. Soc.*, **2014**, 136, 4920–4926.

127 H. A. Laitinen and C. G. Enke, *J. Electrochem. Soc.*, **1960**, 107, 773–781.

128 H. Angerstein-Kozlowska, B. E. Conway and W. B. A. Sharp, *J. Electroanal. Chem. Interfacial Electrochem.*, **1973**, 43, 9–36.

129 N. M. Marković, T. J. Schmidt, V. Stamenković, P. N. Ross, *Fuel Cells*, **2001**, 1, 105–116.

130 S. Koh and P. Strasser, *J. Am. Chem. Soc.*, **2007**, 129, 12624–12625.

131 V. R. Stamenkovic, B. Fowler, B. S. Mun, G. Wang, P. N. Ross, C. A. Lucas, N. M. Marković, *Science*, **2007**, 315, 493–497.

132 P. Strasser, S. Koh, T. Anniyev, J. Greeley, K. More, C. Yu, Z. Liu, S. Kaya, D. Nordlund, H. Ogasawara, M. F. Toney, A. Nilsson, *Nat. Chem.*, **2010**, 2, 454–460.

133 J. Seo, D. Cha, K. Takanabe, J. Kubota and K. Domen, *Chem. Commun.*, **2012**, 48, 9074–9076.

134 J. Chen, K. Takanabe, R. Ohnishi, D. Lu, S. Okada, H. Hatasawa, H. Morioka, M. Antonietti, J. Kubota, K. Domen, *Chem. Commun.*, **2010**, 46, 7492–7494.

135 A. Holewinski and S. Linic, *J. Electrochem. Soc.*, **2012**, 159, H864–H870.

136 R. Ohnishi, M. Katayama, D. Cha, K. Takanabe, J. Kubota and K. Domen, *J. Electrochem. Soc.*, **2013**, 160, F501–F506.

137 J. Seo, D. Cha, K. Takanabe, J. Kubota and K. Domen, *Phys. Chem. Chem. Phys.*, **2014**, 16, 895–898.

138 D. Li, C. Wang, D. Strmcnik, D. V Tripković, X. Sun, Y. Kang, M. Chi, J. Snyder, D. van der Vliet, Y. Tsai, V. Stamenkovic, S. Sun, N. Markovic, *Energy Environ. Sci.*, **2014**, 7, 4061–4069.

139 C. Chen, Y. Kang, Z. Huo, Z. Zhu, W. Huang, H. L. Xin, J. D. Snyder, D. Li, J. A. Herron, M. Mavrikakis, M. Chi, K. L. More, Y. Li, N. M. Markovic, G. A. Somorjai, P. Yang, V. R. Stamenkovic, *Science*, **2014**, 343, 1339–1343.

140 A. M. Gómez-Marín, R. Rizo and J. M. Feliu, *Catal. Sci. Technol.*, **2014**, 4, 1685–1698.

141 W. Vogel, L. Lundquist, P. Ross, P. Stonehart, *Electrochim. Acta*, **1975**, 20, 79–93.

142 T. Zhang and A. B. Anderson, *J. Phys. Chem. C*, **2007**, 111, 8644–8648.

143 J. Durst, A. Siebel, C. Simon, F. Hasché, J. Herranz, H. A. Gasteiger, *Energy Environ. Sci.*, **2014**, 7, 2255–2260.

144 J. Durst, C. Simon, F. Hasche, H. A. Gasteiger, *J. Electrochem. Soc.*, **2014**, 162, F190–F203.

145 H. Yin, S. Zhao, K. Zhao, A. Muqsit, H. Tang, L. Chang, H. Zhao, Y. Gao, Z. Tang, *Nat. Commun.*, **2015**, 6, 6430.

146 J. Kibsgaard and T. F. Jaramillo, *Angew. Chemie Int. Ed.*, **2014**, 53, 14433–14437.

147 E. J. Popczun, J. R. McKone, C. G. Read, A. J. Biacchi, A. M. Wiltrout, N. S. Lewis and R. E. Schaak, *J. Am. Chem. Soc.*, **2013**, 135, 9267–9270.

148 H. Jin, J. Wang, D. Su, Z. Wei, Z. Pang and Y. Wang, *J. Am. Chem. Soc.*, **2015**, 137, 2688–2694.

149 L. Trotochaud, S. L. Young, J. K. Ranney, S. W. Boettcher, *J. Am. Chem. Soc.*, **2014**, 136, 6744–6753.

150 K. Fominykh, J. M. Feckl, J. Sicklinger, M. Döblinger, S. Böcklein, J. Ziegler, L. Peter, J. Rathousky, E.-W. Scheidt, T. Bein, D. Fattakhova-Rohlfing, *Adv. Funct. Mater.*, **2014**, 24, 3123–3129.

151 J. Wang, H. Zhong, Y. Qin, X. Zhang, *Angew. Chemie*, **2013**, 125, 5356–5361.

152 J. Suntivich, K. J. May, H. A. Gasteiger, J. B. Goodenough, Y. Shao-Horn, *Science*, **2011**, 334, 1383–1385.

153 Y. Hang Li, J. Xing, Z. Jia Chen, Z. Li, F. Tian, L. Rong Zheng, H. Feng Wang, P. Hu, H. Jun Zhao, H. Gui Yang, *Nat. Commun.*, **2013**, 4, 2500.

154 M. Yoshida, K. Takanabe, K. Maeda, A. Ishikawa, J. Kubota, Y. Sakata, Y. Ikezawa, K. Domen, *J. Phys. Chem. C*, **2009**, 113, 10151–10157.

155 K. Maeda, K. Teramura, D. Lu, N. Saito, Y. Inoue, K. Domen, *J. Phys. Chem. C*, **2007**, 111, 7554–7560.

156 T. Takata, C. Pan, M. Nakabayashi, N. Shibata, K. Domen, *J. Am. Chem. Soc.*, **2015**, 137, 9627–9634.

157 T. Takata, C. Pan and K. Domen, *ChemElectroChem*, **2015**, DOI: 10.1002/celc.201500324.

158 A. J. Bard and L. R. Faulkner, *Electrochemical methods Fundamentals and applications*, John Wiley & Sons, New York, Second Edi., **2001**.

159 T. Shinagawa, A. T. Garcia-Esparza and K. Takanabe, *Sci. Rep.*, **2015**, 5, 13801.

160 Y. Zheng, Y. Jiao, M. Jaroniec, S. Z. Qiao, *Angew. Chem. Int. Ed.*, **2015**, 54, 52–65.

161 M. R. Gennero de Chialvo and A. C. Chialvo, *J. Electrochem. Soc.*, **2000**, 147, 1619–1622.

162 A. Damjanovic, A. Dey and J. O. Bockris, *Electrochim. Acta*, **1966**, 11, 791–814.

163 B. E. Conway and B. V. Tilak, *Adv. Catal.*, **1992**, 38, 1–147.

164 N. B. Halck, V. Petrykin, P. Krtil, J. Rossmeisl, *Phys. Chem. Chem. Phys.*, **2014**, 16, 13682–13688.

165 D. González-Flores, I. Sánchez, I. Zaharieva, K. Klingan, J. Heidkamp, P. Chernev, P. W. Menezes, M. Driess, H. Dau, M. L. Montero, *Angew. Chemie*, **2015**, 127, 2502–2506.

166 N. Danilovic, R. Subbaraman, K.-C. Chang, S. H. Chang, Y. J. Kang, J. Snyder, A. P. Paulikas, D. Strmcnik, Y.-T. Kim, D. Myers, V. R. Stamenkovic, N. M. Markovic, *J. Phys. Chem. Lett.*, **2014**, 5, 2474–2478.

167 J. R. Galán-Mascarós, *ChemElectroChem*, **2015**, 2, 37–50.

168 X. Chen, S. Shen, L. Guo, S. S. Mao, *Chem. Rev.*, **2010**, 110, 6503–6570.

169 J. K. Nørskov, T. Bligaard, a. Logadottir, J. R. Kitchin, J. G. Chen, S. Pandelov and U. Stimming, *J. Electrochem. Soc.*, **2005**, 152, J23–J26.

170 S. Trasatti, *Electroanal. Chem. Interfacial Electrochem.*, **1972**, 39, 163–184.

171 V. R. Stamenkovic, B. S. Mun, M. Arenz, K. J. J. Mayrhofer, C. A. Lucas, G. Wang, P. N. Ross, N. M. Markovic, *Nat. Mater.*, **2007**, 6, 241–247.

172 W.-F. Chen, J. T. Muckerman and E. Fujita, *Chem. Commun.*, **2013**, 49, 8896–8909.

173 J. Kibsgaard, C. Tsai, K. Chan, J. D. Benck, J. K. Nørskov, F. Abild-Pedersen, T. F. Jaramillo, *Energy Environ. Sci.*, **2015**, 8, 3022–3029.

174 N. S. Alhajri, D. H. Anjum and K. Takanabe, *J. Mater. Chem. A*, **2014**, 2, 10548–10556.

175 N. S. Alhajri, H. Yoshida, D. H. Anjum, A. T. Garcia-Esparza, J. Kubota, K. Domen, K. Takanabe, *J. Mater. Chem. A*, **2013**, 1, 12606–12616.

176 A. T. Garcia-Esparza, D. Cha, Y. Ou, J. Kubota, K. Domen, K. Takanabe, *ChemSusChem*, **2013**, 6, 168–181.

177 X. Fan, H. Zhou and X. Guo, *ACS Nano*, **2015**, 9, 5125–5134.

178 S. T. Hunt, T. Nimmanwudipong, Y. Román-Leshkov, *Angew. Chem. Int. Ed.*, **2014**, 53, 5131–5136.

179 J. Zhu, K. Sakaushi, G. Clavel, M. Shalom, M. Antonietti, T.-P. Fellinger, *J. Am. Chem. Soc.*, **2015**, 137, 5480–5485.

180 T. Xiao, A. Hanif, A. P. E. York, J. Sloan, M. L. H. Green, *Phys. Chem. Chem. Phys.*, **2002**, 4, 3522–3529.

181 J. Ma and Y. Du, *J. Alloys Compd.*, **2008**, 448, 215–218.

182 M. C. Weidman, D. V. Esposito, I. J. Hsu, J. G. Chen, *J. Electrochem. Soc.*, **2010**, 157, F179–F188.

183 M. C. Weidman, D. V. Esposito, Y.-C. Hsu and J. G. Chen, *J. Power Sources*, **2012**, 202, 11–17.

184 Y. C. Kimmel, D. V. Esposito, R. W. Birkmire and J. G. Chen, *Int. J. Hydrogen Energy*, **2012**, 37, 3019–3024.

185 F. Harnisch, G. Sievers and U. Schröder, *Appl. Catal. B Environ.*, **2009**, 89, 455–458.

186 E. J. Popczun, C. G. Read, C. W. Roske, N. S. Lewis, R. E. Schaak, *Angew. Chem. Int. Ed.*, **2014**, 53, 5427–5430.

187 D. W. Wakerley and E. Reisner, *Energy Environ. Sci.*, **2015**, 8, 2283–2295.

188 H. Kato, K. Asakura and A. Kudo, *J. Am. Chem. Soc.*, **2003**, 125, 3082–3089.

189 Y. Miseki, H. Kato and A. Kudo, *Energy Environ. Sci.*, **2009**, 2, 306–314.

190 Y. Inoue, *Energy Environ. Sci.*, **2009**, 2, 364–386.

191 M. Yoshida and K. Takanabe, *J. Phys. Chem. C*, **2009**, 113, 10151–10157.

192 X. Lu, A. Bandara, M. Katayama, A. Yamakata, J. Kubota, K. Domen, *J. Phys. Chem. C*, **2011**, 115, 23902–23907.

193 D. Mitoraj and H. Kisch, *Angew. Chem. Int. Ed.*, **2008**, 47, 9975–9978.

194 T. Ohno, L. Bai, T. Hisatomi, K. Maeda, K. Domen, *J. Am. Chem. Soc.*, **2012**, 134, 8254–8259.

195 Y. Fukasawa, K. Takanabe, A. Shimojima, M. Antonietti, K. Domen, T. Okubo, *Chem. Asian J.*, **2011**, 6, 103–109.

196 Y. Liang, Y. Li, H. Wang, J. Zhou, J. Wang, T. Regier, H. Dai, *Nat. Mater.*, **2011**, 10, 780–786.

197 F. Jiao and H. Frei, *Angew. Chem. Int. Ed.*, **2009**, 48, 1841–1844.

198 R. Abe, M. Higashi and K. Domen, *J. Am. Chem. Soc.*, **2010**, 132, 11828–11829.

199 M. Liao, J. Feng, W. Luo, Z. Wang, J. Zhang, Z. Li, T. Yu, Z. Zou, *Adv. Funct. Mater.*, **2012**, 22, 3066–3074.

200 L. Yuliati, J.-H. Yang, X. Wang, K. Maeda, T. Takata, M. Antonietti, K. Domen, *J. Mater. Chem.*, **2010**, 20, 4295–4298.

201 R. Subbaraman, D. Tripkovic, D. Strmcnik, K.-C. Chang, M. Uchimura, A. P. Paulikas, V. Stamenkovic, N. M. Markovic, *Science*, **2011**, 334, 1256–1260.

202 H. Kotani, R. Hanazaki, K. Ohkubo, Y. Yamada, S. Fukuzumi, *Chemistry*, **2011**, 17, 2777–2785.

203 H. Tada, T. Mitsui, T. Kiyonaga, T. Akita, K. Tanaka, *Nat. Mater.*, **2006**, 5, 782–786.

204 A. Kudo and Y. Miseki, *Chem. Soc. Rev.*, **2009**, 38, 253–278.

205 R. Abe, K. Sayama, K. Domen, H. Arakawa, *Chem. Phys. Lett.*, **2001**, 344, 339–344.

206 C. Chen, W. Cai, M. Long, B. Zhou, Y. Wu, D. Wu, *ACS Nano*, **2010**, 4, 6425–6432.

207 Y. H. Ng, I. V. Lightcap, K. Goodwin, M. Matsumura, P. V. Kamat, *J. Phys. Chem. Lett.*, **2010**, 1, 2222–2227.

208 Y. H. Ng, A. Iwase, A. Kudo, R. Amal, *J. Phys. Chem. Lett.*, **2010**, 1, 2607–2612.

209 S. Min and G. Lu, *J. Phys. Chem. C*, **2011**, 115, 13938–13945.

210 K. Maeda, *J. Photochem. Photobiol. C Photochem. Rev.*, **2011**, 12, 237–268.

211 A. Kudo, K. Sayama, A. Tanaka, K. Asakura, K. Domen, K. Maruya, T. Onishi, *J. Catal.*, **1989**, 120, 337–352.

212 A. Kudo, A. Tanaka, K. Domen, K. Maruya, K. Aika, T. Onichi, *J. Catal.*, **1988**, 111, 67–76.

213 K. Domen, A. Kudo, A. Shinozaki, A. Tanaka, K. Maruya, T. Onishi, *J. Chem. Soc. Chem. Commun.*, **1986**, 356–357.

214 H. Kato and A. Kudo, *Catal. Letters*, **1999**, 58, 153–155.

215 A. Kudo, H. Kato and S. Nakagawa, *J. Phys. Chem. B*, **2000**, 104, 571–575.

216 H. Kato and A. Kudo, *J. Phys. Chem. B*, **2001**, 105, 4285–4292.

217 H. Kato and A. Kudo, *Catal. Today*, **2003**, 78, 561–569.

218 A. Kudo and H. Kato, *Chem. Lett.*, **1997**, 26, 867–868.

219 H. Kato and A. Kudo, *Chem. Phys. Lett.*, **1998**, 295, 487–492.

220 J. Sato, H. Kobayashi and Y. Inoue, *J. Phys. Chem. B*, **2003**, 107, 7970–7975.

221 N. Arai, N. Saito, H. Nishiyama, Y. Shimodaira, H. Kobayashi, Y. Inoue, K. Sato, *J. Phys. Chem. C*, **2008**, 112, 5000–5005.

222 J. Sato, H. Kobayashi, K. Ikarashi, N. Saito, H. Nishiyama, Y. Inoue, *J. Phys. Chem. B*, **2004**, 108, 4369–4375.

223 J. Sato, H. Kobayashi, N. Saito, H. Nishiyama, Y. Inoue, *J. Photochem. Photobiol. A Chem.*, **2003**, 158, 139–144.

224 J. Sato, N. Saito, H. Nishiyama, Y. Inoue, *J. Photochem. Photobiol. A Chem.*, **2002**, 148, 85–89.

225 J. Sato, N. Saito, H. Nishiyama, Y. Inoue, *J. Phys. Chem. B*, **2001**, 105, 6061–6063.

226 K. Maeda, N. Saito, D. Lu, Y. Inoue, K. Domen, *J. Phys. Chem. C*, **2007**, 111, 4749–4755.

227 Y. Lee, T. Watanabe, T. Takata, M. Hara, M. Yoshimura, K. Domen, *J. Phys. Chem. B*, **2006**, 110, 17563–17569.

228 J. Sato, N. Saito, Y. Yamada, K. Maeda, T. Takata, J. N. Kondo, M. Hara, H. Kobayashi, K. Domen, Y. Inoue, *J. Am. Chem. Soc.*, **2005**, 127, 4150–4151.

229 T. Yanagida, Y. Sakata and H. Imamura, *Chem. Lett.*, **2004**, 33, 726–727.

230 M. Hara, T. Kondo, M. Komoda, S. Ikeda, J. N. Kondo, K. Domen, K. Shinohara, A. Tanaka, *Chem. Commun.*, **1998**, 357–358.

231 S. Kakuta and T. Abe, *Electrochem. Solid-State Lett.*, **2009**, 12, P1–P3.

232 A. Paracchino, V. Laporte, K. Sivula, M. Grätzel, E. Thimsen, *Nat. Mater.*, **2011**, 10, 456–461.

233 A. C. Malingowski, P. W. Stephens, A. Huq, Q. Huang, S. Khalid, P. G. Khalifah, *Inorg. Chem.*, **2012**, 51, 6096–6103.

234 Z. Zou, J. Ye, K. Sayama and H. Arakawa, *Nature*, **2001**, 414, 625–627.

235 K. Maeda, K. Teramura, H. Masuda, T. Takata, N. Saito, Y. Inoue, K. Domen, *J. Phys. Chem. B*, **2006**, 110, 13107–13112.

236 K. Maeda, K. Teramura and K. Domen, *J. Catal.*, **2008**, 254, 198–204.

237 T. Ohno, L. Bai, T. Hisatomi, K. Maeda, K. Domen, *J. Am. Chem. Soc.*, **2012**, 134, 8254–8259.

238 E. Nurlaela, S. Ould-Chikh, M. Harb, S. del Gobbo, M. Aouine, E. Puzenat, P. Sautet, K. Domen, J.-M. Basset, K. Takanabe, *Chem. Mater.*, **2014**, 26, 4812–4825.

239 Y. Lee, H. Terashima, Y. Shimodaira, K. Teramura, M. Hara, H. Kobayashi, K. Domen, M. Yashima, *J. Phys. Chem. C*, **2007**, 111, 1042–1048.

240 X. Wang, K. Maeda, Y. Lee, K. Domen, *Chem. Phys. Lett.*, **2008**, 457, 134–136.

241 S. Mubeen, J. Lee, N. Singh, S. Krämer, G. D. Stucky, M. Moskovits, *Nat. Nanotechnol.*, **2013**, 8, 247–251.

242 C. Liu, J. Tang, H. M. Chen, B. Liu, P. Yang, *Nano Lett.*, **2013**, 13, 2989–2992.

243 M. G. Kibria, F. A. Chowdhury, S. Zhao, B. AlOtaibi, M. L. Trudeau, H. Guo, Z. Mi, *Nat. Commun.*, **2015**, 6, 6797.

244 J. Liu, Y. Liu, N. Liu, Y. Han, X. Zhang, H. Huang, Y. Lifshitz, S.-T. Lee, J. Zhong, Z. Kang, *Science*, **2015**, 347, 970–974.

245 C. Pan, T. Takata, M. Nakabayashi, T. Matsumoto, N. Shibata, Y. Ikuhara, K. Domen, *Angew. Chem. Int. Ed.*, **2015**, 54, 2955–2959.

245 T. Takata, C. Pan, M. Nakabayashi, N. Shibata, K. Domen, *J. Am. Chem. Soc.*, **2015**, 137, 9627–9634.

CHAPTER 2

2. A Simplified Guideline for Using Photocatalyst Particles[a]

Particulate photocatalytic water splitting is the most disruptive and competitive solution for the direct production of solar fuels. Despite more than four decades of work in the field of photocatalysis using powder semiconductors decorated with catalyst particles, there is no clear consensus on the factors limiting the solar-to-hydrogen efficiency (STH). This chapter presents numerical simulations to understand the intrinsic limitations of photocatalysis using simplified two-dimensional photocatalytic models employing the classical semiconductor device equations. This section evaluates the sensitivity of quantum efficiency (QE) to the various semiconductor properties, such as absorption properties and carrier mobilities, and to the dispersion of catalyst particles, which create heterojunctions, the driving force for charge separation.

A pinch-off effect was prevalent underneath the hydrogen evolution site, suggesting an undesired energetic barrier for electron diffusion to the catalyst. The simulation, using the values reported in the literature, revealed that the QE was exclusively governed by recombination in the bulk of the photocatalyst particles; hindering the charge separation efficiency before reaching the catalysts on the surface. The simulation shows that a typical defective *n*-type semiconductor particle (~100 nm) ideally exhibits a QE of <5% in the visible light range per

[a] This chapter was reproduced from A. T. Garcia-Esparza and K. Takanabe, *J. Mater. Chem. A.*, **2016**, 4, 2894-2908.© The Royal Society of Chemistry 2016.

particle, which reaches only approximately 10% in a slurry after 4 consecutive absorbing units (1.4% STH, from simulated solar irradiation). Although the presented model contains rigid limitations, researchers may use these trends as an initial guideline to pursue a photocatalysis by design strategy, which may result in possible alternatives to achieve higher efficiencies.

2.1. Introduction

Heterogeneous particulate photocatalytic overall water splitting is one of the most promising systems for sustainable and competitive solar hydrogen generation from an economic point of view.[1] For more than four decades, the development of an efficient artificial photosynthesis process has remained elusive.[2] The process has evolved from the inception of the first photo-electrochemical cells[3] to the development of so-called microphotoelectrochemical cells (i.e., photocatalytic slurry reactors);[4] however, the technology is still far from industrial commercialization. TiO_2 has been one of the most studied photocatalysts for many decades, yet it does not absorb 85% of the usable photons for water splitting available in the solar spectrum (≥1.6 eV).[5,6] Additionally, no clear understanding nor description of the chemical physics of charge separation and transport has been clearly developed.

Many photocatalytic systems in the literature have followed a thermal catalysis structure design of supported metal sites dispersed on the surface of, most frequently, an inert support.[7] One of the main differences between

heterogeneous thermal catalysis and photocatalysis is that the semiconductor absorber is an essential active component. Light absorption introduces the first limiting step to the overall system, and the liquid phase environment influences the active component under illumination.[8] Photonic charge generation can intrinsically determine the overall efficiency of the photocatalytic system. Increasing the amount of photocatalyst will not increase the rate of produced H_2 proportionally (as photon absorption saturates); thus, normalization of a photocatalytic rate of product formation by grams of material is meaningless when the photocatalytic efficiency or reactor/device photonic efficiency is the primary concern.[9]

Particulate photocatalytic water splitting represents an enormous challenge because it involves an extremely complex series of photophysical and electrocatalytic steps.[8,10] One way to tackle this challenge may be to divide the problems into components that can be examined separately. The first part is associated with semiconductor properties, such as light absorption with charge generation, separation and transport (Semiconductor).[11–13] Then, electrochemistry can be used to optimize the required active sites for electrocatalytic hydrogen and oxygen evolution reactions or any other targeted reactions (Electrocatalyst),[14] including mass transport of reactants and solution environment (pH, present ions, temperature, etc.).[15,16] Finally, the critical step is to design all the interfaces (e.g., electrocatalyst-photocatalyst, electrolyte-photocatalyst) when coupling the independently optimized systems (Interface).[14,17–19] The presence of a catalyst and the resultant electrocatalyst-semiconductor contact is essential for successful overall water splitting, not only because it provides an anisotropic energy diagram

in the semiconductor for charge separation, but also the site drives the electrocatalytic redox reactions in the surface.

Until recently, there was a weak consensus on how to evaluate and rigorously compare the efficiency of photocatalytic systems.[20] Different from the photovoltaic solar cell community, there are less consistent theoretical frameworks to describe the physicochemical behaviors of photocatalysts, particularly their charge carrier dynamics.[21–27] The fundamental physical phenomena at the semiconductor-electrolyte interface have been described in the literature, particularly detailed for photoelectrochemical electrodes.[27–30] Recent work provided a theoretical description of the experimental behavior of a Si photoelectrode covered with patterned nanoscale Ni catalysts under bias-control.[31] Rossi and Lewis used a point-dipole approximation, called the Tung model, for the simulation of the current-potential curve of such a photoelectrochemical cell working in a well-defined redox-potential electrolyte.[32] Furthermore, a recent study on the modelling and simulations of semiconductors coated with ion-permeable or dense electrocatalysts described the experimental results obtained from TiO_2 photoelectrodes coated with porous non-noble metal Ni oxyhydroxide catalysts.[33,34] Alternatively, other groups have provided a theoretical reference to model an Fe_2O_3 photoelectrode with a reasonable description of their current-potential behavior under typical experimental conditions found in the literature.[35,36]

Nevertheless, the study of models describing particulate photocatalysis is still limited and only few works can be found in the literature.[37–41] Hisatomi et al. recently reported numerical simulations of a so-called asymmetric one-

dimensional photocatalytic model using $LaTiO_2N$ to understand the fundamental limiting factors of the semiconductor material.[42] However, it is still not possible to model powdered semiconductors and much less venture to predict quantum efficiencies for unbiased photocatalytic systems. In an effort to understand the limitations of the photocatalytic technology, a finite-volume method was used to simulate two-dimensional particulate photocatalytic model systems decorated with metal nanoparticles on the surface of the semiconductor. The classical semiconductor equations describe the electrostatics and charge carrier drift and diffusion. The aim is to humbly calculate reasonable trends to determine the maximum achievable solar-to-hydrogen conversion efficiency (STH) using a powder-form photocatalytic water splitting device.

2.2. Theory

The simulations to solve the potential and current transport in particulate photocatalytic systems were performed using COMSOL Multiphysics. The numerical calculation uses a finite volume method employing Scharfetter-Gummel discretization for particle transport. In COMSOL, the current is implicitly conserved using this method. The model entails numerically solving the semiconductor equations consisting of the Poisson's equation and the current continuity equations for each charge carrier (Equations 2.1-2.3).[43,44]

$$\nabla \cdot (\nabla \phi) = -\frac{q}{\varepsilon_0 \varepsilon_r}(p - n + N_d - N_a) \tag{2.1}$$

$$\frac{1}{q}\nabla \cdot \mathbf{J}_n = U_n \tag{2.2}$$

$$\frac{1}{q}\nabla \cdot \mathbf{J}_p = -U_p \tag{2.3}$$

Electron and hole currents are defined using the general drift-diffusion equations (Equations 2.4 and 2.5 were already discussed as Equation 1.31).

$$\mathbf{J}_n = q\left(\mu_n n\mathbf{E} + D_n \nabla n\right) \tag{2.4}$$

$$\mathbf{J}_p = q\left(\mu_p p\mathbf{E} - D_p \nabla p\right) \tag{2.5}$$

The net recombination rate $U_{p,n}$ in Equations 2.2 and 2.3 was calculated from the generation G and recombination R mechanisms in the model.

$$U_{p,n} = \sum R_{p,n,i} - \sum G_{p,n,i} \tag{2.6}$$

The generation rate term assumes generation of one exciton (electron-hole pair) for each photon absorbed at any point in the semiconductor model (Equation 2.7). Using Lambert-Beer's law, without considering reflection and scattering events, the absorption of light depends on the absorption coefficient α of the material and its thickness x.

$$G_n = G_p = P_0 \alpha e^{(-\alpha x)} \tag{2.7}$$

The photon flux density P_0 is the integration of the incident photons in the AM 1.5G solar spectrum (1000 W m^{-2}) with energies larger than the

semiconductor's band gap. The created electron-hole pairs must be separated into free excited carriers for subsequent transfer to the surface where they may catalyze redox reactions. The mobility and the diffusion of free electrons and holes in the semiconductor are described through the Einstein relations.

$$D = \frac{k_B T}{q} \mu \tag{2.8}$$

$$\mu = q \frac{\tau_c}{m^*} \tag{2.9}$$

Excited conduction band electrons and valence band holes may recombine by traps. The calculation assumes only a defect-assisted recombination type of process called steady-state Shockley-Read-Hall recombination.[44]

$$R_n = R_p = \frac{np - n_i^2}{\tau_p (n + N_C e^{-\frac{E_C - E_T}{k_B T}}) + \tau_n (p + N_V e^{\frac{E_V - E_T}{k_B T}})} \tag{2.10}$$

An ideal and simplified Schottky interface was assumed to calculate the current in the electrolyte-semiconductor interface as

$$\mathbf{n} \cdot \mathbf{J}_n = -q v_n (n - n_0) \tag{2.11}$$

$$\mathbf{n} \cdot \mathbf{J}_p = q v_p (p - p_0) \tag{2.12}$$

$$n_0 = N_C e^{\left(\frac{E_C - E_f}{k_B T}\right)} = N_C e^{\left(\frac{\Phi_B}{k_B T}\right)} \tag{2.13}$$

$$p_0 = N_V e^{\left(\frac{E_f - E_V}{k_B T}\right)} = N_V e^{\left(\frac{E_g - \Phi_B}{k_B T}\right)} \quad (2.14)$$

$$\Phi_B = E_{redox} - \chi \quad (2.15)$$

In Equation 2.11 and 2.12, **n** represents an outward oriented vector normal to the boundary. This assumption treats the rectifying contact as a sink for carriers with specific recombination velocities v_n and v_p:

$$v_n = \frac{A_n^* T^2}{qN_C} \quad (2.16)$$

$$v_p = \frac{A_p^* T^2}{qN_V} \quad (2.17)$$

$$A_{p,n}^* = 4\pi m_{p,n}^* q k_B{}^2 h^{-3} \quad (2.18)$$

$$W_D = \sqrt{\frac{2\varepsilon_0 \varepsilon_r |V_{bi}|}{qN_d}} \quad (2.19)$$

Finally, Equation 2.19 was obtained using the full depletion approximation to solve the one-dimensional Poisson equation as discussed in the band-bending section of the first chapter (Chapter 1 Introduction).[27,36] This equation describes the magnitude of the depletion layer W_D as a function of the defect density in the semiconductor N_d, the potential difference across the semiconductor, which equals the built-in potential V_{bi} generated at the Schottky interface, and the relative dielectric constant of the semiconductor ε_r.

2.3. Model and assumptions

Figure 2.1 shows the geometrical models used to approximate the electrostatics and carrier dynamics of a particulate semiconductor decorated with a metallic catalyst on its surface. The ρ-direction symbolizes the semiconductor surface, x-direction represents the distance from the surface interface into the bulk or it can be understood as the size of the semiconductor particle, r_0 represents the diameter size of the metallic catalyst particle, and the angle θ controls the interparticle distance of the catalysts distributed on the surface of the semiconductor in Model IV. The geometric models were discretized using free-triangular elements. The minimum element size was restricted to 8×10^{-12} m with a growing rate and a maximum element size of 4×10^{-10} m. To solve for the large curvatures and steep gradients in the potential and/or carrier concentration, the mesh spacing is finest at the semiconductor interface with either Schottky or ohmic junctions (Figure 2.2).

In Figure 2.1, Models I and II show two of the simplest box-type models for a semiconductor photocatalyst in contact with an electrolyte and a single or multiple metallic catalysts on its surface. The electrolyte-semiconductor interface and the metal-semiconductor contact were considered to be a Schottky junction in Model I. Dirichlet and Neumann boundary conditions were used in the models.

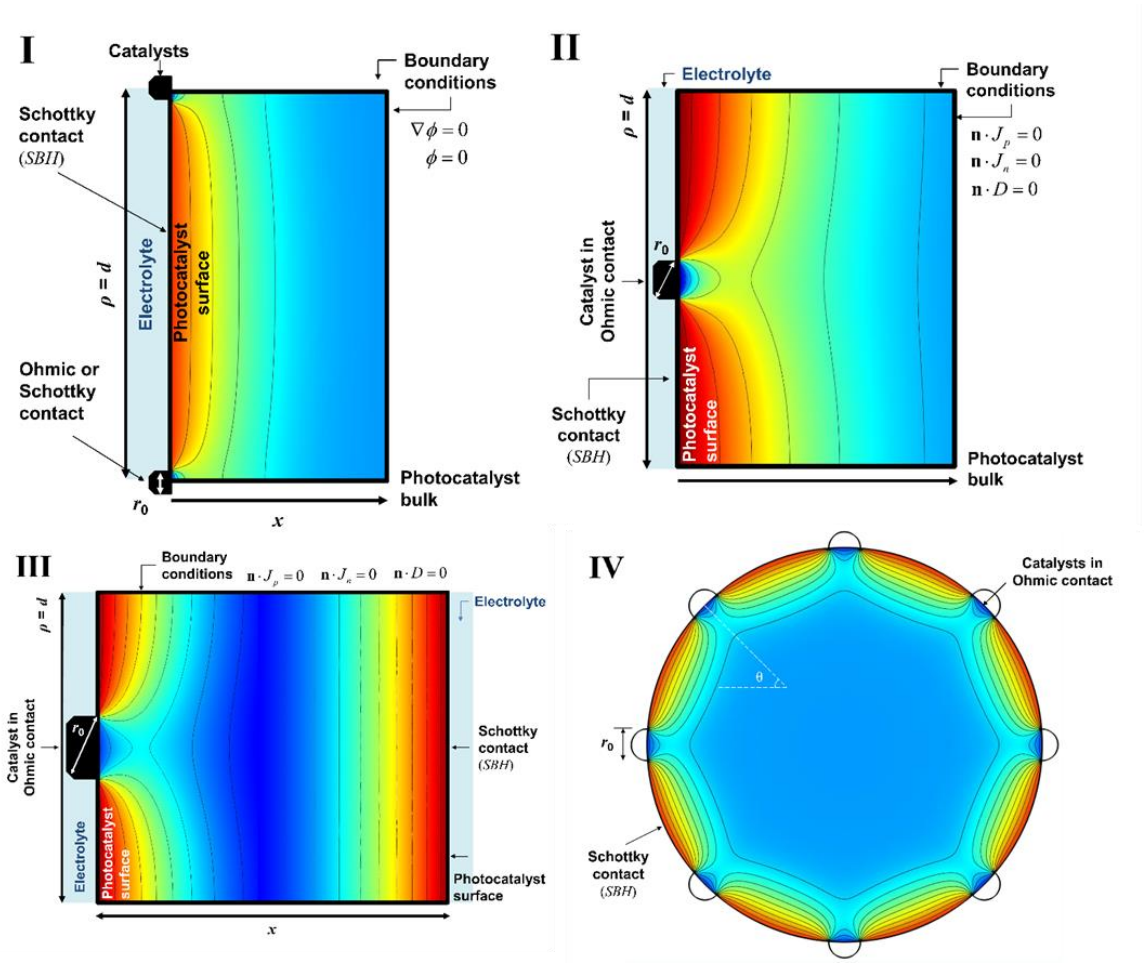

Figure 2.1 Geometric model schemes with the boundary conditions and the assumptions used for the simulations. The *x*-direction represents the distance into the bulk of the semiconductor. The *ρ*-direction represents a position on the surface of the *n*-type model. Model I presents the box-type model used to calculate the equilibrium conditions in the dark for inhomogeneous Schottky contacts. Steady-state illumination conditions are assumed to calculate Models II-IV. Model II describes a single metal site surrounded by the electrolyte. Model III represents a similar geometry considering an electrolyte interface on both sides (left and right). Model IV shows a 100-nm spherical semiconductor particle decorated with metal catalysts. The *θ* variable is used to control the interparticle distance. We assumed an ohmic junction for the metal catalysts in contact with the semiconductor for Models II-IV, whereas a Schottky contact was assumed to calculate the electrolyte interface for all models.

The potential and the gradient changes for Models I and II and the flux of charges in Model III were considered to be negligible when using a suitable scale for the box model (i.e., when the x magnitude is much larger than the depletion layer W_D, then $\phi = \nabla\phi = \mathbf{n}\cdot\mathbf{J}_n = \mathbf{n}\cdot\mathbf{J}_p = \mathbf{n}\cdot\mathbf{D} = 0$).

Periodic conditions can be used to extrapolate the equipotential profile results along the ρ-axis in Models I, II and III. Note that Model III considers an electrolyte interface on both sides along the x-direction. Model IV represents a spherical semiconductor particle with multiple hemispherical metallic catalysts on its surface. Sunlight irradiation was assumed incident to the models in the x-direction from left to right. Shadowing and scattering events arising from the metallic sites in the surface were ignored for the current calculations.

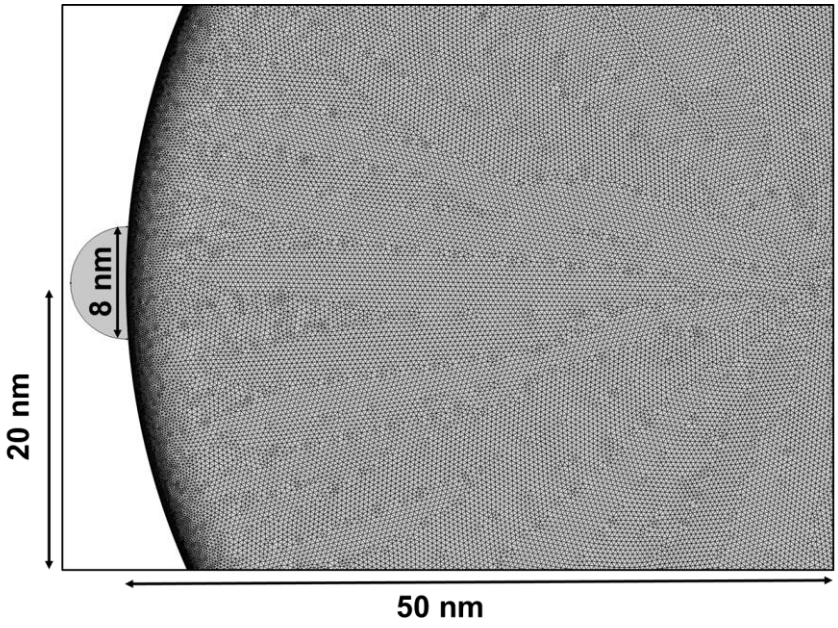

Figure 2.2 An example of a typical mesh used for the simulations. The free-triangular mesh was constructed using a minimum element size of 8×10^{-12} m with a growing element rate restricted to a maximum size of 4×10^{-10} m.

The starting premise is that the surface is under steady-state conditions for redox reactions under illumination; hence, the redox potentials were defined as the working potentials for the hydrogen evolution reaction (HER) and oxygen evolution reaction (OER). For simplicity, the assumption implicates a rather ideal situation where the photocatalyst device is under illumination in steady-state overall water splitting conditions. All these models assume that the electrolyte interface forms a depletion layer with the *n*-type semiconductor, generating band bending in a Schottky-type junction.[30] A steady-state standard overpotential of 300 mV was set for water oxidation, whereas no overpotential was considered for hydrogen production. Here, the metal catalyst is at the standard potential for the HER and forms an ohmic contact with the semiconductor for Models II, III and IV. In the following sentences, we will explain the basis of this critical assumption. During steady-state overall water splitting, the cathodic active site must be at least at the standard potential to generate hydrogen gas (4.44 eV),[35,36] and its partial pressure near the site can be large, affecting the redox potential in such negatively charged site and possibly forming an ohmic junction.[45,46] For the calculations, we assumed that exited electrons in the conduction band transfer directly to the active site already with the required potential for HER through an ohmic-type junction. These assumptions lead to the metallic catalyst being the active site for HER, while the semiconductor surface is the active site for the OER under steady-state illumination conditions.[8,45–47] Table 2.1 presents the material parameters used in the simulations unless otherwise stated.

Model I in Figure 2.1 was used to solve for the equilibrium conditions in the dark, and the simulation results are presented in Figure 2.6 and 2.7. Model II, I-III and IV were solved under the assumption of steady-state illumination, and the results are present in Figure 2.8-2.14. The results of this work will be presented with increasing complexity of the model and the simulation. The implications of the absorption properties of the semiconductor in function of the defect density in *n*-type materials are first analyzed. Then, the potential under equilibrium conditions in the dark was solved to understand the apparent driving force for the drift and diffusion of charges. Later, simulated steady-state solar radiation is introduced to study charge transport. The purpose of the study is to obtain quantum efficiency (QE) trends of the models by perturbing the different semiconductor parameters. Moreover, the effects of the catalyst size and the interparticle distance in the QE are explored.

The properties of Ta_3N_5 were used as a starting point in this investigation because recent literature produced a thorough characterization of the material.[12,13,17,19] The results presented hereafter, however, may well represent any semiconductor material with the parameters described in the calculation details. The aim of this study was to test the typical photocatalysis configuration to explore what is possible to achieve in terms of efficiency and what is possible to learn from these idealized conditions. It is important to understand the ideal conditions for charge generation, separation and transport in photocatalysis before exploring more complete and complicated models. The calculations do not consider surface states, potential determining ions on the surface, inhomogeneous

doping profiles, other recombination mechanisms than trap-assisted recombination, and additional potential losses from kinetics and mass transport. The simulations presented refer to only one semiconductor particle in the particulate system. An important point to remember is that this chapter first discusses calculations for a single absorbing unit, and later an estimation of the accumulated efficiency in the photocatalytic slurry was performed.

Table 2.1 List of semiconductor material parameters required for the numerical simulations. The values of Ta_3N_5 are used as a starting point, but not limited to:

Symbol	Value	Unit
q	1.602×10^{-19}	C
k_B	1.3806×10^{-23}	J K^{-1}
h	6.626×10^{-34}	J s
m_e	9.11×10^{-31}	kg
T	300	K
ε_0	8.854×10^{-12}	F m^{-1}
ε_r	17	
μ_n, μ_p	2×10^{-4} [a]	m^2 V^{-1} s^{-1}
τ_n, τ_p	5×10^{-12} [a]	s
P_0	7×10^{20} [b]	m^2 s^{-1}
α_{550}	6.1×10^{6}	m^{-1}
x	1×10^{-7}	m
ρ	2×10^{-8}	m
r_0	8×10^{-9}	m
r_s	1×10^{-7}	m
χ	4.3	eV
E_g	2.1	eV
E_{redox}	5.97	eV
m^*_n	1.9 [a]	
m^*_p	3.4 [a]	
N_C	6.3×10^{25} [c]	m^{-3}
N_V	1.5×10^{26} [c]	m^{-3}
A^*_n	2.3×10^{6} [c]	A m^{-2} K^{-2}
A^*_p	4.1×10^{6} [c]	A m^{-2} K^{-2}

[a] values obtained from reference 12 and 13.
[b] integrated photons from 300 < λ < 550 nm in AM 1.5G.
[c] calculated value from effective mass.

2.4. Results and discussion

2.4.1. The space charge region

Powder form photocatalysts are, in general, highly defective semiconductors with high carrier densities on the order of >10^{18} cm^{-3}.[17,48] Figure 2.3 shows the effect of the donor density on the magnitude of the depletion width obtained using Equation 2.19 (*n*-type semiconductor case). Based on the assumption of a 1 V built-in potential, is possible to estimate a very narrow depletion space near the interface of less than 50 nm into the bulk of a semiconductor, using a dielectric constant of 17 measured experimentally at high frequency for Ta_3N_5.[12]

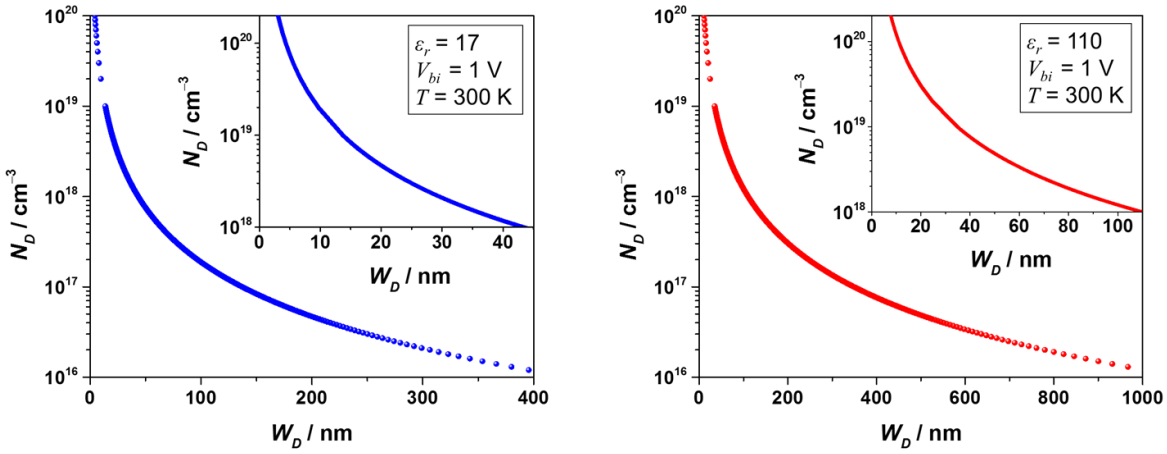

Figure 2.3 Solution to Equation 2.20 representing the description of the depletion layer width with changing donor density assuming a built-in potential of 1 V in an *n*-type semiconductor material with a relative dielectric constant of 17 (left) and 110 (right) at 300 K. The consideration of both the electronic and ionic contributions to the calculation of the dielectric constant, resulted in values >30 but <60 for Ta_3N_5 as an example;[13] in the literature, values larger than 100 have also been used for this material.[49]

For most semiconductors studied in the literature and based on this approximation, to achieve a depletion length larger than 100 nm, it is required to make *n*-type semiconductor crystals with donor densities on the order of $<10^{17}$ cm^{-3}. If the dielectric constant of the semiconductor is 1 order of magnitude larger,[13,49] the depletion length region roughly doubles in magnitude at similar donor densities. Nevertheless, to generate depletion regions larger than 100 nm, the crystal must possess a carrier density of less than 10^{18} cm^{-3} (Figure 2.3). In particulate heterogeneous photocatalyst systems, charge separation only relies on the formation of an effective semiconductor-electrolyte Schottky type of contact, and the efficient diffusion of charge carriers.[8] The depletion layer may be described as a charge separation region that decays in space. Thus, Figure 2.3 provide a qualitative and quantitative expectation of this charge collection region into the semiconductor photocatalyst based on carrier density.

2.4.2. Absorption of photons

To provide a complete idea of the implications of this charge collection layer, the analysis of the absorption properties of some semiconductor materials was done. All semiconductors used in Figure 2.4 have the required energetic conditions for overall water splitting.[1,7,10,48] The band gaps are larger than 2 eV, and the valence and conduction bands are more positive than the standard water oxidation potential and more negative than the water reduction potential, respectively. Figure 2.4 shows the required absorption depth in a single semiconductor particle to absorb available photons in the solar spectrum and attenuate light by e^{-1} to

generate enough charge carriers for hydrogen generation. The figure presents the maximum theoretical STH as a function of the inverse of the absorption coefficient (α). The calculation was performed assuming 100% QE and using the number of incident photons in AM 1.5G. The data points in Figure 2.4 represent experimentally measured absorption coefficients at different wavelengths,[11–13,50–55] where the inverse of this magnitude represents the penetration depth of the light into the semiconductor absorber.

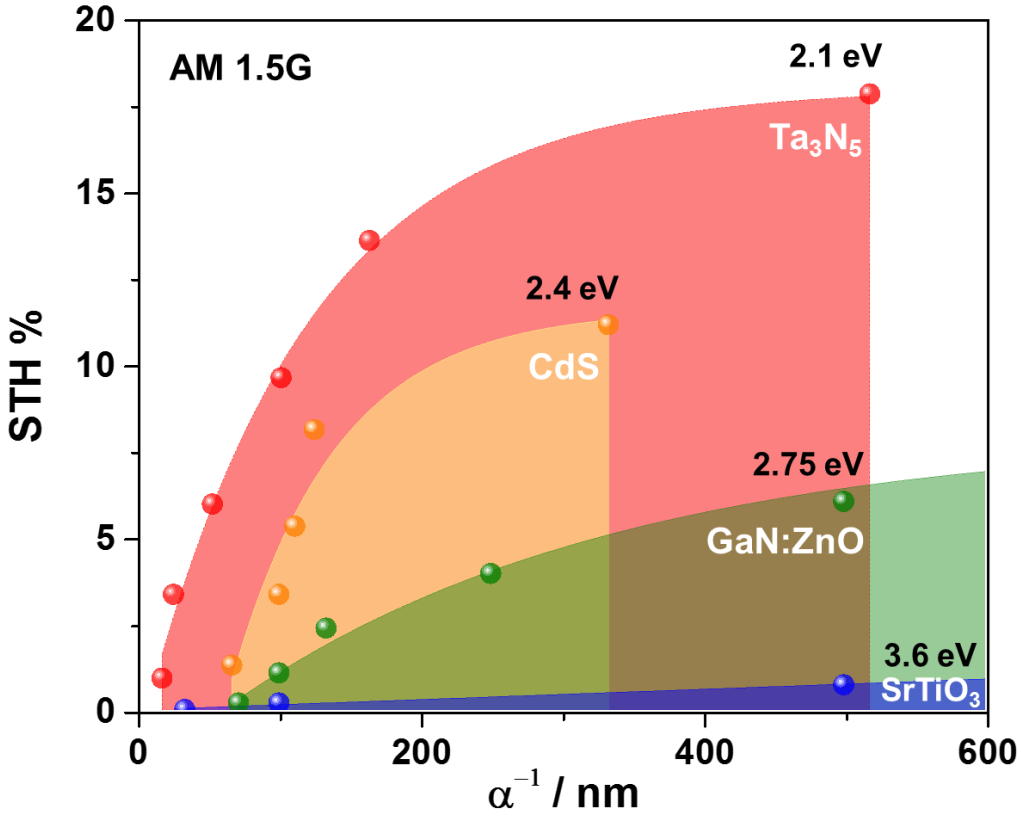

Figure 2.4 Theoretical solar-to-hydrogen conversion efficiency as a function of the penetration depth of light. A 100% QE was assumed utilizing simulated solar radiation (AM 1.5G). The points in the figure represent experimentally obtained absorption coefficients from the literature.

The absorption coefficient changes as a function of the photon wavelength; high energy photons are absorbed closer to the surface due to the high absorption coefficient of semiconductors at shorter wavelengths. $SrTiO_3$ is a large band gap semiconductor material, and similar to TiO_2, only capable of UV-light absorption, limiting its STH efficiency to a maximum of 1.5% while assuming perfect QE (Figure 2.4). Therefore, the large band gap completely renders the semiconductor useless for solar energy applications as the benchmark target is, in general, set to 10% STH to make the technology competitive in the energy market.[8,20] The 10% STH target is generally applied to photoelectrochemical water splitting cells; nevertheless, particulate photocatalytic powders may become commercially viable if it is possible to achieve 5% STH.[1,56]

Almost a decade ago, a GaN:ZnO solid solution with a supported mixed oxide of Rh and Cr on its surface was found to split water efficiently using visible light with a QE of 2.5% at 420-440 nm and less than 1% QE at wavelengths longer than 450 nm (E_g = 2.75 eV).[57] Assuming that it is possible to optimize the QE of this photocatalyst and based on the usable photons, we could expect to achieve only around half of the general benchmark target (i.e. 6% STH for GaN:ZnO in Figure 2.4).

It should be emphasized that the primary factor to determine the efficiency originates from the absorption properties. The use of visible light photons is critical for the practical development of large-scale solar energy conversion via photocatalysis, as can be seen from the achievable maximum STH efficiency due to the different band gap of the materials shown in Figure 2.4. To achieve the 10%

target, researchers must turn to semiconductors with band gaps smaller than 2.4 eV but, in general, larger than 1.8 eV for a single-absorber photocatalytic H_2 producing system. CdS and Ta_3N_5 are promising photocatalysts for overall water splitting with 2.4 eV and 2.1 eV band gaps and maximum theoretical STHs of 11% and 17.8%, respectively.[18,19] Based on the absorption properties, Ta_3N_5 particles with sizes on the order of 100 nm are transparent to 500-600-nm photons with an achievable theoretical STH of <10%. If the particle size is in the range of 50 nm, photons with wavelengths longer than 450 nm will not be absorbed by the particulate material, dropping the attainable STH efficiency to <6%. A 500-nm thickness of Ta_3N_5 particles is required for complete absorption of the usable photons in the solar spectrum to achieve the theoretical maximum efficiency for a 2.1 eV band gap semiconductor. A 100-nm CdS particle can produce <5% STH; hence, the semiconductor requires a minimum penetration depth of 300 nm to reach >10% STH. One of the advantages of particulate systems is the use of multiple absorbing entities dispersed in a solution to fully absorb incident light. The estimations presented in Figure 2.4 apply not only to single particles but also to thin film configurations.

Until this point, I have discussed the absorption properties of semiconductors based solely on their optical band gaps. It is possible to describe a relation between charge generation (Figure 2.4) and charge separation (Figure 2.3) using simple fundamental semiconductor properties. For example, Ta_3N_5 particles with donor densities greater than 10^{18} cm^{-3} generate a depletion layer on the order of tenths of nanometers (Figure 2.3), nevertheless the amount of photons

absorbed in this range is very limited (Figure 2.4), substantially limiting the STH efficiency of the system (i.e., less than 5% STH assuming 100% QE). Systematic semiconductor characterizations and DFT calculations have shown that Ta_3N_5 efficiency may be limited by poor transport properties and fast carrier recombination.[12,13,17,19] Thus, it may be reasonable to assume that the probability of charge separation and transport beyond the space charge region at the interface would be small. That being said, longer wavelengths in the solar spectrum may be used if the quality of the semiconductor crystal is high. Efficient charge separation requires long-range electric fields in the hundreds of nanometers range, comparable to the penetration depth of visible light in the semiconductor material.

2.4.3. Equilibrium in inhomogeneous Schottky junctions

The effects of inhomogeneous Schottky contacts have been previously studied by Tung and coworkers.[58] They modelled the case when a semiconductor-metal interface formed an inhomogeneous Schottky junction.[59] In Tung's system, regions along the interface have Schottky barriers with different magnitudes. Tung used a point-dipole approximation to solve the potential gradient generated under this type of interface into the semiconductor.[60] Numerical simulations have been used to describe the electrostatic phenomena found in these types of contacts with results that are similar to Tung's approximation.[61] As a starting point to validate the photocatalytic model, one of Tung's models was constructed and his results were compared to these calculations (Figure 2.5).

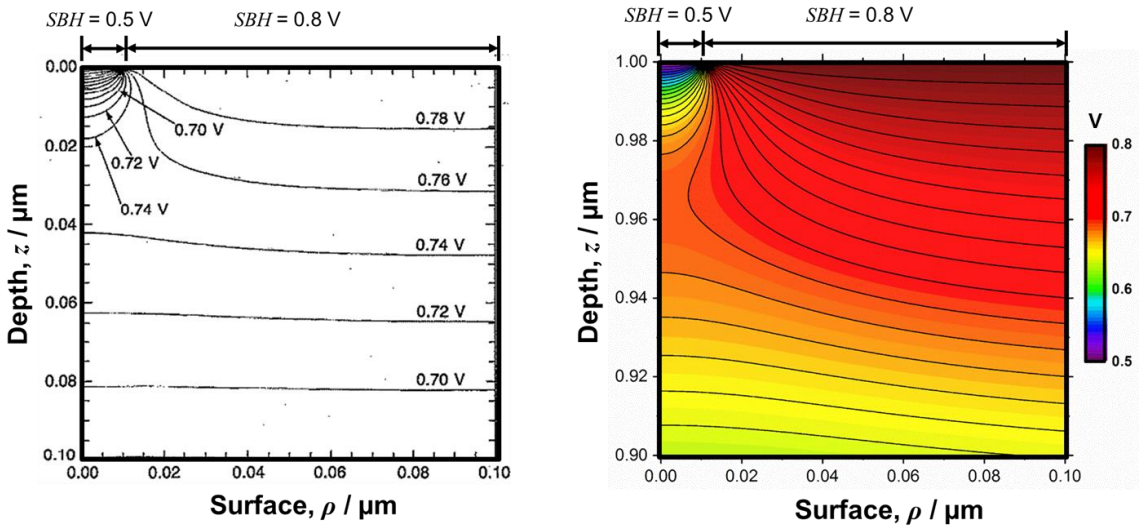

Figure 2.5 Equipotential contours obtained from numerical simulations of a polycrystalline *n*-type Si semiconductor at zero applied bias in contact with an inhomogeneous Schottky interface adapted from reference 3 (left). Numerical simulations obtained in this work for an *n*-type Si slab with similar geometry and in contact with an interface exhibiting two different Schottky barrier heights as previously proposed in the literature (right). The presented results are in reasonable agreement.[3,4] The potential gradients in the modelled geometry exhibited similar distributions and magnitudes as observed in the figure. Left side of the figure was adapted and reprinted with permission from J. P. Sullivan, R. T. Tung, M. R. Pinto, and W. R. Graham, *J. Appl. Phys*., 1991, 70, 7403. Copyright 1991, AIP Publishing LLC.

Equipotential curves were obtained for a Si slab in contact with two regions exhibiting a different Schottky barrier height (SBH) and the obtained results are in reasonable agreement.[61]

Model I in Figure 2.1 represents the case where two catalysts on the surface of a semiconductor photocatalyst may form severe Schottky barriers. Let the Schottky contact with the electrolyte have a lower SBH than the one assumed for the metallic counterpart. Figure 2.6 shows the results obtained for a semiconductor

with a relative dielectric constant of 17 and a donor density of 1×10^{18} cm^{-3} at 300 K. We placed two 20-nm metallic particles on its surface along the *ρ*-direction, forming a high SBH of 1.0 V, whereas the hypothetical electrolyte was assumed to produce an SBH of 0.5 V.

Then, the interparticle distance of the catalysts was changed to study the effects of the potential gradients into the semiconductor as shown in Figure 2.6a, 2.6b and 2.6c. In agreement with the full depletion approximation shown in Figure 2.3, the potential gradient was lost 20 nm into the bulk of the semiconductor due to the high carrier density concentration. Figure 2.6a shows that the potential from the high SBH in the metallic contact extends under the semiconductor-electrolyte interface if the two metal particles are relatively close. When the interparticle distance of the metals is significant and the high SBH region is isolated on the semiconductor surface, the potential influence diminishes as observed from the color gradients in Figure 2.6b and 2.6c. The potential profile under the metal catalyst and under the electrolyte interface into the bulk of the semiconductor are presented in Figure 2.6d and 2.6e, respectively. The figures show the changes in the potential gradient with changing interparticle distance. As observed from these results, the potential that develops under the surface was apparently affected by the high SBH region with changing interparticle distance (Figure 2.6e), whereas the effect under the high SBH contact was almost negligible (Figure 2.6d).

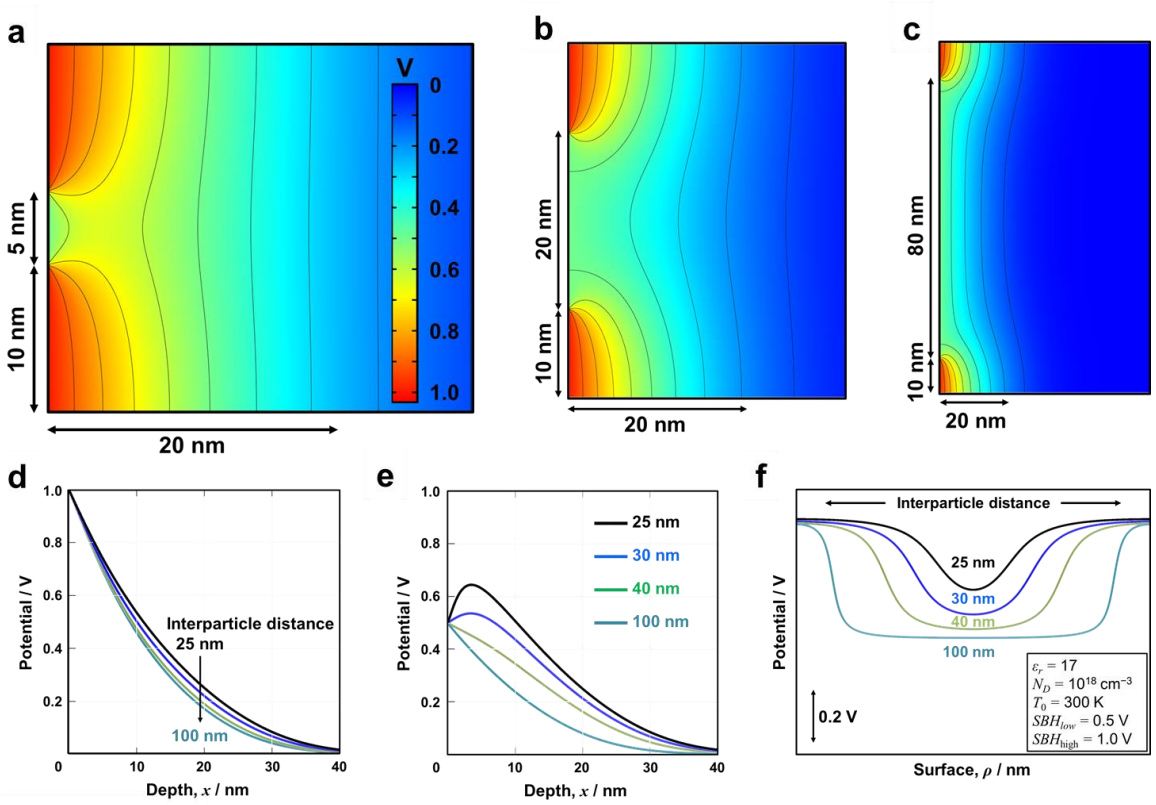

Figure 2.6 Equilibrium-condition simulations for Model I. Inhomogeneous Schottky contacts with different magnitudes are used. The catalysts and the electrolyte are assumed to form a rectifying junction with the semiconductor. The metal sites have a Schottky barrier height of 1 V. The hypothetical electrolyte interface has a barrier height of 0.5 V. The catalysts have an interparticle distance of 5 nm on the surface of the semiconductor (a). The interparticle distance increases to 20 nm (b) and 80 nm (c). The size of the metal catalysts remains constant in all the figures (20 nm). Potential profiles are presented under the catalyst (d) and the electrolyte junctions (e) into the semiconductor bulk. The potential gradients at 2 nm under the surface (ρ-direction) are shown with changing scale while increasing the interparticle distance (f). The potentials are drawn from one catalyst particle to the other. The semiconductor properties used for the calculations are a donor density of 10^{18} cm^{-3}, a relative dielectric constant of 17 and a temperature of 300 K.

The high SBH of 1.0 V produces the depletion region expected from an *n*-type semiconductor-metal Schottky contact. In contrast, a pinch-off effect was observed in the low SBH region of 0.5 V with decreasing interparticle distance. When the interparticle distance between the two metal particles is comparable to the size of these high SBH patches (ca. double or less), the potential gradient under the low barrier region was affected, producing an increase in the barrier height to approximately two-thirds of the magnitude of the higher SBH region (Figure 2.6e). The relative potential difference generated at the Schottky interface was lost 40 nm into the bulk (Figure 2.6d and Figure 2.6e). The potential levels obtained from 20 Angstroms under the semiconductor's surface are presented in Figure 2.6f. The horizontal axis represents the surface of the semiconductor in the *ρ*-direction, and the colored signals represent changing scales with changing the interparticle distance of the metals on the surface. The relative potential magnitudes are represented on the vertical axis. When the metal catalysts are 100 nm apart, it is possible to find two well-defined potential levels. The high potential magnitude equals the high SBH value of 1.0 V under the metal catalyst. The lower potential magnitude in the center of Figure 2.6e represents the low SBH region under the electrolyte (i.e., 0.5 V). The calculations resolve the potential gradient generated from the high potential region to the lower potential levels. The changing gradients observed in Figure 2.6e may represent the one-dimensional charge separation profile for photoexcited charge carriers near the surface. As the interparticle distance decreases to a similar order of magnitude as the high SBH region, the potential gradient decreases, most likely affecting charge separation. It

follows that the observed potential wells provide qualitative evidence of the restricted regions for charge separation in a particulate semiconductor photocatalyst.

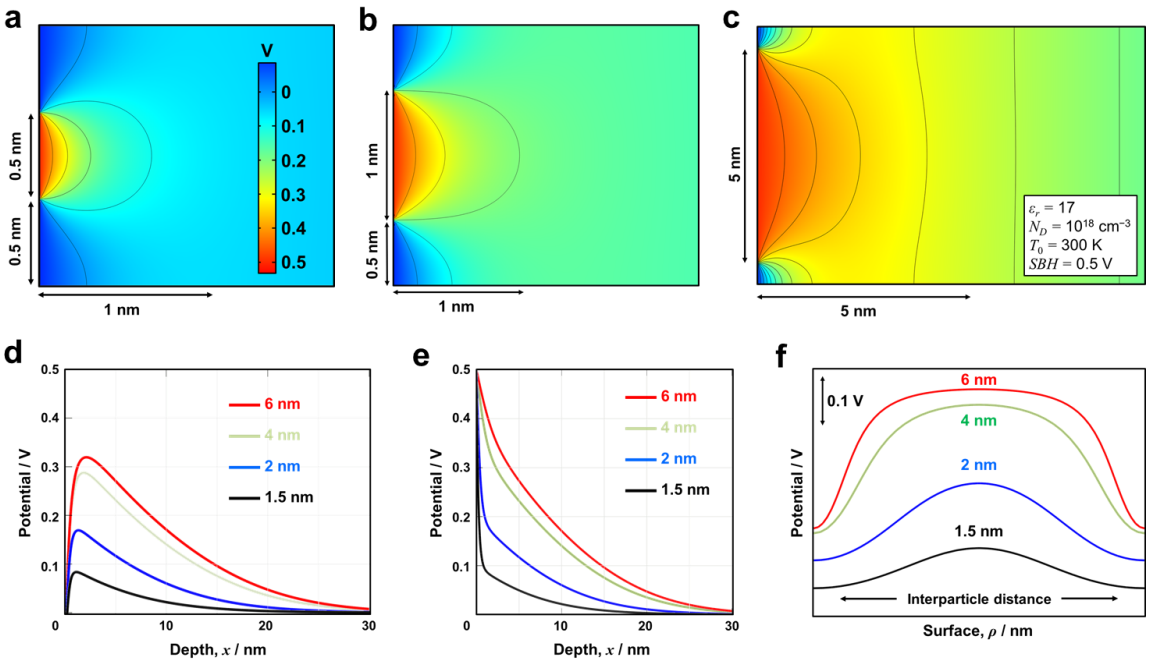

Figure 2.7 Equilibrium-condition simulations for Model I where the catalysts are assumed in ohmic contact with the semiconductor. The electrolyte is considered as a Schottky contact. The electrolyte interface has a barrier height of 0.5 V. Two metallic sites are highly packed and separated by an interparticle distance of 0.5 nm (a). The catalysts size is 1 nm and remains constant in these calculations. The interparticle distance increases to 1 nm (b) and 5 nm (c). Potential profiles are presented under the catalyst (d), and the electrolyte interfaces (e) into the semiconductor bulk. The potential gradients at 0.5 nm under the surface (*ρ*-direction) are shown with changing scale while increasing the interparticle distance (f). The potentials are drawn from one catalyst particle to the other. The semiconductor properties used for the calculations are a donor density of 10^{18} cm^{-3}, a relative dielectric constant of 17 and a temperature of 300 K.

Now, assume that the metal catalysts on the surface are in ohmic contact with the semiconductor particle (Model I, Figure 2.7). The semiconductor-electrolyte Schottky barrier height was assumed to be 0.5 V in this case. For these calculations, the parameters used were a donor density of 1×10^{18} cm^{-3}, a relative dielectric constant of 17 and temperature of 300 K. The effects of the potential gradients with changing interparticle distance of the non-rectifying metallic junctions were studied as shown in Figure 2.7a, 2.7b and 2.7c. Figure 2.7a shows two 1-nm metal particles on the surface of a semiconductor with an interparticle distance of 0.5 nm, thus exposing a very narrow region of the semiconductor surface to the electrolyte. It is interesting to note that, in regions where the metallic nanoparticles are highly packed, the potential gradient extends only a few nanometers into the bulk of the semiconductor. As the nanoparticles become more isolated and are surrounded by large fractions of the electrolyte interface, some potential gradient effects start to become clear. Figure 2.7b and 2.7c show metal nanoparticles with interparticle distances larger than the ohmic junction. The results indicate that the equipotential profiles produced by the semiconductor-electrolyte interface extend well under the ohmic junction. As the interparticle distance increases, the depletion layer formed at the Schottky junction increases to a similar magnitude as observed previously (ca. 30-40 nm, Figure 2.7d and 2.7e). In contrast, the ohmic region under the metal nanoparticles decreases with increasing interparticle distance, extending less than 1 nm into the bulk under the metal contact (Figure 2.7b and 2.7c). In a similar manner, with decreasing interparticle distance, the potential gradient at the electrolyte interface in Figure

2.7a extended less than 1 nm before decreasing to less than 20% of the interface potential difference. Figure 2.7d presents the potential gradients obtained under the nanoparticle contact along the *x*-direction into the bulk of the semiconductor with changing interparticle distance. By definition, an ohmic junction occurs when the SBH is nonexistent. In the model, this metal-semiconductor contact is ohmic; nevertheless, the formation of a Schottky barrier was always observed with increasing interparticle distance. The magnitude of the interparticle spacing is directly related to the relative size of the low SBH region, which in this case, is an ohmic region. As the interparticle distance doubles the size of the nanoparticles, a barrier forms with a magnitude of ca. one-fifth of the value of the high SBH region (i.e., SBH of the electrolyte interface). When the interparticle distance increases, the results showed a barrier height maximum of ca. two-thirds of the potential at the semiconductor-electrolyte junction (Figure 2.7d). The implications of this result may dictate that, even if the photocatalyst system presents an ohmic junction with the active metallic sites, the electrolyte interface generates an energetic barrier for electron transfer around the hydrogen evolution site. This so-called pinch-off effect was first described by Tung for inhomogeneous metal-semiconductor Schottky contacts in solid-state devices; the phenomena is described here for the first time in particulate photocatalytic systems and I propose that it may be detrimental for charge separation and transport. Figure 2.7e shows that the potential gradient under the semiconductor-electrolyte junction was affected in the presence of low barrier height regions if these ohmic junctions are dense in the semiconductor surface. The potential profiles under the surface of the semiconductor were plotted

in Figure 2.7f (gradient along the *ρ*-direction with x = 0.5 nm). The horizontal axis of the figures represents changing scales along the semiconductor surface with changing metal interparticle distance. With increasing interparticle size, the potential minimum required for ohmic behavior was not achieved below the surface. The potential gradient decreases with decreasing interparticle distance. If the nanoparticles are closely packed and the surface exposed to the electrolyte is narrow, the potential gradient was almost non-existent. The results imply that there would be an optimum interparticle distance at which the potential gradient extends sufficiently along the *ρ*-direction with an optimum electric field gradient for charge separation. The potential differences observed on both sides of Figure 2.7f may partially describe the charge separation mechanism used in heterogeneous single-absorber photocatalytic systems. Moreover, it may be the first glimpse of the origin of the low STH efficiency generally observed in particulate photocatalytic water splitting due to the limited charge separation probability of the system.[57,62]

2.4.4. Steady-state overall water splitting simulations

Figure 2.8a and 2.8b show the equipotential profiles and carrier dynamics obtained for an *n*-type Ta_3N_5 decorated with a metallic catalyst in ohmic contact with its surface following Model II and III, respectively. Figure 2.8a shows a single metal catalyst on the surface with a simplified box-type of geometry.

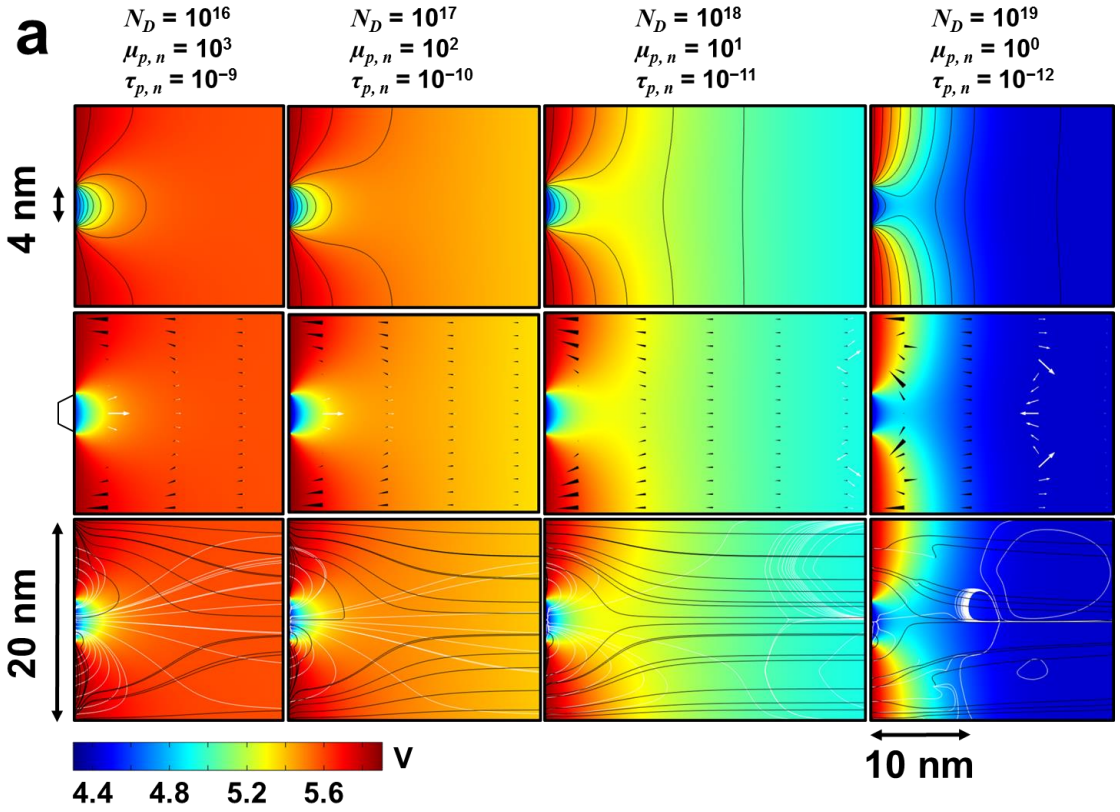
a
N_D = 10^{16}
$\mu_{p,n}$ = 10^{3}
$\tau_{p,n}$ = 10^{-9}
N_D = 10^{17}
$\mu_{p,n}$ = 10^{2}
$\tau_{p,n}$ = 10^{-10}
N_D = 10^{18}
$\mu_{p,n}$ = 10^{1}
$\tau_{p,n}$ = 10^{-11}
N_D = 10^{19}
$\mu_{p,n}$ = 10^{0}
$\tau_{p,n}$ = 10^{-12}
4 nm
20 nm
V
4.4
4.8
5.2
5.6
10 nm

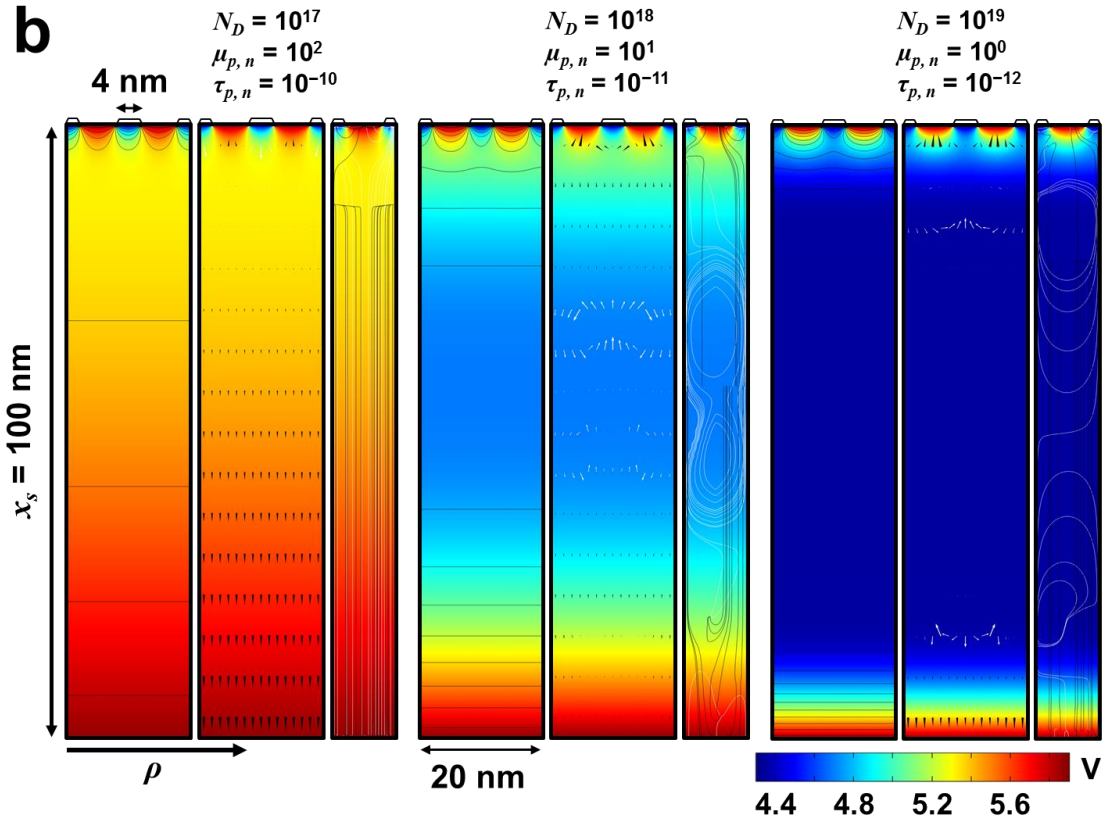
b
N_D = 10^{17}
$\mu_{p,n}$ = 10^{2}
$\tau_{p,n}$ = 10^{-10}
N_D = 10^{18}
$\mu_{p,n}$ = 10^{1}
$\tau_{p,n}$ = 10^{-11}
N_D = 10^{19}
$\mu_{p,n}$ = 10^{0}
$\tau_{p,n}$ = 10^{-12}
4 nm
x_s = 100 nm
ρ
20 nm
V
4.4
4.8
5.2
5.6

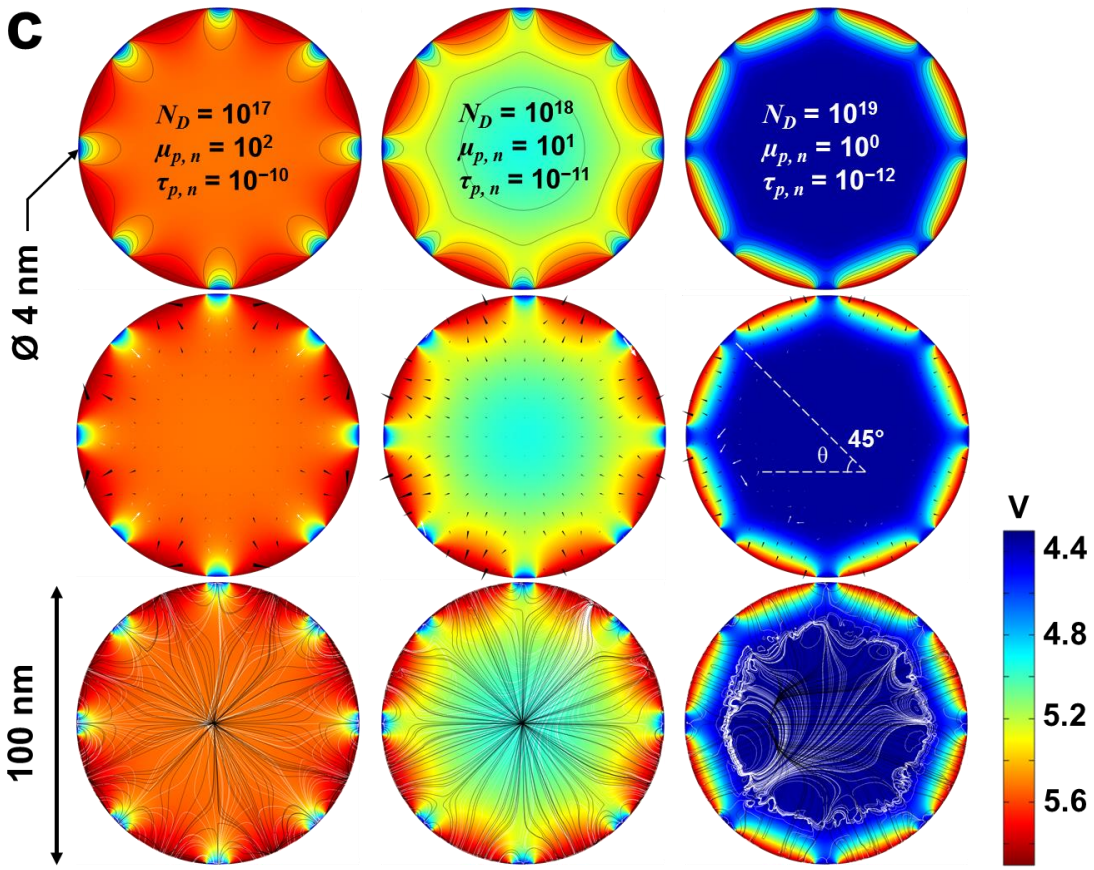

Figure 2.8 Steady-state overall water splitting simulations for models under illumination conditions (Models II-IV). Calculations for Model II were performed with a single 4-nm catalyst on the surface of an *n*-type semiconductor (a). For simplicity, only the results near the surface are shown in (a); nevertheless, the model size is x = 100 nm into the bulk (a, b). The calculations for Model I-III were obtained considering multiple particles on the surface of the semiconductor and an electrolyte interface on both sides of the model (b). Model IV was used to obtained simulations for 100-nm semiconductor spherical particles with supported metal catalysts (c). Equipotential profiles are shown in the top row, current vectors in the middle row and streamlines for carriers transport in the bottom row (a, c). Donor density increases from left to right with the assumption of decreasing mobility and lifetime of the carriers. Metal contacts are assumed to be ohmic whereas the electrolyte interface is assumed as a Schottky contact under water splitting conditions (E_g = 2.1 eV, χ = 4.3 eV, ε_r = 17, m^*_n = 1.9, m^*_h = 3.4, P_0 = 7×10^{20} m^{-2} s^{-1}).

The potentials were calculated relative to the semiconductor electron affinity on an absolute scale. Columns represent models with changing properties (N_d, $\mu_{p,n}$, and $\tau_{p,n}$), and the rows qualitatively and quantitatively describe the electrostatics, charge transport vectors and carrier dynamics streamlines from top to bottom, respectively. Cones and arrows represent hole and electron drift-diffusion currents, respectively. Black and white streamlines were continuously drawn tangentially to the current vector field for holes and electrons, respectively. The donor density increases from left to right.

For the calculations, the following assumption was made: the mobility and lifetime of the carriers increases by one order of magnitude when the defect density decreases by similar proportions. The assumption of increasing lifetime and mobility as a function of decreasing carrier concentration were made following empirical observations in *n*-type and *p*-type Si and GaAs.[63–69]

Crystals with low defect densities showed wider depletion layers (>100 nm). A lower number of defects is generally considered beneficial for charge separation, and well-defined charge mobility profiles were observed from the results (Figure 2.8a, left). The hole currents point towards the electrolyte interface, whereas opposite electron currents appeared under the metal-semiconductor ohmic junction when defects are relatively low. As the donor density increases, the electrostatic profile of the depletion layer decreases to <10 nm and the recombination of carriers seems to increase (Figure 2.8a, N_d = 10^{19} cm^{-3}). At this point, electron currents are ill-defined and far from the ohmic interface with the streamlines appearing to generate recombination pathways. Moreover, the

directions of the electron current vectors were opposite, and with changing directions, which is another possible indication of charge recombination. Figure 2.8b presents the results obtained for Model III with multiple 4-nm nanoparticles on the semiconductor's surface. The size of the semiconductor slab is 100 nm. The metal nanoparticles on the top surface were assumed to produce ohmic junctions under HER conditions. At the bottom of the figure, the surface is completely exposed to the electrolyte and was assumed to be at the OER potential and to have a 300-mV overpotential. When the defect density is relatively low, it is possible to reasonably assume a high carrier mobility and longer carrier lifetimes.[69] In contrast, when the donor density is high, an assumption must be made estimating that lifetime is on the order of picoseconds with a relatively low minority carrier mobility.[12] The results for Model III in Figure 2.8b were similar to the ones observed in Figure 2.8a. Consistently, I observed the formation of large depletion regions with lower donor densities, whereas the potential gradient diminishes at the 10-nm scale with high carrier densities. Homogeneous and well-defined hole and electron currents were observed for donor densities lower than 10^{18} cm^{-3} with reasonable carrier pathways towards the electrolyte and the metal sites, respectively. With increasing donor density, charge recombination regions can be observed in Figure 2.8b. Current vectors for electrons presented opposite directions relative to the ohmic site and streamlines formed random quasi-circular trajectories in the bulk of the semiconductor. The chaotic electron and hole streamlines may represent recombination events in the semiconductor photocatalyst.

Figure 2.8c shows the results for Model IV with a catalyst size of 8 nm and an interparticle distance of approximately 39 nm. The photocatalyst donor density increases from left to right. Similar assumptions were made as before for mobility and lifetime. As the defect density decreases, the mobility and lifetime increase inversely proportional by one order of magnitude for the calculations. The photocatalyst size was assumed to be 100 nm based on literature reports.[17,19] The extents of the potential gradients decrease with increasing carrier density, as expected. No electric fields in the bulk were observed when the donor concentration was 10^{19} cm^{-3}. Under this condition, I assumed a lifetime on the order of picoseconds with a mobility of 1 cm^2 V^{-1} s^{-1} and, thus, a highly defective material. The solution of this system exhibited electron streamlines that do not reach the ohmic site. The direction of the electron arrows for high carrier concentrations do not align with the metallic junction. The chaotic streamlines along with the ill-defined vectors may indicate higher recombination rates when using this parameters for a highly defective semiconductor. On the other extreme, if the donor concentration was below 10^{17} cm^{-3}, the current vectors homogeneously align with their respective carrier collecting sites. The electron and hole streamlines qualitatively show the charge generation and separation from almost any point in the bulk and surface when defects are low. The carriers flow into their respective active site sinks. Note that the size of streamlines, arrows and cones in the figure qualitatively describe the current transport and dynamics. The direction of the vectors accurately represents the calculation. The size and number

of lines presented were arbitrarily selected to facilitate the visualization of the drift and diffusion results in these two-dimensional models.

Cut-lines were taken from the results shown in Figure 2.8b and 2.8c as shown in Figure 2.9a and 2.9b, respectively. Figure 2.10 shows the potential profiles obtained starting from the catalyst junction (i.e., ohmic) and moving into the bulk towards the semiconductor-electrolyte backside interface (i.e., Schottky).

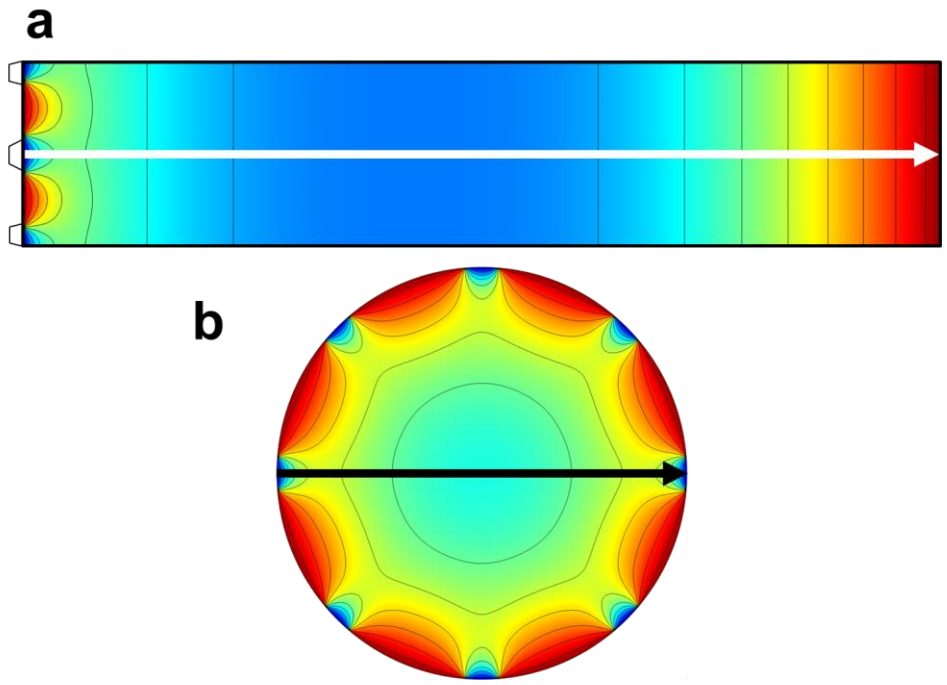

Figure 2.9 The cut-lines were used to draw the potential profile across the semiconductor model. The objective is to illustrate the one-dimensional energy profile across the material from one interface to the other. The cut-line was made under the catalyst in ohmic contact towards the opposite electrolyte interface forming a rectifying junction (a). In Model IV, the potential was drawn starting at the metal site forming an ohmic contact, into the semiconductor hemispherical particle, towards another ohmic interface on the opposite interface (b).

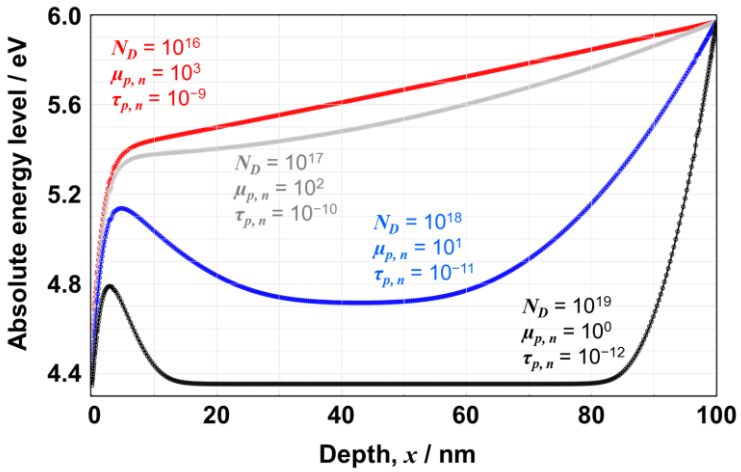

Figure 2.10 Absolute energy levels as a function of distance into the semiconductor bulk as obtained from cut-lines drawn in the results presented in Figure 2.8b. The one-dimensional profiles are taken as illustrated in Figure 2.9a. The energy profile is calculated under the catalyst, into the semiconductor bulk, towards the opposite electrolyte interface (Model III).

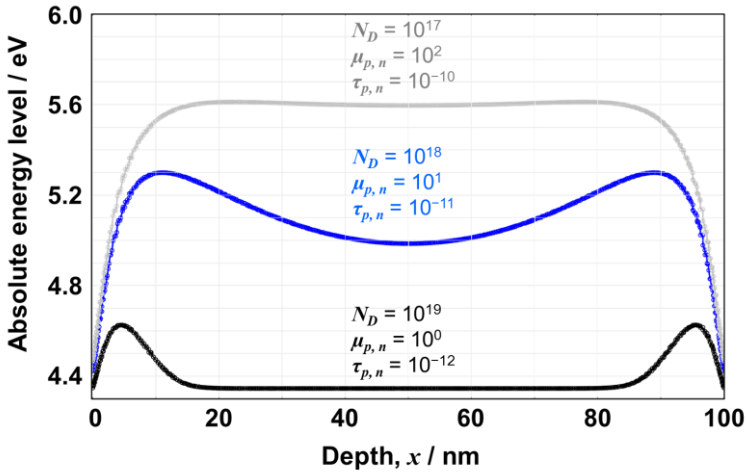

Figure 2.11 Absolute energy levels as a function of distance into the semiconductor bulk as obtained from cut-lines drawn in the results presented in Figure 2.8c. The one-dimensional profiles are taken as illustrated in Figure 2.9b. The potential gradient is presented from one of the catalysts, into the semiconductor bulk, towards another metal nanoparticle in the surface of the semiconductor model (Model IV).

A depletion region was observed in the rectifying junction as expected (Electrolyte interface, right side of Figure 2.10). Consistent with the calculation results in Figure 2.7, a pinch-off effect was observed in the ohmic side at high donor concentrations of $>10^{18}$ cm^{-3}. Such an energetic barrier may be detrimental for electron injection into the hydrogen active site. This pinch-off effect may originate from the electrostatic influence of the electrolyte surrounding the metal site. The potential wells observed in Figure 2.10 may contribute to an increase in the carrier's recombination rate, thus decreasing the efficiency (see below). As the carrier density decreases, it was possible to observe a charging effect in the bulk of the semiconductor. Decreasing the amount of defects in the semiconductor along with increasing mobility and lifetime of the carriers, generated a potential profile across the absorber particle that seems appropriate for efficient charge separation. The results are consistent with the report by Hisatomi et al. using a one-dimensional model and assuming a so-called asymmetric photocatalytic geometric model.[42]

Figure 2.11 exhibits similar potential profiles now obtained from Model IV using the cut-line shown on Figure 2.9b. The plot describes the potential gradient under the metal site across the spherical semiconductor particle into another ohmic region on the surface of the photocatalyst model. In this case, both sides of the junction are in ohmic contact, and the pinch-off effect can be observed at both ends of Figure 2.11. Similar conclusions can be drawn from the models. The potential wells in the bulk may promote charge recombination, and the electrolyte can inhibit

electron transfer into the metallic site due to the formation of a barrier resulting from the pinch-off effect.

The calculated current densities at the Schottky and ohmic interfaces were used to estimate the amount of carriers available for redox reactions. Assuming that each photon generates an electron-hole pair, a local QE per absorbing particle can be estimated by calculating the ratio between incident photons from the solar spectrum (AM 1.5G) and the number of usable charge carriers at the two different terminals in this model, i.e., the Schottky and ohmic junctions. Figure 2.12 shows the QE of one particle as a function of the donor density as well as the changing carrier mobility and lifetime. The QE increases with decreasing donor density, reaching a maximum plateau of 45% at $\leq 10^{17}$ cm^{-3} for Models II, III and I-III. Using Model IV a theoretical maximum QE of 35.7% was calculated for a single absorbing unit. As the carrier density increases the QE decreases, most likely due to the increasing recombination rates as observed from the results in Figure 2.8. It is possible to reasonably speculate that the observed formation of potential wells in the semiconductor bulk along with the pinch-off effect contributed to the calculated low QE. For defective semiconductor powders, a low QE of <10% was obtained for a single absorbing unit. The cross and star symbols in the data in Figure 2.12 represents the results when a longer lifetime was used for the calculations, as described in the figure. It was observed that the calculated QE at high donor densities roughly doubles in magnitude when increasing the carrier lifetime in one order of magnitude, however, there was a clear plateau around a QE of 35%.

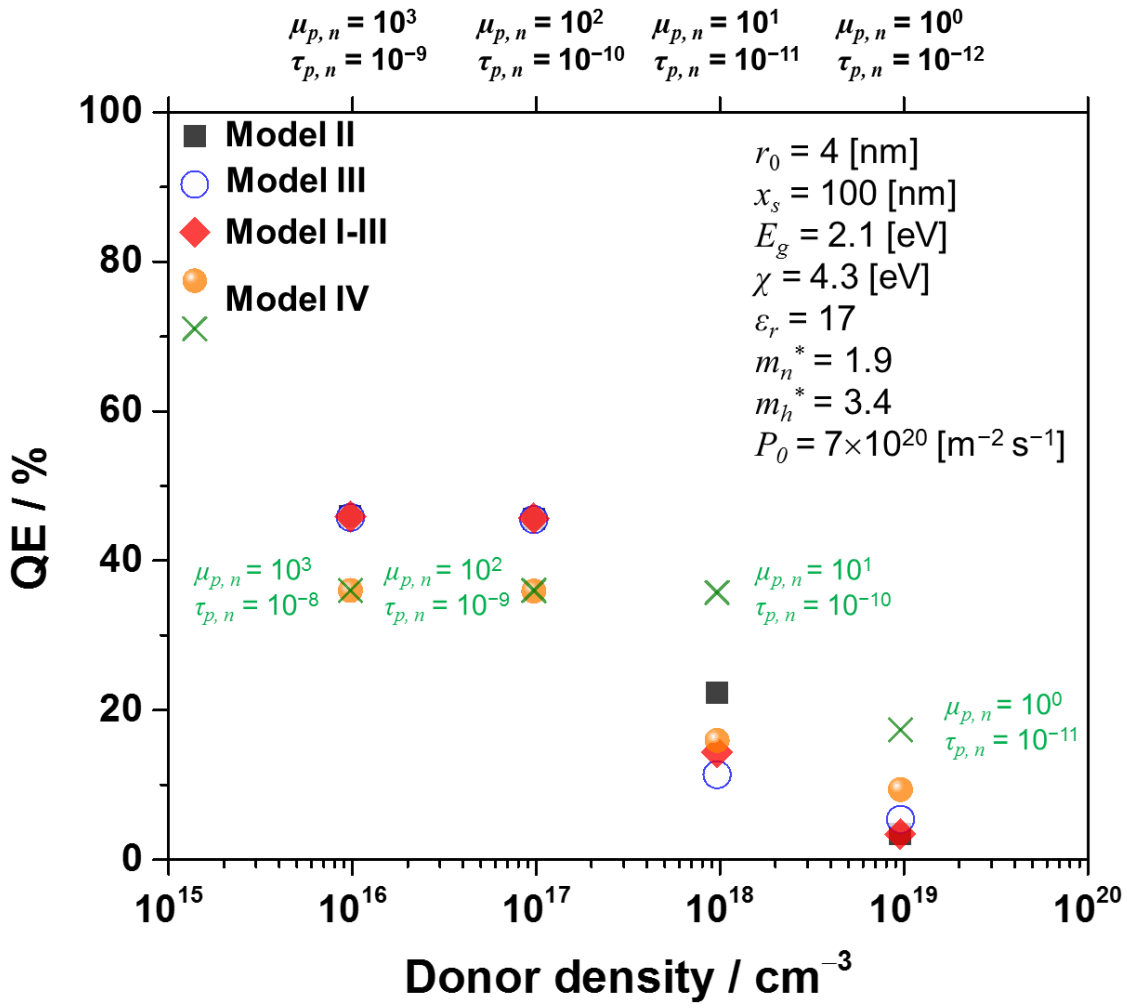

Figure 2.12 Quantum efficiency of a single 100-nm *n*-type semiconductor particle as a function of donor density. It was assumed that charge carrier mobility and lifetime increase with decreasing carrier density. The calculated quantum efficiency was obtained from the Models presented in Figure 2.8 under steady-state conditions for redox reactions under illumination. STH was calculated from simulated solar radiation AM 1.5G for Ta_3N_5 (300 nm < λ < 500 nm).

It is interesting to note that, by increasing the lifetime by one order of magnitude, it was possible to achieve the maximum QE for the configuration at a relatively high donor concentration of 10^{18} cm^{-3}. Moreover, all models used in these calculations resulted in a very similar trends for QE. I confirmed that

increasing the lifetime of the carriers to hundreds of picosecond or longer saturates the attainable QE to the maximum values calculated and presented in this figure (i.e. 35%), even under high carrier concentrations ≥10^{18} cm^{-3}. In contrast to the theoretical values reported in the literature,[42] it was not possible to obtain a QE larger than 50% for a single unit using this typical metal-supported semiconductor photocatalyst configuration. Figure 2.13 presents the calculations for the accumulated quantum efficiency (AQE) for four consecutive particles as a function of changing properties of the semiconductor. The STH efficiency was plotted in the figure by taking the AQE and computing the attainable hydrogen production efficiency if simulated sunlight was used. After four successive particles, AQE efficiencies larger than 90% were observed when the carrier concentration was relatively small. When Model IV was employed for the calculations, the maximum ideal AQE was approximately 70%. At high donor densities, most of the models resulted in AQE of less than 10%, except for Model IV, that generated 18% AQE. The same trends are reflected in the attainable STH. Solar-to-hydrogen efficiencies decrease with increasing carrier densities with a maximum of 12.6% and a minimum of ca. 1%. As mentioned earlier, the star symbol in the data represents the assumption of a larger lifetime of the carriers (Figure 2.13). Ideally and under this set of assumptions, it was possible to observe 10% STH for a semiconductor with a relatively high donor density of 10^{18} cm^{-3} and 5% STH for 10^{19} cm^{-3}; only if it is possible to increase the carrier lifetime by one order of magnitude under this defective conditions (i.e. larger than hundredths of picoseconds).

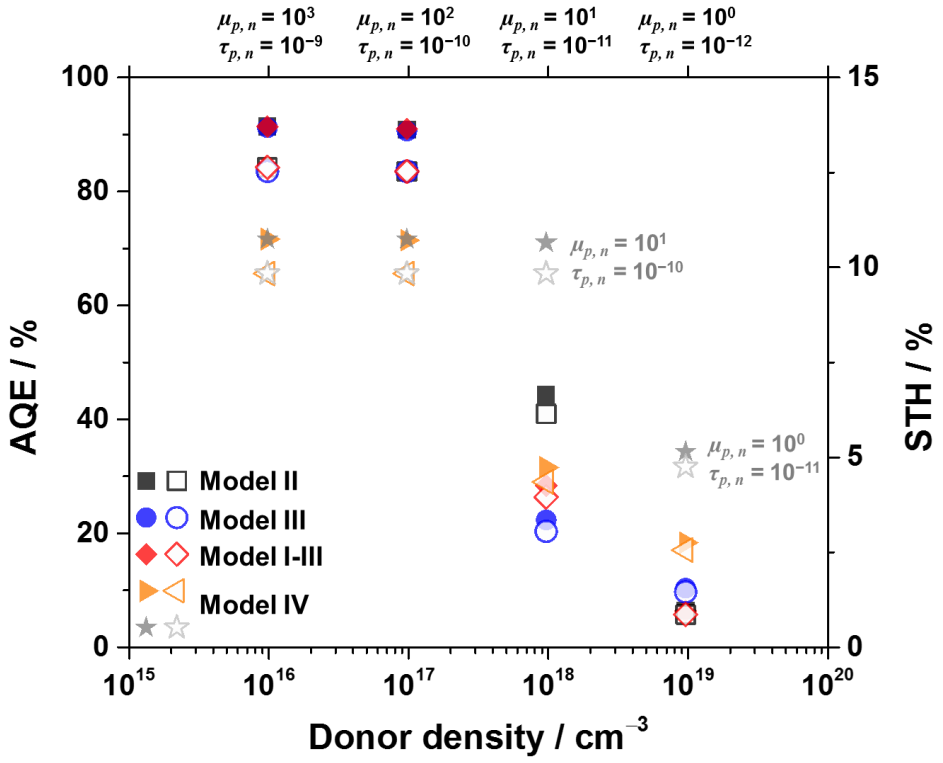

Figure 2.13 Accumulated quantum efficiency (AQE, filled symbols, left y-axis) and solar-to-hydrogen efficiency (STH, open symbols, right y-axis) as a function of donor density calculated after four particles. It was assumed that charge carrier mobility and lifetime increase with decreasing carrier density. The calculated quantum efficiency was obtained from the Models presented in Figure 2.8 under steady-state conditions for redox reactions under illumination. STH was calculated from simulated solar radiation AM 1.5G for Ta_3N_5 (300 nm < λ < 500 nm).

To further test the effect of the interparticle distance of the catalyst and the catalyst size on the QE of the system, Model IV was used to emulate a more complex photocatalyst. A 100-nm semiconductor particle was modelled using the reported properties for *n*-type Ta_3N_5 materials.[12,13,17,19] The surface of the semiconductor was decorated with nanoparticles of different sizes separated by a changing interparticle distance (Figure 2.14).

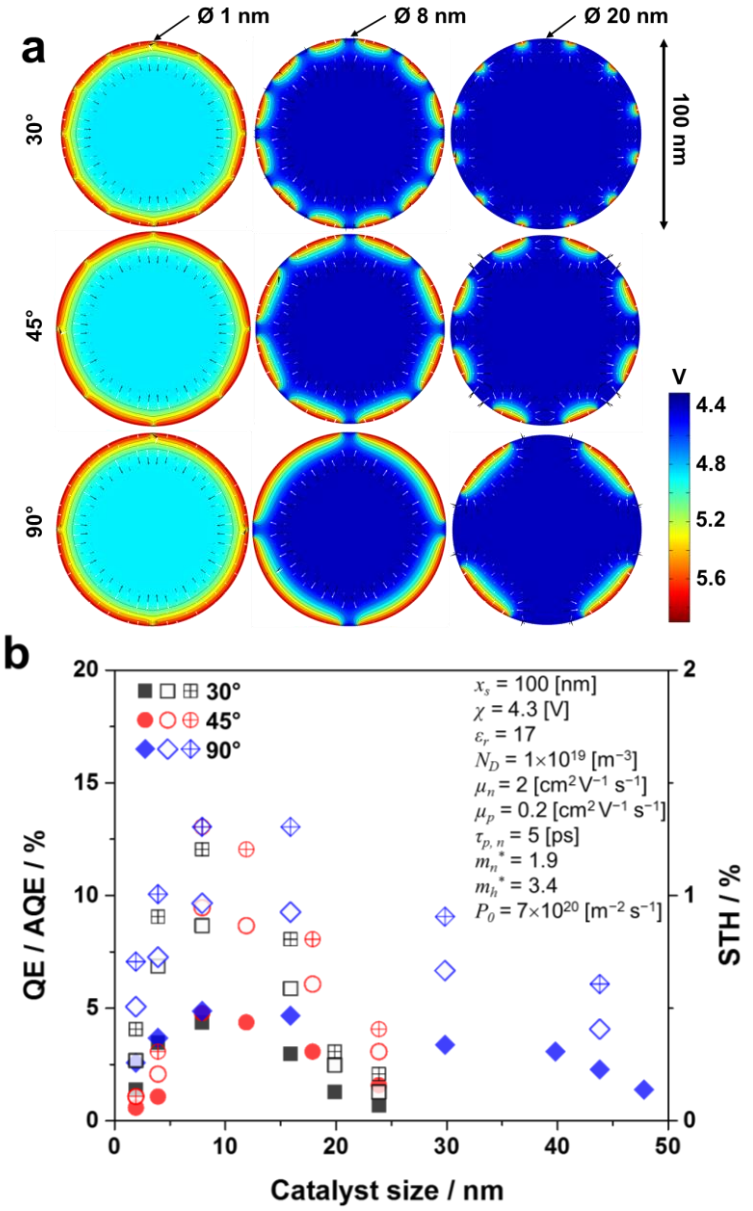

Figure 2.14 Simulations using Model IV with different dispersion and size of the catalysts on the surface of a 100-nm *n*-type semiconductor. The rows show a changing interparticle distance and the columns show a different catalyst size (a). Quantum efficiency (filled symbols) and accumulated QE (open symbols) after four consecutive units as a function of the catalyst size with varied interparticle distance (b). Solar-to-hydrogen efficiency is shown on the left axis and was calculated from AM 1.5G using the simulation results for QE (b, crossed symbols). Typical properties of Ta_3N_5 powders were considered for the calculations (E_g = 2.1 eV, χ = 4.3 eV, ε_r = 17, m^*_n = 1.9, m^*_h = 3.4, μ_n = 2 cm^2 V^{-1} s^{-1}, μ_p = 0.2 cm^2 V^{-1} s^{-1}, $\tau_{p,n}$ = 5 ps, P_0 = 7×10^{20} m^{-2} s^{-1}).

The angle determines the interparticle distance: a 30° angle results in approximately 26 nm, 45° results in approximately 39 nm and a 90° angle isolates the metals at a distance of approximately 79 nm. Figure 2.14a exhibits three representative metal nanoparticle sizes of 1, 8 and 20 nm in diameter assuming a hemispherical particle supported on the semiconductor surface. In an effort to model a realistic defective particulate semiconductor photocatalyst, I used a donor density of 10^{19} cm^{-3}, an experimentally measured lifetime of 5 ps and an electron mobility of 2 cm^2 V^{-1} s^{-1}.[12] In this calculation, the hole mobility was 1 order of magnitude lower than the electron mobility, based on the reported calculations of the effective masses.[13] Figure 2.14b shows the calculated QE and AQE as a function of the catalyst particle size with changing the interparticle distance on the semiconductor surface. It is interesting to note that the maximum attainable efficiency under these parameters was ≤5% QE for a single absorbing unit; such efficiency translates to a maximum of approximately 10% AQE (1.3% STH, AM 1.5G, 300 nm < λ < 500 nm). As the interparticle distance decreased, the optimal particle size for maximum QE had a narrower distribution. Although, there was a minor interparticle distance effect, it was possible to find an efficiency maxima for approximately 8-12 nm catalyst particles. This result must be considered carefully because the size of the catalyst strongly influences the kinetics of electrocatalytic water reduction (and oxidation), which significantly defines the overall STH efficiency of the real photocatalytic system.[19] Nevertheless, the observed maxima may imply that the metal-semiconductor junction size plays a role in charge

separation and must be thoroughly considered when designing new photocatalytic systems.

2.4.5. Quantum efficiency implications for photocatalysis

The developed numerical modeling enabled us to randomly and individually perturb the semiconductor parameters to measure the effects on the overall photocatalytic quantum efficiency within the constraints. Quantitatively, it was possible to obtain 45% QE for one particle if the semiconductor donor density is $\leq 10^{18}$ cm^{-3}. The latter may be technologically challenging in the synthesis of particulate photocatalysts.[48] Nevertheless, multiple absorbing entities in the slurry ideally increases the total achievable QE. Indeed, as previously mentioned, one of the advantages of particulate photocatalytic water splitting is the use of multiple absorbing entities suspended in solution. Based on the calculations, the local charge transport efficiency remains almost constant with light decay up to approximately 4 consecutive particles in the size range of 100 nm. By taking the lowest boundary of 5% QE per absorbing unit (Figure 2.12 and Figure 2.13), the AQE after four particles reached approximately 10% before a significant efficiency decay was observed. While still low for an ideal system, the calculations indicate that it is still possible to increase to approximately 91% AQE after four consecutive semiconductor particles if a single absorbing unit exhibits a QE of approximately 45% corresponding to 12.6% STH for a model Ta_3N_5 absorbing 300 nm < λ < 550 nm in AM 1.5G (Models II, III and I-III).

It is interesting to note that the calculations for Model IV exhibited a maximum of ca. 71% AQE under the most favorable parameters (9.8% STH, AM 1.5G, 300 nm < λ < 500 nm). When taking the lower threshold of the calculations, a single absorbing element, consuming photons from UV to 550 nm with a 20% QE, may achieve a 40% AQE after four particles; representing an STH of approximately 5.5%, which may become economically competitive.[1] Nevertheless, the calculated low-efficiency trends in this ideal model reflect the intrinsic limitations of the ordinary photocatalytic particle.

2.5. Summary

Using simplified simulations of semiconductor devices, crucial properties were identified in metal-supported semiconductor photocatalysts to achieve a basic design for efficient water splitting. In this simulation, the metal as the electrocatalyst on the surface is an integral and vital component in this system to provide anisotropic electronic field within the semiconductor for effective charge separation. Moreover, the electrocatalysts are used to enhance the kinetics of the redox reactions which were omitted from the simulation and will be discussed experimentally on the following chapters. From the knowledge gained from the calculations, I suggest that the classic photocatalytic design with random dispersion of metal nanoparticles on a semiconductor absorber does not improve the efficiency; on the contrary, it may be even hindering the overall development of the system. Future particulate photocatalysts must create an effective path for the transport of electrons and holes into their respective active sites. The

semiconductor-electrolyte interface may be one of the major contributors for charge separation; however, as illustrated in this study, the depletion layer of this interface generates a pinch-off effect, directly affecting electron transport into the hydrogen evolution sites due to Schottky barrier formation. Moreover, the potential gradients observed for charge separation were only present near the semiconductor surface with very limited and constrained space regions (<10 nm). Hence, inefficient charge separation in the bulk limits the efficiency, because most of the generated electron-hole pairs from sunlight's long-wavelength photons are created in the bulk and far from the charge collection region. The trends obtained clearly exhibited an intrinsic limitation of the typical photocatalytic configuration. In the best case scenario, it was only possible to achieve less than half of the ideal QE for a single absorber. Novel synthetic strategies are required, and nanostructuring of the photocatalysts may provide a first step to improving efficiencies. Other than decreasing the semiconductor size to introduce quantum-confinement effects, a photon collection strategy must be implemented to harvest the visible light region of the solar spectrum efficiently without compromising the charge collection probability. More importantly, scientists must rigorously design the majority carrier pathway that is, in general, inhibited by the electrolyte junction. One of such strategies may be to use a metal-insulator-semiconductor type junction or a carefully embedded buried-junction active-site electronically isolated from environmental effects. To achieve a breakthrough, the objective must be to control the charge carrier injection into the kinetically active electrocatalyst using a photocatalysis by design strategy in contrast to a black-box catalysis approach.

2.6. REFERENCES

1 K. Takanabe and K. Domen, *Green*, **2011**, 1, 313–322.

2 J. R. McKone, N. S. Lewis, and H. B. Gray, *Chem. Mater.*, **2014**, 26, 407–414.

3 Fujishima and K. Honda, *Nature*, **1972**, 238, 37–38.

4 M. G. Walter, E. L. Warren, J. R. McKone, S. W. Boettcher, Q. Mi, E. Santori, N. S. Lewis, *Chem. Rev.*, **2010**, 110, 6446–6473.

5 J. Schneider, M. Matsuoka, M. Takeuchi, J. Zhang, Y. Horiuchi, M. Anpo, D. W. Bahnemann, *Chem. Rev.*, **2014**, 114, 9919–9986.

6 L. Linsebigler, G. Lu, and J. T. Yates, *Chem. Rev.*, **1995**, 95, 735–758.

7 Kudo and Y. Miseki, *Chem. Soc. Rev.*, **2009**, 38, 253–278.

8 K. Takanabe, in *Topics in current chemistry*, Springer Berlin Heidelberg, **2015**, 371, 73–103.

9 B. Ohtani, *Chem. Lett.*, **2008**, 37, 216–229.

10 T. Hisatomi, K. Takanabe, and K. Domen, *Catal. Letters*, **2014**, 145, 95–108.

11 M. Harb, P. Sautet, E. Nurlaela, P. Raybaud, L. Cavallo, K. Domen, J.-M. Basset, K. Takanabe, *Phys. Chem. Chem. Phys.*, **2014**, 16, 20548–20560.

12 Ziani, E. Nurlaela, D. S. Dhawale, D. A. Silva, E. Alarousu, O. F. Mohammed, K. Takanabe, *Phys. Chem. Chem. Phys.*, **2015**, 17, 2670–2677.

13 E. Nurlaela, M. Harb, S. del Gobbo, M. Vashishta, K. Takanabe, *J. Solid State Chem.*, **2015**, 229, 219–227.

14 T. Garcia-Esparza, D. Cha, Y. Ou, J. Kubota, K. Domen, K. Takanabe, *ChemSusChem*, **2013**, 6, 168–181.

15 T. Shinagawa, A. T. Garcia-Esparza, and K. Takanabe, *ChemElectroChem*, **2014**, 1, 1497–1507.

16 T. Shinagawa and K. Takanabe, *J. Phys. Chem. C*, **2015**, 119, 20453–20458.

17 E. Nurlaela, S. Ould-Chikh, M. Harb, S. del Gobbo, M. Aouine, E. Puzenat, P. Sautet, K. Domen, J.-M. Basset, K. Takanabe, *Chem. Mater.*, **2014**, 26, 4812–4825.

18 W. Yu, T. Isimjan, S. Del Gobbo, D. H. Anjum, S. Abdel-Azeim, L. Cavallo, A. T. Garcia-Esparza, K. Domen, W. Xu, K. Takanabe, *ChemSusChem*, **2014**, 7, 2575–2583.

19 E. Nurlaela, S. Ould-Chikh, I. Llorens, J.-L. Hazemann, K. Takanabe, *Chem. Mater.*, **2015**, 27, 5685–5694.

20 Z. Chen, T. F. Jaramillo, T. G. Deutsch, A. Kleiman-Shwarsctein, A. J. Forman, N. Gaillard, R. Garland, K. Takanabe, C. Heske, M. Sunkara, E. W. McFarland, K. Domen, E. L. Miller, J. a. Turner, H. N. Dinh, *J. Mater. Res.*, **2011**, 25, 3–16.

21 X. Chen, S. Shen, L. Guo, S. S. Mao, *Chem. Rev.*, **2010**, 110, 6503–6570.

22 H. Kisch, *Angew. Chem. Int. Ed.*, **2013**, 52, 812–847.

23 R. Marschall, *Adv. Funct. Mater.*, **2013**, 24, 2421–2440.

24 J. B. Baxter, C. Richter, and C. A. Schmuttenmaer, *Annu. Rev. Phys. Chem.*, **2014**, 65, 423–447.

25 T. Hisatomi, J. Kubota, and K. Domen, *Chem. Soc. Rev.*, **2014**, 43, 7520–7535.

26 W. J. Albery, *J. Electrochem. Soc.*, **1984**, 131, 315.

27 Z. Zhang and J. T. Yates, *Chem. Rev.*, **2012**, 112, 5520–5551.

28 J. A. Turner, *J. Chem. Educ.*, **1983**, 60, 327–329.

29 M. Grätzel, *Nature*, **2001**, 414, 338–344.

30 K. Rajeshwar, in *Encyclopedia of Electrochemistry*, ed. A. J. Bard, Wiley-VCH Verlag GmbH & Co. KGaA, Weinheim, Germany, **2007**.

31 R. C. Rossi and N. S. Lewis, *J. Phys. Chem. B*, **2001**, 105, 12303–12318.

32 R. C. Rossi, M. X. Tan, and N. S. Lewis, *Appl. Phys. Lett.*, **2000**, 77, 2698–2700.

33 F. Lin and S. W. Boettcher, *Nat. Mater.*, **2014**, 13, 81–86.

34 T. J. Mills, F. Lin, and S. W. Boettcher, *Phys. Rev. Lett.*, **2014**, 112, 148304.

35 J. Bisquert, P. Cendula, L. Bertoluzzi, S. Gimenez, *J. Phys. Chem. Lett.*, **2014**, 5, 205–207.

36 P. Cendula, S. D. Tilley, S. Gimenez, J. Bisquert, M. Schmid, M. Grätzel, J. O. Schumacher, *J. Phys. Chem. C*, **2014**, 118, 29599–29607.

37 H. Gerischer, *J. Phys. Chem.*, **1984**, 88, 6096–6097.

38 Y. Nosaka, K. Norimatsu, and H. Miyama, *Chem. Phys. Lett.*, **1984**, 106, 128–131.

39 J. S. Curran, J. Domenech, N. Jaffrezic-Renault, R. Philippe, *J. Phys. Chem.*, **1985**, 89, 957–963.

40 Y. Nosaka, Y. Ishizuka, and H. Miyama, *Berichte der Bunsengesellschaft für physikalische Chemie*, **1986**, 90, 1199–1204.

41 T. Ioannides and X. Verykios, *J. Catal.*, **1996**, 569, 560–569.

42 T. Hisatomi, T. Minegishi, and K. Domen, *Bull. Chem. Soc. Jpn.*, **2012**, 85, 647–655.

43 S. M. Sze and K. Ng, *Physics of Semiconductor Devices*, John Wiley & Sons Inc., 3rd Ed., **2007**.

44 R. Entner, *Modeling and Simulation of Negative Bias Temperature Instability*, PhD thesis, Technischen Universitat Wien, **2007**.

45 M. Schiavello, *Photoelectrochemistry, Photocatalysis and Photoreactors*, Springer Netherlands, Dordrecht, **1985**.

46 K. Takanabe and K. Domen, in *Heterogeneous Catalysis at Nanoscale for Energy Applications*, eds. F. F. Tao, W. F. Schneider, and P. V. Kamat, John Wiley & Sons, Inc, Hoboken, NJ, **2014**.

47 Z. Zhang and J. T. Yates, *Chem. Rev.*, **2012**, 112, 5520–5551.

48 K. Takanabe and K. Domen, *ChemCatChem*, **2012**, 4, 1485–1497.

49 Y. Li, L. Zhang, A. Torres-Pardo, J. M. González-Calbet, Y. Ma, P. Oleynikov, O. Terasaki, S. Asahina, M. Shima, D. Cha, L. Zhao, K. Takanabe, J. Kubota, K. Domen, *Nat. Commun.*, **2013**, 4, 2566.

50 M. Dou and C. Persson, *Phys. Status Solidi*, **2012**, 209, 75–78.

51 M. Huda, Y. Yan, S.-H. Wei, M. Al-Jassim, *Phys. Rev. B*, **2008**, 78, 195204.

52 Y. Wang and N. Herron, *J. Phys. Chem.*, **1987**, 91, 257–260.

53 W. W. Yu, L. Qu, W. Guo, X. Peng, *Chem. Mater.*, **2003**, 15, 2854–2860.

54 M. Cohen and R. Blunt, *Phys. Rev.*, **1968**, 168, 929–933.

55 C. Lee, J. Destry, and J. Brebner, *Phys. Rev. B*, **1975**, 11, 2299–2310.

56 K. Maeda and K. Domen, *J. Phys. Chem. Lett.*, **2010**, 1, 2655–2661.

57 K. Maeda, K. Teramura, D. Lu, T. Takata, N. Saito, Y. Inoue, K. Domen, *Nature*, **2006**, 440, 295.

58 R. T. Tung, *Appl. Phys. Rev.*, **2014**, 1, 011304.

59 R. T. Tung, *Phys. Rev. B*, **1992**, 45, 13509–13523.

60 R. T. Tung, *Appl. Phys. Lett.*, **1991**, 58, 2821–2823.

61 J. P. Sullivan, R. T. Tung, M. R. Pinto, W. R. Graham, *J. Appl. Phys.*, **1991**, 70, 7403–7424.

62 Pan, T. Takata, M. Nakabayashi, T. Matsumoto, N. Shibata, Y. Ikuhara, K. Domen, *Angew. Chem. Int. Ed.*, **2015**, 54, 2955–2959.

63 H. Ito, T. Furuta, and T. Ishibashi, *Appl. Phys. Lett.*, **1991**, 58, 2936.

64 H. C. Casey, *J. Appl. Phys.*, **1973**, 44, 1281–1287.

65 S. E. Swirhun, Y.-H. Kwark, and R. M. Swanson, in *1986 International Electron Devices Meeting*, IRE, **1986**, vol. 32, pp. 24–27.

66 S. E. Swirhun, J. A. del Alamo, and R. M. Swanson, *IEEE Electron Device Lett.*, **1986**, 7, 168–171.

67 J. A. del Alamo and R. M. Swanson, *IEEE Trans. Electron Devices*, **1987**, 34, 1580–1589.

68 M. S. Tyagi and A. K. Gupta, *Phys. Status Solidi*, **1994**, 143, 79–83.

69 M. E. Law, E. Solley, M. Liang, and D. E. Burk, *IEEE Electron Device Lett.*, **1991**, 12, 401–403.

CHAPTER 3

3. Tungsten Carbide as Electrocatalyst for Efficient Water Splitting[b]

Tungsten carbide exhibits platinum-like behavior, which makes it an interesting potential substitute for noble metals in catalytic applications. In this chapter, tungsten carbide nanocrystals (~5 nm) are directly synthesized through the reaction of tungsten precursors with mesoporous graphite C_3N_4 (mpg-C_3N_4) as the reactive template in flowing inert gas at high temperatures. Systematic experiments that vary the precursor compositions and temperatures used in the synthesis selectively generate different compositions and structures for the final nano-carbide (W_2C or WC) products. Later on this section, the electrochemical measurements demonstrate that the WC phase with a high surface area exhibits both high activity and stability in hydrogen evolution over a wide pH range. The WC sample also shows excellent hydrogen oxidation activity, whereas its activity in oxygen reduction is poor. These tungsten carbides are successful cocatalysts for overall water splitting and give H_2 and O_2 in a stoichiometric ratio from H_2O decomposition when supported on a Na-doped $SrTiO_3$ photocatalyst. Herein, tungsten carbide (on a small scale) is a promising and durable catalyst substitute for platinum and other scarce noble-metal catalysts in catalytic reaction systems used for renewable energy generation.

[b] This chapter was reproduced from A. T. Garcia-Esparza, D. Cha, Y. Ou, J. Kubota, K. Domen, K. Takanabe, *ChemSusChem,* **2013**, 6, 168–181.

3.1. Introduction

Hydrogen is considered a promising energy carrier because of its high energy density. The low-cost, efficient production of hydrogen in a sustainable manner remains a scientific and technological challenge.[1] One of the most economical ways to harness hydrogen is from the photocatalytic overall water-splitting using solar energy.[2] This process requires a semiconductor with suitable band positions and surface active sites (cocatalysts) to enhance electrochemical redox reactions for water splitting.[3] The efficiency of photocatalysts has yet to be improved for commercial application.

During the overall splitting of water, the hydrogen evolution reaction (HER) should take place efficiently.[4,5] It is well known that platinum-group metals (Pt, Rh, Pd, etc.) are excellent HER electrocatalysts providing a low overpotential for the HER.[6] To achieve overall water splitting, the surfaces of the catalysts should also be insensitive to the back-reaction of the produced H_2 and O_2 that produces H_2O, i.e., the oxygen reduction reaction (ORR). One successful method to achieve overall water splitting is to coat metal particles with a Cr layer.[7] A study with a model electrode revealed that the Cr layer functions to selectively permeate proton and hydrogen molecules but not oxygen molecules.[8] Although there are other factors to take into account, such as the semiconductor-cocatalyst interface junction (e.g., Schottky barrier),[2,9] the development of suitable cocatalysts for overall water splitting is still necessary. It also remains challenging to develop highly active HER cocatalysts that have a low cost and utilize abundant materials.[10]

There are many approaches to develop efficient alternatives to noble metal catalysts, such as bimetallic systems,[11] core-shell structures[12,13] and different transition metal compounds[14]. Among them, some sulfides and carbides, such as molybdenum disulfide[10] and tungsten carbide[15], have been reported to exhibit interesting HER performance. Tungsten carbide was first reported to perform with platinum-like behavior in the catalysis of hydrogenolysis by Boudart's group in the 1970s.[16] Later, tungsten carbide was reported to show activity not only for the HER in acidic and neutral conditions[17] but also for the hydrogen oxidation reaction (HOR), thus confirming the potential of this material as a platinum substitute for electrocatalytic application in polymer electrolyte membrane fuel cells and direct methanol fuel cells.[18]

Catalyst particles in the nanometer regime have many active sites on their surfaces, as well as distinct geometric effects with deeply unsaturated coordination sites, which can provide excellent catalytic performance.[19] However, to date, most catalytic studies using tungsten carbide reported the formation of relatively large particles with a low surface area.[20–22] If novel active materials, such as carbides, can be synthesized on a small scale (typically smaller than 5 nm) by developing new synthetic routes, the tailored materials could potentially be used as substitute noble metals in HER/HOR catalysis.

Some methods in the literature can be used to obtain nano-sized carbide materials, such as high-temperature treatment of microporous carbon materials with metal precursors[23] and chemical vapor deposition techniques to prepare carbon-encapsulated metal nanoparticles.[24] A novel synthetic route utilizes

organic compounds, such as urea[20], as carbon sources and also utilizes transition metal precursors. In particular, Antonietti's group developed a simple method to control Mo and W carbide and nitride phases depending on the molar ratio of the metal precursor to urea.[20] In their study, the variation in the urea-to-metal ratio led to phase variation from carbides to nitrides. In contrast, the controlled synthesis of early transition metal nitride nanoparticles has also been reported based in the confinement of ordered pores present in the mesoporous graphitic carbon nitride (mpg-C_3N_4) used as the reactive template.[25–27] The ordered pores reflect the size of the original SiO_2 nanoparticles as a template for mpg-C_3N_4 synthesis and strictly determine the size of the final nitride particles.[26,28]

In this chapter, attempts to synthesize tungsten nanoparticles using mpg-C_3N_4 as the reactive template led to the formation of tungsten carbide nanoparticles rather than their nitride counterparts. It was possible to control the final product phase based on the precursor ratio (metal to mpg-C_3N_4) and temperature applied during the synthesis. The electrocatalytic activity of these tungsten carbide nanoparticles was studied in the HER, HOR, and ORR. The experimental results demonstrated that the WC nanoparticles showed excellent performance in the HER but low activity for the ORR, which suggests that the WC may function as a selective catalyst for the HER during overall water splitting without introducing the back-reaction. Thus, the possibility of using nano-sized tungsten carbide as a cocatalyst for photocatalytic overall water splitting was explored. The results suggest that these nanoparticles may be candidate cocatalysts in the overall water-splitting reaction.

3.2. Results and discussion

3.2.1. Synthesis of mpg-C_3N_4

Figure 3.1 shows the isotherm acquired from the sorption experiment performed on the mpg-C_3N_4 template (inset) as well as the average pore size distribution calculated in the same experiment. The graph in the inset shows a hysteresis loop in the plot and reflects a type IV isotherm associated with the capillary condensation process in the mesopores' structures, according to the International Union of Pure and Applied Chemistry (IUPAC) classification. The specific BET surface area obtained was 248 $m^2\,g^{-1}$, which is consistent with the formation of the mesopores specifically designed by using colloidal silica as a hard template.[25,26]

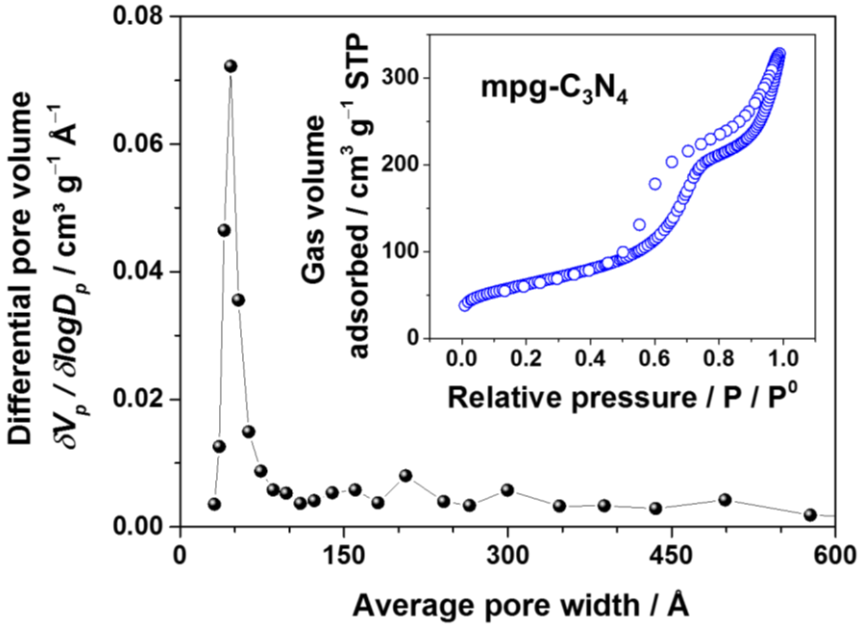

Figure 3.1 The pore size distribution obtained from N_2 desorption and N_2 adsorption-desorption isotherms (inset) at 77 K for the mpg-C_3N_4 template.

From the figure, a high value of the average pore volume (0.51 $cm^3\ g^{-1}$) was obtained based on a Barret-Joyner-Halenda (BJH) plot, and the average desorption pore size was 64 Å with a narrow distribution, which accurately reflects the size of the original silica template used in the synthesis. Table 3.1 presents the textural properties discussed above and the elemental analysis obtained for the mpg-C_3N_4 reactive template used in this investigation. Elemental analysis gave a lower carbon to nitrogen ratio (~0.63) when compared with the stoichiometry of C_3N_4 (0.75), which suggests a nitrogen-rich carbon nitride sample, possible because the surface of the sample is mainly C-NH_2, 2C-NH and hydrogen-bonded OH groups or absorbed water molecules, as corroborated by spectroscopy studies and discussed below.

Table 3.1 Textural properties of the carbon nitride template obtained by N_2 sorption experiments at 77 K and chemical elemental analysis expressed as the weight percentage.

Sample	Sorption Experiments			Elemental Analysis (C, H, N)		
	BET surface area	BJH desorption pore volume	BJH desorption pore size	Carbon	Nitrogen	Hydrogen
	($m^2\ g^{-1}$)	($cm^3\ g^{-1}$)	(Å)	%	%	%
mpg-C_3N_4	248	0.51	64	28.6	52.6	3

A Fourier transform infrared (FTIR) spectrum of the mpg-C_3N_4 template is presented in Figure 3.2. The FTIR spectrum of melamine is also displayed in the figure for comparison. The formation of the mpg-C_3N_4 structure was confirmed by

the existence of a graphite-like sp^2 bonding state and the adsorption peak at 810 cm^{-1}, which corresponds to the breathing mode of triazine (out-of-plane ring bending vibration mode).[29,30] Characteristic stretching vibration signals of the tri-*s*-triazine heterocyclic rings are present in the range of 1200-1600 cm^{-1} with peak maxima at 1233, 1405 and 1565 cm^{-1}.[31,32] The bands observed at 1317 and 1610 cm^{-1} are related to the C(sp^2)-N and C(sp^2)=N stretching modes, respectively, in a graphitic-type of structure.[32,33] The weak signal at 2175 cm^{-1} can be assigned to the cyano group stretching band, which suggests that the condensation of the tri-*s*-triazine network was incomplete.[34]

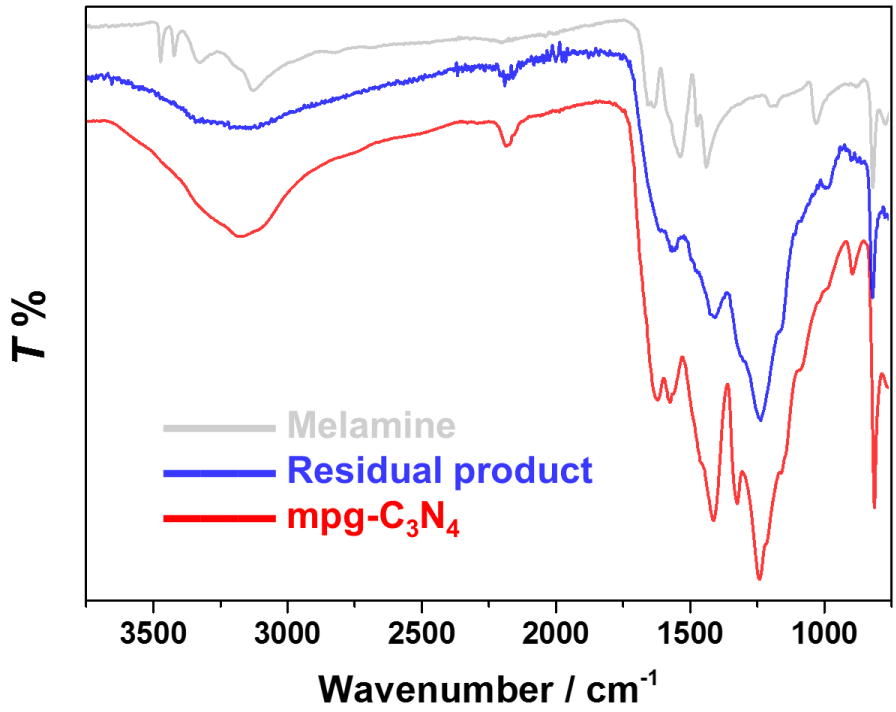

Figure 3.2 Fourier transform infrared spectra of melamine, residual product obtained at the reactor outlet during the temperature-programmed decomposition of mpg-C_3N_4, and the mpg-C_3N_4 template.

The broad peaks observed from 2900 to 3400 cm^{-1} are generally related to the stretching and deformation modes of the residual N-H components and their intermolecular hydrogen bonding. It is possible to compare this region with the melamine spectrum higher than 2900 cm^{-1}, where the signals at 3125, 3325, 3415 and 3466 cm^{-1} are attributed to N-H stretching vibration modes of the amino groups.[35] Residual hydrogen atoms on the edges of the polymeric network bind in $C\text{-}NH_2$ and 2C-NH bonds and are energetically stable.[29] The absorbance of the OH band overlaps in this range and can be attributed to hydrogen-bonded OH groups and absorbed water molecules in the sample.[36] Furthermore, there is no trace of the absorption bands for *v* Si-O-Si at 1000-1200 cm^{-1},[37] which indicates the successful removal of the silica used for the synthesis of mpg-C_3N_4. When the mpg-C_3N_4 was exposed to a high temperature in inert gas flow (>900 K), it was completely decomposed into gaseous products, as confirmed by the complete loss of weight measured by thermogravimetric analysis. Note that the high temperature decomposition of C_3N_4 causes the formation of highly toxic hydrogen cyanide and cyanogen gases. During the decomposition, a thin, yellow solid film at the cooled outlet of the reactor was recovered as a by-product from the reaction. The FTIR spectrum of the film is shown in Figure 3.2. The spectrum shows characteristics almost identical to those of the carbon nitride template but with essential differences. The recovered by-product exhibits the same characteristic vibrations for a CN heterocyclic ring and the dominant ring breath located at 1200-1600 cm^{-1} and 810 cm^{-1},[29–32] respectively. Similarly, a reflecting broad band above 2900 cm^{-1} can be attributed to N-H stretching and deformation modes.[35] The absence of

absorption bands at 1610 cm^{-1} and 1317 cm^{-1} is an indication of the interrupted non-graphitic-like structure.[32,33] The signal at 2175 cm^{-1} assigned to a C≡N or N=C=N stretching band is also a good indicator of the truncated nature of the network.[34] However, the major absorption and broader peaks in the 1100-1250 cm^{-1} region may reflect new C-N stretching vibrations associated with a cross-linked structure. The disordered nature of the decomposition product makes it difficult to give unambiguous IR peak assignments.[30]

Figure 3.3 shows the detection of the main gaseous products found using online mass spectroscopy during the temperature-programmed decomposition of the mpg-C_3N_4 template under Ar flow. The products that remained gaseous after cooling to room temperature were observed between 705 and 1100 K, as reported previously.[30,32]

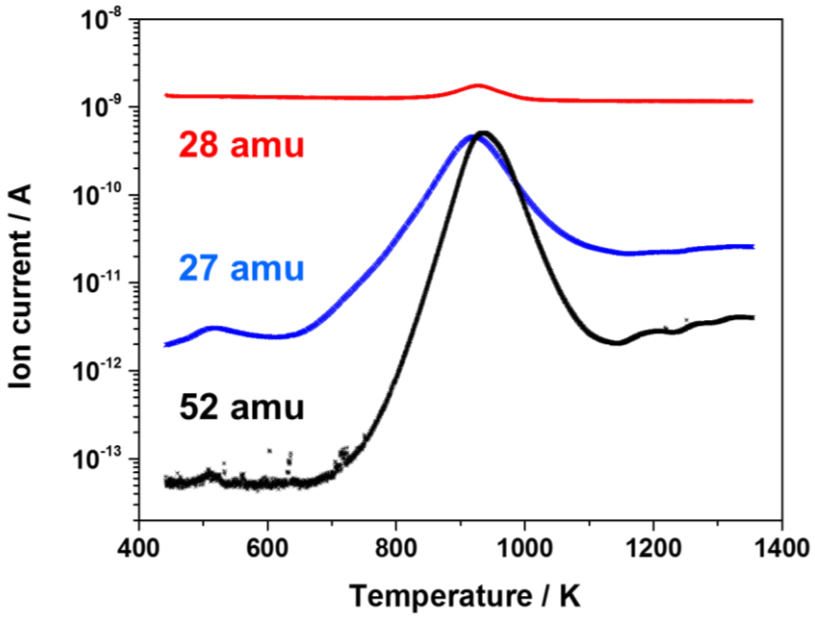

Figure 3.3 In-situ mass signals obtained during the temperature-programmed decomposition of mpg-C_3N_4.

At 940 K, clear peak maxima of the main signals were detected at 27, 28 and 52 amu that were assignable to hydrogen cyanide (HCN, MW=27.02 g mol^{-1}), nitrogen (N_2, MW=28 g mol^{-1}) and cyanogen (C_2N_2, MW=52.03 g mol^{-1}), respectively. These results provide evidence of the formation of cyanogen (52 amu) as the main gaseous product formed during mpg-C_3N_4 decomposition. The recovered polymeric yellow film at the outlet of the reactor indicates the formation of heavier C_3N_x species as a result of the fragmentation of the tri-*s*-triazine heterocyclic rings in the carbon nitride material.[32] Other nitrogen-containing gases and oxygenated hydrocarbons were not observed during the heating process. No remaining materials were recovered after the decomposition experiments, which clearly suggests that complete volatilization occurred during the decomposition of mpg-C_3N_4. From the findings of this study, we can derive the following general equation for the decomposition of mpg-C_3N_4 at high temperatures and under inert conditions:

$$2C_3N_{(4+x)} \rightarrow N_2 + HCN + C_2N_2 + C_3N_{(2x+3)} \qquad x = 0 - 0.75 \qquad (4.1)$$

The hydrogen and excess nitrogen may arise from the surface C-NH_2 and 2C-NH groups as confirmed by FTIR spectroscopy. Moreover, the calculated stoichiometry of the carbon nitride template produced was calculated from elemental analysis results.

3.2.2. Synthesis of tungsten carbide nanoparticles

A reactive hard-templating method using the nanometer-sized confinement encountered in mpg-C_3N_4 has been reported as favorable for the synthesis of metal nitride nanoparticles. TiN,[38] VN,[39] GaN,[39] Ta_3N_5,[26,40] and ternary Al-Ga-N and Ti-V-N[27] have been successfully obtained. The decomposition reaction of the confining matrix serves as a nitrogen source for the metal source found in the pores of the carbon nitride.[28] To the best of my knowledge, carbide materials have not been reported with carbon nitride as the reactive template.

The pores of the reactive template were impregnated with a chloride dialkoxide solution of pentavalent tungsten. A blue solution was prepared from WCl_6 and ethanol as described in the following equations[41]

$$WCl_6 + 2C_2H_5OH \rightarrow \frac{1}{2}Cl_2 + WCl_3(OC_2H_5)_2 + 2HCl \quad (4.2)$$

$$Cl_2 + 2C_2H_5OH \rightarrow CH_3OCHO + 2HCl \quad (4.3)$$

Figure 3.4 shows the mass spectra obtained during the attempted synthesis of tungsten carbide materials from the tungsten source immersed in mpg-C_3N_4 (1:1, WCl_6 to mpg-C_3N_4 weight ratio). The main gaseous products indicated by the 27, 28 and 52 amu signals were assigned as HCN, N_2 and C_2N_2, respectively, as previously observed in the experiments for mpg-C_3N_4 decomposition.

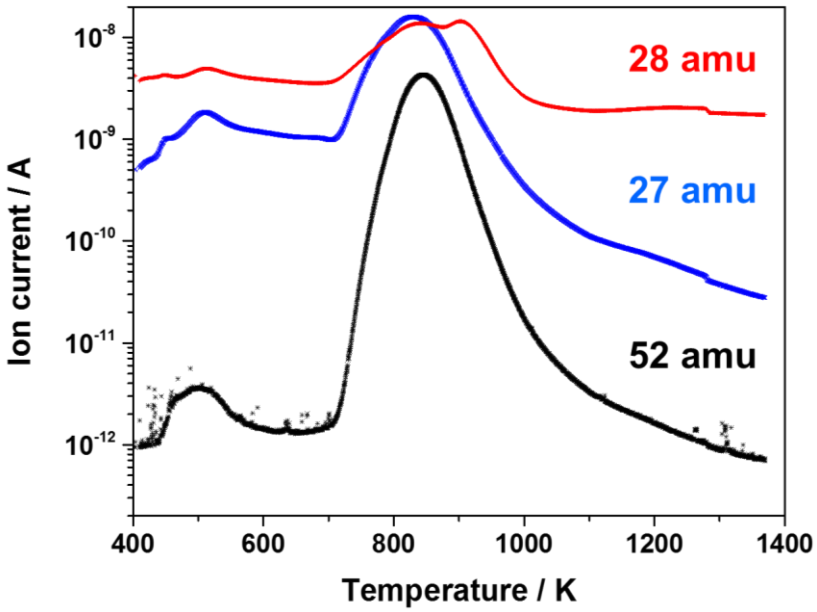

Figure 3.4 In-situ mass signals obtained during the synthesis of tungsten carbide nanoparticles.

However, the peak maxima were shifted to lower temperatures at ~845 K with the tungsten source when compared with those without tungsten species (at 920 K), as shown in Figure 3.3. This reduction of temperature clearly indicates the reactions of mpg-C_3N_4 with the tungsten precursor $WCl_3(OC_2H_5)_2$. Two peaks were observed in the nitrogen signal; the first one corresponds to the reaction of the mpg-C_3N_4 template with the tungsten precursor and the second one (~705 K; Figure 3.4) corresponds to the decomposition of intact mpg-C_3N_4 as indicated by the signal shown in Figure 3.3. A solid white powder recovered at the outlet of the reactor was identified as ammonium chloride (NH_4Cl) by XRD measurement. The crystals were most likely deposited at the outlet walls of the quartz tube as a result of the reaction between HCl and NH_3 and originated from the tungsten precursor solution and carbon nitride decomposition, respectively.

A series of tungsten products was synthesized from the reaction with the mpg-C_3N_4 template under various conditions. First, Figure 3.5 shows XRD patterns of the samples synthesized by varying the starting precursor weight ratio (WCl_6/C_3N_4 ratio) while keeping the temperature constant at 950°C. Other variables studied included the volume of ethanol and heating rate, but no significant effects were observed in the product structure as a result of these changes. Rather, prominent effects on the product structure were observed with variations in the weight ratio of WCl_6 to mpg-C_3N_4.

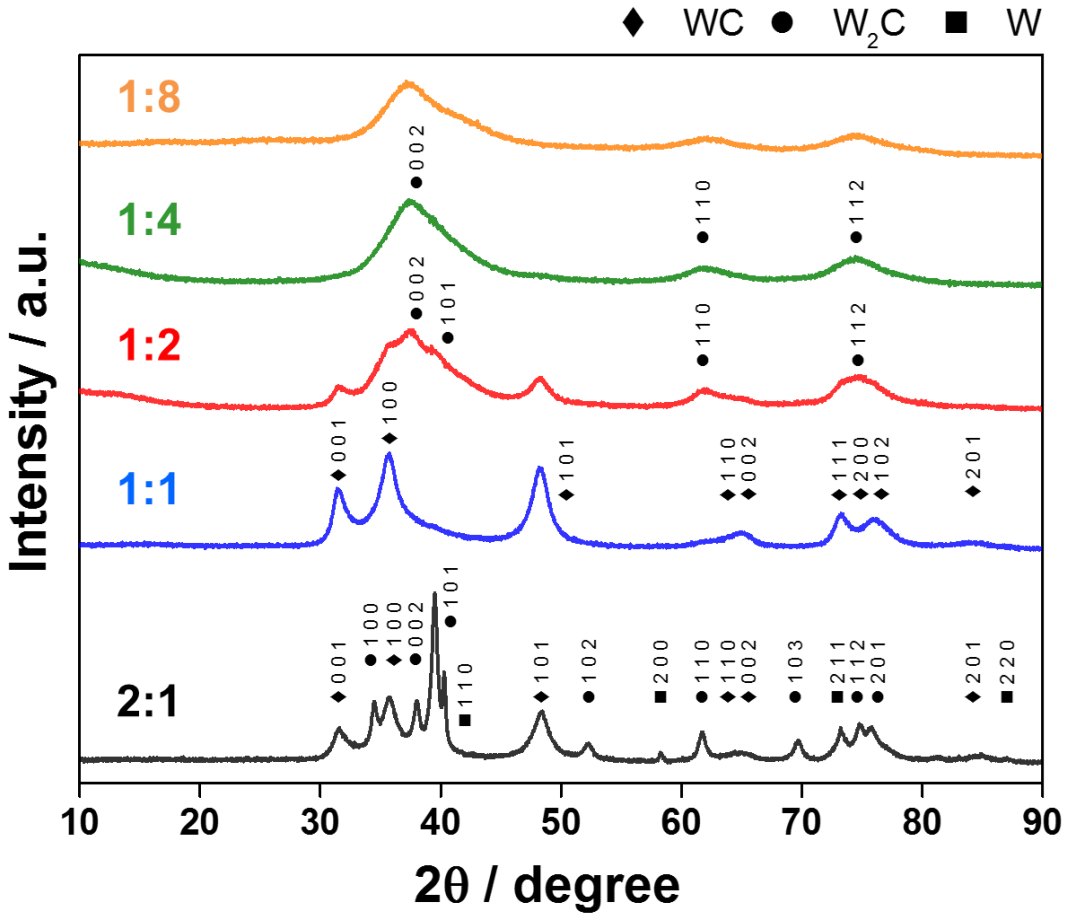

Figure 3.5 The effects of the tungsten to carbon nitride weight ratio on the tungsten-based products. Variation of the WCl_6 to mpg-C_3N_4 weight ratio at 950°C.

A 1:1 ratio gave hexagonal δ-WC with a *P*6*m*2 space group (ICSD-77566), as identified in the XRD pattern (1:1 in Figure 3.5), with primary diffraction peaks detected at 2θ = 31.5° (*d* = 2.858, WC [0 0 1]), 2θ = 35.7° (*d* = 2.511, WC [1 0 0]) and 2θ = 48.2° (*d* = 1.887, WC [1 0 1]). A broad peak was observed between 64.1° and 65.4° that corresponded to *d* = 1.450 (WC [1 1 0]) and *d* = 1.426 (WC [0 0 2]), respectively. In the literature, the δ-WC phase is commonly referred as α-WC, and this designation will be used in this chapter hereafter.[42] As the amount of available carbon increased in the synthesis, a mixture of α-WC and α-W_2C phases was obtained using a 1:2 WCl_6/C_3N_4 ratio, and only broader peaks assigned to the α-W_2C phase were observed at the WCl_6/C_3N_4 ratios, 1:4 and 1:8. This α-W_2C phase has a hexagonal structure with a *P*3*m*1 space group (ICSD-77568), with characteristic diffraction peaks observed at 2θ = 37.9° (*d* = 2.368, W_2C [0 0 2]), 2θ = 61.8° (*d* = 1.498, W_2C [1 1 0]) and 2θ = 74.9° (*d* = 1.266, W_2C [1 1 2]). Finally, when the amount of carbon nitride template was reduced in the synthesis (2:1), a mixture of tungsten carbide phases and tungsten metal was identified. Unstrained cubic W^0 (ICSD-43667) with primary diffraction peaks at 2θ = 40.2° (*d* = 2.239, W^0 [1 1 0]), 2θ = 58.2° (*d* = 1.583, W^0 [2 0 0]) and 2θ = 73.1° (*d* = 1.292, W^0 [2 1 1]) was detected in the diffractogram in conjunction with the characteristic diffractions of the α-WC and α-W_2C phases.

Figure 3.6 shows the XRD patterns of the samples synthesized at different temperatures (800-1100°C) while keeping the ratio of WCl_6/C_3N_4 at 1:1. At relatively low temperatures (<950°C), broad peaks that are characteristic of hexagonal α-W_2C were observed that indicate the formation of small particles, as

expected from utilizing the confinement of the mpg-C_3N_4 pores. Hexagonal α-WC was formed at temperatures above 950°C, whereas α-W_2C was detected above 950°C as the minor phase in the product and was almost undetectable at 1100°C. It is interesting to note that there was a clear phase transition at 1000°C where the primary diffraction peaks assignable to cubic W^0 appeared together with the peaks for the α-WC phase.

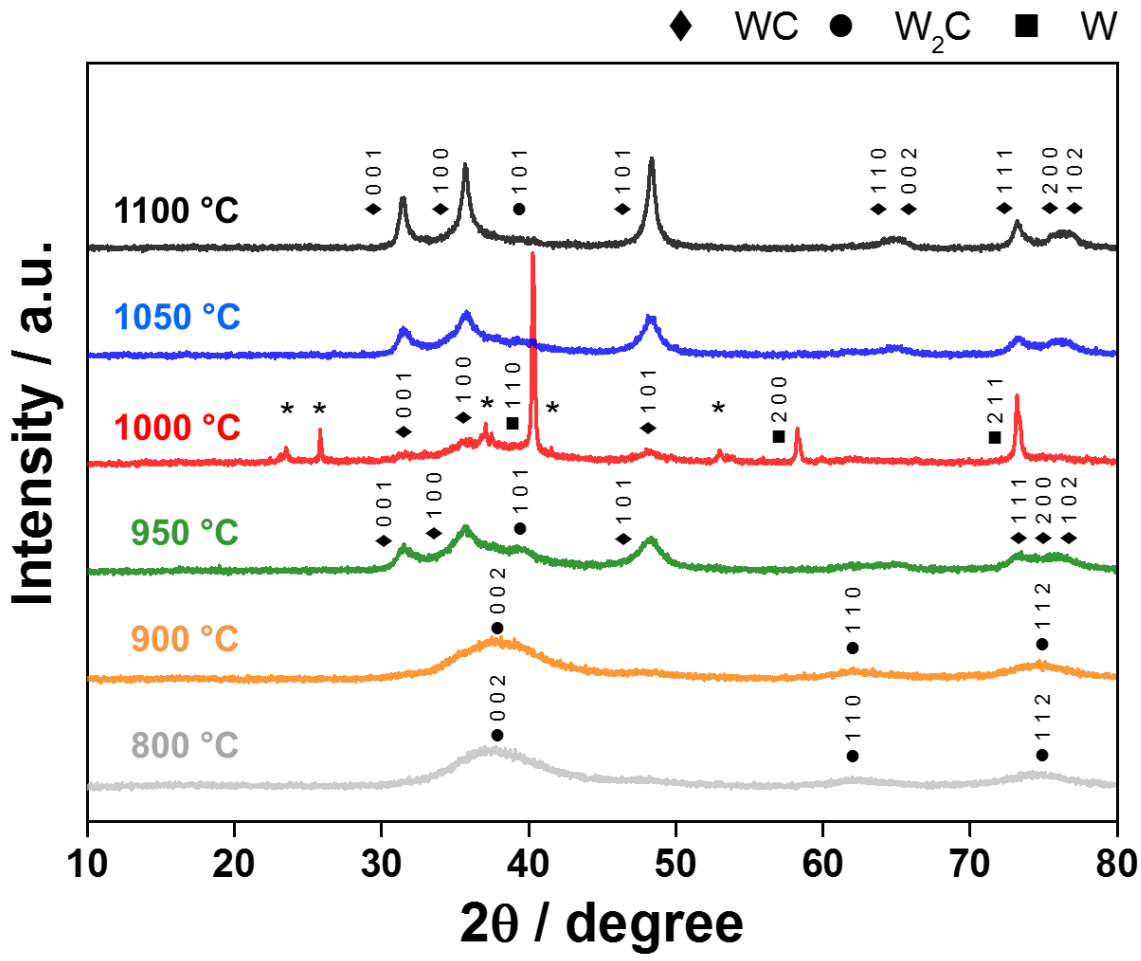

Figure 3.6 Variation of the temperature at a fixed weight ratio of 1:1 for the synthesis of tungsten-based materials. The asterisk-highlighted peaks (*) indicate the formation of tungsten oxide species (WO_2, $W_{18}O_{49}$ and WO_3).

Table 3.2 Phase assignment from the XRD diffractogram and the particle size evaluation from the Scherrer equation of selected samples produced at different temperatures with a constant precursor weight ratio of 1:1.

Temperature (°C)	Phase from XRD	Scherrer size (Å)	Surface area [a] (m^2 g^{-1})
800	W_2C	23	151
900	W_2C	29	120
950	WC W_2C	56	68
1000	WC W_2C W	63	60
1050	WC	70	54
1100	WC	152	25

[a] Non-porous spherical particles with homogeneous size distribution were assumed for calculations.

Some diffraction peaks assigned to WO_2 and WO_3 are also highlighted with an asterisk (*) in the figure; these peaks must have originated from the oxidation of tungsten metal during the passivation process at the end of the synthetic procedure. It was considered that metallic tungsten was formed as a result of the eutectoid decomposition of α-W_2C, in agreement with the W-C phase diagram where metallic tungsten and α-WC could coexist below 1500 K.[42] The peaks for α-WC became sharper at higher temperatures, which clearly indicates an increase in particle size because particle aggregation increases at high temperatures. The Scherrer equation was used to approximate the size of the crystallites in the samples[43] in a range from 56 to 152 Å in the temperature range of 950°C to

1100°C, as listed in Table 3.2. This finding is consistent with a gradual growth of particle size with increasing temperatures. The phase assignments of the products obtained with XRD are also listed in the table.

The results described above can lead to the following conceptual equations:

$$\frac{9}{4}C_3N_4 + WCl_3(OC_2H_5)_2 \xrightarrow{\Delta} 3NH_4Cl + N_2 + 2HCN + C_2N_2 + \frac{9}{4}C + \frac{1}{2}W_2C \quad (4.4)$$

$$W_2C \xrightarrow{\Delta} W + WC \quad (4.5)$$

$$W + C \longrightarrow WC \quad (4.6)$$

$$W + xO_2 \longrightarrow WO_{2x} \quad (4.7)$$

Reaction 4.4 should include extra amine/imide groups from C_3N_4, which form additional ammonia. Reaction 4.5 indicates the disproportionation of α-W_2C to form metallic W and α-WC. Metallic tungsten is not stable, and it reacts with the remaining carbon or with oxygen (passivation).

The role of the W and mpg-C_3N_4 precursor ratio during the synthesis of tungsten carbide nanoparticles was explored in experiments in which the mass of mpg-C_3N_4 was doubled with respect to the amount of the tungsten precursor at different temperatures. It was observed that α-W_2C initially formed at temperatures above 800°C did not transform into α-WC even at 1000°C (Figure 3.7).

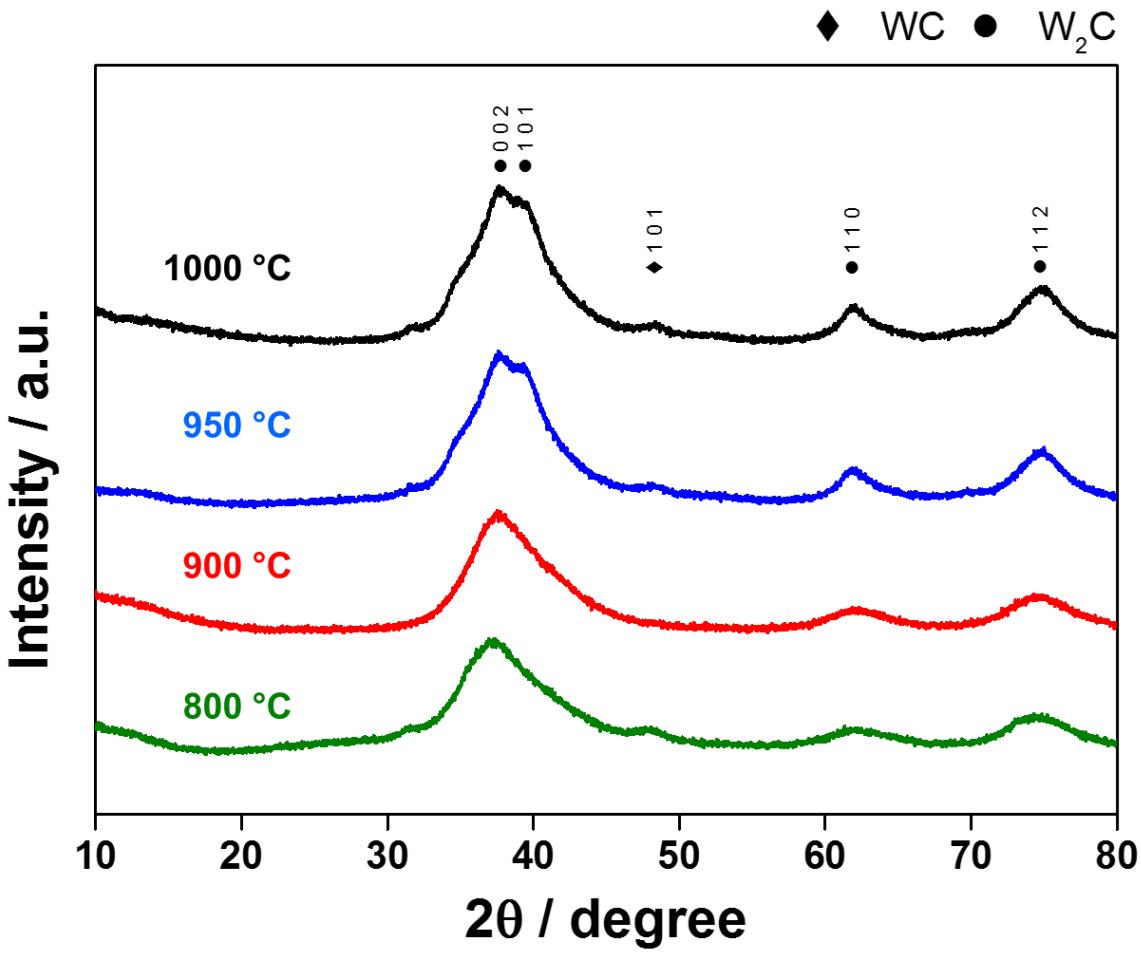

Figure 3.7 Variation of the temperature at a fixed weight ratio of 1:2 for the synthesis of tungsten-based materials.

For all temperatures ranging from 800 to 1000°C, broad peaks were observed, mainly from α-W_2C characteristic diffraction patterns. This result indicates that excess C_3N_4 (thus leading to excess carbon) suppresses the disproportionation of α-W_2C to metallic W and WC (Scheme 4.5). Hereafter, the samples are denoted based on the major phases identified by XRD followed by the temperature used in the syntheses (e.g., W_2C-900, WC-950, WC-1100, etc.).

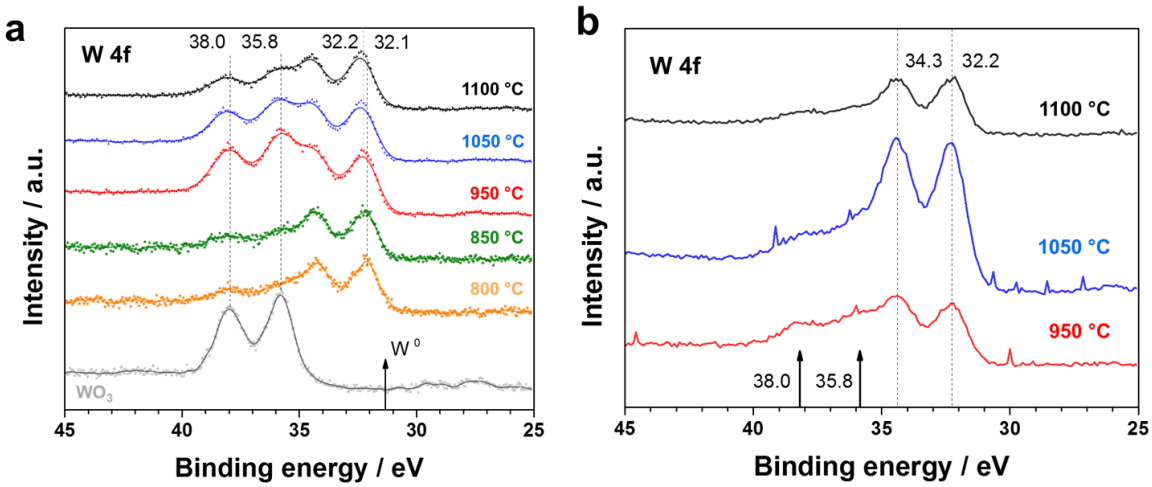

Figure 3.8 W 4f XPS spectra of tungsten-based products obtained at different temperatures. WO_3 spectrum is included as reference for comparison. The metallic tungsten characteristic signal is indicated with an arrow at 31.3 eV (a). The XPS spectra of the samples obtained at temperatures above 950°C after a 15-min exposure to Ar ion sputtering. The WO_3 characteristic binding energies for W $4f_{7/2}$ and W $4f_{5/2}$ at 35.8 and 38.0 eV, respectively, are indicated with arrows (b).

The XPS spectra of W 4f for the synthesized carbide materials obtained at different temperatures are shown in Figure 3.8a. WO_3 was used as reference material for the direct comparison of hexavalent oxidation states and gave spectra with binding energies for W $4f_{7/2}$ and W $4f_{5/2}$ of 35.8 eV and 38.0 eV, respectively, which is consistent with the values in the literature.[44] All of the tungsten carbide samples showed W 4f signals above 31.3±0.1 eV that corresponded to the metallic state of tungsten.[21] For α-WC samples synthesized in the range of 950-1100°C, the W 4f spectra show peaks at binding energies assigned to WC at 32.2 eV (W $4f_{7/2}$) and 34.4 eV (W $4f_{5/2}$), which closely agrees with reported values.[15,44,45] These α-WC samples showed signals emitted from the partially oxidized surface of the materials because of the O_2 passivation treatment and unavoidable exposure of

the nanoparticles to the ambient conditions. The intensity of the W 4f signals assigned to the WO_3 species (35.8 and 38.0 eV) decreased with increasing temperature, whereas the carbidic W 4f signal intensity (32.2 and 34.4 eV) increased with increasing temperature, which corresponds to the concrete formation of WC, as observed in the XRD patterns (Figure 3.6). The α-W_2C produced at lower temperatures (<950°C) reflected a further reduced state of W with the peak location shifted 0.1 eV lower when compared with the α-WC samples.[15] These XPS spectra did not show surface oxidation with any appreciable peaks at 38.0 or 35.8 eV. When α-WC samples were treated under substantial Ar ion sputtering, the intensity of the oxidative phase was diminished, which suggests the removal of consecutive layers of the oxide species without an effect on the W 4f carbidic signals (Figure 3.8b).

Table 3.3 shows the results (in mass percentages) of the elemental analysis (C, H, N) of the synthesized W samples to confirm the formation of the carbide rather than the nitride form of the transition metal. The nitrogen content for all samples (0.1-0.8%) was well below the possible stoichiometric values for tungsten nitride (7.07 and 3.66% for WN and W_2N, respectively). As listed in Table 3.3, the carbon content in the samples obtained below 950°C (6.12%) exceeded the stoichiometric value (3.16%), as assigned from XRD (α-W_2C).

Table 3.3 Elemental analysis and calculated BET surface area of tungsten carbide products obtained at varying temperatures while maintaining the precursor weight ratio of 1:1.

Sample [a]	Weight Ratio [b]	Carbon %	Nitrogen %	Hydrogen %	BET surface area ($m^2\ g^{-1}$)
W_2C-800	1:2	13.3	0.8	0.2	145
W_2C-900	1:2	18.2	0.7	0.2	141
W_2C-950-A	1:8	22.3	1.0	0.6	-
W_2C-950-B	1:4	18.8	0.8	0.6	-
W_2C-950-C	1:2	12.8	0.6	0.3	125
WC-950	1:1	8.3	0.6	0.1	104
WC-1000	1:1	1.9	0.1	0.1	60
WC-1050	1:1	8.8	0.4	0.1	85
WC-1110	1:1	8.3	0.4	0.1	80

[a] The sample ID indicates the assigned phase from the XRD diffractogram and the synthesis temperature in Celsius at which the product was obtained.

[b] Experimental precursor weight ratio (WCl_6:mpg-C_3N_4).

The samples produced at higher temperatures with an assigned stoichiometry of α-WC exhibited closer agreement with the theoretical carbon content. In the WC-1000 sample, the carbon content was 1.9%, which was well under the stoichiometric value and supports earlier observations from XRD and XPS where a phase transition was observed at 1000°C and metallic tungsten led to the oxidation of the carbide phase. All of the samples produced at higher temperatures (>950°C) and identified by XRD as α-WC showed similar carbon

contents, which is a good indication of the reproducibility of the procedure and is in reasonable agreement with the results observed by XRD and shown in Figure 3.6. To further characterize the tungsten content in the resulting tungsten carbide samples, thermogravimetric analysis coupled with differential scanning calorimetry (TGA/DSC) was utilized to simultaneously monitor the heat flow in the experiment in addition to the weight change. For a WC-1100 sample under flow of air (Figure 3.9), the mass of the sample increased throughout the heating process until it was 16.5% higher than that of the original product. The final theoretical stoichiometric mass gain of 18% (for α-WC) is represented in Figure 3.9 by a dashed line. The 1.5% difference correlates to the findings observed in elemental analysis where excess carbon was present in the sample. There are two subtle shoulders in the weight signal during the weight increment process, which is also reflected in the heat flow signal as two exothermic peaks with maxima at 713 K and 800 K.

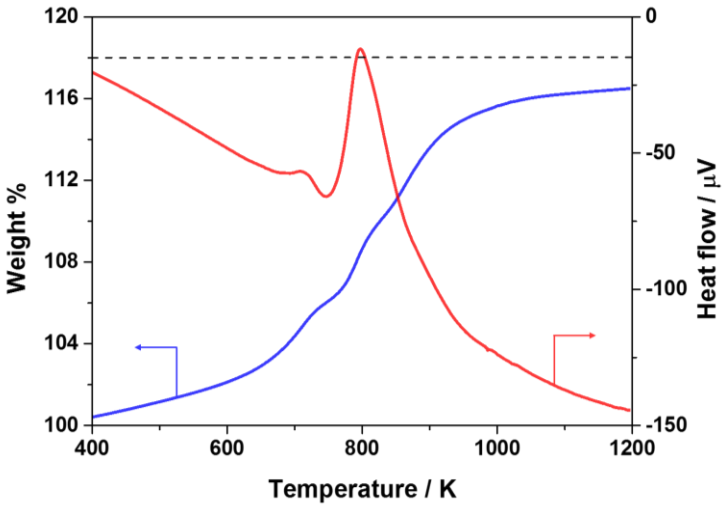

Figure 3.9 TGA-DSC signals obtained using WC-1100. (10 K min^{-1}, 100 ml min^{-1} flow of air) The final theoretical stoichiometric mass gain is represented with a dashed line at 118%.

The first peak can be attributed to the partial oxidation of the material towards possible intermediate mixed valence species (i.e., WO_2, W_2O_3, and/or $W_{18}O_{49}$) with the release of CO_x.[46] The main peak represents the full oxidation of the sample towards WO_3, as observed by the color change from black to bright yellow at the end of the experiment. The tungsten mass content in the original sample could be calculated from this experiment to be approximately 92.5%, which is in close agreement with the stoichiometric value of 94% for WC and further confirms the results obtained from elemental analysis and XRD.

Nitrogen sorption experiments were performed on the samples to obtain the BET surface area. Table 3.3 compiles the values of the surface areas of the materials. The surface area of the products decreased with increasing temperature. Higher surface areas were attained for W_2C products when compared with the WC products. The α-WC sample with the highest surface area (~104 $m^2\ g^{-1}$) was obtained at 950°C with the precursor weight ratio maintained at 1:1. However, it is worth noting that the measured BET surface area for the tungsten carbide nanomaterials may be affected by the presence of excess carbon, especially at low temperatures where the amount of carbon is higher (>12%, Table 3.3). As evaluated using the Scherrer equation in the XRD diffractogram, the nano-crystallite size was found to be 6-15 nm at higher temperatures (950-1100°C) and ~2-3 nm at lower temperatures (800-900°C) (Table 3.2). Using these sizes and assuming non-porous spherical particles with a homogeneous size distribution, the surface area of the W_2C or WC particles can be approximated, as shown in Table 3.2. The obtained surface areas were slightly

lower than the measured BET surface areas, and the difference between these calculations may originate from the presence of carbon and the error generated from the assumption of sphericity.

Figure 3.10 shows the results obtained from the transmission electron microscope (TEM) investigations on W_2C-800 (a, b), WC-950 (c, d) and WC-1100 (e, f). Low- and high-magnification micrographs are shown for representative samples obtained at different temperatures. As observed in Figure 3.10a, 3.10c and 3.10e, the particle size increases with increasing temperature, which is in agreement with the results observed from XRD and calculated from the Scherrer equation. The W_2C-800 sample exhibited a uniform particle size distribution (~5 nm) that accurately reflects the original pore size of the mpg-C_3N_4 template, as observed in Figure 3.10a. The high resolution transmission electron microscope (HRTEM) image of the WC-950 sample showed a greater extent of aggregation and sintering, with nanoparticle sizes up to 10 nm. Finally, the samples obtained at an even higher temperature (WC-1100) showed sizes up to 25 nm.

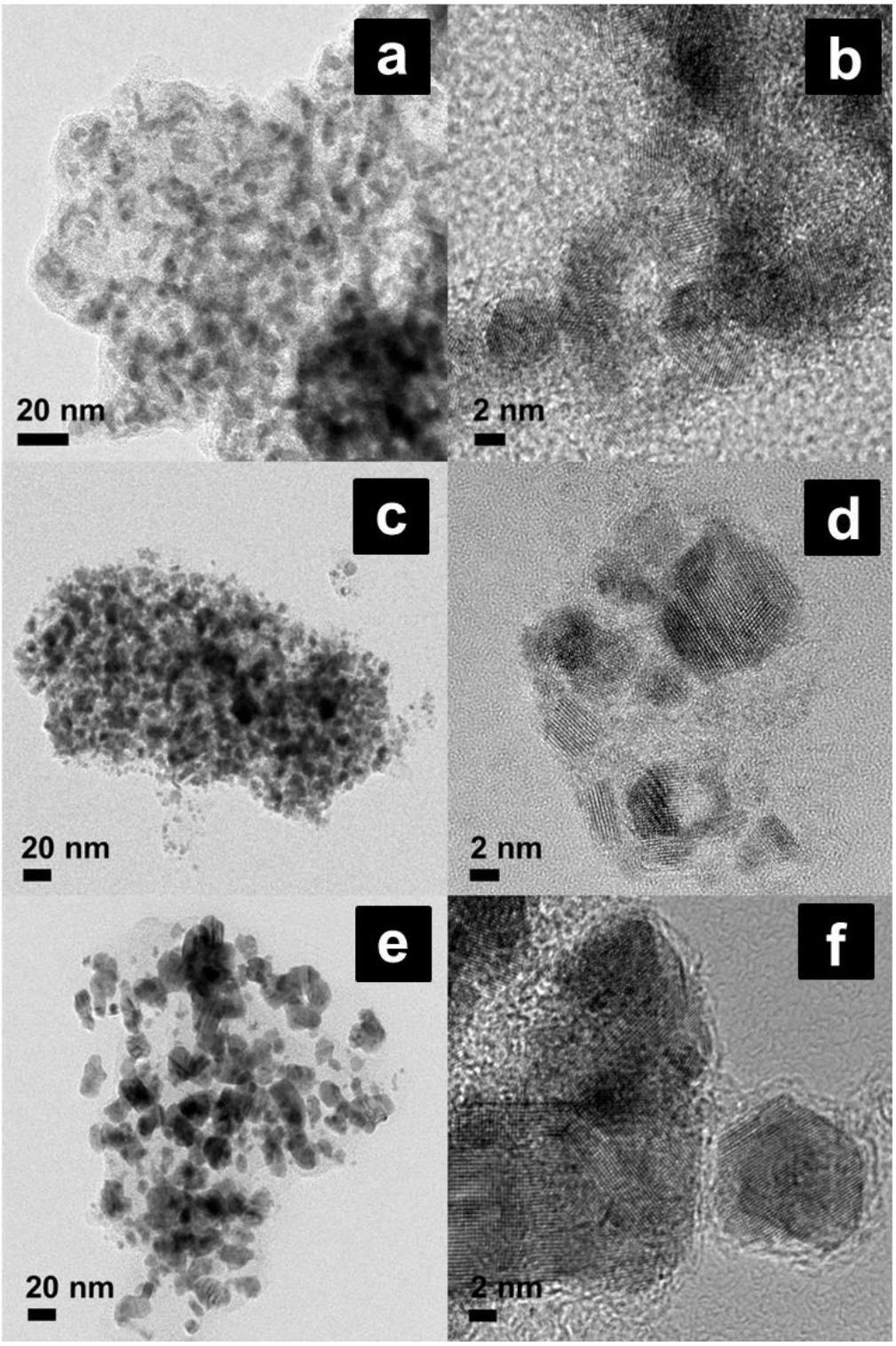

Figure 3.10 HRTEM micrographs of W_2C-800 (a, b), WC-950 (c, d) and WC-1100 (e, f). The WCl_6 to mpg-C_3N_4 weight ratio used for the synthesis was 1:2 (a, b) and 1:1 (c-f).

The HRTEM images on the right (Figure 3.10b, 3.10d and 3.10f) allowed us to observe the crystalline nature of the produced tungsten carbide nanoparticles in detail. It was possible to observe the remaining carbon present in the samples, as indicated by elemental analysis and TGA. Although it was not possible to quantify the amount of carbon present, energy-dispersive X-ray (EDX) spectroscopy was performed to confirm the chemical composition of the crystalline nanoparticles. A line profile of EDX was performed to study the local environment for a single nanoparticle observed in scanning transmission microscope (STEM) mode; the result shows that the nanocrystal is composed of tungsten and carbon; moreover, carbon was also observed in the surroundings of the nanoparticles (Figure 3.11).

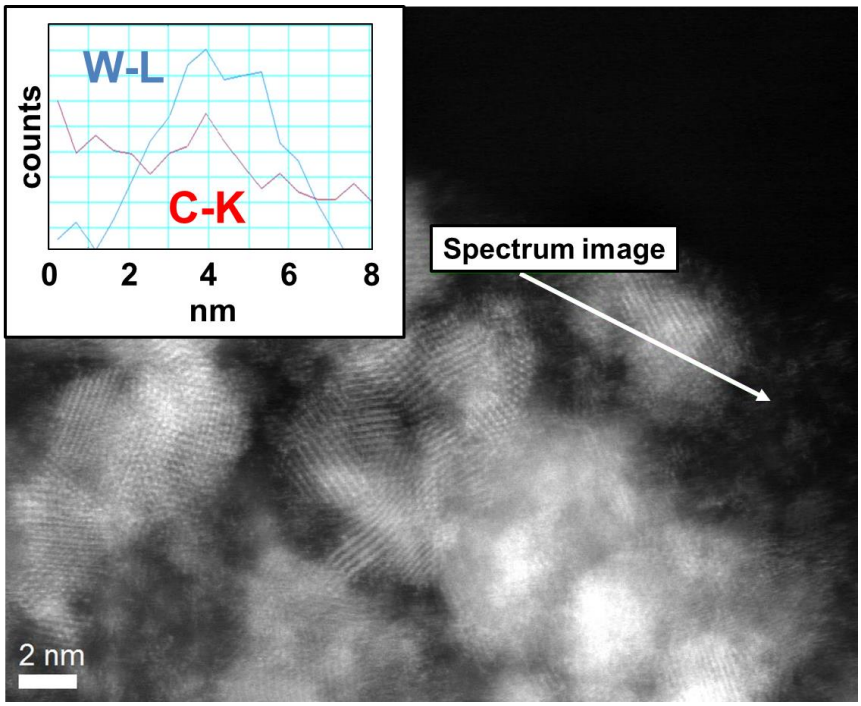

Figure 3.11 STEM-EDX line profile for WC-950. Elemental distribution of the spectrum obtained for carbon (C-K) and tungsten (W-L) is presented in the inset along with the line profile investigated in the sample

In summary, it was shown that by tuning the synthesis conditions, it was possible to obtain materials with the desired tungsten carbide phase and a high surface area. This synthetic method led to the formation of extra carbon in addition to the tungsten phase, which plays an important role to inhibit transformation of the α-W_2C phase to the α-WC phase. As shown in the mass spectrometry experiments, the tungsten precursor reacted with mpg-C_3N_4 inside the nano-confinement of the mesoporous template to control the particle size of the "seeds" at relatively low temperatures (500-750°C). When the synthetic conditions were optimized to obtain α-WC at higher temperatures (>950°C), only α-WC was present in the final product, as confirmed by XRD, XPS, TGA and elemental analysis. The high-surface-area tungsten carbide obtained can be utilized as a catalytic active site, and in the following section of this chapter, investigations of the electrochemical activity in water redox reactions was performed.

3.2.3. Electrocatalysis by tungsten carbides

The electrochemical stability of WC under acidic conditions at room temperature was evaluated for the WC-950 sample. A cyclic voltammetry (CV) experiment with a wide potential window (0.05-1.05 V vs. RHE) was performed to evaluate the stability of tungsten carbide materials. Tungsten carbide showed a major oxidation peak starting at 0.7 V vs. RHE, which was consistent with similar observations found in the literature (Figure 3.12).[47] The oxidation peaks completely vanished after several cycles, which indicates the irreversible nature of WC oxidation process. Great care must be taken to retain the original nature of the

carbide structure to be able to correctly evaluate and compare the electrocatalytic performance of the materials.

The WC-950 sample was tested for HOR activity in acidic solution, and the results were comparable to those obtained for 40% Pt/C. The polarization curve of the WC-950 material is presented in Figure 3.13. The HOR was evaluated using a rotating disk electrode (RDE) with the rotation speed ω varying from 400 to 2500 rpm. For WC-950, the HOR current was primarily controlled by a region of mixed kinetic-diffusion control at overpotentials up to 0.15 V vs. RHE. Diffusion-limiting currents were prominent above 0.2 V vs. RHE for curves obtained under rotational speeds below 900 rpm. It is worth noting that a wider overpotential region (0-0.3 V vs. RHE) can be used for kinetic analysis in the 2500 rpm polarization curve (Figure 3.13a) where the measured current is primary kinetically controlled. Platinum polarization curves showed that diffusion-limited currents were rapidly obtained at 0.06 V vs. RHE (Figure 3.13b).

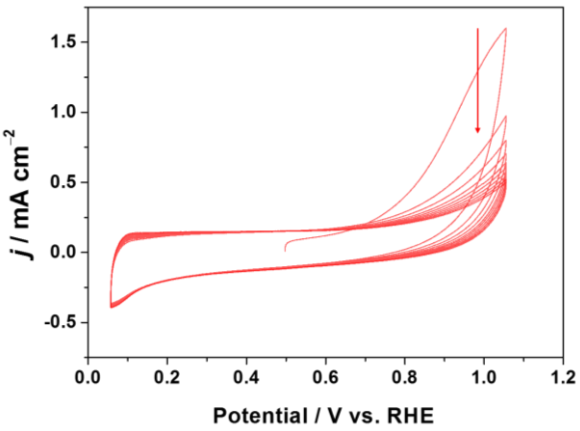

Figure 3.12 Cyclic voltammograms of WC-950 at 0.05-1.05 V vs. RHE. (0.5 M H_2SO_4, 50 mV s^{-1}, 298 K).

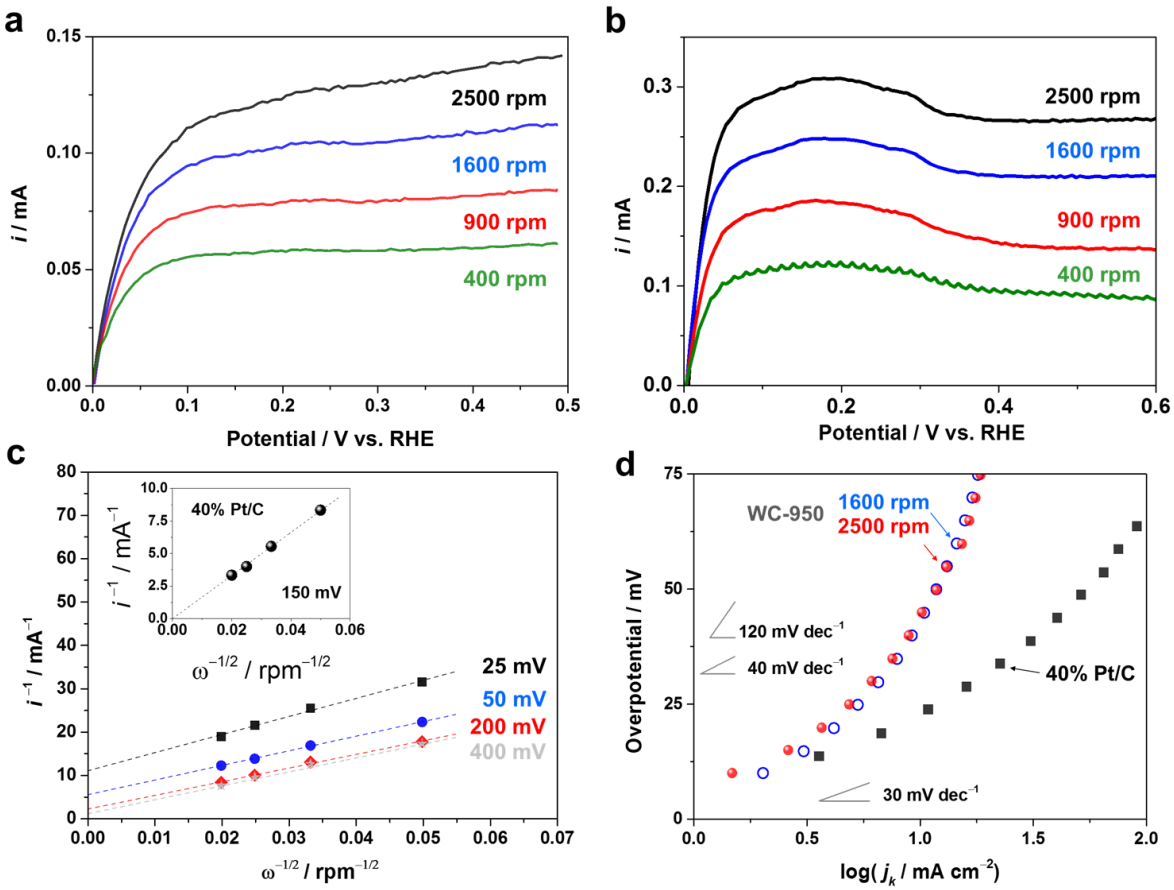

Figure 3.13. HOR polarization curves on WC-950 at varying rotation rates obtained using a rotating disk electrode (a). HOR polarization curves of 40% Pt on carbon at different rotation rates (b). HOR Koutecký-Levich plots for WC-950 obtained at varying overpotentials (mV vs. RHE). The inset shows the Koutecký-Levich plot for 40% Pt/C obtained at 150 mV vs. RHE. (c) Tafel plots using mass-transport-corrected HOR currents of the WC-950 sample and 40% Pt/C (H_2-saturated 0.5 M H_2SO_4, 50 mV s^{-1}, 298 K).

The results indicated that the HOR anodic currents were kinetically controlled in a very narrow potential range (0-0.05 V vs. RHE), in agreement with the literature.[48] The linearity and intercept to zero observed in the inset of Figure 3.13c proved that at sufficient overpotentials (i.e., 150 mV vs. RHE) the current is mainly diffusion-limited and proportional to the square root of the rotational speed

ω.[49] This total mass-transfer-limited condition is described by the Levich equation in the following form

$$i_L = 0.62zFAD^{\frac{2}{3}}\omega^{\frac{1}{2}}\nu_k^{-\frac{1}{6}}C_0 = B_L C_0 \omega^{\frac{1}{2}} \quad (4.8)$$

The Levich current is generally identified as i_L, B_L is the Levich constant, z is the number of electrons transferred in the half reaction, F is the Faraday constant, A is the surface area, D is the diffusion coefficient (298 K, 3.7×10^{-5} cm^2 s^{-1}, estimated from the product of H_2 diffusivity at infinite dilution and the ratio of the dynamic viscosities of the electrolyte and pure water),[48] ω is the angular rotational speed, ν_k is the kinematic viscosity (298 K, 1.2×10^{-2} cm^2 s^{-1}) and C_0 is the H_2 saturation concentration (298 K, 7.14×10^{-4} M).[50] From the 40% Pt/C experimental data obtained at 0.15 V vs. RHE (shown in the inset of Figure 3.13c), the least-squares regression fit returned a slope of $B_L C_0 = 6.0\times10^{-3}$ mA rpm$^{-0.5}$. At sufficient overpotential and at a specific rotational speed it is possible to estimate the surface area of the catalyst from Equation 4.8. Thus, the platinum surface area calculated from the Levich equation was 0.03 cm^2. When a kinetic limitation is involved in the electron transfer reaction, as in the case for tungsten carbide (Figure 3.13a), the currents at the RDE are described by the Koutecky-Levich equation.

$$\frac{1}{i} = \frac{1}{i_k} + \frac{1}{i_L} = \frac{1}{i_k} + \frac{1}{0.62zFAD^{\frac{2}{3}}\omega^{\frac{1}{2}}\nu_k^{-\frac{1}{6}}C_0} \quad (4.9)$$

The current in the absence of any mass-transport effects and, hence, the current determined only by kinetic limitations is represented as i_k. From Equation 4.9, the plot of the inverse of the current as a function of the inverse of the square root of the rotational speed will produce a straight line with an intercept corresponding directly to the kinetic current i_k^{-1} and a slope of $(B_L C_0)^{-1}$. Figure 3.13c depicts the Koutecky-Levich plots for tungsten carbide (WC-950) at different overpotentials (mV vs. RHE). There is a noticeable contribution of the kinetic limitation over a wide range of overpotentials (0.025-0.2 V vs. RHE). Non-zero intercepts shown in the figure indicate that the rate of the electron transport process was the limiting factor. However, at sufficient overpotentials (0.4 V vs. RHE), I considered the kinetic component negligible and it is possible to assume complete diffusion-limiting conditions. From the least-squares regression lines obtained from Figure 3.13c, the average slope observed from 0.075 to 0.4 V vs. RHE was $B_L C_0$ = 3.1×10^{-3} mA rpm$^{-0.5}$. Similarly to the platinum calculations, the estimated tungsten carbide surface area was calculated to be 0.015 cm^2. The mass-transport-corrected kinetic current was normalized by using the calculated surface area approximations from the Koutecky-Levich equation. Hence, diffusion-corrected Tafel plots of the polarization curves obtained from 40% Pt/C (2500 rpm) and WC-950 (1600 rpm and 2500 rpm) are presented in Figure 3.13d. The kinetic current was independent of the rotation rate above 1600 rpm, as observed in the figure, which is a good indication of the accuracy of the i_k determination for WC-950 in this rotation range. From the Tafel analysis $\eta = A_T + B_T \log(j)$ in Figure 3.13d, the (A_T) term in the empirical Tafel equation can be extrapolated from the Tafel

linear region to an intercept with value of $RT\alpha_T^{-1}F^{-1}\ln(j_0)$ and represents the electrochemical reaction rate near equilibrium conditions.[49,51] Where R is the ideal gas constant, T is the absolute temperature, α_T is the transfer coefficient, j_0 is known as the exchange current density and F is the Faraday constant. This kinetic parameter can be described as any system's capacity to facilitate a net current (reaction rate) without incurring significant energy losses from activation.[49] The Tafel slope (B_T) can be empirically calculated from the polarization curve in between specific overpotentials (η), which provides insight into the possible mechanism of the reaction. In the literature,[6,52-54] three elementary reaction steps depict the mechanism for hydrogen oxidation/evolution on solid state catalytic sites:

1. The dissociative adsorption of hydrogen molecules on the catalyst surface known as the Tafel reaction or recombination reaction for hydrogen evolution.

$$\mathrm{H_2} + 2* \rightleftharpoons \mathrm{H_{ads}} + \mathrm{H_{ads}} \qquad (4.10)$$

2. The direct reaction of hydrogen molecules through the Heyrovsky reaction, also known as the ion-plus-atom reaction.

$$\mathrm{H_2} + \mathrm{H_2O} + * \rightleftharpoons \mathrm{H_{ads}} + \mathrm{H_3O^+} + e^- \qquad (4.11)$$

3. The ionization of the H atom to produce one electron and one hydronium ion in solution, which results in an empty active site in the reaction known as the Volmer reaction (charge transfer reaction).

$$H_{ads} + H_2O \rightleftharpoons H_3O^+ + e^- \quad (4.12)$$

In the elementary steps mentioned above, H_{ads} represents atomic hydrogen that was chemisorbed to a metal surface (i.e., Pt) and the symbol ***** (asterisk) denotes a free adsorption site. From equations 4.10 to 4.12, it is possible to theoretically calculate the expected Tafel slope from surface coverage assumptions using microkinetic analysis. For a detailed description of the theoretical derivations the reader is referred to reference 54. For the HER, the first common step is represented by the Volmer equation or discharge reaction (Equation 4.12). Then, there are two possibilities, either electrochemical desorption (Equation 4.11) or a recombination step (Equation 4.10). The reversible reactions (HOR) follow a Tafel-Volmer or Heyrovsky-Volmer mechanism. As mentioned previously, platinum is one of the most studied catalysts for the HOR and HER in the literature. Exchange current densities are difficult to obtain because of the fast kinetics and lack of accuracy during correction for mass transport limitations in most cases. However, several groups have found that the Pt(110) surface is the most active for both the HOR and HER, as it exhibits Tafel slopes of approximately 30 mV dec^{-1} that may correspond to a Tafel-Volmer mechanism (Equation 4.10 and 4.12).[48,51,55] The recombination reaction or Tafel step may be the rate determining step (RDS), as reflected at low overpotentials with a measured Tafel slope of 28 mV dec^{-1} for the HOR in Figure 3.13d (40% Pt/C), which is also in agreement with the findings for well-characterized polycrystalline Pt.[48,56] The HOR Tafel plot obtained for WC-950 seems to have two apparent Tafel slopes of 43 mV dec^{-1} (0.1-0.4 V vs. RHE) and 150 mV dec^{-1} (0.4-

0.7 V vs. RHE) (Figure 3.13d). There is no clear linear region in the kinetic HOR polarization curve, which possibly indicates a potential-dependent reactive intermediate coverage or low surface coverage conditions.[50,54] Because the HOR polarization cannot be simplified into a single linear Tafel region, it is difficult to determine the kinetic parameters accurately. It is also very challenging to unambiguously resolve the reaction mechanism from this experimental evidence. Nevertheless, on the basis of the Tafel slopes obtained, the WC-1223 sample may follow a Heyrovsky-Volmer HOR mechanism with the ion-atom reaction as the rate-determining step at low surface coverage. At higher overpotentials, the rates of the electrochemical desorption and the discharge reaction may become comparable, which makes it difficult to define the RDS.

The catalysts synthesized at different temperatures were also examined for activity in the HER in 0.5 M H_2SO_4 at 298 K using a RDE to achieve steady-state current conditions without diffusion effects on the measurements. Figure 3.14 demonstrates the voltammograms of tungsten carbide synthesized at different temperatures along with voltammograms of Pt/C and GCE. The acquired currents were tentatively normalized by the surface area calculated from the Levich analysis performed earlier for the HOR. The electrochemically active surface area (ECSA) of the Pt catalyst was calculated to be similar to the geometric area of the electrode. Cathodic currents attributed to the HER were observed for all carbide samples with an onset potential of approximately −0.1 V vs. RHE.

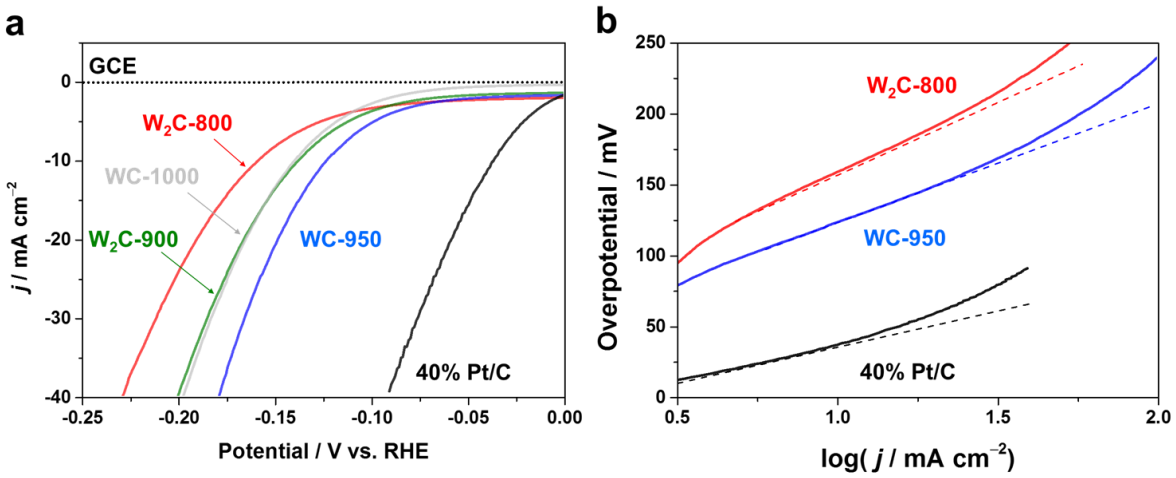

Figure 3.14 HER voltammograms of tungsten carbide samples synthesized at different temperatures (W_2C-800, W_2C-900, WC-950 and WC-1000) along with voltammograms of a Pt/C electrode and glassy carbon electrode (a). HER Tafel plots for W_2C-800, WC-950 and Pt/C electrode (b) (0.5 M H_2SO_4, in Ar, 50 mV s^{-1}, 298 K).

The WC-950 sample exhibited the highest HER current among all of the samples with a hydrogen evolution overpotential of ca. 80 mV, and it thus outperformed the rest of the samples. Figure 3.14b shows Tafel plots for the HER of the W_2C-800 and WC-950 samples. Pt was an excellent catalyst for the HER as expected, as it produced an extrapolated exchange current density of $j_0 \approx 1$ mA cm^{-2} with a Tafel slope of 34 mV dec^{-1} consistent with the literature expecting Tafel as the RDE.[54] Among the synthesized tungsten-based nanoparticles, WC-950 had the highest activity with an estimated $j_0 \approx 0.35$ mA cm^{-2}, followed by the W_2C-800 sample with $j_0 \approx 0.28$ mA cm^{-2}, which is consistent with the polarization curves exhibited in Figure 3.14. However, it should be noted that for tungsten carbide materials, the exchange current density was normalized by the estimated surface area from Koutecky-Levich experiments rather than the electrochemically active

surface area as for the Pt electrode. The WC-950 sample exhibited a Tafel slope of 84 mV dec^{-1} (0.1 to 0.15 V vs. RHE), whereas the W_2C-800 sample exhibited a slope of 102 mV dec^{-1} (0.13 to 0.19 V vs. RHE). The results may indicate a Volmer-Heyrovsky HER mechanism catalyzed by the tungsten carbide samples (WC-950) with a rate-determining electrochemical desorption step from the ion to the atom reaction, as shown in the equations above.[52,53,57] When the tungsten carbide phase is different (W_2C-800), the HER mechanism most likely changes to the extent that the discharge step or the Volmer reaction becomes rate-limiting.[54] The high values for the Tafel slope most likely resulted from variation in the surface coverage of the adsorbed hydrogen.[54] Thus, it is possible that the rates of the discharge reaction and the electrochemical desorption are comparable, which then results in intermediate values of Tafel slopes between 40 and 120 mV dec^{-1}. In Table 3.4, a steeper Tafel slope was obtained for the samples where WC was the major phase present, which indicates a clear difference in the reaction mechanism pathways for different carbide phases (W_2C and WC). The higher slopes obtained in the HOR correlate with the values obtained for the HER, which possibly indicates that the reversible hydrogen reaction may proceed via the same mechanism with a similar rate-determining step. The higher current density observed for the WC-950 sample (Figure 3.14) could be attributed to the monocarbide phase of the sample (as resolved by elemental analysis, XRD, TGA and XPS) in combination with the high surface area of the material (Table 3.3).

Table 3.4 HER evaluation and Tafel parameters calculated from kinetic measurements in an Ar-purged 0.5 M H_2SO_4 solution for selected samples at room temperature with a 50 mV s^{-1} scan rate.

Sample	Onset potential at 3 mA cm^{-2} (mV)	Overpotential to achieve 10 mA cm^{-2} (mV)	Overpotential range for Tafel analysis (mV)	Exchange current density j_o (mA cm^{-2})	Tafel slope B_T (mV dec^{-1})
W_2C-800	95	158	130 - 190	0.28	102
WC-950	78	122	100 - 150	0.35	84
Pt	12	36	10 - 30	1	34

α-WC exhibits a better hydrogen evolution performance than α-W_2C under acidic conditions even though α-W_2C has a higher surface area. This trend may be explained by the volcano plot of exchange current as a function of the hydrogen binding energy of the material, developed by Nørskov and coworkers,[6] and is consistent with recent DFT and experimental studies on transition metal carbides.[15] Hence, the Pt-like electronic structure allowed α-WC to show higher activity than any other sample in this study, even though the α-W_2C samples exhibited a higher surface area. However, as the synthesis temperature increased, the HER current decreased along with the decrease in the surface area of the samples because of the reduction in the number active sites available for hydrogen evolution.

The stability test of the material with the best performance for the HER is shown in Figure 3.15. The first and the 800th polarization cycles are shown in the inset of the figure to have no significant difference; hence, the WC-950 carbide sample demonstrated negligible current loss after 800 charging-discharging cycles between −0.3 and 0.1 V vs. RHE in a 0.05 M H_2SO_4 solution at 298 K. This finding clearly indicates the high stability of the carbide material under acidic conditions. The HER activity was also evaluated under neutral and alkaline conditions and compared with that of the Pt catalyst.

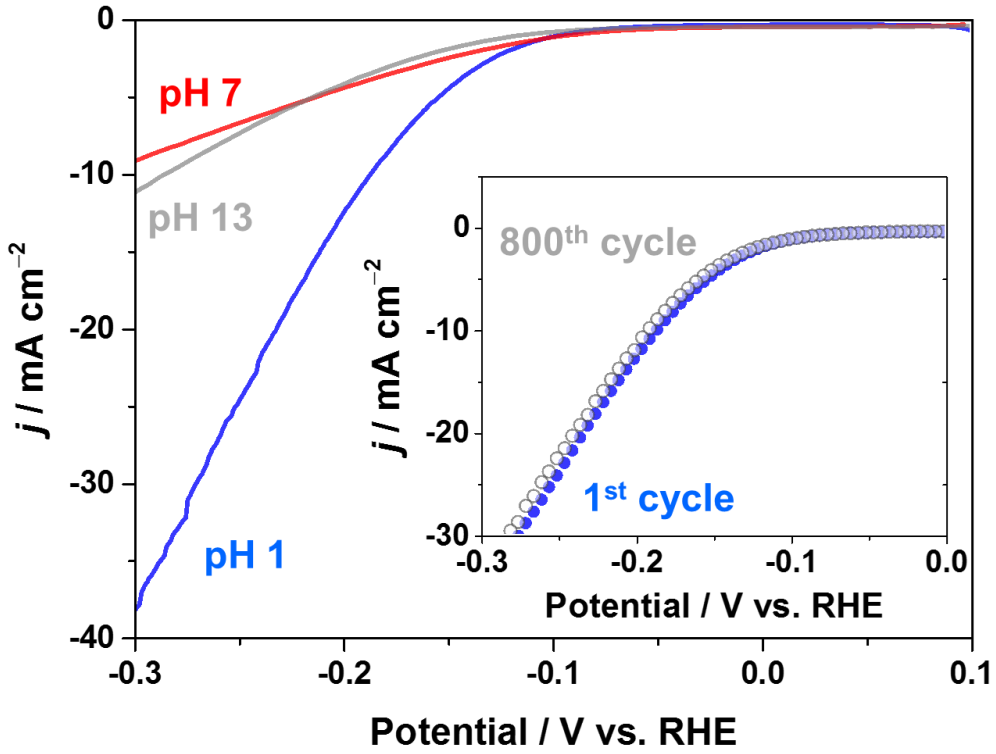

Figure 3.15 The stability test of the WC-950 sample under a wide range of pH conditions. The first and the 800th polarization cycles for the WC-950 sample are shown in the inset of the figure. (0.5 M Na_2SO_4 as supporting electrolyte with the pH adjusted using H_2SO_4 or NaOH; The conditions for the inset are 0.05 M H_2SO_4, in Ar, 50 mV s^{-1}, 298 K).

Figure 3.15 shows the polarization curves obtained at different pH conditions, and the results were compared with those obtained using 40% Pt/C (Table 3.5). The onset potential for non-acidic conditions was very similar at −0.15 V vs. RHE, although the current was lower than that under acidic conditions. The trend for WC-950 was similar to that of 40% Pt/C; the activity decreased to 20% of the original performance at neutral pH and then recovered to approximately 30% of the activity observed under acidic conditions at pH 13. This result relates the electronic structure of WC, which is similar to that of Pt, and is reflected with the HER behavior, as previously discussed.[15–17,21,47]

Table 3.5 Hydrogen evolution current comparison between WC-950 and 40% Pt/C samples in 0.5 M Na_2SO_4 with varying pH values.

pH	Current density at η = 300 mV (mA cm^{-2})	
	WC-950	Pt
1	38	98
7	9	21
13	12	34

Figure 3.16 shows the experiments performed for the ORR on W_2C-900, WC-950, and WC-1100 samples and a Pt disk electrode. In this case, the recorded currents for the materials were normalized using the geometrical surface area of

the electrode (j_{geom}). Special care must be taken when evaluating the ORR on tungsten carbides to prevent oxidation of the catalyst. As previously discussed, tungsten carbide oxidation was observed at positive potentials higher than 0.6 V vs. RHE. Therefore, the polarization experiments were performed only for positive potentials below 0.5 V vs. RHE to ensure that the catalytic nature of the material was unaltered. As shown in the figure, the ORR activity for all of the tungsten-based samples was low, and cathodic currents attributed to the ORR were observed at potentials below 0.3 V vs. RHE for the best WC sample. As expected, the Pt catalyst exhibited excellent performance towards the ORR with an onset potential of ca. 0.9 V vs. RHE. The reduced ORR activity observed for tungsten carbide materials was hypothesized as an advantage for the overall water-splitting reaction.

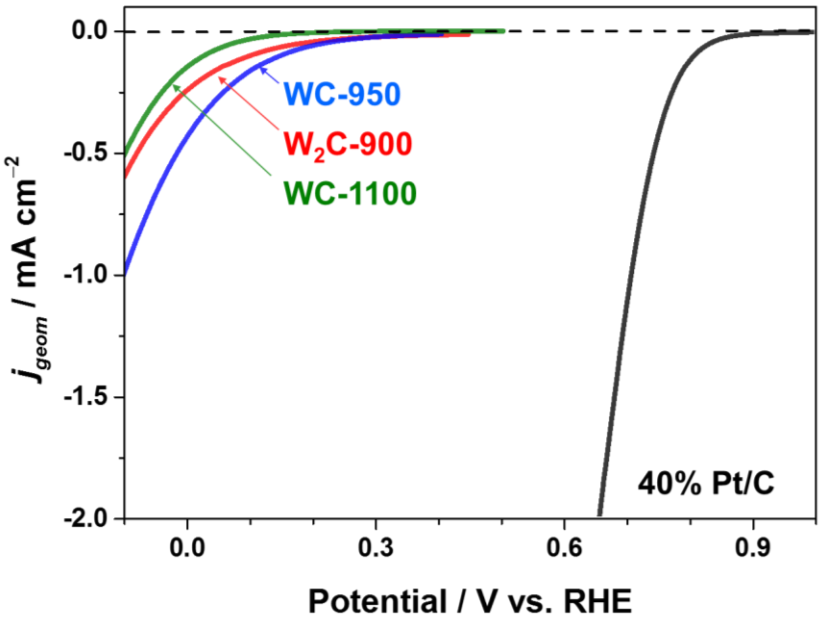

Figure 3.16 Polarization curves in saturated O_2 obtained for W_2C-900, WC-950, WC-1100 and the Pt disk electrode (0.5 M Na_2SO_4, pH 3.6, 50 mV s^{-1}, 298 K).

3.2.4. Photocatalytic overall water splitting

As described previously, Pt-group metal surfaces catalyze proton reduction but are also highly active in inducing the back-reaction from H_2 and O_2 to water.[58] In the literature, the Ni/NiO[59,60] core-shell structure and RuO_2[61] have been extensively utilized as successful cocatalyst for overall water splitting. Recently, a Cr shell was studied as a possible selective membrane to prevent O_2 permeation to the metal surfaces.[7] Apparently, the core-shell structure of the Cr-based layer protects the metallic nanoparticle surfaces to suppress the ORR (back-reaction) while maintaining HER (i.e., proton reduction).[8] Moreover, photocatalytic overall water splitting in a particulate type of system has been achieved only on metal/metal-oxide surfaces with a core-shell structure. Therefore, based on the results obtained from HER and ORR experiments where WC materials catalyzed hydrogen evolution but revealed poor performance for the ORR, the samples were considered to be potential so-called cocatalysts for the water-splitting reaction.

Overall water splitting was attempted under varying loading conditions on a Na-doped $SrTiO_3$ (STO) photocatalyst, and the results are shown in Figure 3.17. This photocatalyst was active for overall water splitting under UV irradiation when impregnated with Rh and Cr species giving ~300 μmol h^{-1} H_2 and ~150 μmol h^{-1} O_2, as discussed elsewhere.[57] The photocatalyst with 2.75 wt.% WC/$SrTiO_3$:Na showed the highest activity with the production of stoichiometric amounts of H_2 and O_2 in the experiment.

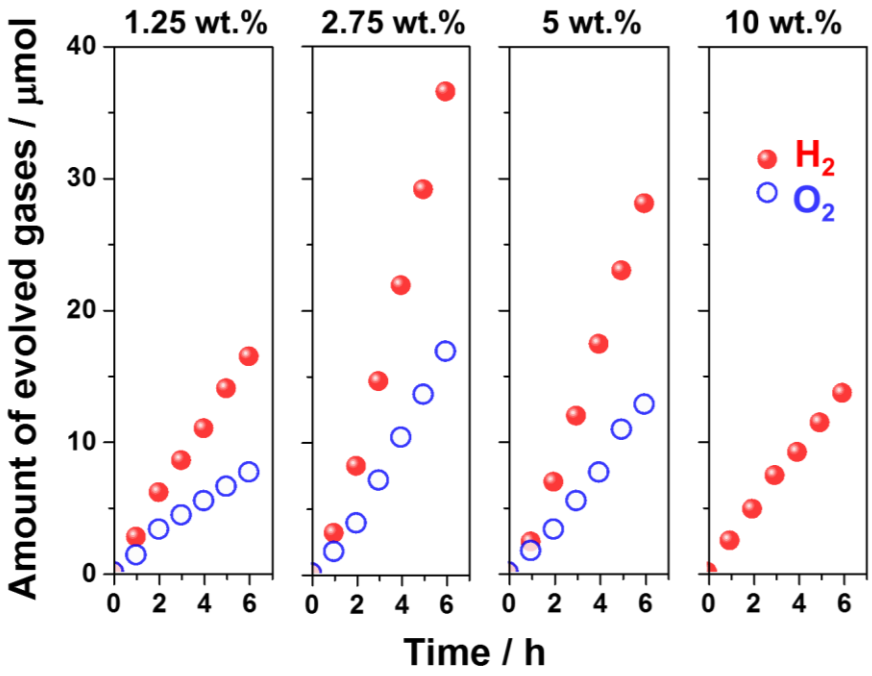

Figure 3.17 Overall water-splitting experiments performed on a recirculating reactor unit using the $SrTiO_3$:Na photocatalyst with varying loadings of the WC sample (300 W Xe lamp containing UV light, 100 ml milli-Q H_2O and 50 mg photocatalyst).

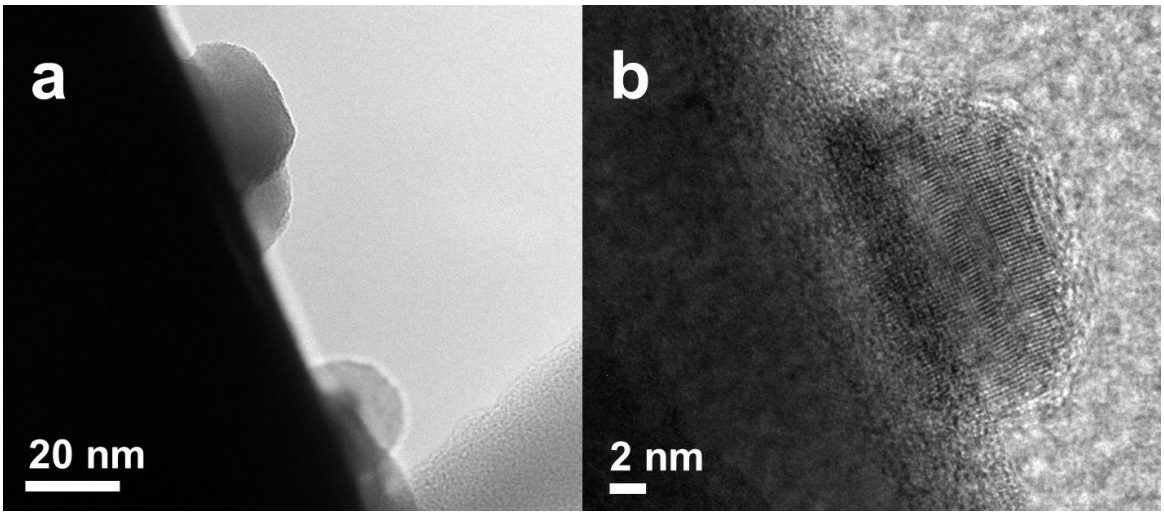

Figure 3.18 HRTEM micrographs of dispersed WC nanoparticles on the surface of $SrTiO_3$:Na photocatalyst.

HRTEM images are presented in Figure 3.18 and show a representative WC particle supported on the $SrTiO_3$:Na photocatalyst. When the loading of WC on the semiconductor photocatalyst reached 10 wt.%, the H_2 production rate decreased and O_2 gas was not observed as a product, like in the case of non-modified $SrTiO_3$:Na. The lack of O_2 production may be indicative of the oxidation of impurities or of surface hydroxyl groups. In summary, overall water splitting was achieved at low oxygen and hydrogen partial pressures in the WC/$SrTiO_3$:Na system. WC showed reasonably high electrochemical hydrogen evolution activity while exhibiting poor oxygen reduction performance, which may explain the system's ability to catalyze overall water splitting. WC was used as a electrocatalyst for photocatalytic water splitting and functioned as a hydrogen evolution site while preventing the back-reaction in a dual-role system. The similarity of the electronic structure of WC to that of Pt may be reflected in its ability to improve charge separation and serve as a hydrogen evolution active site. It is also possible, as demonstrated by XPS, that WC undergoes oxidation on its surface to prevent back-reactions while reflecting the low activity observed in the overall water splitting experiments. Although further optimization of the synthetic and reaction conditions is needed, WC shows promise in the search for non-noble-metal electrocatalysts for overall water splitting. Furthermore, these findings show that WC can be used for water splitting without a core-shell structure, which opens new possibilities in the design of so-called cocatalysts for photocatalytic overall water splitting.

3.3. Summary

In this chapter, tungsten carbide nanoparticles were made with a size of approximately 5 to 15 nm from the confinement of the pores of a mpg-C_3N_4 template. The results show the formation of carbide nanoparticles, rather than the nitride phase, from the carbon nitride template and indicate the role of mpg-C_3N_4 as a carbon source. The phase transformation of tungsten carbide was clarified by XRD studies. Two phases (α-WC and α-W_2C) can be obtained from this synthetic procedure by optimizing the precursor weight ratio and the synthesis temperature. For the first time it was possible to control the desired phase in the product and to obtain carbide particles in the nanometer range. The WC phase can only be obtained at temperatures above 950°C when the precursor weight ratio is maintained at 1:1. W_2C was always produced below this temperature regardless of the precursor ratio. The synthesis of the carbon nitride template was evaluated by means of mass spectroscopy, and the main gaseous products produced during the synthesis of WC were identified as cyanogen gas (C_2N_2), hydrogen cyanide (HCN) and nitrogen gas. High-surface-area WC (~104 m^2 g^{-1}) samples were obtained, and the carbidic phase was confirmed by elemental analysis, XRD, XPS and TGA. Electrochemical studies showed that the WC-950 sample exhibited the highest and most stable HER activity in an acidic medium among the samples prepared in this study. WC was one of the most active non-noble-metal transition metal electrocatalyst for HER in acidic media. The same sample also demonstrated the ability to catalyze HOR with good catalytic kinetics. Interestingly, WC showed poor catalytic activity in the ORR, which makes it a potential

electrocatalyst candidate for photocatalytic water splitting. Overall water splitting was achieved under UV irradiation by loading the WC on a Na-doped $SrTiO_3$ photocatalyst. Stoichiometric amounts of H_2 and O_2 were observed with different loading conditions; the 2.75 wt.% loading gave the highest overall water-splitting rate. Although the performance of the WC sample is not yet comparable to that of platinum, this study introduces the great potential of WC as a non-noble-metal alternative for use as a cathode catalyst in water electrolysis, as an anode catalyst in PEFC and as a dual-role cocatalyst in overall water splitting.

3.4. Experimental methods

3.4.1. Synthesis

The reactive template mesoporous graphitic C_3N_4 (mpg-C_3N_4) was synthesized as previously reported.[26] Briefly, carbon nitride was synthesized from cyanamide (CN_2H_2, 99% Aldrich) and an aqueous colloidal silica suspension composed of silica nanoparticles (LUDOX SM-30, 30 wt.%, Aldrich; ~ 6 nm average diameters). The weight ratio of SiO_2 and cyanamide (CA) was maintained at 1:1 for all the samples. Usually, cyanamide was dissolved in the required volume of colloidal silica and the suspension was slowly heated to 353 K until a solid homogeneous product was obtained. The solids were placed in a closed alumina crucible and heated under static air at 823 K for 4 h with a heating rate of 2.3 K min^{-1}. A 4 M ammonium bifluoride (NH_4HF_2, ≥98.5% Fluka) aqueous solution was

utilized to remove silica from the final product, followed by a washing procedure with H_2O (18.2 MΩ cm^{-1}) and ethanol (≥99.8% Aldrich).

In a typical synthesis to obtain tungsten carbides, 0.5 g of tungsten hexachloride (WCl_6, ≥99.9% Aldrich) was dissolved in 0.56 ml of ethanol. The metal precursor reacted vigorously with the alcohol to produce hydrochloric acid and form a stable metal-orthoester precursor. Sonication of the mixture was used to aid the rapid solubilization of the metal precursor. Then, a drop-impregnation type of process was performed on 0.5 g of the mpg-C_3N_4 template to keep the weight ratio of the precursor compounds at 1:1. The final composite precursor was placed in an alumina boat crucible for heating under flowing N_2 (100 ccm). The temperature was varied from 1073 K to 1373 K. Other synthetic variables investigated included heating rate, concentration of precursor solution, pore size of the carbon nitride templates and carbon-to-metal precursor ratio. CAUTION: High temperature decomposition of C_3N_4 causes the formation of hydrogen cyanide and cyanogen gases.

The UV-responsive photocatalyst $SrTiO_3$:Na was synthesized using the flux-assisted method, as reported in a recent review.[58] The precursors used in the synthesis were strontium carbonate ($SrCO_3$, 99.9% Aldrich) and titanium oxide anatase (TiO_2, 99.9% Aldrich) in a 1:1 molar ratio. Strontium chloride hexahydrate ($SrCl_2 \cdot 6H_2O$, 99.9% Aldrich) molten salt was used in excess as the reaction medium, and sodium carbonate (Na_2CO_3, 99% Aldrich) was introduced to induce sodium doping into the final semiconductor crystal. In a typical synthesis, 50 mmol of $SrCl_2 \cdot 6H_2O$, 5 mmol of $SrCO_3$, 5 mmol of TiO_2 and 0.125 mmol of Na_2CO_3 were

placed in that order into a mortar. The reagents were ground for 20 minutes until a very fine powder was obtained. The dry mixture was treated under atmospheric conditions at high temperature inside a platinum crucible. The temperature was changed at a rate of 6.25 K min^{-1}, and the final temperature of 1423 K was maintained for 10 h using a muffle furnace. Later, the product was washed with 500 ml of deionized water and filtered using a 0.45-μm membrane. The collected powder was dried at 363 K for 2 h under vacuum conditions.

3.4.2. Characterization

Samples were characterized by elemental analysis, N_2 sorption experiments, mass spectrometry (MS), Fourier transform infrared (FTIR) spectroscopy, X-ray diffraction (XRD), X-ray photoelectron spectroscopy (XPS), thermogravimetric analysis (TGA) and transmission electron microscope (TEM). MS was used to determine the decomposition products and probable reaction pathways using an OMNI Star (GSD 320 O1) portable mass spectrometer with a tungsten filament from Pfeiffer Vacuum. The MS experiments were performed using a tubular furnace under an Ar flow (100 ml min^{-1}) with a heating rate of 3.75 K min^{-1} from room temperature to 1123 K. Quartz wool was placed to stop any solids from blocking the capillary inlet of the mass spectrometer. Identical experimental conditions for the synthesis of tungsten carbide nanoparticles were used for the MS investigations as described above. Spectra were recorded using a PerkinElmer Spectrum 100 FTIR spectrometer. Elemental analysis was performed in a Flash 2000 Thermo Scientific CHNS/O analyzer. The Brunauer-

Emmett-Teller (BET) surface area, Barret-Joyner-Halenda (BJH) pore size and pore volume were approximated at 77 K in a Micrometrics ASAP 2420 surface area and porosity analyzer using N_2 as the probe molecule. A BRUKER D8 Advance diffractometer (DMAX 2500) operated with a Cu K_α energy source at 40 kV and 40 mA was used to crystallographically characterize the materials. The XPS spectrum was calibrated against the C 1s photoelectron signal at 285 eV on an AMICUS/ESCA 3400 from KRATOS Analytical operated with dual Mg/Al anodes with an energy source at 12 kV and 10 mA. Thermogravimetric analysis was performed in a Mettler-Toledo TGA/DSC1 Star system under air (100 ml min^{-1}). TEM was used to characterize the morphology and the particle size distribution of the synthesized products. Microscopy characterizations were performed on a TITAN ST transmission electron microscope from FEI operated at 300 kV. The samples were prepared by suspending them in ethanol and dispersing them by sonication. A drop of the solution was poured onto a copper-grid-supported carbon film. Finally, the grid was dried in air prior to observation.

3.4.3. Electrochemistry

The hydrogen evolution reaction (HER), hydrogen oxidation reaction (HOR) and oxygen reduction reaction (ORR) were evaluated by electrochemical methods using a rotating disk electrode (RDE). A glassy carbon electrode (GCE) with a geometric surface area of 0.071 cm^2 was loaded with 1 mg cm^{-2} tungsten carbide nanoparticles. Typically, 9 mg of tungsten carbide sample was dispersed in 445 µl of ethanol with 15 minutes of ultrasonication. Then, 3.5 µl of the suspension was

drop-coated into the GCE and dried in open air. The electrode was later treated under static air conditions at 473 K for 1 h. A Pt/C (~40%, FC-12, Ishifuku) electrode was used in the experiments for evaluation purposes. The electrolyte used for the HER and HOR electrochemical investigations was a 0.5 M H_2SO_4 solution, and a 0.5 M Na_2SO_4 solution was used for the ORR experiments. The pH was adjusted using H_2SO_4 or NaOH to the required pH value for each experiment. The measurements were performed using a 16-channel research-grade potentiostat system (VMP3) from BioLogic Science Instruments in a conventional three-electrode single electrochemical cell. The working electrode was mounted on a rotator (RRDE-3A, BAS). Ag/AgCl electrode and a Pt wire were used as the reference electrode and counter electrode, respectively. The Ag/AgCl (sat. KCl) reference electrode was calibrated against the reversible hydrogen electrode (RHE) potential and all potentials are expressed in RHE scale. Prior to all measurements, the electrochemical cell was bubbled for 30 minutes with Ar, H_2 or O_2 for HER, HOR and ORR measurements, respectively. CV experiments were conducted with a 50 mV s^{-1} scan rate between −0.4 V and 0.1 V vs. RHE for HER, 0.0 V to 0.3 V vs. RHE for HOR under different rotational speeds and −0.1 V and 0.6 V vs. RHE for ORR. A constant rotational speed of 1600 rpm was used for all the HER and ORR experiments.

3.4.4. Photocatalysis

WC materials were tested as cocatalysts for the overall water-splitting reaction. The obtained products were loaded on Na-doped strontium titanate

($SrTiO_3$:Na) using an incipient-wetness impregnation procedure.[58] The loading amount and heating temperature under oxidizing or reducing conditions were explored. In a typical experiment, the required amount of WC nano-powder was suspended in 50 ml of ethanol and sonicated for 15 minutes to obtain a stable dispersion. Later, an appropriate amount of $SrTiO_3$:Na was added and the solution was heated to 363 K under vigorous stirring until all of the solvent was completely evaporated. The recovered product was dried under vacuum for 2 h at 363 K. Two different heat treatment procedures were employed, i.e., in an oxidative environment (static air conditions) and a reducing atmosphere (5% H_2 in argon flow, 100 ml min^{-1}). The temperature used for the heat treatment was varied from 473 K to 623 K. Overall water-splitting experiments were performed using a recirculating reactor unit. The accumulated gaseous products were analyzed using a Shimadzu GC with a Molecular Sieve 13X column and a TCD detector. Photocatalytic overall water splitting was performed under UV light irradiation using a 300 W Xe lamp with a cold mirror (260-500 nm). Experiments for overall water splitting were performed using 100 ml of H_2O (pH 7, 18.2 MΩ cm^{-1}) and 50 mg of photocatalyst.

3.5. REFERENCES

1 J.A. Turner, *Science* **2004**, *305*, 972–974.

2 K. Takanabe, K. Domen, *Green* **2011**, *1*, 313–322.

3 Kudo, Y. Miseki, *Chem. Soc. Rev.* **2009**, *38*, 253–278.

4 X. Chen, S. Shen, L. Guo, S.S. Mao, *Chem. Rev.* **2010**, *110*, 6503–6570.

5 M.G. Walter, E.L. Warren, J.R. McKone, S.W. Boettcher, Q. Mi, E. a Santori, N.S. Lewis, *Chem. Rev.* **2010**, *110*, 6446–6473.

6 J.K. Nørskov, T. Bligaard, a. Logadottir, J.R. Kitchin, J.G. Chen, S. Pandelov, U. Stimming, *J. Electrochem. Soc.* **2005**, *152*, J23–J26.

7 K. Maeda, K. Teramura, D. Lu, T. Takata, N. Saito, Y. Inoue, K. Domen, *Nature* **2006**, *440*, 295.

8 M. Yoshida, K. Takanabe, *J. Phys. Chem. C* **2009**, *113*, 10151–10157.

9 X. Lu, A. Bandara, M. Katayama, A. Yamakata, J. Kubota, K. Domen, *J. Phys. Chem. C* **2011**, *115*, 23902–23907.

10 T.F. Jaramillo, K.P. Jørgensen, J. Bonde, J.H. Nielsen, S. Horch, I. Chorkendorff, *Science* **2007**, *317*, 100–102.

11 B. Lim, M. Jiang, P. Camargo, E. Cho, J. Tao, *Science* **2009**, *324*, 1302–1305.

12 V.R. Stamenkovic, B.S. Mun, M. Arenz, K.J.J. Mayrhofer, C. a Lucas, G. Wang, P.N. Ross, N.M. Markovic, *Nat. Mater.* **2007**, *6*, 241–247.

13 P. Strasser, S. Koh, T. Anniyev, J. Greeley, K. More, C. Yu, Z. Liu, S. Kaya, D. Nordlund, H. Ogasawara, M.F. Toney, A. Nilsson, *Nat. Chem.* **2010**, *2*, 454–460.

14 X. Ma, H. Meng, M. Cai, P.K. Shen, *J. Am. Chem. Soc.* **2012**, *134*, 1954–1957.

15 D.V. Esposito, S.T. Hunt, Y.C. Kimmel, J.G. Chen, *J. Am. Chem. Soc.* **2012**, *134*, 3025–3033.

16 R.B. Levy, M. Boudart, *Science* **1973**, *181*, 547–549.

17 F. Harnisch, G. Sievers, U. Schröder, *Appl. Catal., B* **2009**, *89*, 455–458.

18 Y. Hara, N. Minami, H. Itagaki, *Appl. Catal., A* **2007**, *323*, 86–93.

19 K. Yamamoto, T. Imaoka, W.-J. Chun, O. Enoki, H. Katoh, M. Takenaga, A. Sonoi, *Nat. Chem.* **2009**, *1*, 397–402.

20 C. Giordano, C. Erpen, W. Yao, M. Antonietti, *Nano Lett.* **2008**, *8*, 4659–4663.

21 P. Ross, P. Stonehart, *J. Catal.* **1977**, *59*, 42–59.

22 J. Lemaître, B. Vidick, *J. Catal.* **1986**, *427*, 415–427.

23 Q. Zhu, S. Zhou, X. Wang, S. Dai, *J. Power Sources* **2009**, *193*, 495–500.

24 N. Hugot, a. Desforges, S. Fontana, J.F. Marêché, C. Hérold, a. Albiniak, G. Furdin, *J. Solid State Chem.* **2012**, *194*, 23–31.

25 J. Chen, K. Takanabe, R. Ohnishi, D. Lu, S. Okada, H. Hatasawa, H. Morioka, M. Antonietti, J. Kubota, K. Domen, *Chem. Comm.* **2010**, *46*, 7492–7494.

26 Y. Fukasawa, K. Takanabe, A. Shimojima, M. Antonietti, K. Domen, T. Okubo, *Chem. --Asian J.* **2011**, *6*, 103–109.

27 Fischer, J.O. Müller, M. Antonietti, A. Thomas, *ACS Nano* **2008**, *2*, 2489–2496.

28 Fischer, M. Antonietti, A. Thomas, *Adv. Mater.* **2007**, *19*, 264–267.

29 Y. Zhao, Z. Liu, W. Chu, L. Song, Z. Zhang, D. Yu, Y. Tian, S. Xie, L. Sun, *Adv. Mater.* **2008**, *20*, 1777–1781.

30 J.R. Holst, E.G. Gillan, *J. Am. Chem. Soc.* **2008**, *130*, 7373–7379.

31 G. Zhang, J. Zhang, M. Zhang, X. Wang, *J. Mater. Chem.* **2012**, 8083–8091.

32 V. Khabashesku, J. Zimmerman, J. Margrave, *Chem. Mater.* **2000**, *12*, 3264–3270.

33 X. -a. Zhao, C.W. Ong, Y.C. Tsang, Y.W. Wong, P.W. Chan, C.L. Choy, *Appl. Phys. Lett.* **1995**, *66*, 2652–2654.

34 M.J. Bojdys, J.-O. Müller, M. Antonietti, A. Thomas, *Chem. --Eur. J.* **2008**, *14*, 8177–8182.

35 Y. Wang, A. Mebel, C. Wu, *J. Chem. Soc., Faraday Trans.* **1997**, *93*, 3445–3451.

36 Jürgens, E. Irran, J. Senker, P. Kroll, H. Müller, W. Schnick, *J. Am. Chem. Soc.* **2003**, *125*, 10288–10300.

37 V. Zeitler, C. Brown, *J. Phys. Chem.* **1957**, *61*, 1174–1177.

38 J. Chen, K. Takanabe, R. Ohnishi, D. Lu, S. Okada, H. Hatasawa, H. Morioka, M. Antonietti, J. Kubota, K. Domen, *Chem. Comm.* **2010**, *46*, 7492–7494.

39 H. Zhao, M. Lei, X. Yang, J. Jian, X. Chen, *J. Am. Chem. Soc.* **2005**, *127*, 15722–15723.

40 L. Yuliati, J.-H. Yang, X. Wang, K. Maeda, T. Takata, M. Antonietti, K. Domen, *J. Mater. Chem.* **2010**, *20*, 4295–4298.

41 O. Klejnot, *Inorg. Chem.* **1965**, *4*, 1668–1670.

42 A.S. Kurlov, A.I. Gusev, *Russ. Chem. Rev.* **2006**, *75*, 617–636.

43 J.I. Langford, A.J.C. Wilson, *J. Appl. Crystall.* **1978**, *11*, 102–113.

44 L. Leclercq, A. Almazouari, M. Dufour, G. Leclercq, *The Chemistry of Transition Metal Carbides and Nitrides*, Blackie Academic And Professional, Glasgow, UK **1996**.

45 L. Leclercq, M. Provost, H. Pastor, J. Grimblot, A.M. Hardy, L. Gengembre, G. Leclercq, *J. Catal.* **1989**, *117*, 371–383.

46 T. Xiao, A. Hanif, A.P.E. York, J. Sloan, M.L.H. Green, *Phys. Chem. Chem. Phys.* **2002**, *4*, 3522–3529.

47 M.C. Weidman, D.V. Esposito, Y.-C. Hsu, J.G. Chen, *J. Power Sources* **2012**, *202*, 11–17.

48 N. Markovic, B. Grgur, P. Ross, *J. Phys. Chem. B* **1997**, *5647*, 5405–5413.

49 A.J. Bard, L.R. Faulkner, *Electrochemical Methods Fundamentals and Applications*, John Wiley & Sons, New York, US **2001**.

50 S.N. Pronkin, A. Bonnefont, P.S. Ruvinskiy, E.R. Savinova, *Electrochim. Acta* **2010**, *55*, 3312–3323.

51 Wieckowski, J.K. Nørskov, *Fuel Cell Science Theory, Fundamentals and Biocatalysis*, John Wiley & Sons Inc., New Jersey, US **2010**.

52 J. Thomas, *Trans. Faraday Soc.* **1961**, *57*, 1603–1611.

53 J.O.M. Bockris, I.A. Ammar, A.K.M.S. Huq, *J. Phys. Chem.* **1957**, *61*, 879–886.

54 T. Shinagawa, A. T. Garcia-Esparza, K. Takanabe, *Sci. Rep.,* **2015**, 5, 13801.

55 S.J. Yoo, H.-Y. Park, T.-Y. Jeon, I.-S. Park, Y.-H. Cho, Y.-E. Sung, *Angew. Chem.* **2008**, *120*, 9447–9450.

56 J. Barber, S. Morin, B.E. Conway, *J. Electroanal. Chem.* **1998**, *446*, 125–138.

57 Merki, H. Vrubel, L. Rovelli, S. Fierro, X. Hu, *Chem. Sci.* **2012**, *3*, 2515–2525.

58 K. Takanabe, K. Domen, *ChemCatChem* **2012**, *4*, 1485–1497.

59 H. Kato, K. Asakura, A. Kudo, *J. Am. Chem. Soc.* **2003**, *125*, 3082–3089.

60 Y. Miseki, H. Kato, A. Kudo, *Energy Environ. Sci.* **2009**, *2*, 306-314.

61 Y. Inoue, *Energy Environ. Sci.* **2009**, *2*, 364–386.

CHAPTER 4

4. Thermally Oxidized Copper for Efficient Solar Fuel Production[c]

This chapter discusses the use of a facile and highly scalable synthesis process to control growth products of earth-abundant Cu-based oxides and their application in relevant photoelectrochemical and electrocatalytic solar systems. Characterizations of the synthesized Cu(I)/Cu(II) oxides indicate that their surface morphology and chemical composition can be simply tuned by varying two synthesis parameters (time and temperature). UV-Vis spectroscopy and impedance spectroscopy studies are performed to estimate the band structures and electronic properties of these *p*-type semiconductor materials. Photoelectrodes made of Cu oxides possess favorable energetic band structures for hydrogen production from water; the position of their conduction band is ≈ 1 V more negative than the water-reduction potential. High acceptor concentrations on the order of 10^{18}-10^{19} cm^{-3} are obtained, producing large electric fields at the semiconductor-electrolyte interface. The highly crystalline pristine samples used as photocathodes in photoelectrochemical cells exhibit high photocurrents under AM 1.5G simulated illumination.

[c] This chapter was reproduced from A. T. Garcia-Esparza, K. Limkrailassiri, F. Leroy, S. Rasul, W. Yu, L. Lin, K. Takanabe, *J. Mater. Chem. A*, **2014**, 2, 7389–7401.

4.1. Introduction

The sustainable creation of fuels from solar power is a promising renewable-energy technology that harnesses sunlight for the production of hydrogen/hydrocarbon from water/CO_2 feedstock *via* the photocatalytic dissociation of water and the (photo)-electrocatalytic reduction of CO_2, respectively.[1] Growing interest in solar energy has arisen from global concern over depleting fossil-fuel reserves and irreparable damage to the environment caused by greenhouse-gas emissions. Among all forms of solar energy, water splitting has the advantage of capturing sunlight, an intermittent energy resource, and storing it in the form of a chemical bond, H_2, which can be burned and utilized as electricity on demand.[2,3] Moreover, the wide-scale implementation of solar and other renewable sources of energy requires an improved means of energy storage, such as the reduction of CO_2 to CO or energy-rich hydrocarbons.[4] CO_2 must be introduced as a key component in the value chain of chemical industries.[5,6] For solar fuel production to provide a clean, abundant source of renewable energy that is also competitively priced compared to current energy resources, scalable processing methods and earth-abundant starting materials will be required.[2]

To this end, metal-oxide semiconductors have emerged as desirable materials for the working electrodes in photoelectrochemical (PEC) cells and as catalysts for (photo)-electrochemical CO_2 reduction.[4,7] Of the metal oxides, cuprous oxide (Cu_2O) has gained particular attention for PEC water splitting because of the earth abundance of the metal.[8] Generally, Cu_2O exhibits *p*-type

semiconductivity with a reported 2.0 eV direct band gap, making this material highly attractive as a photocathode for the direct generation of hydrogen from water.[9] On the basis of its band-gap energy, Cu_2O has a maximum conversion efficiency of 18% and a maximum theoretical photocurrent of 14.7 mA cm^{-2}.[10] Paracchino *et al*. have reported a photocurrent for Cu-oxide-based photoelectrodes of −7.6 mA cm^{-2} at 0 V *vs*. a reversible hydrogen electrode (RHE) using electrodeposited Cu_2O and protected the photocathode with carefully tuned oxide multi-layers of ZnO (4 nm) and Al_2O_3 (0.17 nm) followed by an 11 nm TiO_2 film decorated with a Pt cocatalyst. Although a significant contribution to the reported photocurrents in the literature originates from the reduction of Cu_2O, they and others have proved that when a protection strategy was applied, significant amounts of hydrogen were generated by the oxide photocathode.[8,11] The synthesis of Cu_2O photocathodes is generally achieved through electrochemical deposition methods,[10,12,13] physical deposition techniques,[14,15,16] the electrochemical anodization of Cu,[17,18] and solution-phase methods.[19,20] However, the reliable, scalable and mass-producible synthesis of high-quality *p*-type semiconductors that can efficiently drive the half-reaction of hydrogen production remains an important challenge.[21]

In this section, the use of a facile synthesis procedure is presented to make highly crystalline *p*-type Cu_2O semiconductors by thermal oxidation of copper foils with and without CuO nanowires on their surfaces. In these composite materials, the semiconductor is in intimate ohmic contact with the Cu substrate. Understanding the intrinsic nature of the copper-based composites synthesized in

this manner is the main focus of the chapter, which have attracted tremendous interest for potential scalable applications. It is essential to understand the redox properties and the semiconductive nature of these Cu-oxide-based composites. Systematic studies were conducted using electrochemical characterizations, PEC measurements and impedance spectroscopy. In the PEC measurements, the pristine, as-processed planar Cu-oxide-based semiconductor photocathodes achieved high photocurrents under simulated air-mass 1.5 global irradiation (AM 1.5G). Remarkably, the sample produced at higher temperature (500°C, 2h) exhibited onset potentials of approximately 0.8 V *vs*. RHE generating ≈ 1 mA cm^{-2} photocurrents at a positive potential of 0.5 V *vs*. RHE. Furthermore, the synthesis of the photocathodes was highly reproducible because of the simplicity of the synthesis procedure, fulfilling a prerequisite for the possibility of high-yield mass production in the future.

4.2. Results and discussion

4.2.1. Bulk characterization

Cu-based electrodes were prepared from high-purity Cu foil with a 25 μm thickness, which was cut into samples of 1.0 cm by 3.0 cm, cleaned and subjected to different thermal-oxidation treatments. The representative electrodes are further discussed below, and they were prepared using three different time and temperature combinations during oxidation: 300°C for 0.5 h (henceforth referred to as the “red” samples for convenience), 300°C for 10 h (“deep red”) and 500°C

for 2 h (“black”). The cross-sectional and top-view SEM micrographs of the red sample are shown in Figure 4.1a and 4.1d (also see Figure 4.2a and 4.2b).

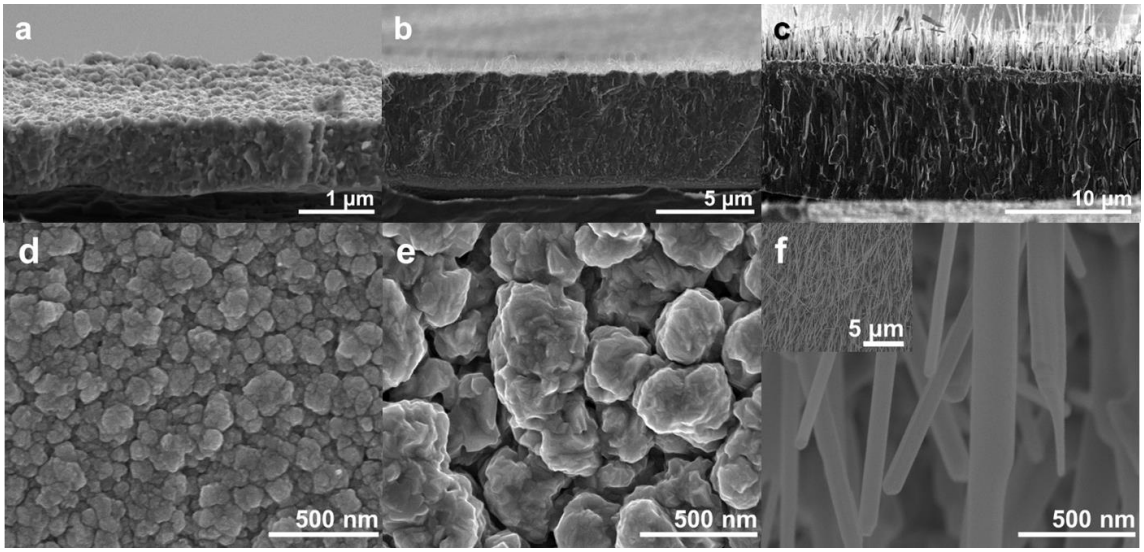

Figure 4.1 The top and cross-sectional SEM views of (a, d) the red sample treated at 300°C for 0.5 h, (b, e) the deep red sample treated at 300°C for 10 h and (c, f) the black sample treated at 500°C for 2 h.

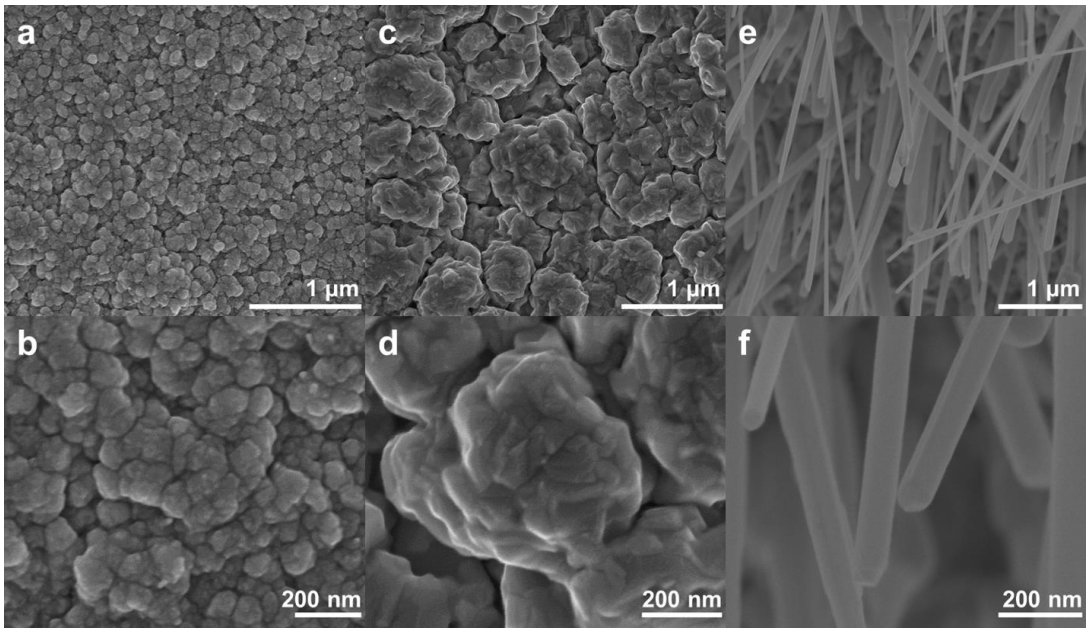

Figure 4.2 SEM top view of the pristine (a, b) red, (c, d) deep red and (e, f) black samples.

The granular surface contains particles ranging from 100 to 300 nm in diameter. Grains with a similar diameter can be observed in the cross section along with voids interspersed between the grains. This layer was confirmed to be Cu_2O on the basis of the X-ray diffraction (XRD) pattern shown in Figure 4.3.

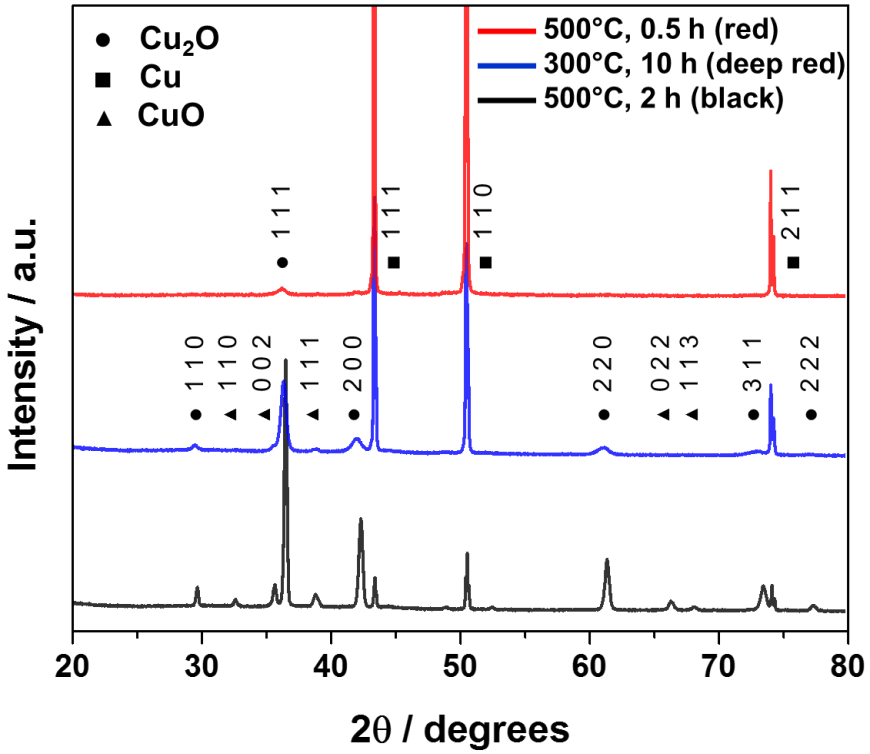

Figure 4.3 XRD diffractograms of samples treated under different thermal-oxidation conditions, coded as the red, deep red and black samples

The thickness of the Cu_2O layer in the red sample was estimated to be 1 μm. Increasing the oxidation time from 0.5 to 10 h expanded the diameters of the surface particles to 400 to 1000 nm and led to the formation of more crystalline and void- free Cu_2O (Figure 4.1b, 4.1e, 4.2c and 4.2d). This treatment also led to

the onset of CuO growth, as indicated by the nanowire structures on the Cu_2O surface in Figure 4.1b. The cupric oxide phase was also confirmed *via* XRD and X-ray photoelectron spectroscopy (XPS, *vide infra*). The CuO nanowire growth on the deep red sample is sparse compared to the black samples, whose top views are shown in Figure 4.1f, 4.2e and 4.2f. The significant increase in CuO-nanowire growth at 500°C is consistent with other reports that such growth has been observed throughout the oxidation-temperature range of 500 to 700°C.[25] In the black sample, the nanowires average 8 μm in length and 50 to 150 nm in diameter. A ~400 nm layer of CuO at the base of the nanowires can be distinguished from the darker underlying Cu_2O in the cross section of the black sample shown in Figure 4.1f. The thickness of the Cu_2O layer increases from 1 μm (red) to ≈ 5 μm (deep red) to ≈ 10 μm (black). The weak CuO signals in the XRD pattern of the deep red and black samples, despite the highly dense growth of CuO nanowires on the latter, are attributed to the presence of a much thicker and more space-efficient Cu_2O layer. As expected, the XRD peaks display a decrease in the Cu signals and an increase in the Cu_2O signals while transitioning from the red sample to the deep red to the black (Figure 4.3). This observation is in agreement with the increased Cu consumption and conversion to Cu_2O observed with increasing oxidation time and temperature. The sharp Cu_2O (111) peak, the tallest of all the Cu_2O signals, suggests that the Cu_2O layer is highly crystalline and that this orientation was maximized. The (111) orientation has been reported to offer better hole collection efficiency, lower resistivity and higher carrier concentrations than (100)-oriented films.[26]

4.2.2. The surface of oxidized copper

XPS was used to study the surface state of the pristine samples. Figure 4.4 presents the XPS spectra recorded for the oxidized Cu electrodes. The signals were corrected using the adventitious carbon peak C 1s at 284.8 eV as the reference. There were clear similarities in the analysis of the Cu 2p region for all samples, even though the thermal-oxidation treatment clearly affected the surface morphology and the oxide phase of the Cu-based materials, as first observed *via* SEM and indicated by the XRD results. In Figure 4.4a, the Cu 2p peaks are broad, thus making the unambiguous assignment of the oxidation states of Cu challenging. However, it is apparent that the surface contains mixed-valence higher oxidation states. The XPS signal of the red sample, in which the bulk XRD result shows no signs of CuO, exhibits broad Cu $2p_{3/2}$ and Cu $2p_{1/2}$ peaks with maxima at 933.9 and 953.8 eV, respectively, along with satellite peaks at 941.7, 944.4 and 963.0 eV.

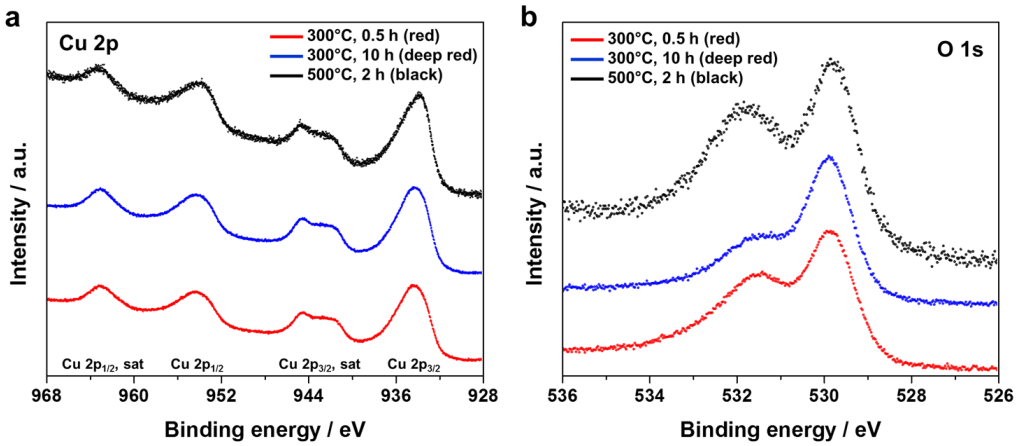

Figure 4.4 Core-level Cu 2p (a) and O 1s (b) XPS spectra for the pristine Cu-based samples.

In fact, all of the samples reveal similar peak-maximum positions with an uncertainty of ±0.1 eV. The peaks located at 933.9 and 953.8 eV are assigned to the binding energies of Cu $2p_{2/3}$ and Cu $2p_{1/2}$, respectively, from Cu^{2+} on the surface.[27] Nevertheless, Cu^{+} with a reported doublet for Cu_2O located at 932.7 and 952.5 eV from Cu $2p_{2/3}$ and Cu $2p_{1/2,}$ respectively, could explain the broadness of the observed peaks in these energy regions.[28,29] The detected satellite peaks at 941.7, 944.4 and 963.0 eV are in good agreement with the values reported in the literature, suggesting a partially filled Cu $3d^9$ shell, which confirms the presence of CuO on the surfaces of all electrodes.[29,30] In the red sample, Cu^{2+} may be present as a native cupric oxide layer that forms under the atmospheric conditions in which the sample was treated and subsequently exposed to air prior to the XPS measurement. This native oxide has been commonly reported to be 2 nm in thickness.[8] The subtle shoulder and the observed broadness toward higher binding energies for the Cu $2p_{3/2}$ signal of the black sample may be assigned to $Cu(OH)_2$ on the surface, which has a reported maximum of 934.7 eV. The formation of CuO nanowires was observed *via* SEM and confirmed with XRD for the deep red and black samples, and this finding is in agreement with the signals obtained from the Cu 2p XPS spectrum. Nevertheless, Auger spectra is needed to unambiguously resolve the chemical state of the Cu species on the surface. The O 1s core-level XPS signal is presented in Figure 4.4b. Two broad peaks can be clearly identified for the samples, with apparent maxima at 529.9 and 531.5 eV. The former is assigned to CuO, and the latter, which has an extended broadness to 531.8 eV, can be attributed to ionically bonded hydroxide oxygen.[29] The O 1s signal for Cu_2O

is generally found at 530.5±0.2 eV in the literature and may explain the broadness of the peak observed for all samples in Figure 4.4b.[29] The black sample exhibited a relatively broader O 1s peak at higher binding energies (≈ 531.5 eV), most likely caused by the overlapping signals attributed to chemisorbed water, chemisorbed hydroxyl oxygen and hydroxide oxygen.[27,29]

Based on the bulk and surface characterizations, the Cu substrates are oxidized primarily to Cu_2O at temperatures below 400°C. Although a very thin native CuO layer forms at low temperatures in air, as revealed *via* XPS, a longer and more severe thermal-oxidation treatment (>500°C) promotes the growth of a CuO layer on the surface of the Cu_2O, as indicated by the XRD, XPS and SEM observations. The growth of this layer may be kinetically limited, and the slow rate of formation of CuO ensures a low vapor pressure of the Cu(II) phase, thus creating nanowires with uniform diameters (Figure 4.2f).[25] Based on the XPS and XRD results, the nanowires were confirmed to be CuO with a plausible $Cu(OH)_2$ layer on their surfaces.

4.2.3. Optoelectronic properties

To the naked eye, the surfaces of the black samples are far less reflective than those of the red and deep red samples; the black samples exhibit a dark, velvet-like appearance. UV-Vis diffuse reflectance spectra were transformed into the Kubelka-Munk function, as shown in Figure 4.5, revealing estimated band-gap energies of 2.07, 1.45 and 1.42 eV for the red, deep red and black samples, respectively (see the Tauc plots in Figure 4.5b and 4.5c).

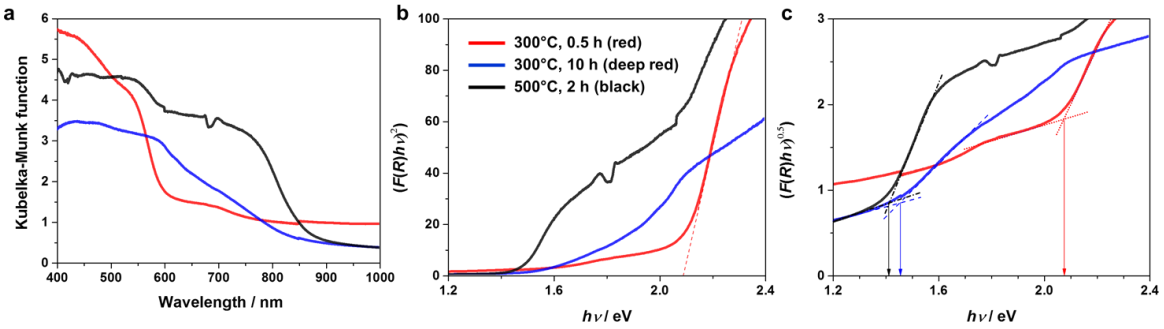

Figure 4.5 Diffuse reflectance UV-Vis spectroscopy results transformed into the Kubelka-Munk function for the Cu-based red, deep red and black samples (a). Allowed direct band gap (b) and allowed indirect band gap (c) Tauc plots of the Cu-oxide-based materials obtained using the Kubelka-Munk radiative-transfer model assuming that $F(R)$ is proportional to the absorption coefficient

The estimated band gaps are in agreement with the reported values for Cu_2O (2.0 eV) and CuO (1.4 eV).[8,10,12,31] The Tauc plots suggest the existence of an allowed direct transition near 2.08 eV for the red sample, which is assigned to Cu_2O and is in good agreement with the literature (Figure 4.5b).[10] The black sample exhibited a downward slope that is steeper than the slope of the deep red sample when the Tauc plot was analyzed in allowed-indirect-transitions mode (Figure 4.5b), which could possibly be attributed to the dense CuO on the surface of the black sample and is consistent with reports of CuO characterized as an indirect-band-gap *p*-type semiconductor.[14,32,33] The literature contains both allowed and forbidden direct transitions along with allowed indirect transitions near 2.0 eV for Cu_2O, in reasonable agreement with these results.[3] Compared to the deep red and black samples, the red sample has a large background irrespective of the wavelength, most likely originating from a thicker underlying Cu layer as a

result of the shorter oxidation time. Cu is reflective at long wavelengths, and therefore, photons are given additional opportunities to be absorbed by Cu_2O upon reflection from the Cu layer. At short wavelengths, Cu is absorptive, so the large Kubelka-Munk function can be attributed to absorption by both Cu_2O and Cu.

4.2.4. Electrochemical redox properties

The electrochemical behavior of the Cu-based electrodes treated at different conditions was evaluated in 0.1 M sodium acetate electrolyte (pH 7.9) at 5 mV s^{-1}, and the results of two consecutive cycles are presented in Figure 4.6 for the red, deep red and black samples. Cyclic voltammetry (CV) experiments were used to evaluate the stability of the oxides under various applied potentials. When the potential range of the CV was limited from 0.5 to 0.8 V *vs*. RHE, no significant faradic currents were detected, and only double-layer capacitance was observed for all samples (black lines in Figure 4.6). The CV results for the red sample are shown in Figure 4.6a; when the studied potential window was sufficiently large, three faradic processes were observed (AI, RI and RIII). The CV was performed beginning from the open-circuit potential of the electrode and progressing toward more reducing conditions, and a cathodic signal appeared at potentials just above 0 V *vs*. RHE (RIII). Based on the SEM, XPS and XRD results, we assigned this cathodic current to the reduction of the relatively thin Cu_2O layer on the surface of the Cu electrode. This reduction wave is consistent with the literature.[8,34]

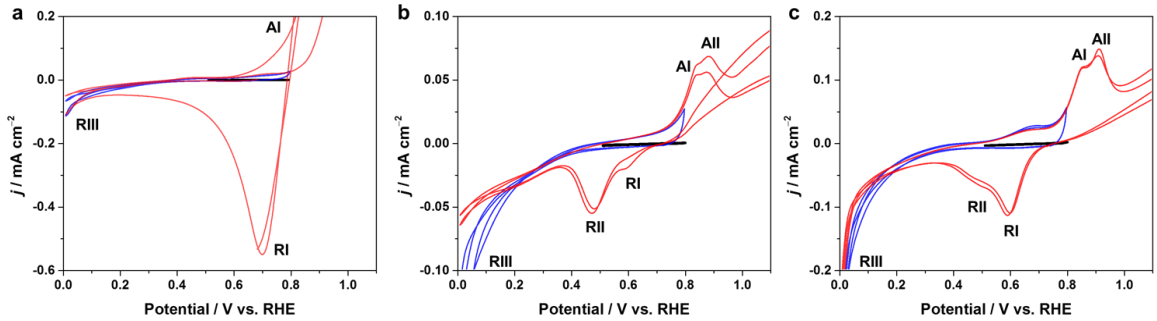

Figure 4.6 Current-potential characteristics of the (a) red, (b) deep red and (c) black samples in the dark from the second and third cycles of the cyclic voltammetry experiments. A potential range limited to 0.5-0.8 V (black lines), 0.0-0.8 V (blue lines) or 0.0-1.2 V *vs*. RHE (red lines) was applied to study the redox reactions in the samples. (0.1 M sodium acetate, pH 7.9, 5 mV s^{-1}, Ar saturated).

$$Cu_2O + H_2O + 2e^- \leftrightarrow 2Cu + 2OH^-$$

$$E° = 0.46 \text{ V } vs. \text{ SHE} \qquad (5.1)$$

When the scanning direction was shifted toward more positive potentials, anodic processes were observed starting at 0.8 V *vs*. RHE. The polarization curve exhibited a broad anodic wave; this anodic current was attributed to the oxidation of metallic copper. Moreover, the broad anodic redox peak was not unambiguously resolved; thus, the simultaneous formation of cuprous oxide and cupric oxide and the possible dissolution of Cu^{2+} into solution were also considered.[35,36]

$$Cu_2O + H_2O \leftrightarrow 2CuO + 2H^+ + 2e^-$$

$$E° = 0.67 \text{ V } vs. \text{ SHE} \qquad (5.2)$$

$$Cu_2O + 3H_2O \leftrightarrow 2Cu(OH)_2 + 2H^+ + 2e^-$$

$$E° = 0.73 \text{ V } vs. \text{ SHE} \qquad (5.3)$$

On the next cycle, a new cathodic peak appeared centered at ≈ 0.7 V *vs*. RHE. The broad peak in Figure 4.6a (RI) may be assigned to the simultaneous reduction of both cuprous oxide and copper hydroxide to Cu_2O.[13,34] When the anodic scan was limited to 0.8 V *vs*. RHE (blue line in Figure 4.6a), the broad cathodic redox peak RI observed at ≈ 0.7 V *vs*. RHE disappeared. Only the reduction process at ≈ 0.1 V *vs*. RHE was detected (RIII), indicating that neither the formation of CuO nor the dissolution of copper occurred, and only the reduction of the Cu_2O layer was observed.[8] Figure 4.6b and 4.6c represent the CV experiments performed on the deep red and black samples, respectively. Note that the surfaces of the deep red and black samples are composed of two or three phases: Cu_2O and $CuO/Cu(OH)_2$, as previously discussed and confirmed *via* SEM, XRD, XPS and UV-Vis. The voltammograms obtained for both samples exhibit similar features, with two main anodic and two main cathodic redox peaks (AI, AII, RI and RII). For the anodic scan, the peak positions for both samples are the same: 0.85 (AI) and 0.90 (AII) V *vs*. RHE. Similarly, the positions of the cathodic peaks are the same for both samples: 0.59 (RI) and 0.49 (RII) V *vs*. RHE. This result may be an indication that the same redox reactions are occurring in both samples. When the potential scan of the deep red and black samples was limited to between 0 and 0.8 V *vs*. RHE, only the reduction wave RIII was observed (blue lines in Figure 4.6b and 4.6c). Nakayama *et al*. recently developed an electroanalytical method of elucidating the reduction mechanism of copper oxides using a strongly

alkaline electrolyte.[37,38] They proved that under strong and weak alkaline conditions, the reduction of both oxides followed the same trend, in which the reduction of CuO was followed by the reduction of Cu_2O in one step toward the metallic state. It is therefore important to note the possibility of a one-step reduction for both Cu_2O and CuO in RIII (Equation 5.1 and 5.4).

$$CuO + H_2O + 2e^- \leftrightarrow Cu + 2OH^- \quad (5.4)$$

Large cathodic and anodic waves were detected at potentials more negative than 0.2 V *vs*. RHE and more positive than 1.0 V *vs*. RHE. As previously discussed, the former is assigned to the reduction of the copper oxides and the latter to the oxidation of Cu_2O.[8] Under the studied pH conditions, the third large anodic wave at high positive potentials has been attributed in the literature to the dissolution of Cu_2O, the probable formation of a metastable Cu_2O_3 phase just before oxygen evolution, or the plausible formation of a hydrated-polymeric form of cupric oxide.[35,39–41] The AI peak is assigned to the electro-oxidation of Cu metal and the formation of hydrous Cu_2O (the reverse reaction of Equation 5.1).[40] The AII peak is associated with the formation of complex hydrous CuO, most likely resulting in a duplex structure and forming a passive layer of $Cu(OH)_2$ on the surface of the sample (Equations 5.2 and 5.3).[40,41] The RI and RII peaks are assigned to the reduction of CuO (the reverse reaction of Equation 5.2) and the electrodeposition of Cu_2O from dissolved Cu^{2+} ions, respectively. The RI peak is in good agreement with the previously reported electrochemical characterizations of Cu_2O thin films obtained through electrodeposition.[8,42] There is a difference in the RI and RII reduction peaks between the deep red and black samples. The RI peak from the

deep red electrode is smaller than the one observed for the black electrode. The opposite is observed for the R2 peak, where the area of the peak in the deep red sample is larger than the one recorded for the black sample. This result most likely arises because the black sample contains a larger amount of CuO on the surface, whereas in the deep red sample, Cu_2O may be exposed to the electrolyte (as indicated by the SEM and XPS results). Therefore, in the deep red sample, the oxidation of Cu_2O generates a higher concentration of Cu(II) cations dissolved in the electrolyte, increasing the charge of RII. The $CuO/(CuOH)_2$ in the black sample may function as a passivation layer reducing the dissolution process, and because the amount of CuO is larger, the RI redox peak for the reversible Equations 5.3 and 5.4 is more prominent, forming more Cu_2O from CuO.

4.2.5. Mott-Schottky analysis

Electrochemical impedance spectroscopy (EIS) was used to characterize the flat-band potentials of the samples and to estimate their intrinsic acceptor densities. A frequency scan from 0.01 Hz to 100 kHz at a fixed potential of 0.55 V *vs*. RHE produced depressed semicircles in the Nyquist plot. Thus, a modified Randles circuit using a constant-phase element was used to study the semiconductor-electrolyte interface.[43] The Mott-Schottky analysis was performed by sweeping the potential at fixed high frequencies with amplitude of 10 mV (1-100 kHz). The space-charge capacitance of the semiconductor was obtained from the imaginary part of the impedance, and the Mott-Schottky plots are presented in Figure 4.7. According to the Mott-Schottky equation, a linear fit produces a slope

that can be used to approximate the majority-charge-carrier concentration, and by extrapolation, one can estimate the flat-band potential of the system.[10,43]

$$\frac{1}{C^2} = \frac{2}{qA^2\varepsilon_r\varepsilon_0 N_a}(V - V_{fb} - \frac{k_B T}{q}) \qquad (5.6)$$

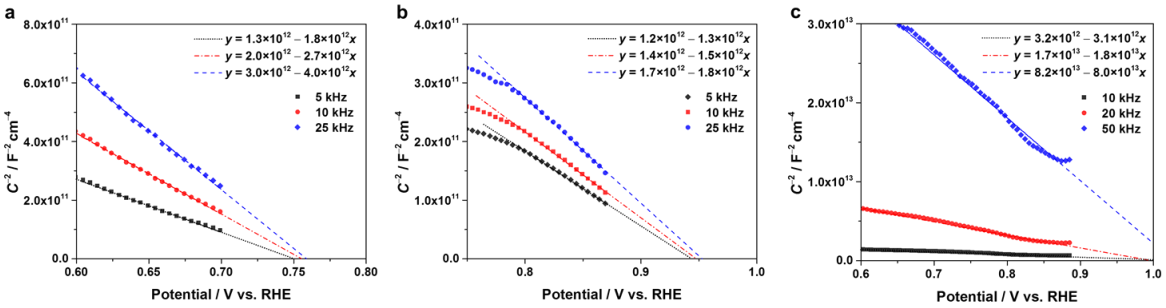

Figure 4.7 Mott-Schottky plots of red (a), deep red (b) and black (c) samples using a sinusoidal AC signal superimposed over the studied potential range with amplitude of 10 mV at high frequencies. (1-100 kHz, 0.1 M sodium acetate, pH 7.9, Ar saturated).

C is the interfacial capacitance and V is the applied potential. Here, the constant A is the area, ε_r is the dielectric constant of the semiconductor, ε_0 is the permittivity of vacuum, T is the absolute temperature, q is the electronic charge, and k_B is the Boltzmann constant. As shown in Figure 4.7, a plot of C^{-2} versus potential may yield a straight line from which the flat-band potential (V_{fb}) and the carrier concentration (N_a) can be extracted. Based on the Mott-Schottky slopes, the samples demonstrated the characteristic *p*-type character of the oxide layers.[33,44] The extrapolated flat-band potentials are 0.75, 0.94 and 1.1 V *vs*. RHE for the red, deep red and black electrodes, respectively. For the red and deep red samples, minor frequency dependence can be observed from the slopes of the linear fits. This negligible effect most likely originates from contributions from the

double-layer capacitance at the interface.[43] Nevertheless, for a dielectric constant of $\varepsilon_{r(\infty)}$ = 6.6 for Cu_2O,[45] the carrier concentration can be reasonably estimated to be on the order of 10^{18} and 10^{19} cm^{-3} at high frequencies for the red and deep red samples, respectively. Based on the above estimations, it was possible to compute the maximum attainable electric field ($E_{\max}$) and the width of the space-charge region (W_D).[46]

$$E_{\max} = \frac{qN_aW_D}{\varepsilon_r\varepsilon_0} \tag{5.7}$$

For the red sample, the calculations estimate a depletion width of 18 nm with an electric field of 8×10^5 V cm^{-1}. When the oxidation temperature increases (i.e., the deep red sample) the width of the space-charge layer is reduced to 7 nm, accompanied by an increase in the electric field to 3×10^6 V cm^{-1}. Assuming an effective hole mass of 0.58 m_0,[47] I was able to estimate the effective density of states for holes at the top of the valance band, N_V.[46] The computed acceptor concentration places the Fermi level at 61 and 2 meV above the valance band for the red and deep red samples, respectively. Based on the optical spectra, a 2.0 eV band gap was assumed for the Cu_2O layer and placed the conduction band and valence band at −1.26 and 0.81 V *vs*. RHE, respectively, for the red sample. The relative band positions of the deep red sample are −1.13 and 0.94 V *vs*. RHE for its conduction and valence bands, respectively. These results demonstrate that the position of the conduction band of the composites is more negative (relative to the water-reduction potential) than is generally reported in the literature for electrochemically deposited copper oxides. In the case of the black sample (Figure

4.7c), there is a significant frequency dependence, which indicates that the rudimentary Randles circuit model may be insufficient to describe the complex interface found in this electrode.[3]

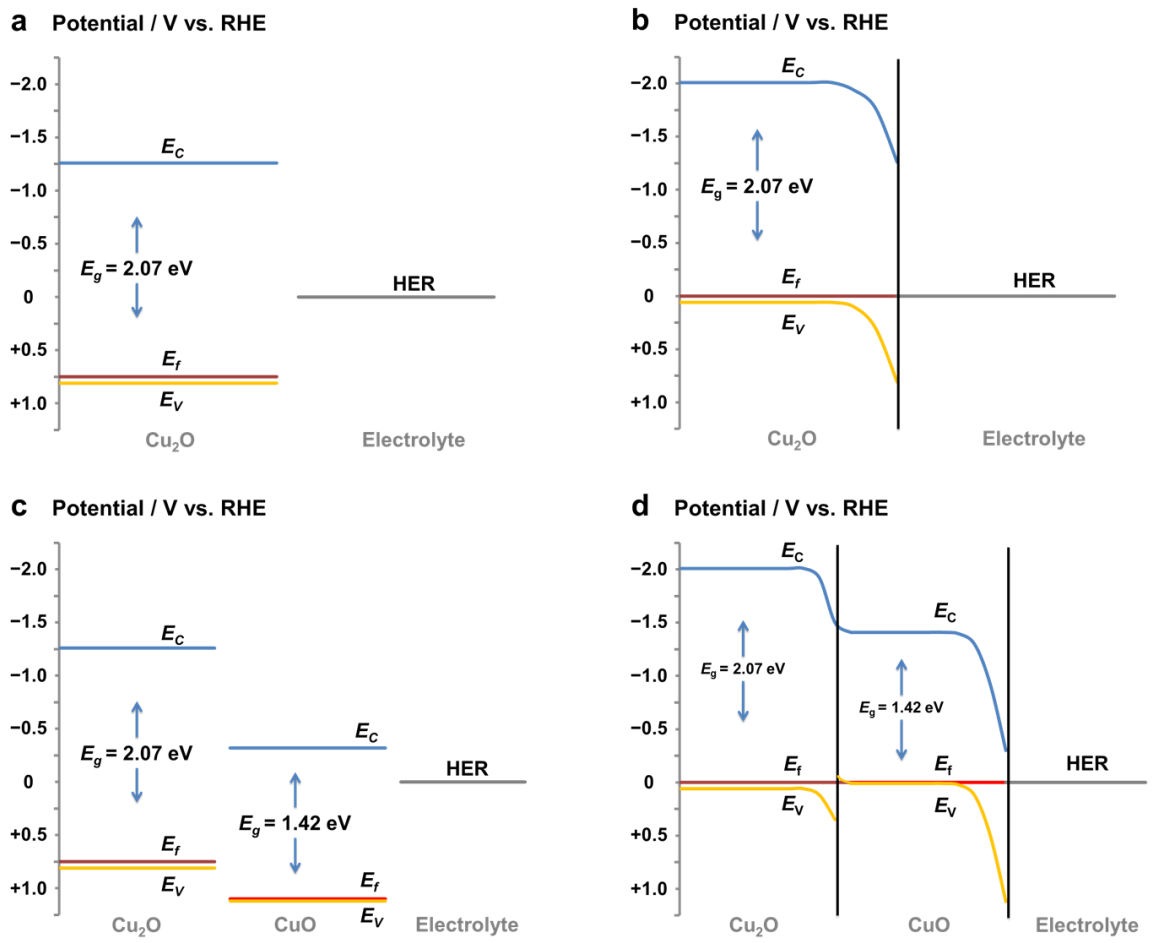

Figure 4.8 Calculated representation of the ideal energy-band diagram for the red (a, b) and black samples (c, d) before contact (a, c) and for the photocathodes biased at 0 V vs. RHE in the dark in contact with an electrolyte (b, d). A band-edge-pinning assumption was employed to schematically illustrate the band bending at the interface, taking the electrochemical potential of the solution to be the standard potential of the hydrogen evolution reaction (HER) and built-in potentials at the interfaces as the difference in Fermi levels.

I can reasonably speculate that this sample may contain a larger density of low-energy surface/trap states, which generate localized levels in the forbidden region of the band gap.[48] Moreover, the high aspect ratio of the CuO nanowires on the black sample may introduce a significant double-layer capacitance component, making the calculation of the carrier density difficult. However, the Mott-Schottky results presented in Figure 4.7 display a similar trend: the fitted lines have different slopes at different frequencies, but all of the signals converge to the same flat-band potential intercept. Hence, these results may yield accurate values for the extrapolation of flat-band conditions and reasonable carrier-concentration trends for the composite materials.[3] As mentioned before, the extrapolated flat-band potentials for the black samples are greater than 1 V *vs*. RHE (1.1±0.1 V *vs*. RHE), most likely as a result of the top ≈ 400 nm thick CuO layer at the interface. The obtained V_{fb} is in reasonable agreement with the values reported in the literature for CuO in contact with alkaline electrolytes.[44] Furthermore, this result implies the probable formation of a staggered *p-P* heterojunction in the black sample. Figure 4.8 presents an estimated energy-band diagram based on the above results.

4.2.6. Photoelectrochemistry of p-type semiconductors

The photoelectrochemical (PEC) characterization of the samples was evaluated in a three-electrode single-compartment cell with a Pt wire and an Ag/AgCl (saturated KCl) electrode as the counter and reference electrodes, respectively.

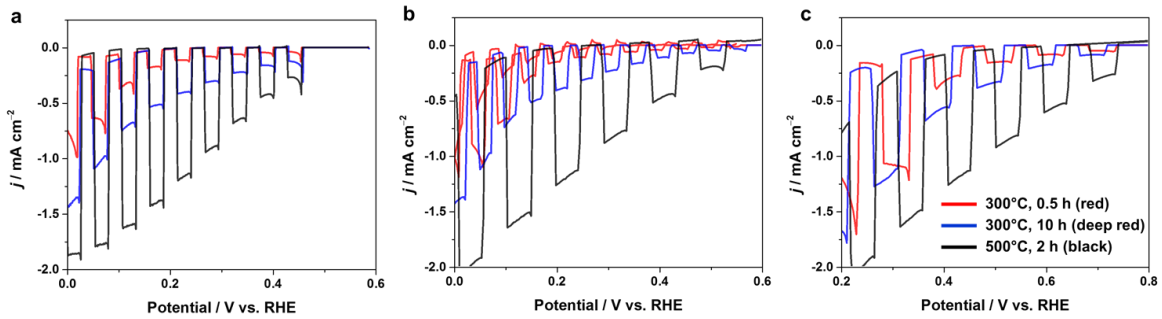

Figure 4.9 Photoelectrochemical characterizations of red, deep red and black samples under simulated AM 1.5G solar irradiation at pH 4.9 (a), pH 6.1 (c) and pH 10.1 (e). LSV under chopped illumination for the monitoring of the dark currents and photocurrents (0.5 M Na_2SO_4, 10 mV s^{-1}, Ar saturated).

Figure 4.9 presents the PEC current-potential characteristics of the samples under simulated AM 1.5G chopped illumination in a 0.5 M Na_2SO_4 electrolyte under various pH conditions. The cathodic photocurrents were recorded for all samples and imply that the system exhibits band bending and a *p*-type nature, which is in agreement with the Mott-Schottky results and is attributed to the photo-assisted redox reactions at the semiconductor-electrolyte interface. The onset potentials of the photo-response of the samples at pH 4.9 (Figure 4.9a), pH 6.1 (Figure 4.9b) and pH 10.1 (Figure 4.9c) were estimated *via* extrapolation to be approximately 0.5, 0.6 and 0.8 V *vs*. RHE, respectively. Based on the impedance measurements, this trend is consistent with the observed increase in the flat-band potential position with increasing thermal-oxidation treatment.

For a *p*-type photocathode, there is charge depletion at the electrolyte interface that produces band bending and transport of photoexcited electrons to the surface and holes into the bulk, toward the external circuit through the back

contact and, finally, to the counter electrode, which drives the oxidation reaction.[10] Therefore, the extracted cathodic photocurrents may originate from photoexcited electron-hole pairs probably separated by the electric field generated due to the heterojunction shown in Figure 4.8, and due to the semiconductor-electrolyte interface. At pH 10.1 and 6.1, the red and deep red samples exhibited similar responses at potentials close to 0 V *vs*. RHE (Figure 4.9b and 4.9c), whereas the black sample outperformed the other samples under all pH conditions. The largest photocurrents at pH 4.9 were recorded for the black and deep red samples, with average values of 1.8 and 1.4 mA cm^{-2}, respectively, under simulated solar illumination at 0 V *vs*. RHE. It is interesting to note that at pH 10.1, cathodic photocurrents of ≈ 1 mA cm^{-2} were observed from the black sample at positive potentials as high as 0.5 V *vs*. RHE. It is remarkable that in the absence of a cocatalyst (e.g., Pt), the reported photocurrents in the literature were generally found to be only several microamperes per square centimeter at 0.5 V *vs*. RHE.[11–13,41–45] The high crystallinity and intimate ohmic contact with the Cu substrate of Cu_2O may play a significant role in the reproducible large photocurrents observed for the deep red and black samples. Although the samples have different thicknesses which may produce higher resistance affecting charge transport, this effect was completely outweighed by other factors as measured photocurrents increase in the order of black > deep red > red sample. The high activity was attributed further to the highly efficient charge separation induced by the large electric fields generated near the interface, as confirmed by the Mott-Schottky

calculations. It is possible that the *p-P* heterojunction may play a significant role on the efficienct charge separtion.

The stability of the electrodes was studied in chronoamperometry experiments at a fixed potential of 0.25 V *vs*. RHE under chopped illumination periods of 20 s, and the results are presented in Figure 4.10 for various pH conditions. The initially high photocurrents were lost in less than 1 minute, as previously reported by other groups.[8,10,11,46] After 20 minutes of illumination, the samples exhibited stable photocurrents of 0.2, 0.08 and 0.05 mA cm^{-2} for the black, deep red and red samples, respectively, at both pH 4.9 and 6.1. It appears that the most stable condition for the black electrode is under neutral conditions (pH 6.1). The measured photocurrents for the black sample decreased to ca. 16%, 40% and 25% of their initial values in pH 4.9, 6.1 and 10.1, respectively after 600 s of intermittent illumination.

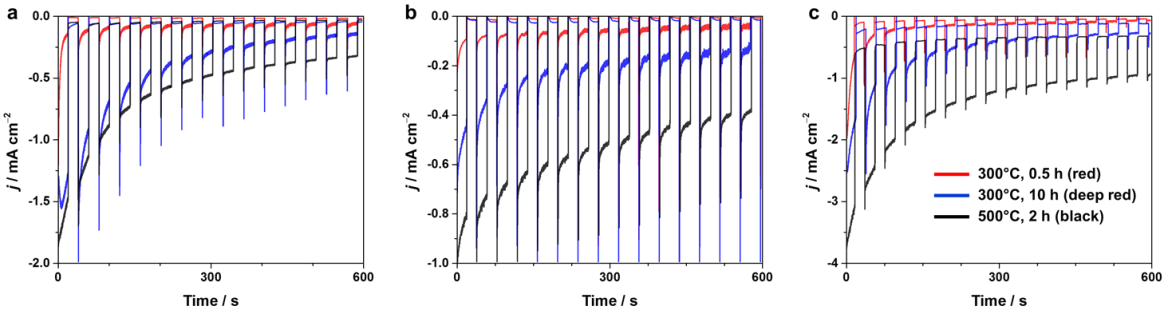

Figure 4.10 Photoelectrochemical stability characterizations of red, deep red and black samples under simulated AM 1.5G solar irradiation at pH 4.9 (a), pH 6.1 (b) and pH 10.1 (c). The stability tests for the electrodes were performed under 20 s illumination and dark periods at a constant potential of 0.25 V *vs*. RHE. (0.5 M Na_2SO_4, Ar saturated).

Increasing the pH appears to improve the stability of the materials; nevertheless, persistent dark currents were observed for the black electrode at 0.25 V *vs*. RHE under alkaline conditions (Figure 4.10c). Based on the photoelectrochemical characterization, it is probable that the photocathodes lost their activity because a significant percentage of the recorded photocurrents originate from the reduction of the Cu oxides on the surface, which are in contact with the electrolyte, as has been suggested in the literature (see Figure 4.11).

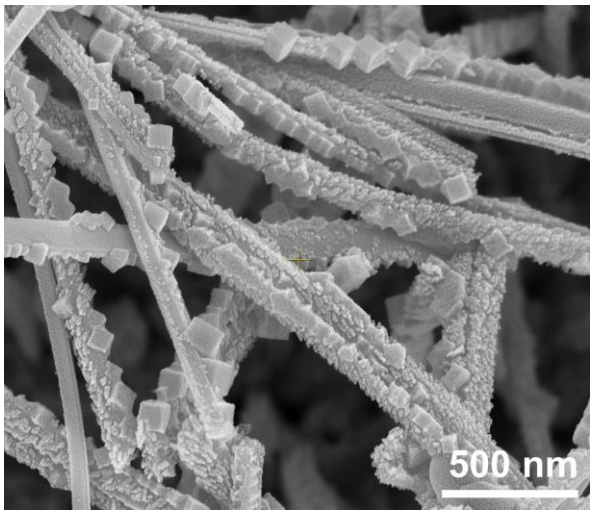

Figure 4.11 Typical SEM micrograph of the black sample after a 20-minute photoelectrochemical stability test. The black sample was subjected to alternating 20 s periods of simulated solar illumination and dark conditions while a constant potential of 0.25 V vs. RHE was applied (AM 1.5G, 0.5 M Na_2SO_4, pH 6.1).

The observed cubic nanoparticle crystals on the surfaces of the nanowires may have originated from the reduction of Cu(II) to Cu(I) and metallic Cu, consistent with a previous report concerning electrodeposited Cu_2O.[10] The observation suggests that the photo-excited electrons generated in the Cu_2O can be collected by CuO and react at the electrolyte interface. This result correlates

with the possibility of electronic communication through the crystals (Cu_2O/CuO) and the plausible formation of a staggered *p-P* heterojunction as discussed earlier based on the Schottky-Mott relation and the UV-Vis spectroscopy results. Indeed, when using airtight single-compartment cells in a three-electrode configuration with online gas chromatography, it was not possible to detect hydrogen although the corresponding photocurrents were within the detection limits of H_2 (0.1 mA cm^{-2}-equivalent), in agreement with other reports in the literature.[8,14,46] In the literature, it was already demonstrated that once Cu_2O was protected from the electrolyte interface, the generated photoelectrons were efficiently collected in an energetically well aligned oxide-catalyst layer inhibiting the reduction of the Cu_2O, and H_2 was produced.[8,11] If a large number of the excited carriers generated under illumination are efficiently collected at the interface and selectively react with protons/water, the efficient production of hydrogen using the composite photocathode seems feasible. Surface protection becomes a common strategy for Cu_2O and other semiconductor materials that are sensitive for photo-corrosion (i.e. multilayer oxide protection using SiO_2, Al_2O_3, ZnO, NiO, TiO_2, etc).[8,11,49,50,51,52,53] A stabilization strategy with a proper water-reduction catalyst similar to the multi-layer protection used recently by Paracchino *et al*. must be employed to obtain quantitative amounts of hydrogen from this semiconductor photocathode system.[8,54]

4.2.7. CO_2 reduction with a Cu-based electrocatalyst

The development of efficient CO_2 conversion is desired because of the growing environmental concerns regarding greenhouse gas emissions.[22] It is well known that polycrystalline Cu metal catalyzes the electrochemical reduction of CO_2 to higher hydrocarbons more actively than other metals. However, this activity comes at the expense of the large overpotential that is required to favor CO_2 reduction over hydrogen evolution. Recently, it has been reported that copper oxides and other metal oxides exhibit higher selectivities than metal electrodes for electrochemical CO_2 reduction.[23,24] The selective design of the metal-oxide surface composition remains an important scientific challenge for the practical large-scale application of the electrocatalysis of CO_2 reduction. The Cu-based composite materials presented in this work could become versatile energy materials with a wide range of applications. Chronopotentiometry experiments with the samples at −1.67 mA cm^{-2} using online gas chromatography (μGC) measurements are presented in Figure 4.12. In the literature, when a Cu plate has been used as the catalyst for the electrochemical reduction of CO_2, a large overpotential (i.e., > 1 V *vs*. RHE) has been required for the production of hydrocarbons.[55] The red sample is a representative example that exhibits some similarities with the metallic case. When a constant current was applied to a red electrode in a two-compartment three-electrode electrolysis cell (0.1 M $KHCO_3$, CO_2 saturated, pH 6.8), a noticeable potential shift was observed during the first three minutes of the experiment (Figure 4.12a).

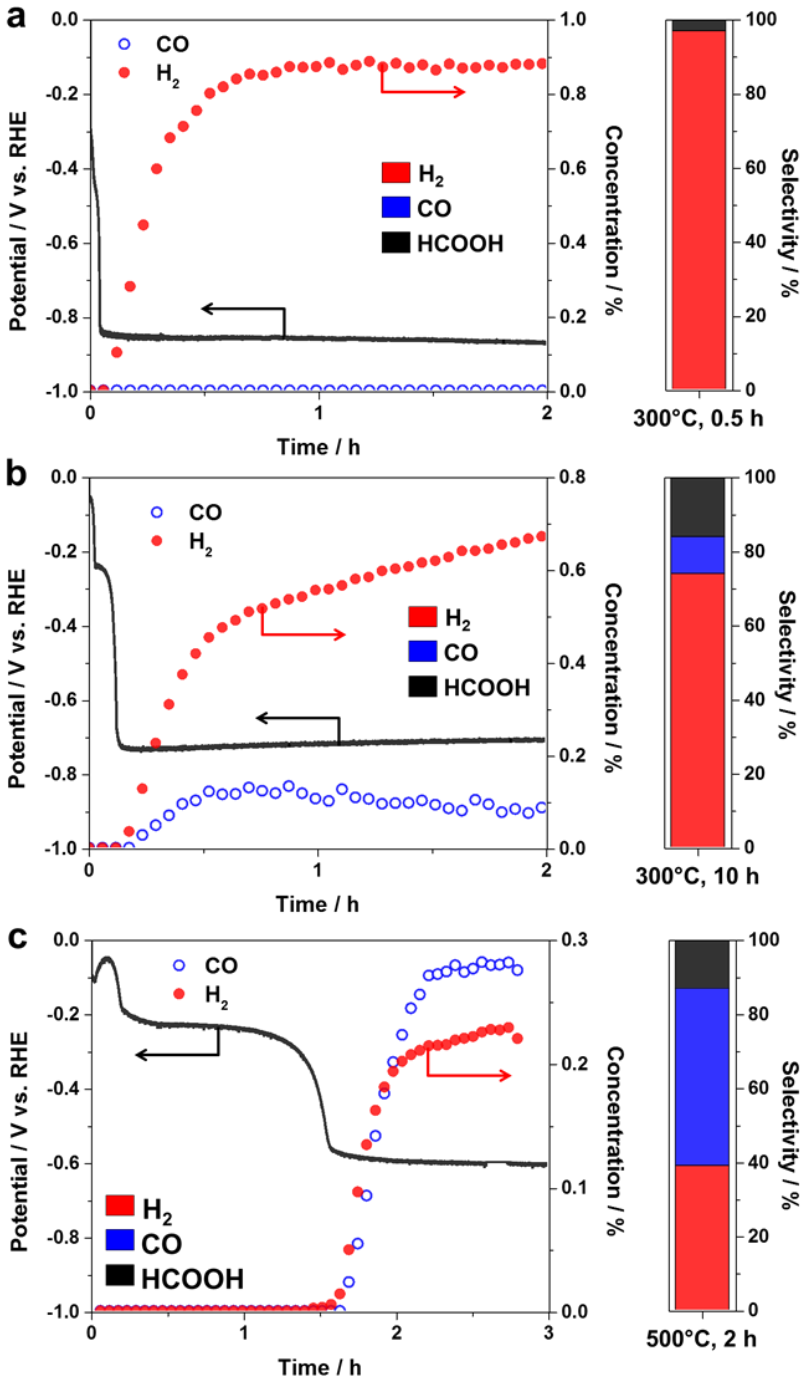

Figure 4.12 Chronopotentiometry experiments at a constant current density of −1.67 mA cm^{-2} for the red (a), deep red (b) and black samples (c) for the electrocatalytic reduction of CO_2. (0.1 M $KHCO_3$, CO_2 saturated, pH 6.8).

During this transition time, the potential changed from 0.2 to −0.85 V *vs*. RHE. This change was attributed to the reduction of most of the oxide layer. Once the reduction was completed and the potential stabilized, it was possible to detect steady rates of hydrogen gas evolution with a Faradaic efficiency greater than 80%. A similar trend was observed for all samples; the steady-state rates of gas generation were detected once the potential reached a stable value. Moreover, it was confirmed *via* high-pressure liquid chromatography (HPLC) that no liquid products were produced before the potential stabilized. The stabilization was achieved after 3, 9 and 120 minutes of galvanostatic experiments for the red, deep red and black samples, respectively, directly correlated with the different oxide thicknesses found in the samples. Interestingly, the potential reached a relatively stable value of −0.85 V *vs*. RHE for the red samples (Figure 4.12a), −0.7 V *vs*. RHE for the deep red (Figure 4.12b) and −0.6 V *vs*. RHE for the black (Figure 4.12c); the latter exhibited a considerable 250 mV shift in the overpotential required for the more selective reduction of CO_2 with respect to the red electrode (i.e., similar metallic-Cu behavior). A significant generation of CO was detected for the deep red and black samples and consistent with the literature.[23] As the oxidizing thermal treatment increased, the selectivity for CO_2 reduction over H_2 production increased. The deep red sample exhibited 75% selectivity for generating H_2 while forming CO with 10% selectivity. The black sample exhibited 60% selectivity for CO_2 reduction under constant-current conditions (−1.67 mA cm^{-2}) with a recorded potential of −0.6 V *vs*. RHE (Table 4.1 and Table 4.2).

Table 4.1 Summary of Faradic efficiencies under potentiostatic control (-0.6 V vs. RHE) for all samples produced and their respective selectivity. Other hydrocarbons were not detected in this study. (0.1 M $KHCO_3$, pH 6.8, saturated CO_2, geometric area of 3 cm^2).

		Faradaic efficiency (η_F)				Selectivity (%)			
	Annealing Time (h)	H_2	CO	HCOOH	CH_3COOH	H_2	CO	HCOOH	CH_3COOH
Cu	-	96	1	3	0	96	1	3	0
300°C	0.5	82	4	7	0	88	4	8	0
300°C	10	50	6	18	0	66	8	24	0
500°C	2	37	23	26	6	40	25	28	7

Table 4.2 Summary of cathodic current density as rate of product formation under constatn potential electrolysis in CO_2 saturated cabonate electrolyte (-0.6 V vs. RHE, 0.1 M $KHCO_3$, pH 6.8, saturated CO_2, geometric area of 3 cm^2).

	Annealing Time (h)	j_{total} mA cm^{-2}	j_{H_2} mA cm^{-2}	j_{CO} mA cm^{-2}	j_{HCOOH} mA cm^{-2}
Cu	-	1.2	1.15	0.01	0.04
300°C	0.5	2.2	1.8	0.1	0.15
300°C	10	2.2	1.1	0.1	0.4
500°C	2	2.6	1	0.6	0.7

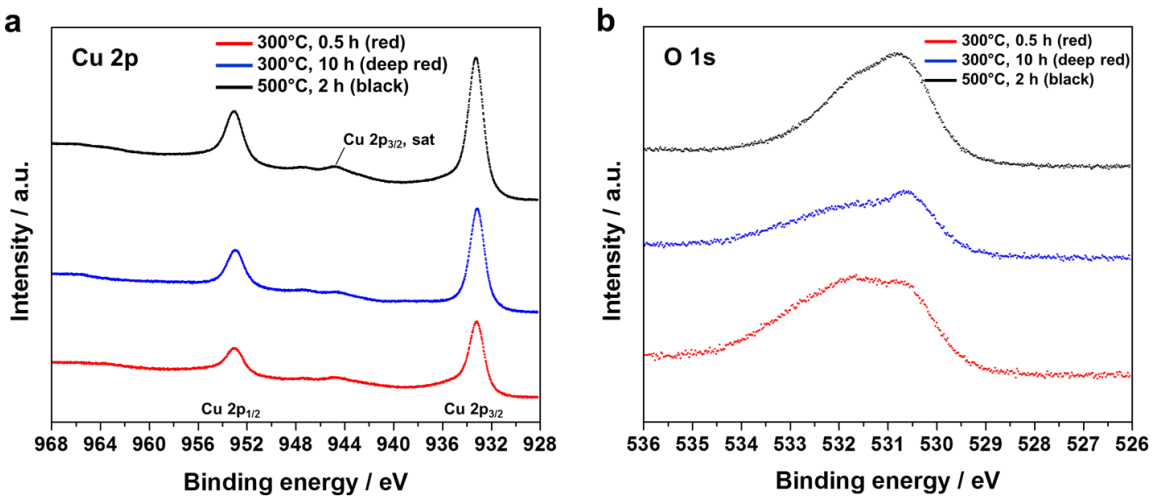

Figure 4.13 Cu 2p (a) and O 1s (b) XPS spectra of the Cu-based electrodes after the electrocatalytic reduction of CO_2. (−1.67 mA cm^{-2}, 2 h, 0.1 M $KHCO_3$, CO_2 saturated, pH 6.8).

Based on the above observations, when the thermally oxidized samples are further treated under galvanostatic conditions for different periods of time, the oxide layers are largely reduced, creating new and selective active sites for the electrochemical reduction of CO_2 that are stable.

The reduced Cu-based electrodes were characterized after the electrocatalytic reduction of CO_2. The surfaces of the electrodes were studied *via* XPS, and the results are presented in Figure 4.13. The Cu 2p region clearly indicates a significant difference in comparison with the pristine samples (Figure 4.4a compared to Figure 4.13a). In all samples, the peaks in the XPS Cu 2p spectrum are shifted toward lower binding-energy values, indicating a more reduced state of the Cu species on the surface. The peak maxima are located at 933.0 and 952.9 eV for Cu $2p_{3/2}$ and Cu $2p_{1/2}$, respectively. These results indicate

the presence of Cu^{+} and Cu^{0} on the surfaces of the electrodes. An unambiguous assignment is not possible, therefore, there is the possibility of the existence of Cu_2O or some metastable oxide surface species.[23] No Cu $2p_{3/2}$ signals attributed to CuO were detected; nevertheless, there is a small broad signal in the black sample that appears in the characteristic satellite position assigned to Cu^{2+} in CuO (i.e., Cu $2p_{3/2}$, sat. at 944.6 eV). The O 1s spectrum is presented in Figure 4.13b. The peaks are significantly broader than those of the pristine samples because of the clear shift of the peak maxima toward 530.5 eV for the lower-binding-energy O 1s peak. As previously discussed, the second peak located at higher binding energies can be attributed to chemisorbed water or hydroxyl oxygen. Most importantly, it has been reported that the differentiation of copper species may involve the use of the O 1s line position.[27] In this case, the shift from 529.9 eV (Figure 4.4b) to 530.7 eV (Figure 4.13b) can be attributed to the presence of Cu^{+} in the form of Cu_2O and the absence of CuO on the surface.[27,29] This result is most likely an indication of the existence of cuprous oxide in the vicinity of metallic copper on the surface after the electrocatalytic reaction under highly reducing conditions.

To clarify the extent of the reduction, bulk XRD diffractograms were obtained from the reduced samples, and the results are presented in Figure 4.14. In contrast to the pristine samples, only Cu-metal diffractions were detected for the red and deep red samples, which is a possible indication of the consumption of the Cu_2O layer to produce Cu^{0}. Interestingly, the (111) and (220) Cu_2O diffractions remained in the black sample after the severe cathodic galvanostatic experiment.

The Cu_2O diffractions in the black sample became smaller and broader after the electrochemical-reduction step, but the signals were not completely lost as in the case of the red and deep red samples, most likely because of the thicker and passivated $Cu_2O/CuO/Cu(OH)_2$ structure.

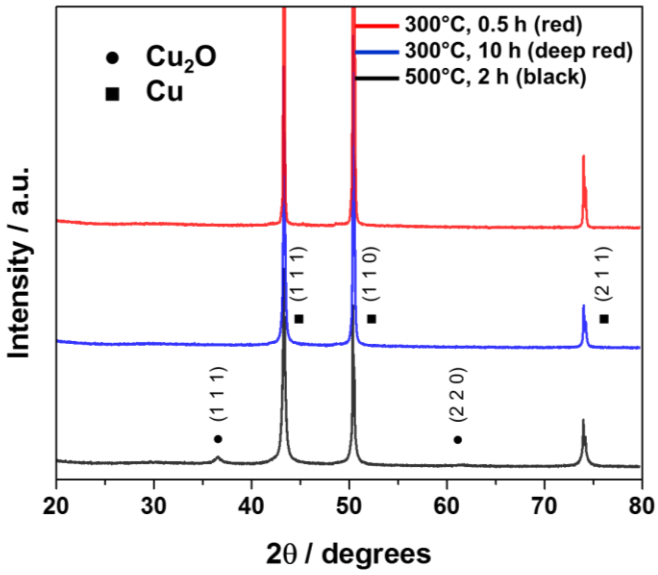

Figure 4.14 XRD patterns of the composite electrodes after the electrocatalytic reduction of CO_2 (−1.67 mA cm^{-2}, 2 h, 0.1 M $KHCO_3$, CO_2 saturated, pH 6.8).

The morphology of the reduced Cu-based electrodes was studied *via* SEM, and the micrographs are shown in Figure 4.15 and Figure 4.16. The formation of nanoparticles (< 10 nm) on the surfaces of the composite materials is observed for the red, deep red and black samples. The broadness of the previously discussed XRD peaks for the Cu_2O phase may originate from the formation of smaller crystals during the cathodic reaction. The original texture and morphology of the pristine samples are mostly intact, but it is possible to observe increased surface roughness.

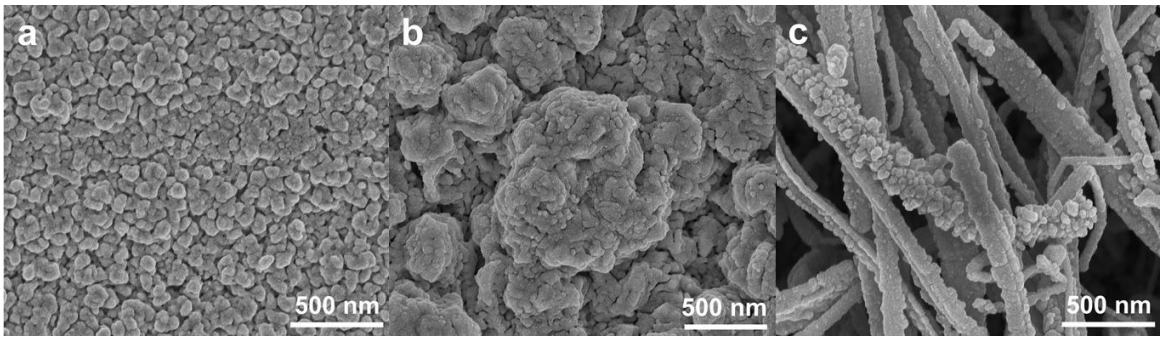

Figure 4.15 Top SEM view of the red (a), deep red (b) and black samples (c) treated under galvanostatic conditions for 2 h for the electrochemical reduction of CO_2. (−1.67 mA cm^{-2}, 0.1 M $KHCO_3$, CO_2 saturated, pH 6.8).

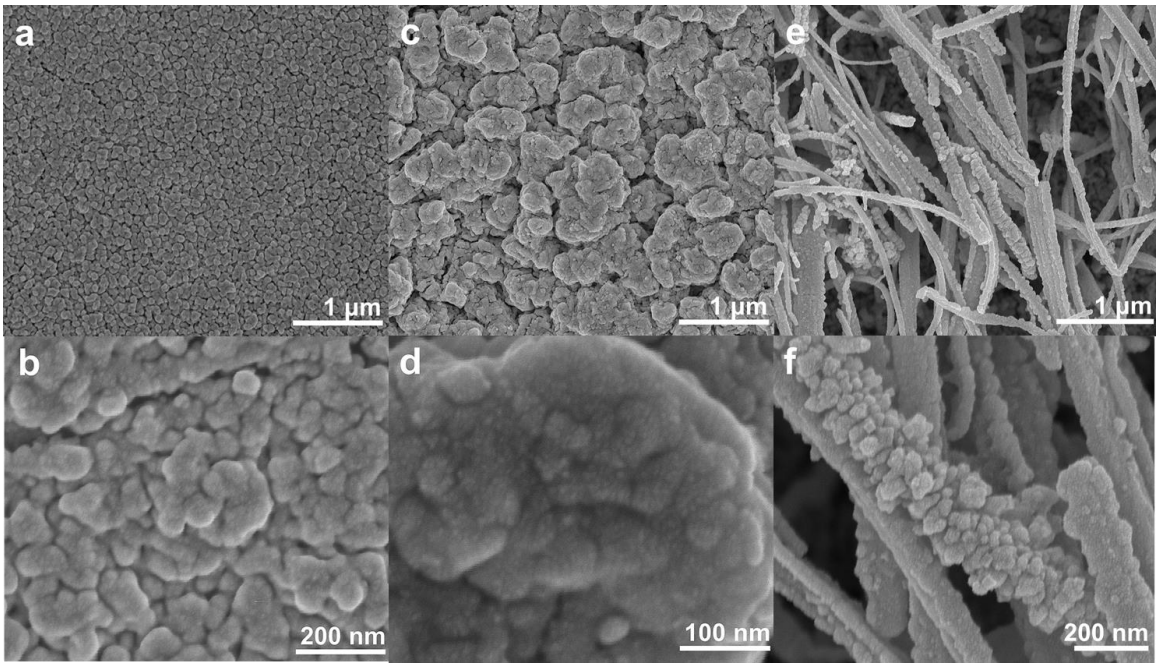

Figure 4.16 SEM images of the red (a), deep red (b) and black samples (c) after exposure to galvanostatic reduction conditions for 2 h during the electrochemical reduction of CO_2. Homogeneously distributed nanoparticles of various sizes were formed on the surfaces of the composites. (1.67 mA cm^{-2}, 0.1 M $KHCO_3$, CO_2 saturated, pH 6.8)

The aggregates observed in the red sample decreased in size, and smaller nanoparticles are homogenously distributed on the surface (Figure 4.16). A similar observation can be made for the deep red sample, where nanoparticles are clearly observed on the surfaces of the grains and the surface area seems to be higher because of the decrease in secondary-particle size (compare Figure 4.2c with Figure 4.16c and examine the details in Figure 4.2d and Figure 4.16d). The nanowires on the surfaces of the black samples are mostly covered by nanoparticles of various sizes (Figure 4.16c). The nanoparticles aggregated on the surfaces of the wires into larger particles while preserving the morphology, although with a small increase in the diameter of the nanowires. It follows that after the electrochemical reduction of CO_2, the surfaces of the oxides in contact with the electrolytes were gradually reduced and formed Cu nanoparticles homogeneously distributed on the surfaces of the electrodes, as confirmed by the XPS, XRD and SEM results. Impedance spectroscopy revealed a significant decrease in the charge-transfer resistance of the samples after the galvanostatic step, most likely an indication of the metallic state at the interface (Figure 4.17).

Based on these observations, different Cu_2O thicknesses were obtained depending on the thermal-oxidation treatment. As the oxidizing treatment increased, a CuO layer and nanowires formed on the outer layer of the electrode and most likely functioned as a passivation layer. During the galvanostatic experiment, when the surface was activated for CO_2 reduction, CuO may have first reduced to Cu_2O,[37] while Cu nanoparticles simultaneously formed on the surface, changing the solid-liquid interface.

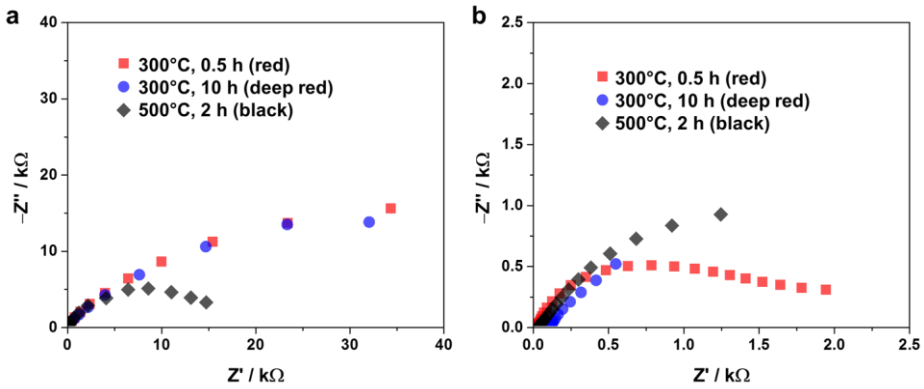

Figure 4.17 Nyquist plots for the red, deep red and black samples at 0.55 V vs. RHE (a) before and (b) after the electrochemical-reduction step for the electrocatalysis of CO_2 reduction. The amplitude of the superimposed AC signal was 10 mV, and the probed frequency range was from 0.01 Hz to 100 kHz. (0.1 M sodium acetate, pH 7.9).

Moreover, once the metallic nanoparticles homogeneously covered most of the surface, the Cu_2O-electrolyte interface required for the reduction reaction was lost. It has been reported that an overpotential as high as −1.3 V relative to the Cu/Cu_2O reversible potential is required to completely reduce the oxide to metallic Cu in CO_2-saturated 0.5 M $KHCO_3$.[56] After the electrocatalytic test, bulk and surface characterizations of the black sample indicated the incomplete reduction of the underlying Cu_2O layer. Recent DFT calculations have shown the beneficial effect of oxygen impurities at the subsurface of Cu(111) improving the binding ability of CO_2 to the altered copper surfaces.[57] Based on the results, a certain threshold oxide thickness along with the CuO passivation layer may be required for the stabilization of such sites that are selectively active for CO_2 reduction. The coexistence of the metallic Cu state with Cu^+ cannot be ruled out for the reason of improved CO_2 reduction as demonstrated in this section. In the electrochemical

CO_2 reduction reaction, CuO_x reduction was found to be essential before CO_2 conversion. Given that pure metallic copper does not facilitate CO_2 reduction under the same conditions (i.e., H_2 evolution is favored), thorough characterization revealed that the coexistence of metal and oxidized copper appears to be beneficial for CO_2 reduction.

4.3. Summary

The chapter discusses the use of a facile, versatile and scalable synthesis process to obtain copper oxide materials along with two different applications for solar fuel generation.

First, using electrochemical methods, XRD, XPS, UV-Vis and SEM, the controlled formation of Cu_2O of various thicknesses was confirmed *via* the careful variation of time and temperature conditions for the thermal oxidation of Cu foils. CuO nanowires can be formed on the surface of the Cu_2O under high oxidation temperature. The electrochemical stability and redox properties of the samples were evaluated at pH 7.9. Impedance spectroscopy was utilized to estimate the energy-band diagrams and elucidate the semiconductive nature of each sample in contact with the electrolyte. As the treatment temperature increased, the carrier concentration in each sample increased (10^{18}-10^{19} cm^{-3}). Hence, a large electric field (≈ 10^6 V cm^{-1}) was formed at the interface. This electric field was significantly larger than the values previously reported in the literature. With extended thermal-oxidation treatments, a large positive shift in the flat-band potential was observed. The PEC evaluations of the pristine Cu-oxide-based photocathodes resulted in large photocurrents. The black samples produced photocurrents of 1 mA cm^{-2} at 0.5 V *vs*. RHE (pH 10.1). Furthermore, the photocurrent onset potential for the black sample was recorded at 0.8 V *vs*. RHE under alkaline conditions. The outstanding photoactivity of the as-obtained electrodes was attributed to the high crystallinity of the Cu_2O layer and the plausible staggered *p*-P heterojunction,

which generated a large electric field that provided efficient charge separation at the semiconductor-electrolyte interface. Although a protection strategy is still required to inhibit the reduction of the oxide species at the electrolyte interface and efficiently produce hydrogen from water reduction, the results exhibited the potential of these composite materials for large-scale PEC applications.

Second, it was demonstrated that when the Cu-based-oxide materials were galvanostatically reduced, they can be used as effective electrocatalysts for the electrochemical reduction of CO_2 at low overpotential with good selectivity. Based on systematic characterization and the electrolysis results, I suggest that longer thermal-oxidation treatments lead to thicker Cu_2O/CuO layers, which are required to stabilize the active sites for selective CO_2 reduction. XRD and XPS spectroscopy provided evidence of the beneficial coexistence of Cu(I) and metallic copper for the selective reduction of CO_2.

4.4. Experimental methods

4.4.1. Photoelectrodes

Cu foils (25 μm in thickness, 99.99%, Sigma-Aldrich) were first cut to the desired electrode size (1×3 cm) and cleaned for several minutes in 1 M HCl. The electrodes were then rinsed with Milli-Q water and dried. The Cu electrodes were tightly wrapped around glass microscope slides and inserted into a muffle furnace under ambient air conditions for thermal oxidation. This procedure was recently reported to produce non-flaking highly crystalline oxide samples in intimate contact

with the Cu substrate.[58] The temperature and time of the electrode treatment were varied from 573 to 773 K and from 0.5 to 10 h, respectively. Electrical wires were attached to the backsides of the copper oxide samples, which were abraded to remove the surface oxide and to ensure ohmic, low-resistance contacts. Epoxy was applied to mask all but the active area of the copper oxide surface for further testing.

4.4.2. Electrochemistry

All electrochemical and PEC procedures were performed using Milli-Q water (18 MΩ). Sodium sulfate (Na_2SO_4, ≥99.99%, Aldrich), sodium acetate (CH_3COONa, NaOAc, ≥99.0%, Sigma-Aldrich), sodium hydroxide (NaOH, 99.99%, Sigma-Aldrich), sulfuric acid (H_2SO_4, 99.999%, Aldrich) and potassium bicarbonate ($KHCO_3$, ≥99.99%, Sigma-Aldrich) were used as received to prepare the required electrolytes. All experiments were performed using a research-grade, multi-channel potentiostat (VMP3, BioLogic Science Instruments). A Pt wire and an Ag/AgCl (saturated KCl) electrode were used as the counter and reference electrodes, respectively. All experiments were recorded against this reference electrode, which was calibrated against an RHE. The results were then reported on the RHE scale using:

(*V vs.* RHE) = (*V vs*. Ag/AgCl) + 0.197 + 0.0591*pH

The CV experiments were performed using a regular one-compartment electrochemical cell with a three-electrode configuration. Each Cu-oxide-based

sample was used as the working electrode without further modification. During the experiments, it was ensured that only the desired active area was in contact with the electrolyte. The electrical contact was established by polishing one side of the electrode until a clean connection was obtained with the Cu underlayer. The CV results were recorded at 5 mV s^{-1} (except when noted) using a 0.1 M NaOAc solution (pH 7.9).

4.4.3. Electrochemical impedance spectroscopy

The EIS was performed in the dark using a three-electrode cell and 0.1 M NaOAc (pH 7.9). The pH of the electrolyte was selected based on the Pourbaix diagram of Cu to increase the stability of the system. Moreover, the experimental potential range was selected based on the results obtained from the CV characterization (black lines in Figure 3) and considering the pH-potential thermodynamics. The samples generated Nyquist plots with characteristic depressed semicircles at fixed potentials, where no faradic processes were detected over a wide frequency range (0.1 Hz to 100 kHz, Figure S2). Thus, a modified Randles equivalent circuit with a constant-phase element was used to electrically approximate the semiconductor-electrolyte interface. The amplitude of the AC signal applied to the system was 10 mV, and the probed frequency range for the Mott-Schottky calculations was 1-100 kHz. Based on the frequency response (Figure S3), high frequency values were selected for the Mott-Schottky analysis (1-10 kHz).

4.4.4. Photoelectrochemistry

The characterization of the samples was performed in 0.5 M Na_2SO_4 (pH 4.9, adjusted with 2 M H_2SO_4) under simulated AM 1.5G solar irradiation calibrated to 60 mW cm^{-2} over the range 300-800 nm. The CV results were recorded at 10 mV s^{-1} under defined periods of dark and illuminated conditions. The PEC stability tests were recorded for the same electrolyte conditions (0.5 M Na_2SO_4, pH 4.9) and at a fixed potential (0.25 V *vs*. RHE) for 20 minutes with an illumination time of 20 s.

All electrolytes were purged for 30 minutes with Ar (99.9999 %) before and during the experiments (i.e., CV, EIS and PEC).

4.4.5. Electrocatalytic CO_2 reduction reaction

The Cu-based electrodes were galvanostatically reduced with a constant current of −5 mA (exposed geometric area: 3 cm^2) in a 0.1 M $KHCO_3$ electrolyte saturated with CO_2 (pH 6.8). Chronopotentiometry was recorded during the galvanostatic reduction of the electrode. The CO_2 electro-reduction experiments were performed in an airtight, two-compartment electrochemical cell. The Pt-wire counter electrode was isolated from the main cell using a ceramic frit, and the same electrolyte was used in both compartments. The cathodic compartment was saturated with CO_2 (99.995%) at 5 sccm for 30 minutes before and during the electrolysis runs. The gas mixture was delivered directly to the sampling loop of a gas chromatograph (μGC, T-3000 SRI instruments). Sampling points were

collected every 3 minutes, and the gaseous products were analyzed using packed MolSieve 5A and packed HaySep Q columns coupled with thermal conductivity detectors (TCD). Ar (99.9999%) and He (99.9999%) were used as the carrier gases for the analysis. The liquid products (HCOOH and CH_3COOH) were analyzed using a high-pressure liquid chromatography (HPLC, Agilent technologies) system equipped with Agilent 1200, 1260 and 1290 Infinity liquid chromatography technology. All experiments were performed at room temperature (298 K) and under atmospheric conditions (101.3 kPa).

4.5. REFERENCES

1 Harriman, *Philos. Trans. A. Math. Phys. Eng. Sci.*, **2013**, 371, 20110415.

2 K. Takanabe and K. Domen, *Green*, **2011**, 1, 313–322.

3 Z. Chen, T. F. Jaramillo, T. G. Deutsch, A. Kleiman-Shwarsctein, A. J. Forman, N. Gaillard, R. Garland, K. Takanabe, C. Heske, M. Sunkara, E. W. McFarland, K. Domen, E. L. Miller, J. A. Turner, H. N. Dinh, *J. Mater. Res.*, **2011**, 25, 3–16.

4 S. C. Roy, O. K. Varghese, M. Paulose, C. A. Grimes, *ACS Nano*, **2010**, 4, 1259–1278.

5 T. L. Frölicher, M. Winton, and J. L. Sarmiento, *Nat. Clim. Chang.*, **2014**, 4, 40–44.

6 G. Centi, E. A. Quadrelli, and S. Perathoner, *Energy Environ. Sci.*, **2013**, 6, 1711–1731.

7 Y. Chen and M. W. Kanan, *J. Am. Chem. Soc.*, **2012**, 134, 1986–1989.

8 Paracchino, V. Laporte, K. Sivula, M. Grätzel, E. Thimsen, *Nat. Mater.*, **2011**, 10, 456–461.

9 M. G. Walter, E. L. Warren, J. R. McKone, S. W. Boettcher, Q. Mi, E. a Santori, and N. S. Lewis, *Chem. Rev.*, **2010**, 110, 6446–6473.

10 1A. Paracchino, J. C. J. Brauer, J.-E. Moser, E. Thimsen, M. Grätzel, *J. Phys. Chem. C*, **2012**, 116, 7341–7350.

11 G. Morales-Guio, S. D. Tilley, H. Vrubel, M. Grätzel and X. Hu, *Nat. Commun.*, **2014**, 5, 3059.

12 Li, Y. Li, and J.-J. Delaunay, *ACS Appl. Mater. Interfaces*, **2014**, 6, 480–486.

13 Z. Zhang and P. Wang, *J. Mater. Chem.*, **2012**, 22, 2456.

14 P. E. De Jongh, D. Vanmaekelbergh, and J. J. Kelly, *Chem. Mater.*, **1999**, 11, 3512–3517.

15 Morales-Acevedo, K. Akimoto, S. Ishizuka, M. Yanagita, Y. Nawa, G. K. Paul, T. Sakurai, *Sol. Energy*, **2006**, 80, 715–722.

16 S. Ishizuka, T. Maruyama, and K. Akimoto, *Jpn. J. Appl. Phys.*, **2000**, 39, L786–L788.

17 P. Singh, N. R. Neti, A. S. K. Sinha, O. N. Srivastava, *J. Phys. Chem. C*, **2007**, 111, 1638–1645.

18 Caballero-Briones, J. M. Artés, I. Díez-Pérez, P. Gorostiza, F. Sanz, *J. Phys. Chem. C*, **2009**, 113, 1028–1036.

19 Y. Tan, X. Xue, Q. Peng, H. Zhao, T. Wang, Y. Li, *Nano Lett.*, **2007**, 7, 3723–3728.

20 L. Gou and C. J. Murphy, *Nano Lett.*, **2003**, 3, 231–234.

21 M. S. Prévot and K. Sivula, *J. Phys. Chem. C*, **2013**, 117, 17879–17893.

22 D. T. Whipple and P. J. A. Kenis, *J. Phys. Chem. Lett.*, **2010**, 1, 3451–3458.

23 C. W. Li and M. W. Kanan, *J. Am. Chem. Soc.*, **2012**, 134, 7231–7234.

24 Y. Chen, C. W. Li, and M. W. Kanan, *J. Am. Chem. Soc.*, **2012**, 134, 19969–19972.

25 X. Jiang, T. Herricks, and Y. Xia, *Nano Lett.*, **2002**, 2, 1333–1338.

26 K. Mizuno, M. Izaki, K. Murase, T. Shinagawa, M. Chigane, M. Inaba, A. Tasaka, Y. Awakura, *J. Electrochem. Soc.*, **2005**, 152, C179–C182.

27 N. S. McIntyre, *J. Vac. Sci. Technol.*, **1981**, 18, 714.

28 C.-K. Wu, M. Yin, S. O'Brien, and J. T. Koberstein, *Chem. Mater.*, **2006**, 18, 6054–6058.

29 S. Poulston, P. M. Parlett, P. Stone, M. Bowker, *Surf. Interface Anal.*, **1996**, 24, 811–820.

30 M. Yin, C.-K. Wu, Y. Lou, C. Burda, J. T. Koberstein, Y. Zhu, S. O'Brien, *J. Am. Chem. Soc.*, **2005**, 127, 9506–9511.

31 E. Rakhshani, *Solid. State. Electron.*, **1986**, 29, 7–17.

32 T. D. Golden, M. G. Shumsky, Y. Zhou, R. A. VanderWerf, R. A. Van Leeuwen, J. A. Switzer, *Chem. Mater.*, **1996**, 8, 2499–2504.

33 M. Heinemann, B. Eifert, and C. Heiliger, *Phys. Rev. B*, **2013**, 87, 115111.

34 C. J. Engel, T. A. Polson, J. R. Spado, J. M. Bell, A. Fillinger, *J. Electrochem. Soc.*, **2008**, 155, F37–F42.

35 J. Ambrose, R. G. Barradas, and D. W. Shoesmith, *J. Electroanal. Chem. Interfacial Electrochem.*, **1973**, 47, 47–64.

36 J. M. M. Droog, C. A. Alderliesten, P. T. Alderliesten, G. A. Bootsma, *J. Electroanal. Chem. Interfacial Electrochem.*, **1980**, 111, 61–70.

37 S. Nakayama, A. Kimura, M. Shibata, S. Kuwabata, T. Osakai, *J. Electrochem. Soc.*, **2001**, 148, B467–B472.

38 S. Nakayama, T. Kaji, M. Shibata, T. Notoya, T. Osakai, *J. Electrochem. Soc.*, **2007**, 154, C1-C6.

39 S. T. Mayer, *J. Electrochem. Soc.*, **1992**, 139, 426–434.

40 R. Babić, M. Metikoš-Huković, and M. Lončar, *Electrochim. Acta*, **1999**, 44, 2413–2421.

41 M. Metikoš-Huković, R. Babić, and I. Paić, *J. Appl. Electrochem.*, **2000**, 30, 617–624.

42 P. E. de Jongh, D. Vanmaekelbergh, and J. J. Kelly, *Chem. Commun.*, **1999**, 1069–1070.

43 K. Gelderman, L. Lee, and S. W. Donne, *J. Chem. Educ.*, **2007**, 84, 685–688.

44 P. Koffyberg, *J. Appl. Phys.*, **1982**, 53, 1173–1177.

45 E. Heltemes, *Phys. Rev.*, **1966**, 141, 803–805.

46 D. Handoko and J. Tang, *Int. J. Hydrogen Energ.*, **2013**, 38, 13017–13022.

47 J. W. Hodby, T. E. Jenkins, C. Schwab, H. Tamura, D. Trivich, *J. Phys. C Solid State Phys.*, **1976**, 9, 1429–1439.

48 W. Schmickler and E. Santos, in *Interfacial electrochemistry*, Springer Berlin Heidelberg, Berlin, Heidelberg, 2nd Editio., **2010**, 131, 117–131.

49 Orecchini, J.-N. Nian, C.-C. Hu, H. Teng, *Int. J. Hydrogen Energy*, **2008**, 33, 2897–2903.

50 S. D. Tilley, M. Schreier, J. Azevedo, M. Stefik, M. Grätzel, *Adv. Funct. Mater.*, **2014**, 24, 303–311.

51 C-Y. Lin, Y-H. Lai, D. Mersch, E. Reisner, *Chem. Sci.*, **2012**, 3, 3482–3487.

52 B. Seger, T. Pedersen, A. B. Laursen, P. C. K. Vesborg, O. Hansen, I. Chorkendorff, *J. Am. Chem. Soc.*, **2013**, 135, 1057–1064.

53 Z. Zhang, R. Dua, L. Zhang, H. Zhu, H. Zhang, P. Wang, *ACS Nano*, **2013**, 7, 1709–1717.

54 Paracchino, N. Mathews, T. Hisatomi, M. Stefik, S. D. Tilley, M. Grätzel, *Energy Environ. Sci.*, **2012**, 5, 8673–8681.

55 W. Tang, A. A. Peterson, A. S. Varela, Z. P. Jovanov, L. Bech, W. J. Durand, S. Dahl, J. K. Nørskov, I. Chorkendorff, *Phys. Chem. Chem. Phys.*, **2012**, 14, 76–81.

56 M. Le, M. Ren, Z. Zhang, P. T. Sprunger, R. L. Kurtz, and J. C. Flake, *J. Electrochem. Soc.*, **2011**, 158, E45–E49.

57 J. Xiao, T. Frauenheim, A. Kuc and T. Heine, *J. Mater. Chem. A*, **2014**, 2, 4885-4889.

58 F. Mumm and P. Sikorski, *Nanotechnology*, **2011**, 22, 105605.

CHAPTER 5

5. Conclusion and Outlook

Harvesting solar energy in the form of chemical bonds seems to be the most viable option to sustainably supply energy to the world. To this end, photocatalytic overall water splitting is the only technology that does not generate any carbon footprint. For practical large-scale energy conversion, photocatalysis is the most promesing cost-competitive way to generate clean hydrogen at a disruptive price in the energy market. Since the influential work on TiO_2 by Honda and Fujishima. Research in photocatalytic water splitting (i.e. artificial photosynthesis) has exploded but a viable commercial photocatalyst has not been developed yet. Due to the complexity of the problem, highly interdisciplinary groups must be formed to solve this problem. Over the past 40 years, photocatalysis has improved substantially, however more work needs to be done before it can be used to solve our global energy needs.

Theoretical simulations were presented to understand the low efficiency of particulate semiconductors. The numerical results presented in Chapter 2 indicate that typical photocatalytic devices generate electronic structures that are not beneficial for charge separation. The dispersion of metal nanoparticles on the semiconductor surface is done with the objective of efficiently collecting electrons; nevertheless, the semiconductor-liquid junction generates electric fields that obscure the electronic pathway of the electrons (for the *n*-type case). Actually,

there is no scientific control of the electronic profiles intended for charge transport and the carriers transfer by random motion based on diffusion. In this work, the calculations showed a pinch-off effect (i.e. energy barrier) that may inhibit the electron or hole transfer (majority carriers) to the active sites in *n*-type and *p*-type semiconductors, respectively. For the first time, quantum efficiency trends were provided as a result of the calculations. The calculated trends, under the rigid set of assumptions presented in Chapter 2, show that it was not possible to achieve quantum efficiencies larger than 35.7% for a single absorbing unit (for the ideal case). With the assumption of a simple exponential decay via the absorption coefficient, it was shown that a photocatalytic slurry should be able to achieve 71% $AQE_{300\text{-}550nm}$ (9.8% STH) without considering the kinetic losses under AM 1.5G.

This contribution represents one of the few examples in the literature for the simulation of particulate semiconductors. The proposed reasons behind non-ideal quantum efficiencies are as follows.

- In general, the semiconductor-electrolyte junction inhibits majority charge injection into the electrocatalysts. For the *n*-type case, a Schottky-type of barrier was observed even if the metal hydrogen site is negatively charged. Simply, the *device design* must be changed. For four decades, researchers have used dispersed catalysts on the surface of semiconductor particles. The heterogeneous catalysis approach is not optimal for solar energy conversion via photocatalysis.

- Potential gradients used for charge separation are limited and constrained near the surface of the semiconductor particle. Nonetheless, charge generation occurs in the bulk of the material due to the large penetration depth of sunlight in most semiconductor materials ($\lambda \geq 450$ nm). Charge separation in the bulk may limit the photocatalytic efficiency. Unless the quality of the crystal is improved, with low defect density, the probability of using the carriers for reaction is low. Synthesis of highly *pure* semiconductors in powder form is technologically challenging. Hence, to use intrinsically defective materials (high surface areas) it is necessary to design effective electronic strategies for charge separation via interface engineering.

One of the most significant assumptions of the simulations performed in this work is that the photocatalytic particles have perfect electrocatalysts on their surface. The design of active and selective catalysts for the generation of hydrogen in the presence oxygen is of paramount importance. It is also a big challenge to precisely control the size of immobilized non-noble nanoparticles under the 10 nm range. Chapter 3 presented the first successful example of the synthesis of WC nanoparticles on a small scale (5-10 nm). A systematic protocol was developed to obtained different carbide phases with high surface area (WC and W_2C). Following the report of this generalized method, other researchers reported the successful synthesis of transition metal carbides and nitrides nanoparticles (e.g. Mo_2C, TaC, Ta_2CN and TaN). The tungsten carbide materials exhibited significant activity for hydrogen evolution and oxidation reactions.

At the time of the discovery, nanoparticles of WC were one of the most active non-noble metal electrocatalysts with a benchmark overpotential values of $\eta_{3\ \mathrm{mA\ cm^{-2}}}$ = 78 mV and $\eta_{10\ \mathrm{mA\ cm^{-2}}}$ = 122 mV with high stability and one of the lowest Tafel slopes (84 mV dec^{-1}). To this day and to the best of my knowledge, the WC nanoparticles presented in Chapter 3 are the most active metal carbide materials for the electrocatalytic generation of hydrogen. Particularly relevant for photocatalysis, WC was not active for the reduction of oxygen (i.e. water-forming reaction). Photocatalytic overall water splitting was achieved using the monocarbide phase (WC) supported on Na-doped $SrTiO_3$ photocatalyst in pure water. As a proof-of-concept, UV-light driven water splitting was accomplished using a selective WC electrocatalyst; the first example of overall water splitting without the use of a metal oxide layer to inhibit the reverse reaction of water-formation.

Systematic kinetic electrochemical investigations provide a strong foundation for the evaluation of potential cocatalysts for photocatalytic water splitting. As discussed in Chapter 1, the study of photocatalysis may be separated and independently studied via electrochemical and photoelectrochemical methods for electrocatalysts and semiconductors, respectively. In Chapter 3, a generalized protocol for materials development was discussed in a top-down type of approach. Using the pyramid analogy presented in Chapter 1, it is possible to analyze (to dissect) photocatalysis and start at the *top* of the problem with the aid of electrochemistry techniques. From this view, a potentiostat becomes a perfect semiconductor that the researcher can control; thus, allowing us to focus on

catalysis and mass-transport problems without the effects of the semiconductor interface.

On the other hand, photoelectrochemistry can be use to study intrinsic semiconductor properties. Chapter 4 focus on the development of a highly crystalline, benign and earth abundant *p*-type semiconductors. A comprehensive characterization of the Cu_2O/CuO composites *p*-type photoelectrodes was presented. Following the same aforementioned top-down approach, the Cu-based materials were reported as potential candidates for electrocatalysis or as semiconductors for photocatalytic water splitting; depending on the required application. When used as photoelectrodes, they are capable of generating photocurrents with onset potentials of 0.8 V vs. RHE (pH 10.1). When used as electrocatalysts, the reduced Cu-based materials reduce CO_2 to CO and HCOOH at low overpotentials. The study demonstrated via detailed characterizations that there was an incomplete reduction of the CuO_x composite. This work proposes that the outermost oxidized Cu layer may be required to stabilize active and selective sites for CO_2 electroreduction that compete with water reduction. It is not possible to rule out the stabilization of Cu^+ near metallic Cu sites or the existence of oxygen impurities at the subsurface, perturbing the active surface and creating a beneficial synergetic effect for the improved the binding and catalysis of CO_2.

Future work may attempt to elucidate the role of the energetic barriers formed at the nanoscale interfaces and their impact in water splitting. The manipulation of the band bending may be the limiting factor for efficient charge transfer. The fundamental understanding of the effects of the degree of band

bending in photocatalytic activity is yet to be established. The use of local probe techniques in the nanoscale will elucidate the mechanisms involved in potential shifts. Direct imaging of potentials under dark and illumination may be obtained from *in-situ/operando* characterizations. Ideally, local measurement of the built-in potential (i.e. energy barrier height) under dark and illumination in environmental conditions (i.e. electrolytes) could be a direct indication of the system's efficiency for water splitting. Quantification of the potential with atomic scale resolution at the surface of the photocatalyst semiconductor can provide insights into the mechanisms for charge transfer. Rationalization of the local potential shifts at the nanoscale in a photocatalytic system with its photocatalytic activity for water splitting will provide a coherent design of nanostructured photocatalysts. Such studies will answer fundamental questions about the photocatalytic phenomena.

Although it is challenging, it is critical to understand the electronic structures occurring at the interface and how they affect the photocatalytic rates. I propose that by understanding the potential shifts generated at the different interfaces, proper manipulation of the band-bending is possible. Thus, the rational design of efficient photocatalytic systems for overall water splitting seems feasible.

LIST OF PUBLICATIONS

(*In preparation*) “An oxygen tolerant Pt surface for water splitting”
A. T. Garcia-Esparza, T. Shinagawa, S. Ould-Chikh, X. Y. Peng, D. Nordlund, T. C. Weng, D. Sokaras, J. Kubota, K. Takanabe, **2016.**

(8) “Cu-Sn Bimetallic Catalyst for Selective Aqueous Electroreduction of CO_2 to CO”
S. S. Akhtar, A. T. Garcia-Esparza, A. Jedidi, L. Cavallo, K. Takanabe, *ACS Catal.,* **2016**, DOI: 10.1021/acscatal.6b00269

(7) “A simplified theoretical guideline for overall water splitting using photocatalyst particles”
A. T. Garcia-Esparza, K. Takanabe, *J. Mater. Chem. A,* **2016**, 4, 2894-2908.

(6) “Insight on Tafel slopes from a microkinetic analysis of aqueous electrocatalysis for energy conversion”
T. Shinagawa, A. T. Garcia-Esparza, K. Takanabe, *Sci. Rep.*, **2015**, 13801.

(5) “Tethering metal ions to photocatalyst particulate surfaces via bifunctional molecular linkers for efficient hydrogen evolution”
W. Yu, T. Isimjan, S. Del Gobbo, D. H. Anjum, S. Abdel-Azeim, L. Cavallo, A. T. Garcia-Esparza, K. Domen, W. Xu, K. Takanabe, *ChemSusChem*, **2014**, 7, 2575–2583.

(4) “Mechanistic switching by hydronium ion activity for hydrogen evolution and oxidation over polycrystalline Pt disk and Pt/C electrodes”
T. Shinagawa, A. T. Garcia-Esparza, K. Takanabe, *ChemElectroChem*, **2014**, 1, 1497–1507.

(3) “Photoelectrochemical and electrocatalytic properties of thermally oxidized copper oxide for efficient solar fuel production”
A. T. Garcia-Esparza, K. Limkrailassiri, F. Leroy, S. Rasul, W. Yu, L. Lin, K. Takanabe, *J. Mater. Chem. A*, **2014**, 2, 7389–7401.

(2) “Synthesis of Tantalum Carbide and Nitride Nanoparticles using a Reactive Mesoporous Template for Electrochemical Hydrogen Evolution”
N. S. Alhajri, H. Yoshida, D. H. Anjum, A. T. Garcia-Esparza, J. Kubota, K. Domen, K. Takanabe, *J. Mater. Chem. A,* **2013**, 1, 12606–12616.

(1) “Tungsten carbide nanoparticles as efficient cocatalysts for photocatalytic overall water splitting”
A. T. Garcia-Esparza, D. Cha, Y. Ou, J. Kubota, K. Domen, K. Takanabe, *ChemSusChem*, **2013**, 6, 168–181.

LIST OF CONFERENCES

2016 KCC Symposium Catalysis for Artificial Photosynthesis
(*Second place poster*) KAUST, Saudi Arabia.

2015 KCC Scientific Advisory Board Meeting
(selected *poster presentation*) KAUST, Saudi Arabia.

2015 KCC Catalytic carbon and hydrogen management symposium
(*poster presentation*) KAUST, Saudi Arabia.

2015 KAUST-Waseda University joint workshop
(*oral presentation*) KAUST, Saudi Arabia.

2014 226th Electrochemical Society, ECS meeting
(*oral presentation*) Cancun, Mexico.

2014 20th IPS - International Conference on Photochemical Conversion and Storage of Solar Energy
(*oral presentation*) Berlin, Germany.

2014 Berkeley Sensors & Actuators Center, BSAC seminar
(*Invited speaker*) Berkeley, USA.

2014 Joint Center for Artificial Photosynthesis, JCAP
(*summer workshop*) Berkeley, USA.

2013 XI European Congress on Catalysis, EuropaCat-13
(*oral presentation*) Lyon, France.

2013 1st International workshop on Energy Storage
(*First place poster*) KAUST, Saudi Arabia.

2013 Material Research Society, MRS Spring meeting
(oral presentation) San Francisco, USA

2013 President's International Advisory Council, IAC-session
(*selected poster presentation*) KAUST, Saudi Arabia.

2012 15th International Congress on Catalysis, ICC
(poster presentation) Munich, Germany.

VITA

Angel Tonatiuh Garcia Esparza was born in Torreon, Mexico, on January 3rd, 1987. He went on to obtain his Bachelor of Science degree in Mechatronics Engineering at Tecnologico de Monterrey (Mexico) in 2008. In September 2009, he entered Graduate School at King Abdullah University of Science and Technology (KAUST) in Saudi Arabia. Here, he earned a Master of Science degree in Environmental Science and Engineering in 2011 and a Doctorate of Philosophy in Chemical Science in 2016 under the guidance of Prof. Kazuhiro Takanabe.